SYNTHESIS OF NANOSTRUCTURED CATALYSTS FOR LOW TEMPERATURE METHANE COMBUSTION

by

Yiling Dai

B.Sc., Nankai University, 2015

A THESIS SUBMITTED IN PARTIAL FULFILLMENT OF

THE REQUIREMENTS FOR THE DEGREE OF

DOCTOR OF PHILOSOPHY

in

THE FACULTY OF GRADUATE AND POSTDOCTORAL STUDIES

(Chemistry)

THE UNIVERSITY OF BRITISH COLUMBIA

(Vancouver)

December 2019

The following individuals certify that they have read, and recommend to the Faculty of Graduate and Postdoctoral Studies for acceptance, the dissertation entitled:

Synthesis of Nanostructured Catalysts for Low Temperature Methane Combustion

submitted by Yiling Dai in partial fulfillment of the requirements for

the degree of Doctor of Philosophy

in The Faculty of Graduate and Postdoctoral Studies (Chemistry)

Examining Committee:

Mark MacLachlan
Co-supervisor

Michael Wolf
Co-supervisor

Andrew MacFarlane
Supervisory Committee Member

Madjid Mohseni
University Examiner

Dan Bizzotto
University Examiner

Additional Supervisory Committee Members:

Sarah Burke
Supervisory Committee Member

Curtis Berlinguette
Supervisory Committee Member

Abstract

The number of natural gas vehicles (NGVs) is increasing rapidly due to the growing concern for the environmental impact of gasoline and diesel-powered automobiles. However, the main component of natural gas, methane, is a potent greenhouse gas. Thus, removal of unburned methane from the exhaust of NGVs is important and this requires catalysts for methane oxidation at low temperature (less than 500-550 °C).

In this thesis, different types of nanostructured catalysts were developed. Noble metal catalysts, like Pd-based catalysts, and non-precious metal catalysts, such as spinel catalysts, were synthesized, characterized and examined for catalytic methane combustion.

To enhance the catalytic activity, $NiCo_2O_4$ catalysts with a unique bowtie-structure were synthesized. The morphology, growth mechanism, catalytic and kinetic performance were explored. These $NiCo_2O_4$ catalysts exhibited excellent activity for methane oxidation, but were unable to maintain their performance in the presence of water vapor.

In addition, active site distribution plays an important role on catalytic activity. Taking this into account, MnO_2 aerogels supporting precious or non-precious metal oxide catalysts were explored. Both types of catalysts showed enhanced catalytic activity. The hydrothermal stability and sulfur tolerance were studied for PdO/MnO_2, and the deactivation mechanism was explored.

Besides outstanding activity, commercial catalysts must be stable in practical usage. In order to improve the stability of Pd-based catalysts, nanostructured materials were prepared by embedding Pd into CeO_2 inside the channels of a mesoporous host, SBA-15. It was found that the materials showed excellent catalytic activity and improved activity after hydrothermal treatment. However, their performance in the presence of water vapor still needs to be enhanced.

Furthermore, to solve the problem of poor water stability and sulfur tolerance, $CoCr_2O_4$ composites were selected as catalysts. Nanospheres of $CoCr_2O_4$ were prepared by a straightforward solvothermal method. These materials achieved 100% methane conversion below 500 °C and they also displayed excellent stability even in the presence of 10% water vapor and 5 ppm SO_2. Furthermore, the $CoCr_2O_4$ catalysts were scaled up and coated onto cordierite monoliths via a modified wash-coating method. The coated monolith showed excellent activity and stability, and these materials have potential to be applied for NGVs.

Lay Summary

Environmental issues like global warming and pollution are growing concerns around the world. The transportation sector contributes about 15% of the total greenhouse gas emissions from society. Therefore, it is crucial to develop vehicles that use clean energy. Natural gas vehicles (NGVs) have higher fuel efficiency and produce less CO_2 and pollution than gasoline and diesel-powered vehicles. However, unburned methane present in the exhaust of NGVs is a problem since methane is a serious greenhouse gas that is much worse than CO_2. The goal of this thesis is to develop active and stable catalysts for methane combustion at lower temperature (< 500 °C). New nanostructured materials were created that are effective at oxidizing methane at low temperature. These catalysts showed excellent stability to water vapor and other exhaust components. The new materials developed in this thesis may be applied to catalytic convertors in NGVs or to other industrial applications.

Preface

This thesis contains five chapters. All the work was conducted under the guidance of Prof. Mark MacLachlan and Prof. Michael Wolf. Catalytic measurements and analysis involved collaboration with Prof. Kevin Smith and his coworkers Chujie Zhu, Dr. Haiyan Wang and Dr. Shida Liu in the Department of Chemical and Biological Engineering, UBC. X-ray photoelectron spectroscopy (XPS) measurements were performed by Dr. Ken Wong in the Interfacial Analysis & Reactivity Laboratory, UBC. Elemental analyses were conducted at the UBC Mass Spectrometry Centre. Scanning Transmission Electron Microscopy experiments were carried out at 4D LABS, Simon Fraser University (SFU) with the assistance of Dr. Xin Zhang.

Chapter 2 has been published as: Dai, Y.; Pavan Kumar, V.; Zhu, C.; MacLachlan, M. J.; Smith, K. J.; Wolf, M. O., Mesoporous Silica-Supported Nanostructured PdO/CeO_2 Catalysts for Low-Temperature Methane Oxidation. *ACS Appl. Mater. Interfaces* **2018**, *10*, 477-487. I conducted all the synthesis and characterization and wrote the manuscript with Pavan Kumar, Drs. MacLachlan and Wolf. Chujie Zhu carried out the catalytic activity tests. Reprinted with permission from footnote [1] Copyright 2018 American Chemical Society.

Chapter 3 has been published as: Dai, Y.; Pavan Kumar, V.; Zhu, C.; Wang, H.; Smith, K. J.; Wolf, M. O.; MacLachlan, M. J., Bowtie-shaped $NiCo_2O_4$ Catalysts for Low-Temperature Methane Combustion. *Adv. Funct. Mater.* **2019**, *29*, 1807519. I designed, synthesized and characterized the material with the assistance of Pavan Kumar. Chujie Zhu helped with catalytic

[1] Dai, Y.; Pavan Kumar, V.; Zhu, C.; MacLachlan, M. J.; Smith, K. J.; Wolf, M. O., Mesoporous Silica-Supported Nanostructured PdO/CeO_2 Catalysts for Low-Temperature Methane Oxidation. *ACS Appl. Mater. Interfaces* **2018**, *10*, 477-487.

activity and stability measurement. Haiyan Wang carried out CO uptake experiments. I wrote the draft with Drs. MacLaclan and Wolf. Reproduced with permission from John Wiley & Sons, Inc.

The work in Chapter 4 has been submitted as a provisional patent and will be submitted for publication. I designed, carried out most of the experiments and wrote the draft of manuscript, with Drs. MacLachlan and Wolf. Haiyan Wang and Shida Liu helped with the CO uptake, H_2 – TPR, O_2 – TPR measurements and kinetics calculation.

The work in Chapter 5 will be submitted for publication. I designed, synthesized, characterized the sample and wrote the manuscript with Drs. MacLachlan and Wolf. Catalytic and kinetics measurements were conducted with the assistance of Haiyan Wang and Shida Liu.

Table of Contents

List of Tables

List of Figures

List of Schemes

List of Symbols

θ	Bragg angle
*	an oxygen vacancy site on catalysts
τ	the loading of grafted groups
α	surface density of loaded APTS
A	pre-exponential factor
E_a	activation energy
g	gram
h	hour
k	rate constant (s^{-1})
K	Kelvin
mL	milliliter
M_N	the atomic mass of nitrogen
N_A	Avogadro's number
N_{CH_4}	methane flow rate (μmol/s)
nm	nanometer
O_{ads}	adsorbed oxygen
O_{latt}	lattice oxygen
P_{CH_4}	methane partial pressure (Pa)
pH	power of hydrogen
ppm	parts per million

r_{CH_4}	reaction rate (μmol/s)
T	temperature
$T_{50\%}$	light-off temperature
V/V	volume basis
wt	weight basis
X	conversion of methane
Δ	change
$\Delta W_N\%$	the weight percent of nitrogen
$\Delta W_{SiO_2}\%$	the weight percent of SiO_2
μm	micrometer
ν	stretching or bending vibrations

List of Abbreviations

1D	1-Dimensional
2D	2-Dimensional
3D	3-Dimensional
acac	Acetylacetonate
ALD	Atomic layer deposition
APTS	(3-aminopropyl)trimethoxysilane
ASAP	Accelerated Surface Area & Porosity
BET	Brunauer−Emmett−Teller
BJH	Barrett−Joyner−Halenda
CF	Cerium formate
cus	Coordinately unsaturated
CVD	Chemical vapor deposition
DI	De-ionized
DP	Deposition-precipitation
EA	Elemental analysis
EDX	Energy-dispersive X-ray
ESC	European Stationary Cycle
FFT	Fast Fourier Transform
FTIR	Fourier Transform Infrared Spectroscopy
GHSV	Gas hourly space velocity

HAADF	High-angle annular dark-field imaging
HRTEM	High resolution transmission electron microscopy
IWI	Incipient wetness impregnation
LTMOX	Low-temperature methane oxidation
NGVs	Natural gas vehicles
NO_x	Nitrogen oxide
PID	Proportional–integral–derivative
PXRD	Powder X-ray diffraction
QMS	Quadrupole mass spectrometer
RC	Reactive calcination
SAR	Surface-assisted reduction
SCS	Solution combustion synthesis
SEM	Scanning electron microscopy
SO_x	Sulfur oxide
STEM	Scanning transmission electron microscopy
STP	Standard temperature and pressure
TCD	Thermal conductivity detector
TEM	Transmission electron microscopy
TEOS	Tetraethylorthosilicate
TGA	Thermal gravimetric analysis
TOF	Turnover frequency
TPD	Temperature programmed desorption

TPO	Temperature programmed oxidation
TPR	Temperature programmed reduction
XPS	X-ray photoelectron spectroscopy

Acknowledgements

First of all, I would like to offer my enduring gratitude to my supervisors Prof. Mark MacLachlan and Prof. Michael Wolf. Their enthusiasm and wide knowledge impressed me deeply. They gave me enough freedom during my studies and supportive guidance when I met problems. I learned a lot both academically and in general from them and felt so lucky to have them as my supervisors.

Then, I would like to express my gratitude to my committee members Dr. Andrew MacFarlane, Dr. Sarah Burke, and Dr. Curtis Berlinguette for their helpful comments and suggestions during my PhD studies.

Special thanks owed to Dr. Vanama Pavan Kumar, who taught me a lot about nano-synthesis, characterization and analysis. His patience and generous assistance made my research go smoothly during the first two years of my PhD program.

I sincerely thank the collaboration of Prof. Kevin Smith and his students Chujie Zhu, Dr. Haiyan Wang, and Dr. Shida Liu from Chemical and Biological Engineering Department, UBC. They assisted and trained me with all the catalytic measurements and analysis. I learned a great deal of catalysis knowledge from them.

I'd like to thank the staff both inside and outside UBC who helped me complete my work: Anita Lam carried out small angle PXRD experiments, and trained me with wide angle PXRD measurement and analysis; Derrick Horne and Bradford Ross assisted me with TEM, SEM and EDX; Ken Wong ran all the XPS samples for me; Xin Zhang from SFU trained me on STEM, HRTEM and tomography study.

Thanks to all the former and present colleagues in MacLachlan and Wolf groups. Their passion for chemistry, friendly assistance and discussion created a wonderful environment. I'm pleased to work with them here.

In addition, I would like to acknowledge the Natural Sciences and Engineering Research Council (NSERC) of Canada and Westport Fuel Systems Inc. for funding this project, and UBC for a Four Year Fellowship (4YF) to make my PhD research possible.

Finally, I would like to thank my parents and sister for their support and encouragement as always. Their understanding and support mean so much to me.

Dedication

To my parents and sister

大道至简

穷尽细节

Chapter 1: Introduction

1.1 Low-temperature methane oxidation (LT-MOX)

1.1.1 Natural gas vehicles

Natural gas, composed primarily of methane, is an abundant resource with worldwide reserves estimated at 10200 to 15400 trillion cubic feet according to the US Geological survey.[1] Importantly, combustion of natural gas produces less pollution (CO_2, NO_x, SO_x) per unit energy delivered than either gasoline or diesel,[2-3] making natural gas vehicles (NGVs) attractive alternatives to mitigate the effects of climate change by reducing vehicular CO_2 emissions. There are now more than 20 million natural gas vehicles (NGVs) around the world, and this number is anticipated to grow to more than 30 million by 2024.[4]

A significant concern with NGVs, however, is the release of residual unburned methane in the exhaust stream. Methane is a greenhouse gas that is as much as 28 times more potent than CO_2.[5] Without post-engine treatment, a lean-burn natural gas bus typically emits 3 g CH_4/kWh on the European Stationary Cycle (ESC),[6] which is substantially higher than the limit of 0.5 g/kWh mandated by the Euro VI standards.[7] Therefore, to meet current standards, the emission of methane must be reduced by approximately 85% through catalytic treatment of the exhaust emissions.

At present, in automobiles, 3-way catalytic convertors are used to treat exhaust to remove SO_x, NO_x, and to oxidize CO and hydrocarbons. Unfortunately, methane oxidation in the exhaust of NGVs is a much more challenging prospect. Due to the lack of a dipole moment and a strong C-H bond (440 kJ mol^{-1}), methane is the least reactive hydrocarbon. Combustion of methane happens higher than 800 °C and it is not readily oxidized by conventional catalytic convertors.[8]

Furthermore, the exhaust from NGVs has a low residual methane concentration (500-1000 ppm) and relatively low temperature (< 500-550 °C), and significant quantities of water vapor (10-15%), SO_x (~ 1 ppm) and NO_x are present.[6, 9] For these reasons, there is a great deal of effort being devoted to develop stable catalysts that can oxidize methane at low temperature (below 500 °C).

1.1.2 Surface catalyzed mechanism for low temperature methane oxidation

The mechanism for catalytic methane oxidation has been explored widely since the 1990s.[10] It has been proposed that catalytic methane combustion on metal oxides may follow the Eley-Rideal[11], Langmuir-Hinshelwood[12] or Mars-van Krevelen[13-16] mechanisms.

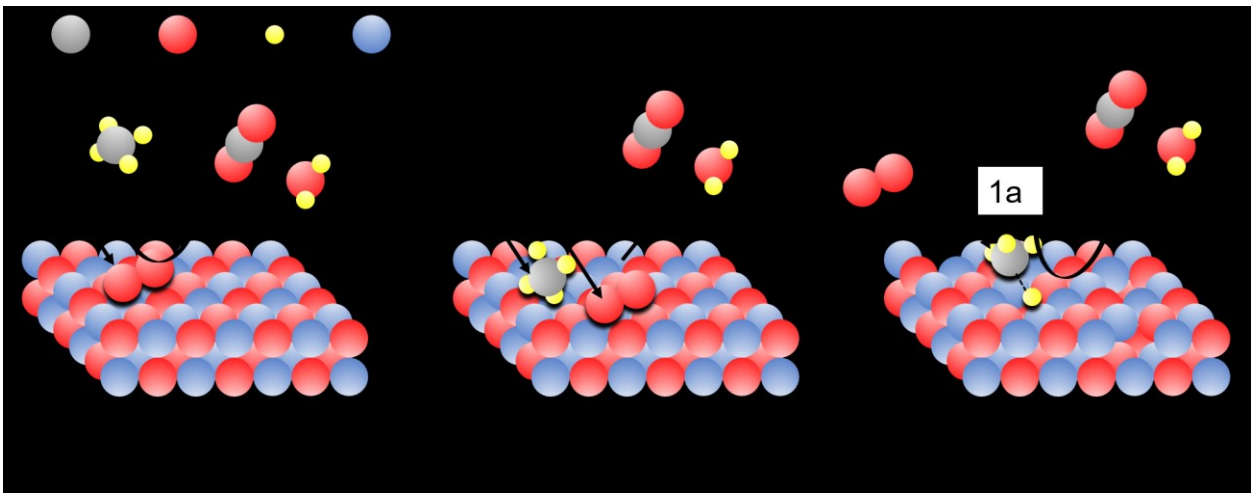

Figure 1.1 Proposed mechanisms for catalytic methane oxidation. Left: The Eley-Rideal mechanism, where adsorbed O_2 molecules react with CH_4 in the gas phase; centre: the Langmuir-Hinshelwood mechanism, where both reagents adsorb on the catalysts surface, and surface diffusion and interaction initiate the reaction; right: The Mars-van Krevelen mechanism, where CH_4 molecules form chemical bonds with the catalyst surface. The lattice oxygen are involved in the CH_4 oxidation reaction and, after product desorption, oxygen vacancies are left on the surface.

As shown in Figure 1.1, in the case of the Eley-Rideal process, only one of the reagents adsorbs on the surface of the catalyst, and directly interacts with another gaseous reagent to form the final product. For methane combustion, the hypothetical process has adsorbed O_2 molecules react with gaseous CH_4 and yield CO_2 and H_2O.

In the Langmuir-Hinshelwood mechanism, both reagents adsorb on the catalyst. The interaction between reagents via surface diffusion initiates the reaction. In this case, CH_4 and O_2 adsorb on the surface of metal oxide together at the beginning. Then the diffusion of CH_4 and O_2 facilitates the interaction between them and results in the oxidation reaction.

The Mars-van Krevelen mechanism involves the reaction between reactants and surface atoms. One reagent forms a chemical bond with surface metal atoms, then this reacts with another adsorbed or gaseous reagent. After desorption of products, vacancies are left on the catalyst surface which can be filled by reagent again. In the case of methane oxidation, CH_4 reacts with the metal oxide to form metal-CH_3 and O-H bonds initially. Then, a series of oxidation steps occur with neighboring O provided by lattice oxygen or adsorbed oxygen. The remaining vacancies resulting from CO_2 desorption are refilled by O_2.

During catalytic methane oxidation, the PdO ↔ Pd transformation was detected by in situ studies. Therefore, among the possibilities, the dual site Mars-van Krevelen mechanism which involves lattice oxygen reduction, oxygen vacancy formation and their regeneration is the most accepted mechanism for the oxidation of methane on metal oxides.[17]

1.1.3 Assessment of catalysts for low temperature methane oxidation

Typically, catalytic activity for methane oxidation is measured by temperature-programmed oxidation (TPO). A gaseous mixture containing CH_4, O_2, and balanced with inert He

or Ar is fed into a reactor at a constant gas hourly space velocity (GHSV), which relates the reactant gas flow rate to the reactor volume. GHSV is measured at standard temperature and pressure (STP). The calculation for GHSV is shown in Equation 1.1.

$$\text{GHSV} = \frac{flow\ rate\ (mL/min)\times 60(min/h)}{m_{catalysts}(g)}\ (mL\ (STP)\cdot g^{-1}\cdot h^{-1}) \quad \text{Equation 1.1}$$

A specific amount of catalyst is diluted and loaded into the reactor to ensure isothermal reaction conditions. Then, the reactor is heated up to a given temperature at a fixed rate. CH_4 conversion can be calculated by variation of the amount of CH_4 (Equation 1.2) or the overall C balance (Equation 1.3).

$$X_{CH_4} = \frac{n_{CH_4 inlet} - n_{CH_4\ outlet}}{n_{CH_4 inlet}} \quad \text{Equation 1.2}$$

$$X_{CH_4} = \frac{n_{CO_2}}{n_{CH_4} + n_{CO_2}} \quad \text{Equation 1.3}$$

Temperature-programmed oxidation (TPO) experiments result in a catalytic curve, giving the methane conversion as a function of temperature. Typically, a higher GHSV shifts the light-off curve to higher temperatures due to the shortening of contact time between the feed gases and the catalyst.

1.1.4 Catalysts for low-temperature methane oxidation

Efficient catalytic materials for low-temperature methane oxidation (LTMOX) must have low light-off temperatures (< 500 °C) and they must remain active in the presence of water vapor, SO_x, and NO_x for application in natural gas vehicles.[6] Heterogeneous catalysts have the potential to meet this challenge.[18] Over the past several decades, different types of catalysts have been developed for low-temperature methane combustion.[19] These include noble metal-based (e.g., Pd,[20-23] Pt,[24-25] Au[26-27]), single metal oxide-based (e.g., CuO,[28] Co_3O_4,[29] CeO_2,[30] MnO_x,[31]), binary

metal oxides like perovskite,[32] spinel,[33] and hexaaluminate catalysts.[34] Following a discussion of palladium-based catalysts that have demonstrated very high activity for LTMOX, I discuss some of the other catalyst types relevant to this thesis.

1.2 Development of Pd-based catalysts for LT-MOX

Extensive research has been conducted investigating different kinds of metal oxide and supported noble metal catalysts in order to identify suitable catalysts for effective low temperature methane oxidation. It is not surprising that noble metal catalysts such as those based on palladium, platinum and gold exhibit outstanding activity.[35-36] By using these catalysts on supports, thermal degradation through particle sintering is reduced by dispersing the noble metal over a larger surface area. As metal oxide-supported PdO catalysts are generally considered to represent the state-of-the-art for methane combustion catalysts,[37-38] the following discussion will focus on Pd-based catalysts.

1.2.1 Catalytic activity

The catalytic performance of Pd-based catalysts has been studied extensively. To further improve the catalytic activity for methane combustion, researchers have investigated the influence of many different factors, including the structure, Pd precursor, supports, and preparation method. Each of these factors can affect the light-off temperature of the catalyst as well as its stability in the presence of water and other exhaust by-products.

1.2.1.1 Structure effects

It is well known that nanostructured catalysts exhibit superior catalytic performance because of their larger surface area and exposure of reactive facets or surface defect sites. The synthesis of nanostructured PdO and supports significantly improves the activity of these catalysts for methane combustion.[18, 39] Many studies have shown that methane oxidation over Pd-based

catalysts is structure sensitive. Researchers have explained this issue from several different viewpoints. Murata *et al*.[40] investigated the effect of particle size (1-20 nm) on Pd nanoparticles supported on alumina with different crystalline phases. α-Al_2O_3 and θ-Al_2O_3 have weak interactions with Pd, and the Pd nanoparticle catalysts anchored on these substrates showed increased catalytic activity from 1.5 to 7.3 nm. Then, the activity gradually decreased as Pd particle size reached 19 nm. On the other hand, Pd nanoparticles anchored on γ-Al_2O_3, where there are strong Pd-substrate interactions, exhibited increased activity with an increase in Pd nanoparticle size. It was found that for the Pd/θ-Al_2O_3 samples, 1.5 nm Pd presents an amorphous-like structure and 7.3 nm spherical Pd particles yield a high fraction of Pd step sites, which are highly active for catalysis. With 19 nm Pd particles, they formed well-faceted structures, which are less active. The different activity of surface sites on the substrate explains the particle size effect. For Pd/γ-Al_2O_3 catalysts, the strong interaction disturbs the formation of spherical particles and results in distorted structures with large numbers of unsaturated sites; this leads to an improvement in the catalytic performance. Therefore, larger particle sizes with more unsaturated sites presents better activity. Fujimoto *et al*.[16] studied Pd/ZrO_2 with Pd nanoparticle sizes ranging from about 2 to 10 nm. Catalysts with smaller Pd particle size exhibited poorer catalytic performance. It was found that smaller crystallites have stronger Pd-O bonds and fewer vacancies. The strong Pd-O bond stabilizes PdO particles and decreases the oxygen mobility, which is detrimental to the activity. Wills *et al*.[41] synthesized uniform Pd nanoparticles with sizes of 2.5, 3.7, 4.3, 6.0, and 8.2 nm, which were deposited onto different types of supports (acidic Al_2O_3, basic MgO, inert SiO_2, and redox-active $Ce_{0.8}Zr_{0.2}O_2$). The catalysts with Pd particle sizes of approximately 4-5 nm exhibited the highest reaction rates on all of the supports investigated. It was proposed that PdO (101) facets are more active but less stable than Pd (100) facets. The good catalytic performance is attributed

to the optimized ratio of PdO (101) facets to PdO (100) facets. Also, the formation of oxygen vacancies in the substrate is crucial to the activity.

Above all, the particle size of PdO influences the proportion of step sites, the strength of the Pd-O bonds, the exposed facets and the density of oxygen vacancies, which all contribute to the overall catalytic behavior. PdO nanoparticles with sizes of 4-7 nm exhibited the best activity.

1.2.1.2 Precursor effect

It was reported that using different palladium precursors (e.g. $Pd(NO_3)_2$, palladium(II) acetylacetonate ($Pd(acac)_2$), and $PdCl_2$) affects the catalytic behavior due to the following reasons. 1) Precursors leave residual by-products: chloride ions are considered to be poisonous to catalysts - chloride ions adsorb on the supports after activation when using a chloride precursor. During the methane oxidation process, Cl^- ions desorb in the form of HCl, which competes with CH_4 on PdO active sites, and inhibits the activity.[42] 2) Precursors affect final detailed structure: $Pd(acac)_2$ precursor leads to higher Pd dispersion and smaller Pd crystallite size, which shows better catalytic activity.[43] Small Pd particles, however, agglomerate into large ones during the reaction and deactivate quickly. The weak interaction between the organic precursor and support results in sintering of Pd.[44] The use of $Pd(NO_3)_2$ precursor yields particles that are larger and have lower Pd dispersion, but show better catalytic performance for low temperature methane oxidation.[45]

1.2.1.3 Support effects

The nature of the catalyst support plays an important role in catalytic activity as it affects the PdO-support interaction. Also, sintering of palladium is a significant problem for Pd-based catalysts during methane oxidation reaction. The support can be used to stabilize the active metal

and facilitate the oxidation reaction. Typically, γ-Al_2O_3 with a high surface area is used as support because it is effective at dispersing the metal and maintains good catalytic activity. However, sintering of Al_2O_3 at high temperature leads to significant loss of activity. Therefore, the modification of the support to obtain higher activity has prompted extensive exploration.

1.2.1.3.1 Nature of supports

The properties of supports such as specific surface area, acidity and redox behavior have pronounced effects on the catalytic behavior of Pd-based catalysts. It is accepted that supports with high surface area typically improve the dispersion of Pd, leading to enhanced activity. Typically, mesoporous silica with well-ordered channels, such as SBA-15 or MCM-41, with high surface areas are used as a support. Successful incorporation of Pd catalysts into the pores of a mesoporous host support not only leads to good dispersion, but also addresses the Pd sintering problem[46-47].

In an investigation of the role of substrate acidity, Yoshida *et al*.[48] reported that moderate acidity of the support led to the best activity for Pd catalysts. They compared the catalytic activity of Pd nanoparticles supported on different oxides as they varied the acidity of the support with the following materials (in order of increasing acidity): MgO < ZrO_2 < Al_2O_3 < SiO_2 < SiO_2-ZrO_2 < SiO_2-Al_2O_3 < SO_4^{2-}-ZrO_2. They found that Pd/Al_2O_3 and Pd/SiO_2 exhibited better catalytic performance than the more or less acidic supports. It was proposed that the acidity of the support controls the oxidation state of palladium on the surface. The basic support is beneficial to stabilize higher oxidation states of Pd, which are thought to be more active species. However, when the support is too basic, it results in excessive stabilization of PdO and the formation of binary oxides (e.g. Pd-Mg-O) on the interface, which decreases the catalytic activity.

Supports with good redox properties significantly enhance the catalytic behavior of Pd-based catalysts for low temperature methane oxidation. During the reaction, the redox behavior of the Pd/PdO couple facilitates the total oxidation of methane. Redox-active supports such as SnO_2,[49] Co_3O_4,[50] and CeO_2[51] serve as an oxygen reservoir, enabling them to facilitate the oxidation of methane by supplying lattice oxygen to the active site. Supports that can be reduced at low-temperature generally have more oxygen vacancies and good oxygen mobility, which contributes to the catalytic activity. Also, Ercolino *et al*.[50] proposed that the hydroxyl groups formed on PdO during methane oxidation could transfer to the Co_3O_4 support and form CoOOH species, which facilitates the regeneration of PdO. Furthermore, these redox-active metal oxide supports can be used as promoters, doped on Al_2O_3 or SiO_2 supports, for better catalytic performance.

1.2.1.3.2 Modification of supports

After understanding the properties and effects of supports, it is attractive to modify the support to enhance the oxygen vacancies and mobility, and improve the interaction between the support and active PdO sites in order to improve the activity and stability of the catalyst. The mixed metal oxide and bimetallic or multi-metallic supports with different structures including spinels, perovskites and hexaaluminates have been widely studied. For example, Muto *et al*.[52] compared Pd catalysts prepared on three different supports made by chemical vapor deposition (CVD): silica, alumina, and silica-coated alumina. They found that the support made with 5 wt% silica deposited on alumina exhibited the best catalytic performance. They proposed that the interaction between PdO and alumina-supported silica domains kept good Pd dispersion and inhibited sintering due to steric effects.

Zou *et al.*[53] prepared a series of Pd/xNiO/γ-Al_2O_3 catalysts for methane combustion. The doping of NiO in Al_2O_3 forms spinel $NiAl_2O_4$ on the surface, which strongly interacts with PdO, where it favors the distribution of PdO and inhibits the accumulation of hydroxyl groups on PdO. They found that a small amount of NiO (0.5 wt%) loading led to the best catalytic performance. On the other hand, increasing the amount of $NiAl_2O_4$ led to larger PdO particles, lower surface area and weaker interactions with PdO, effects that are detrimental to the activity.

Hexaaluminates with a formula of $AAl_{12}O_{19}$ are not active for methane combustion, while the substitution of Al sites with transition metals can afford materials with good catalytic activity and thermal stability. Xu *et al.*[54] synthesized 3D-ordered macroporous $LaMnAl_{11}O_{19}$ supported Pd catalysts that were highly active for the total oxidation of methane. The excellent performance of these materials is attributed to the uniform distribution of Pd, large number of adsorbed oxygen atoms, and low-temperature reducibility.

Li *et al.*[55] reported the synthesis of ultrathin Co_3O_4 nanosheets supporting PdO/CeO_2 catalysts. The incorporation of 10% CeO_2 with large oxygen capacity promotes methane oxidation by supplying oxygen species to the active site. The synergistic effect between PdO, CeO_2 and Co_3O_4 improved the oxidizability of PdO and accelerated the total oxidation of intermediate products of carbon oxygenates.

1.2.1.4 Preparation method

The preparation method used to create the catalyst strongly affects the catalytic behavior by impacting the Pd distribution, Pd particle size, and Pd-support interaction. Typically, Pd-based catalysts are synthesized by the incipient wetness impregnation (IWI) method. In this method, active metal precursor is dissolved in aqueous or organic solvent, and added to the support. Then

the catalyst is dried and calcined, which leads to the distribution of active metal on the support surface. This simple and scalable procedure gives materials with moderate catalytic activity. To further improve the catalytic activity, researchers have extensively investigated different synthesis methods.

The sol-gel method of catalyst preparation involves the transformation from monomer to colloidal solution and finally to a gel-like integrated network. This method results in large Pd particles and poor Pd dispersion,[56] which is detrimental to catalytic activity. However, the support prepared by this method presents a high surface area and good porous structure. Therefore, the sol-gel method is suitable for the modification of supports.

Xiao *et al*.[57] reported Pd/CeO_2 synthesized by deposition-precipitation (DP) with high activity. In the DP method, the support is suspended into the solution of active metal salt, and then the precipitating agent (e.g. NaOH, Na_2CO_3) is added to the solution to increase the pH of the mixture and precipitate the active precursor. Catalysts prepared via the DP method increase the interaction between the PdO and support due to the presence of cationic Pd species. Also, there are more defects and oxygen vacancies on the surface of CeO_2. These factors contribute to the high catalytic activity for methane oxidation.

The solution combustion synthesis (SCS) method of catalyst preparation involves a one-step, simple procedure. Typically, an aqueous solution containing metal nitrate is heated to 300-600 °C; the metal nitrate functions as oxidizing agent and organic molecules (e.g. glycine and urea) as fuel. After the water has been evaporated, the precursor decomposes and yields a crystalline powder. Different types of Pd-based catalysts such as Pd/Co_3O_4,[58] $PdCeO_2$,[59] and $Pd/LaMnO_3/ZrO_2$[60] were prepared by the SCS method and exhibit excellent catalytic performance for methane oxidation. The advantage for SCS is the insertion of Pd metal into the supported metal

oxide lattice, which results in the formation of highly dispersed, small-sized and stable PdO particles with higher reactivity.

Danielis *et al*.[61] reported a series of PdO/CeO_2 catalysts prepared by dry ball-milling. The mechanical milling leads to a unique arrangement of Pd-O-Ce interfaces. Due to the different hardness of palladium metal and ceria, mechanical mixing facilitates the spreading of softer ceria and Pd particles on the surface, which gives rise to a configuration with Pd nanoclusters embedded in a Pd-CeO_2 amorphous shell. The excellent oxygen exchange properties of ceria and unique structure promotes the formation of Pd^{4+} ions, which are highly active for methane oxidation. As well, the shell structure improves the thermal and hydrothermal stability of catalysts.

Our group previously reported the preparation of nanostructured PdO/CeO_2 by a new "surface-assisted reduction" (SAR) method through a two-step procedure.[62] In the first step, cerium formate hollow spheres were prepared by hydrothermal treatment of cerium nitrate and ethylene glycol. In the second step, reactive formate groups on the surface of the nanostructured cerium precursor act to reduce Pd^{2+} onto the surface, yielding nanostructured CeO_2 substrates coated with highly dispersed Pd after calcination. These catalysts showed 50% conversion for the oxidation of methane below 300 °C.

Above all, by optimizing the structure of PdO, selecting the most efficient precursor and support, and developing novel and effective synthesis methods, the activity for Pd-based catalysts can be significantly improved, and they are promising to reduce methane emission from NGVs at low temperature.

1.2.2 Catalytic stability at operating conditions

In addition to showing good catalytic activity, catalysts must be stable under operating conditions in order to be useful for real-life applications. For Pd-based catalysts, the sintering of both PdO nanoparticles and the support can deactivate the catalysts. Furthermore, the emissions from natural gas vehicles contain large amounts of water vapor (10%-15%) and gases including SO_2 and NO_x that gradually deactivate the catalysts. Thus, developing catalysts that can withstand the harsh conditions of operating NGV engines, showing long-term durability and high tolerance to poisonous gases, poses a daunting challenge.

1.2.2.1 Thermal stability

As described before, sintering of catalytic particles to form larger particles with lower activity is problematic. In addition, PdO transforms into metallic Pd at high temperature (above 600 °C) and loses its activity. Although the temperature of the NGV exhaust is lower than that of PdO/Pd transformation, the methane oxidation reaction is highly exothermic, so the temperature of a catalyst surface could be higher than the surroundings and induce the decomposition of PdO. Researchers have explored many solutions to this problem, such as using thermally stable supports such as ZrO_2[63], perovskite[60] and hexaaluminate[64], doping Ce[65], Si[66], Zr[23] to stabilize PdO and La[67], or Ba[68] to stabilize the Al_2O_3 support.

Cargnello *et al*.[18] reported the synthesis of PdO@CeO_2 supported on modified hydrophobic alumina. The core-shell structure maximized the interfacial surface area, which enhances the interaction between PdO and CeO_2. The crystallites of CeO_2 also help to maintain the small particle size of PdO. Moreover, the hydrophobic Al_2O_3 surface improves the adsorption of Pd@CeO_2, and leads to good dispersion and separation of active sites. The catalysts exhibit excellent thermal

stability and are still active after high temperature (850 °C) treatment for 12 h, and following run-up, cool-down reactions for 5 cycles.

Onn *et al*.[21] synthesized Pd/Al_2O_3 coated with a thin layer (~ 1 nm) ZrO_2 film using atomic layer deposition (ALD). Applying the ZrO_2 films over active PdO and Al_2O_3 supports helped stabilize the PdO particles against sintering.

Onn *et al.*[69] also incorporated Pd particles into a thin film of $LaFeO_3$ (<1.5 nm), and coated this on porous $MgAl_2O_4$. The high surface area $LaFeO_3$ prepared by ALD enables the reversible exsolution of Pd undergoing redox cycles and uniform Pd distribution. The catalysts exhibit high thermal stability (> 900 °C).

1.2.2.2 Hydrothermal stability

As one of the main components of NGV emission, water may be detrimental to the performance of methane oxidation catalysts. Many researchers have investigated the mechanism of this phenomenon and have identified two main effects: inhibition and deactivation of the catalysts. First, from a kinetic point of view, the presence of a large amount of water vapor slows down desorption of water, a product of methane oxidation, from the surface of catalysts.[70] Subsequently, the accumulation of hydroxyl groups or H_2O molecules on active sites blocks the further adsorption of CH_4, which inhibits the catalytic reaction.[22] Second, with respect to the deactivation effect, water can accelerate the thermal sintering of catalytic particles. The binding of hydroxyl groups on supports suppresses the oxygen mobility[20] and the formation of $Pd(OH)_2$ contributes to the irreversible loss of catalytic activity.[71]

Following the water deactivation mechanism, it is crucial to decrease the effect of hydroxyl groups from H_2O on Pd and supports. It is accepted that enhanced interaction between PdO and

supports improves stability by stabilizing PdO and inhibiting the formation of $Pd(OH)_2$. For example, the presence of stabilizing spinel $NiAl_2O_4$, $MgAl_2O_4$[72], CeO_2[73] or ZrO_2[23] in the support, which were suggested to strengthen this interaction, all led to improved hydrothermal stability for the resulting PdO/support catalysts. Furthermore, the lower acidity of a support suppresses formation of $Pd(OH)_2$.[72] Hydrophobic supports, like ZSM-5,[47] and supports with higher oxygen mobility[74] decrease the direct coverage of water vapor.

Besides improvements to the support, the synthesis of bimetallic nanoparticles (e.g., Pd-Pt[75-77] and Pd-Au[78-79]) also benefits the catalyst stability. The addition of Pt induces a Pd-Pt interaction, which weakens the PdO bond and prevents the formation of bulk PdO. The structure of PdO in close contact with a Pd/Pt alloy phase significantly improves the catalytic behavior under wet conditions. As another example of a bimetallic structure influencing the catalyst stability, Pd-Au alloy nanoparticles were shown to alter the reaction pathway. Doping of the Pd with Au weakens the bonding between active Pd sites and reaction intermediates, and enriches the adsorbed oxygen species on the surface, which contributes to good stability.

1.2.2.3 Sulfur tolerance

Although the concentration of sulfur dioxide is low in NGV emissions – only a few ppm – sulfur can have a detrimental impact on methane oxidation catalysts. Pd-based catalysts are sensitive to SO_2; they show irreversible loss of catalytic activity in the presence of SO_2 due to the formation of inactive $PdSO_4$.

It has been proposed that sulfating supports like Al_2O_3 and ZrO_2 slow the deactivation rate because SO_2 adsorbs on both PdO and supports.[80] Also, bimetallic Pd-Pt exhibits better sulfur tolerance than Pd alone since Pt doesn't adsorb SO_2, and subsequently suppresses coverage of SO_2

on PdO.[81-82] The formation of a core-shell structure like PdO-CeO_2@SiO_2 can also protect the catalyst, with the SiO_2 shell acting as a diffusion barrier that blocks the direct interaction with SO_2.[83]

Unfortunately, the synergic effect of water and sulfur can speed up the deactivation of Pd-based catalysts. The solutions discussed above – substrate optimization and employing bimetallic catalysts – just slow down the deactivation rate, but do not completely solve the problem. Additional research is needed to further improve the stability.

In summary, the poor thermal stability of PdO can be enhanced by using thermally stable supports and modifying the structure, which are qualified to maintain excellent activity under real conditions. However, the hydrothermal stability and sulfur tolerance of Pd-based catalysts still need to be further improved to satisfy the requirements for practical usage.

1.2.3 The catalytic mechanism for LTMOX by PdO

It is well accepted that catalytic methane oxidation on Pd-based catalysts follows the Mars-van-Krevelen mechanism which involves lattice oxygen reduction and regeneration. The coordinative unsaturated $Pd_{(cus)}$-$O_{(cus)}$ pairs are crucial to the C-H dissociation of adsorbed CH_4, that is:

$$CH_{4(g)} + (*)_{Pd(cus)} + (*)_{O(cus)} \rightarrow (CH_3)_{Pd(cus)} + (H)_{O(cus)}$$

which is considered the rate-determining step.[84] The adsorption of O_2 molecules is located on $(*)_{Pd(cus)}$, and form $(O)_{Pd(cus)}$ species. Then, the further catalytic reaction follows different steps under different conditions suggested by Stotz.[17] At lower temperature (200-400 °C), the intermediates $(CH_3)_{Pd(cus)}$ first combine with $(O)_{Pd(cus)}$ nearby to generate $(CH_2OH)_{Pd(cus)}$ and $(*)_{Pd(cus)}$ species. After that, a series of dehydrogenation steps follow:

$$(CH_2OH)_{Pd(cus)} + (*)_{O(cus)} \rightarrow (CH_2O)_{Pd(cus)} + (H)_{O(cus)}$$

$$(CH_2O)_{Pd(cus)} + O_{Pd(cus)} \rightarrow (CHO)_{Pd(cus)} + (OH)_{Pd(cus)}$$

$$(CHO)_{Pd(cus)} + O_{Pd(cus)} \rightarrow (CO)_{Pd(cus)} + (OH)_{Pd(cus)}$$

And finally, $(CO)_{Pd(cus)}$ oxidizes to CO_2, which is then desorbed from the catalyst surface. $(H)_{O(cus)}$ species would interact with $(OH)_{Pd(cus)}$, which forms water, and regenerates $(*)_{Pd(cus)}$ and $(*)_{O(cus)}$ species.

At higher temperature, significant amounts of $(OH)_{Pd(cus)}$ are formed due to the water dissociative adsorption and vacancy formation as follows:

$$H_2O_{(g)} + O_{Pd(cus)} + (*)_{Pd(cus)} \leftrightarrow 2(OH)_{Pd(cus)}$$

$$(H)_{O(cus)} + (*)_{Pd(cus)} \leftrightarrow (OH)_{Pd(cus)} + (v)_{O(cus)}$$

In the presence of a large amount of water (10-15%), H_2O takes up most of the $(*)_{Pd(cus)}$ sites, which inhibits the catalytic reaction. The higher concentration of $(H_2O)_{Pd(cus)}$ induces a large number of $(OH)_{Pd(cus)}$ and $(H)_{O(cus)}$ species. So the preferred process is that $(CH_3)_{Pd(cus)}$ first interacts with $(OH)_{Pd(cus)}$ and decomposes to $(CH_2)_{Pd(cus)}$. Then $(CH_2)_{Pd(cus)}$ species transfer on $(*)_{O(cus)}$, which forms $(CH_2)_{O(cus)}$. The intermediate $(CH_2)_{O(cus)}$ further reacts with $(*)_{Pd(cus)}$ and oxidizes to $(CH_2O)_{Pd(cus)}$. The further dehydrogenation steps are the same as under low temperature (200-400 °C) conditions.

1.3 Development of non-noble metal catalysts for LT-MOX

Although Pd-based catalysts exhibit the best catalytic activity for low-temperature methane oxidation and the improved structures developed during recent decades have led to significant enhancement of the thermal and chemical stability of these catalysts, their long-term durability for real application is still insufficient. Furthermore, the high price and scarcity of palladium limits its application in practice.

Non-noble metals that are inexpensive and abundant are attractive alternatives to precious metals that have attracted wide attention recently for application in catalysis. For example, single metal oxides, spinels, perovskites and hexaaluminate catalysts based on non-precious metals all show moderate MOX catalytic behavior, and some of them exhibit excellent stability. These catalysts have the potential to be used for industry and NGVs, and are discussed in more detail in the following sections.

1.3.1 Single metal oxides

Non-noble transition metals from groups 3-12 of the periodic table form oxides with various positive oxidation states that play an important role for catalytic reactions.[85] Non-noble metal catalysts, which use harder metal ions than the precious metal-based catalysts, can show higher sulfur tolerance and even overcome sulfur poisoning that is detrimental to Pd-based catalysts. Ordonez *et al*.[86] compared the catalytic performance and sulfur resistance for different types of metal oxides (Cr_2O_3, Mn_2O_3, Co_3O_4, NiO, CuO). They found that Co_3O_4 and Mn_2O_3 show the best catalytic activity in the absence of SO_2, but significantly deactivate in the presence of 40 ppm SO_2 at high temperature (625 °C). Co_3O_4 maintained only 40% conversion after 60 h

treatment under these conditions. Mn_2O_3 was fully deactivated after 50 hours. NiO and CuO, which showed lower activity, lost activity even more quickly with only 8 and 20 hours lifetime, respectively, in the presence of SO_2. Cr_2O_3 exhibited excellent stability without appreciable deactivation after 60 h treatment. Mn, Co and Cr oxides were selected for stability tests at lower temperature (425 °C). It was observed that Co_3O_4 deactivated more quickly, while Mn_2O_3 maintained very low conversion of about 4% after 50 hours in the presence of SO_2. Although Cr_2O_3 catalysts are not the most active, they show high SO_2-resistance with no deactivation after 50 h treatment. This section will focus on the active single metal oxide of Co_3O_4, MnO_2 and stable Cr_2O_3 catalysts.

1.3.1.1 Co_3O_4

Co_3O_4 exhibits good activity for methane combustion attributed to a spinel-type structure with Co^{2+} cations in the tetrahedral sites and Co^{3+} cations in the octahedral sites, lower energy of the Co-O bond and a high density of oxygen vacancies on the surface.[87] Hu *et al.*[88] carried out theoretical investigations for methane combustion on Co_3O_4 using density functional theory calculations, and suggested that the preferential pathway over Co_3O_4 (110) facets follow the sequence of:

1. First C-H activation: $CH_4 + Co^{3+}\text{-}O_{2c} \rightarrow CH_3\text{-}Co\text{-}O_{2c}H$

2. First C-O coupling: $CH_3^* + O_{2c} \rightarrow CH_3O_{2c}$

3. Second C-H activation: $CH_3O_{2c} + O_{2c} \rightarrow CH_2O_{2c} + O_{2c}H$

4. Second C-O coupling: $CH_2O_{2c} + O_{2c} \rightarrow O_{2c}CH_2O_{2c}$

5. Third C-H activation: $O_{2c}CH_2O_{2c} + O_2^* \rightarrow O_{2c}CHO_{2c} + OOH^*$

6. Reconstruction: $O_{2c}CHO_{2c} \rightarrow O_{2c}CHO^*$

7. Fourth C-H activation: $O_{2c}CHO^{*} + OH^{*} \rightarrow CO_2 + O_{2c}H_2$

where low-coordinated O_{2c} located over the surface of Co_3O_4 (110) but not on (100) facets. The presence of O_{2c} over Co_3O_4 (110) facets facilitates the first C-H bond breakage, which is assumed to be the rate-controlling step for methane oxidation. It was proposed that the H over Co_3O_4 (110) surface is easier to transfer for the formation of H_2O and regenerate the active O_{2c} sites. Therefore Co_3O_4 (110) facets exhibit superior catalytic activity for methane oxidation, enabling complete methane conversion below 400 °C.

Additionally, Hu *et al.*[89] explored the methane combustion performance on different exposed facets of Co_3O_4. They proposed that the catalytic activity for Co_3O_4 would be in the order: nanosheets {112} > nanobelts {110} >> nanocubes {001}. Nanosheets of Co_3O_4 with exposed {112} exhibit excellent methane oxidation behavior with 50% conversion at 313 °C (GHSV= 40000 h^{-1}), which is comparable to Pd-based catalysts. Sun *et al.*[90] investigated Co_3O_4 with different dimensional structures, and found the following activity sequence: nanoplates (2D structure with ~ 20 nm in thickness and specifically exposed (112) facets) > nanorods (1D, 40–60 nm in length and 10 nm in diameter, (011) and (001)) > nanoparticles (0D, ~ 20 nm, (111) and (001)) >> mesoporous (3D, pore size is about 4-5 nm, (011)) >> microporous (3D, pore size is about 2-3 nm, (111)). They found that adsorbed oxygen is more active than lattice oxygen for catalysis and Co^{2+} is crucial for the breakage of C-H bonds. Therefore, it was proposed that not only the exposed facets, but also the active species on the surface like adsorbed oxygen and Co^{2+} play an important role for catalytic behavior.

Wang *et al.*[91] synthesized Co_3O_4 nanoparticles with excellent catalytic activity from a carbon-encapsulated cobalt precursor. During the sintering process, the Co atoms at defect sites react faster than the region encapsulated with graphite. The atomic diffusion of metallic Co into

an oxygen rich phase led to the breakage of structure and formation of defects on the surface and disordered channels inside the Co_3O_4 particles. The unique structure contributes to the significant activity and reactant mass transfer, which gave 50% conversion at 376 °C (GHSV= 18,000 $mL \cdot g^{-1}h^{-1}$).

1.3.1.2 MnO_x

Manganese oxide is one of the most efficient catalysts for oxidation reactions due to its multiple valence states.[92] The diverse crystalline phases of manganese oxide with different coordination geometries and oxidation states for the metal also contribute to varied catalytic performance. Wang *et al*.[93] explored the combustion of methane with different types of manganese oxide, including α-MnO_2, β-MnO_2, meso-MnO_2 and α-Mn_2O_3. It was found that α-MnO_2 exhibits the best catalytic activity and water resistance, which the authors attributed to the mono-μ-oxo bridged corner-shared [MnO_6] structure. The unique constitution leads to a higher surface concentration of Mn^{4+}, more surface oxygen vacancies and lower reducibility. As methane dissociates on Mn^{4+} sites, a process that is assumed to be the rate-determining step, the ratio of Mn^{4+} on the catalyst surface is crucial to the oxidation of methane.

Yu *et al*.[94] reported the preparation of highly active MnO_2 from perovskite $LaMnO_3$ by combining ball-milling with acid etching. These two methods created more oxygen vacancies and surface defects, which enhanced the catalytic behavior. These catalysts have higher Mn^{4+} content and active surface oxygen than α-MnO_2 prepared by traditional methods and show 50% conversion at 398 °C (GHSV= 21,000 $mL \cdot g^{-1}h^{-1}$), which is approximately 60 °C lower than α-MnO_2.

1.3.1.3 Cr_2O_3

The catalytic activity of Cr_2O_3 is affected by particle size and morphology. Kantserova *et al.*[95] reported that for temperatures up to 450 °C, the smaller particle size of Cr_2O_3 catalysts show improved activity. As well, when crystallization of Cr_2O_3 during thermal decomposition of Cr-containing precursor was not complete, crystallites were surrounded by amorphous Cr_2O_3 or within agglomerates. The presence of this amorphous Cr_2O_3 led to catalysts that were more active than crystalline Cr_2O_3.

Owing to the poor activity of bulk Cr_2O_3 catalysts, there have been few studies of pure Cr_2O_3 for low-temperature methane oxidation. Chromium is often used as a doping agent of metal oxides for the improvement of stability and sulfur tolerance. It can be incorporated into spinel[96-97] or perovskite[98-99] structures to give mixed metal catalysts with enhanced activity and stability.

1.3.2 Spinel catalysts

Spinel-type bimetallic oxides are oxides with an AB_2O_4 formula. Divalent A cations occupy the tetrahedral sites, and trivalent B cations occupy the octahedral sites in these systems. Spinel oxides belong to a cubic crystal system, and there are a wide variety of compositions such as $MgAl_2O_4$, $NiCo_2O_4$, $CoCr_2O_4$, $MnAl_2O_4$ and $MnCo_2O_4$.

Bimetallic $NiCo_2O_4$ has been shown to have better catalytic activity than any single metal oxide due to structural disorder with the insertion of Ni^{2+} into octahedral sites of spinel structure,[100] making this a particularly enticing candidate for catalysis, as well as energy conversion and storage applications.[101] The effect of the Co/Ni ratio in nickel cobalt oxides on methane oxidation has been investigated, and it was found that distorted $NiCo_2O_4$ spinel catalysts show excellent activity with 90% conversion at ~470 °C (GHSV = 60,000 $mL \cdot g^{-1} \cdot h^{-1}$).[100] Trivedi developed a $NiCo_2O_{4-\delta}$ spinel

catalyst by a reactive calcination (RC) method in which calcining precursors in a reactive mixture of CO and air exposed more active sites.[102] With this catalyst, the researchers achieved 98% methane conversion at 422 °C (GHSV = 12,000 $mL \cdot g^{-1} \cdot h^{-1}$). Tao *et al.* investigated the mechanism of complete methane oxidation on $NiCo_2O_4$ via *in situ* studies and theoretical simulations.[87] They reported that methane dissociated on nickel cations to form $-CH_3$ groups with a following oxidation to $-CH_2OH$. $-CH_2OH$ transformed to $-CH_2O$, -CHO, -COOH and finally CO_2 following dehydrogenation and oxidation steps.

Recently, $CoCr_2O_4$ spinel-type oxide catalysts, synthesized by sol-gel or co-precipitation methods, have been applied to methane oxidation. Hu *et al.*[96] prepared $CoCr_2O_4$ by a sol-gel method and the catalyst showed 90% conversion of methane to CO_2 at 750 °C (GHSV = 48,000 h^{-1}). Chen *et al.*[103] prepared a series of cobalt chromium oxides with different Co/Cr ratios via co-precipitation and evaluated these for methane combustion. $CoCr_2O_4$ showed the best catalytic activity with 90% conversion at 464 °C (GHSV = 36,000 h^{-1}) and excellent resistance to water vapor. Although these results are promising and demonstrate the potential of Co/Cr mixed oxides in methane oxidation catalysis, the catalytic activity for $CoCr_2O_4$ is still insufficient to meet the demanding conditions encountered in NGVs.

1.3.3 Perovskite catalysts

Perovskites represent a class of oxides with the chemical formula of ABO_3. A-sites are occupied by alkaline earth, rare-earth or other large elements. B-sites are always transition metals like Mn, Fe, Co, and Ni.[104] Normally, for unsubstituted perovskites, the catalytic activity is dependent on B-sites. As the perovskite surface preferentially exposes A-sites[105] and the perovskite catalysts have poor surface area, they typically exhibit high stability but relatively low activity.

Plenty of efforts have been made to solve this problem. It was proposed that different types of B-site elements could exhibit different catalytic activity. Partial substitution of A-site ions may cause the distortion of the lattice structure, which creates more vacancies and facilitates oxygen mobility. For example, Xiang *et al.*[106] prepared a series of $La_{1-x}Ce_xFeO_3$ by a sol-gel method. They found the incorporation of Ce into A-sites increases the O_2 adsorption energy and activates the O-O bond. The $T_{90\%}$ for $La_{0.7}Ce_{0.3}FeO_3$ is 510 °C (GHSV= 12,000 $mL \cdot g^{-1} \cdot h^{-1}$), which is approximately 80 °C lower than $LaFeO_3$. Also the mesoporous structure of perovskite catalysts with higher surface area results in high catalytic activity. For instance, 3D macro/mesoporous $La_{1-x}Ce_xCoO_3$[107] and $La_{0.6}Sr_{0.4}MnO_3$[108] synthesized by a hard-soft template combination method have increased surface area and present improved catalytic activity. However, the catalytic performance still needs to be further enhanced for practical usage.

1.3.4 Hexaaluminate catalysts

Hexaaluminate salts are a class of hexagonal aluminates with the general formula $AB_xAl_{12-x}O_{19}$. The sites are normally alkali or alkaline earth and rare earth metals, while the B sites are transition metals from period 4. The unique layered and close-packed structure and various components makes these attractive for catalytic oxidation.

Kim *et al.*[109] synthesized manganese substituted $La_xSr_{1-x}MnAl_{11}O_{19}$, which exhibited excellent thermal stability. The mixing of La and Sr at A-sites and the incorporation of Mn in B-sites improved the specific surface area and reducibility. $La_{0.6}Sr_{0.4}MnAl_{11}O_{19}$ presented the best catalytic activity with $T_{90\%}$ at 675 °C (GHSV= 60,000 $mL \cdot g^{-1} \cdot h^{-1}$). The poor catalytic activity but significant stability of hexaaluminate make it a better support material instead of active phase.

1.4 Monolith coating for natural gas vehicles

Powder catalysts cannot be used directly in practice. Typically, monolithic cordierite (a silicate mineral) with square channels serves as a support of active catalysts for conventional usage. The honeycomb structure enhances the mass and heat transfer, and does not induce a significant pressure drop or result in hot spots. Cordierite is made from magnesium aluminosilicate ($Mg_2(Al_4Si_5O_{18})$) without meso/micro porous structure, which leads to very low surface area (<1 m^2/g).[110] It is essential to obtain strong interaction between monolith and catalysts, and maintain good activity and stability of active sites.

Normally, an alumina washcoat with a high surface area is a good candidate to improve the distribution of active catalysts. In addition, common coating methods include impregnation, sol-gel, and hydrothermal treatment combined with calcination.

Liao *et al.*[111] prepared $PdO/(Ce,Y)O_2/\gamma\text{-}Al_2O_3$/monolith by impregnation and sol dipping method. The impregnation method led to a rugged surface, while sol dipping results in more even surface coverage with a porous structure. The monolith synthesized by sol dipping, using $Pd(NO_3)_2$ as precursor, presented the best catalytic activity with 90% conversion at 421 °C (GHSV= 10,000 h^{-1}).

Ren *et al.*[112] reported the successful coating of $M_xCo_{3-x}O_4$ (M=Co, Zn, Ni) nanowires on a monolith. The spinel $M_xCo_{3-x}O_4$ nanoarrays were formed on the monolith via urea hydrolysis and annealing process. $Ni_{0.5}Co_{2.5}O_4$ monolith exhibits the best catalytic performance with complete conversion below 600 °C (GHSV= 45,000 h^{-1}).

In conclusion, monolith coating is an essential step to make powder catalysts suitable for practical application. An efficient coating method is crucial for catalysis testing. Although

researchers have developed many coating methods, it is important to investigate the specific method that is suitable for coating nanostructured catalysts on large monoliths (~500 mL) in order to obtain strong binding between catalysts and monolith, and maintain its high activity and stability.

1.5 Goals and scope of the thesis

According to the literature, Pd-based catalysts exhibit excellent catalytic activity by optimizing the structure of PdO, the reducibility of the support and the interaction between active site PdO and support. The hydrothermal stability and sulfur tolerance for Pd-based catalysts still needs to be further improved. For non-precious metal oxides, they have potential to reach a comparable activity as Pd-based catalysts like Co_3O_4 and bimetallic spinel oxides. Their catalytic activity can be enhanced by increasing the number of active sites and oxygen vacancies, improving the reducibility of the metal oxides. The aim of this thesis is to develop new, qualified catalysts for low temperature methane oxidation. The catalysts should have high catalytic activity with 100% conversion below 500 °C, long-term durability in the presence of water and poisoning gases, and be inexpensive. To satisfy this goal, different types of catalysts are selected that already have either good catalytic activity or high stability. For example, noble metal Pd-based catalysts with low Pd loading have good activity but low thermal and hydrothermal stability. Efforts were made to improve their stability. Non-noble metal catalysts that are inexpensive such as spinel Co_3O_4 and MnO_2 exhibit moderate activity. Also Cr_2O_3 with excellent SO_2 tolerance was chosen to increase resistance against poisoning gases. This thesis takes advantage of various approaches to optimize the structure and property of catalysts to improve their catalytic activity and stability. Factors such as particle size, crystalline phase, surface area, morphology and reducibility contribute to catalytic performance and have been investigated in this thesis using multiple characterization techniques for better understanding the relationship between structure and catalytic behavior.

In Chapter 2, I combined the advantages of surface assisted reduction for Pd deposited on CeO_2, and the protective function of mesoporous silica to obtain catalysts with enhanced stability.

The developed novel catalysts with highly active PdO/CeO_2/PdO located in the ordered channels of SBA-15 maintained excellent catalytic activity and exhibited interesting hydrothermal performance. The unexpected increase of methane conversion in the presence of water and after water cut off was studied in detail.

Chapter 3 focused on non-noble metal spinel catalysts. According to previous research, bimetallic catalysts induce distortion in the lattice structure, which leads to enriched vacancies and active sites. Also, the exposure of specific high index facets plays an important role in catalytic performance. Therefore, I synthesized spinel $NiCo_2O_4$ catalysts with unique bowtie-shaped structures via a simple hydrothermal method. The formation mechanism of the unique bowtie-shaped $NiCo_2O_4$ was investigated in detail.

In Chapter 4, I took advantage of the hydrothermal method to incorporate Cr into spinel cobalt oxide. The formed spherical $CoCr_2O_4$ nanoparticles exhibit enhanced catalytic activity with 100% conversion below 500 °C. $CoCr_2O_4$ maintained high SO_2 tolerance and excellent hydrothermal stability, which improves the potential for these catalysts to be used in NGVs. Furthermore, the catalysts were coated on monoliths by a dipping and sintering method. The coated monolith which is a smooth surface still maintains significant activity and durability.

In Chapter 5, a series of non-noble metal catalysts was synthesized using MnO_2 aerogel nanowires as support. They displayed improved catalytic activity, which are comparable to Pd-based catalysts. Then PdO was loaded onto MnO_2 aerogel with or without surface modification by deposition-precipitation method. PdO/MnO_2 exhibited excellent catalytic activity, and both its hydrothermal stability and sulfur tolerance were enhanced.

Chapter 2: Mesoporous Silica-Supported Nanostructured PdO/CeO_2 Catalysts

2.1 Introduction

Pd supported on ceria (CeO_2) has received substantial attention due to its large oxygen storage capacity and the improvement in catalytic activity and stability. Our group reported the preparation of nanostructured PdO/CeO_2 by a new "surface-assisted reduction" (SAR) method,[62] which yields nanostructured CeO_2 substrates coated with highly dispersed PdO after calcination. These catalysts show 50% conversion for the oxidation of methane below 300 °C.

The activity of heterogeneous catalysts is influenced by many factors, including particle size,[113] and in many cases, nanoparticles give rise to the best catalytic performance;[114] sintering, however, can reduce performance over time. Confining nanoparticle catalysts in mesoporous silica such as SBA-15 is an approach to overcome the sintering problem.[115] In fact, SBA-15 has been used to construct nanoparticles of various materials,[116] some of which have been explored for catalysis.[117]

Here, we report the preparation of new nanostructured catalysts based on $PdO/CeO_2/PdO$ materials supported on SBA-15. These materials have been constructed using a novel double deposition approach, where SAR of Pd is carried out inside the channels of a mesoporous host for the first time. Importantly, the SBA-15 host constrains the size of the resulting Pd and CeO_2 particles, whereas the SAR ensures excellent distribution of Pd on the nanostructured CeO_2. The materials are evaluated for LTMOX catalysis.

2.2 Experimental

2.2.1 Preparation of Pd on SBA-15 catalysts

The synthesis of SBA-15 was carried out according to a previous report.[115] From gas adsorption measurements, the SBA-15 has a Brunauer−Emmett−Teller (BET) surface area of 821 $m^2\ g^{-1}$ and a Barrett−Joyner−Halenda pore size of 9.2 nm. The SBA-15 was surface-modified with the silane (APTS) ($H_2N(CH_2)_3$-$Si(OCH_3)_3$), with a loading of 2−3 mmol g^{-1}. In a typical procedure, 1.0 g of SBA-15 was combined with 0.66 g APTS in 50 mL of ethanol. The mixture was heated to reflux for 12 h. The product was isolated on a Büchner funnel, washed with ethanol, and dried (denoted as SBA-15(M)). Subsequently, palladium was anchored to the mesoporous silica by adding 50 mL of ethanol solution containing a specific amount of $Pd(NO_3)_2$ (Table 2.1, step 1) to 0.15 g of SBA-15(M). The mixture was vigorously stirred at room temperature for 12 h and then heated to 60 °C to evaporate the solvent under stirring.

2.2.2 Preparation of CF/Pd on SBA-15 catalyst precursor.

Potassium oxalate (Table 2.1) was dissolved in 50 mL of deionized water, and Pd/SBA-15(M) was added to give a molar ratio of Pd/potassium oxalate = 1:5, and the mixture was continuously stirred for 12 h, then dried at 90 °C. The resulting powder was added to 10 mL of cerium nitrate ethanol solution and dried at 60 °C with stirring. Cerium formate was synthesized by adding the above mixture to 10 mL of ethylene glycol and transferring the mixture into a 23 mL Teflon-lined stainless steel autoclave. The sealed reaction vessel was maintained at 145 °C for 15 h. The product was then recovered by centrifugation and washed with ethanol three times.

2.2.3 Preparation of Pd/CF/Pd on SBA-15 catalysts

Surface assisted reduction was used to load another layer of Pd on the cerium formate. In a typical reaction, the CF/Pd on SBA-15 precursor was added to 10 mL of a calculated amount of $Pd(NO_3)_2$ (Table 2.1, step 2) aqueous solution and stirred for 12 h. The solid was collected by centrifugation and calcined at 400 °C for 3 h to give the final Pd/CF/Pd SBA-15(M) product.

2.2.4 Preparation of Pd/CF on the surface of SBA-15 catalysts

Control samples were prepared by dissolving cerium nitrate (Table 2.1) in ethylene glycol with stirring. SBA-15(M) (0.15 g) was then added, and the mixture was stirred for 30 min. The mixture was then transferred into a 23 mL Teflon-lined stainless steel autoclave vessel and sealed and heated at 145 °C for 15 h. After washing using centrifugation, the precursor was dispersed into a $Pd(NO_3)_2$ (sum of $Pd(NO_3)_2$ mass in step 1 + step 2, Table 2.1) aqueous solution and stirred for 12 h. The product was collected by centrifugation and calcined in a furnace at 400 °C for 3 h.

2.2.5 Characterization

Powder X-ray diffraction (PXRD) data were acquired on a Bruker D8 Advance X-ray diffractometer in the Bragg-Brentano configuration operating with Cu Kα radiation at 40 kV and 40 mA. BET surface area, pore volume and pore size were determined using nitrogen adsorption on a micromeritics accelerated Surface Area & Porosity (ASAP) 2020 system at 77 K. Transmission electron microscopy (TEM) images were obtained using a Hitachi H7600 electron microscope with an accelerating voltage of 80 kV. Energy-dispersive X-ray (EDX) spectra of the samples were obtained from a Hitachi S2600 Variable Pressure SEM with an X-ray detector. Fourier transform infrared (FT-IR) spectra were collected on a Nicolet 4700 spectrometer (Thermo

Scientific). X-ray photoelectron spectroscopy (XPS) measurements were obtained in an ion-pumped chamber (1×10^{-9} Torr) of a Leybold Max200 spectrometer. (Al Kα, hν = 1486.6 eV). High-angle annular dark-field (HAADF) images and EDX mapping data were collected on a FEI Tecnai Osiris S/TEM under an operating voltage of 200 kV.

2.2.6 Catalyst testing

The catalytic activity was measured by temperature-programmed oxidation (TPO) of methane. The TPO instrument contains a stainless steel fixed-bed microreactor (length = 4.5 cm; i.d. = 0.7 cm) within an electric tube furnace with proportional-integral-derivative (PID) temperature control. Two thermocouples (K-type) inside the reactor were used to measure the temperature at the top and bottom of the catalyst bed. The flow mixture of 1000 ppmv CH_4, 10% (V/V) O_2, balanced by Ar and He, was fed to the reactor at a total flow rate of 300 mL (STP) min^{-1} (space velocity 180,000 mL (STP)$\cdot g^{-1}\cdot h^{-1}$) by electric mass flow controllers (Brooks 5850 TR). High space velocity shortens the contact time between reagents and catalysts, which leads to decreased catalytic activity. We selected a high space velocity (180,000 mL (STP)$\cdot g^{-1}\cdot h^{-1}$) to mimic real engine conditions. The 0.1000 g catalyst was diluted with SiC at a volume ratio of catalyst/SiC = 1:4 to ensure isothermal reaction conditions. The mixture of feed gas was preheated at 120 °C before entering the reactor. The reactor was heated from 120 to 600 °C at a rate of 5 °C$\cdot min^{-1}$. The slow ramp rate ensures equilibrium conversion at any temperature. The emitted gas was analyzed using a VG ProLab quadrupole mass spectrometer (QMS; ThermoFisher Scientific) and component intensities were calibrated using standard gas mixtures (Praxair, certified purity), from which the CH_4 conversion and overall C balance were calculated. The stability of the catalysts was measured over a 24 h period at constant temperature and gas flowrate

(space velocity 180,000 mL (STP)·g^{-1}·h^{-1}) with 5% H_2O pumped into the dry feed gas prior to the preheater using a liquid syringe pump (Harvard Apparatus Model 44). Although 5% H_2O is lower than that present in emission from NGVs (10-15%), it's acceptable to evaluate the effect of water vapor on catalysts and avoid destroying the catalysts after injection. If the conversion decreases to 0% after water injection, it is difficult to investigate the deactivation mechanism of catalysts.

Table 2.1 Quantities of reagents for synthesis of catalysts

	Reagent (g)((mmol))			
Catalysts	$Pd(NO_3)_2$ (step 1)	$K_2C_2O_4$	$Ce(NO_3)_3$	$Pd(NO_3)_2$ (step 2)
PdCFPdSBA-15(M) 1%Pd	0.0033 (0.014)	0.013 (0.071)	0.056 (0.13)	0.00050 (0.0021)
PdCFPdSBA-15(M) 5%Pd	0.026 (0.11)	0.11 (0.57)	0.25 (0.57)	0.0022 (0.0095)

2.3 Results and Discussion

2.3.1 Synthesis of SBA-15 supported PdO/CeO_2/PdO nanoparticles

Nanoparticles of PdO/CeO_2/PdO were loaded onto SBA-15 using a multistep sequence (Scheme 2.1). Table 2.1 shows the quantities of reagents used at each stage, and Table 2.2 shows the gas adsorption measurements after each stage (detailed N_2 sorption isotherms and pore size distribution plots are shown in Figure 2.1). In the first step, SBA-15 with a pore size of 9.2 nm was functionalized with (3-aminopropyl)trimethoxysilane (APTS) to incorporate amino groups onto the surface of SBA-15 for improved trapping of Pd^{2+}.

Scheme 2.1 Synthesis of Nanostructured Materials

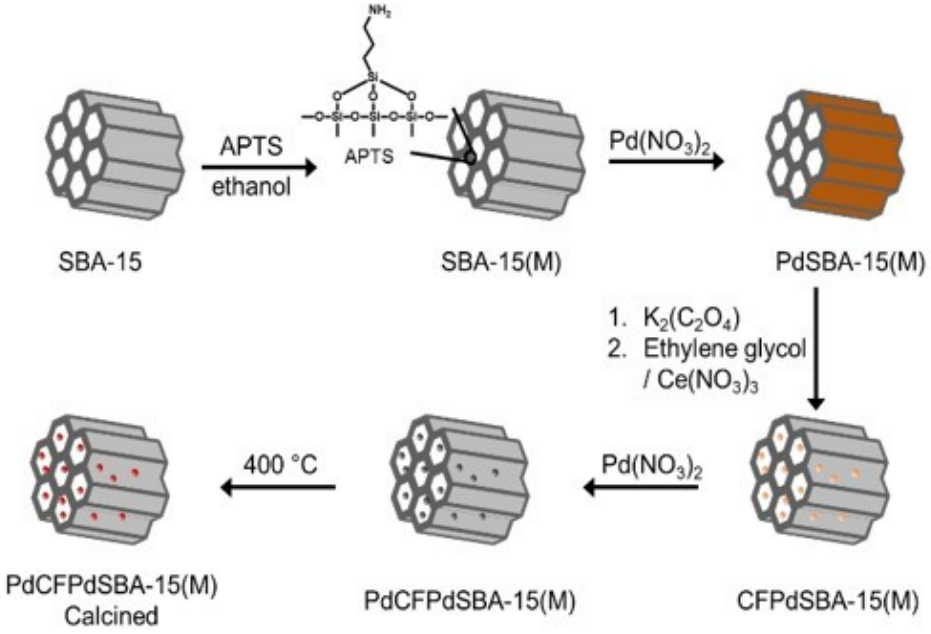

Table 2.2 Surface area, pore size and volume of SBA-15 with different catalyst loading

Sample	Surface area (m^2/g)	Pore size (nm)	Volume (cm^3/g)
SBA-15	821	9.2	1.2
SBA-15(M)	463	7.3	0.7
CFPdSBA-15(M) 1%Pd	272	7.3	0.5
PdCFPdSBA-15(M) 1%Pd	526	9.1	1.0
CFPdSBA-15(M) 5%Pd	169	7.4	0.3
PdCFPdSBA-15(M) 5%Pd	340	7.8	0.5

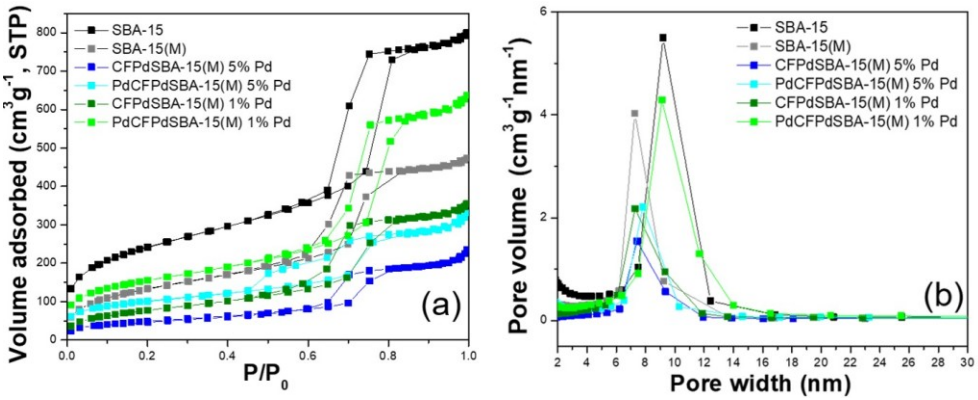

Figure 2.1 Nitrogen adsorption–desorption isotherms (a) and pore size distribution plots (b).

After surface modification, the surface area, pore size and pore volume of SBA-15 decrease, indicating the successful incorporation of APTS. From transmission electron microscopy (TEM) (Figure 2.2) and powder X-ray diffraction (PXRD) (Figure 2.3), the sample retained the hexagonal P6mm symmetry of SBA-15. Elemental analysis indicated that the sample contains 2.0 mmol amino groups/g SiO_2, giving a surface density of grafted groups of 2.6 nm^{-2}. Furthermore, IR bands at 2941 and 1557 cm^{-1} correspond to a stretching band of methylene groups and the bending vibration of amino groups from APTS,[118] respectively (Figure 2.4).

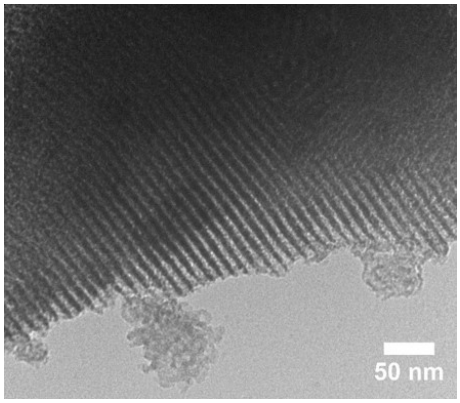

Figure 2.2 TEM image for SBA-15(M).

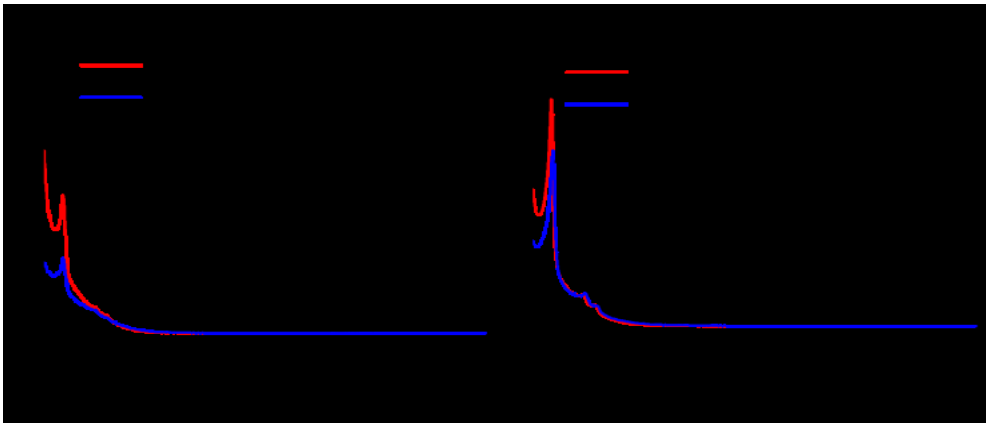

Figure 2.3 Small angle PXRD patterns of catalysts with (a) 5% and (b) 1% Pd loading.

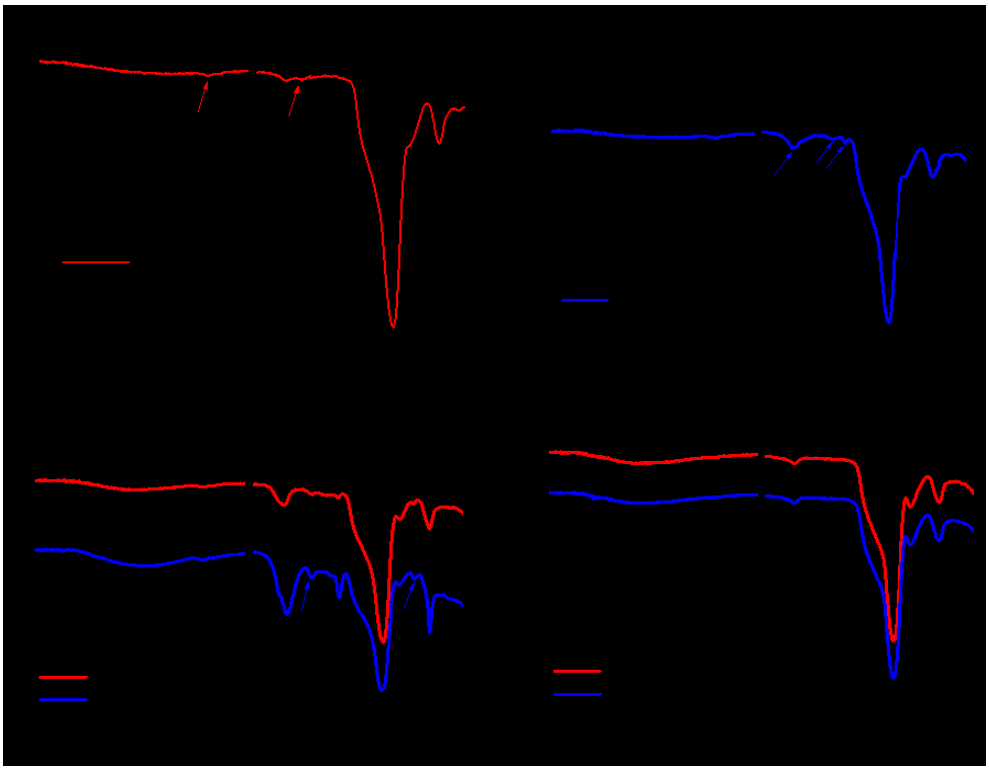

Figure 2.4 (a) FTIR spectra of SBA-15 and surface modified SBA-15 (SBA-15(M)). The red arrows point to the stretching band of the methylene groups at 2941 cm^{-1} and bending vibration of amino groups at 1557 cm^{-1}, (b) FTIR spectra of PdC_2O_4 on SBA-15(M) compared with SBA-15(M). The blue arrows point to the O-C=O stretching modes at 1381 and 1311 cm^{-1}, and oxalate antisymmetric stretching mode at 1620 cm^{-1}, (c) FTIR spectra of CFPdSBA-15(M) with different Pd loading. The blue arrows point to the carbonate ion vibrational modes at 1465 and 881 cm^{-1}, (d) FTIR spectra of calcined PdCFPdSBA-15.

In the next step, Pd^{2+} ions were incorporated into the material. Then, oxalate groups were incorporated into the silica pores. FT-IR spectroscopy confirmed the presence of the oxalate groups: bands at 1381 and 1311 cm^{-1} are assigned to the O–C=O stretching mode, and a band around 1620 cm^{-1} is due to the oxalate antisymmetric stretching mode.[119]

Next, the materials were reacted with cerium nitrate in ethylene glycol at high temperature to give CF/Pd on SBA-15(M) precursor. The low-angle PXRD pattern (Figure 2.3) shows three

well-resolved peaks, consistent with maintaining the hexagonal symmetry of the SBA-15 starting material. The decreased intensity of the PXRD peaks with increased catalyst loading does not indicate decreased order in the structure. Rather, this result is consistent with the loading of the channels of mesoporous silica, as observed previously.[120] With the partial loading of the channels, the contrast difference between the pores and walls of the mesoporous host is diminished, leading to decreased diffraction intensity. This result confirms that both palladium and cerium are inside the channels and not only located on the surface.

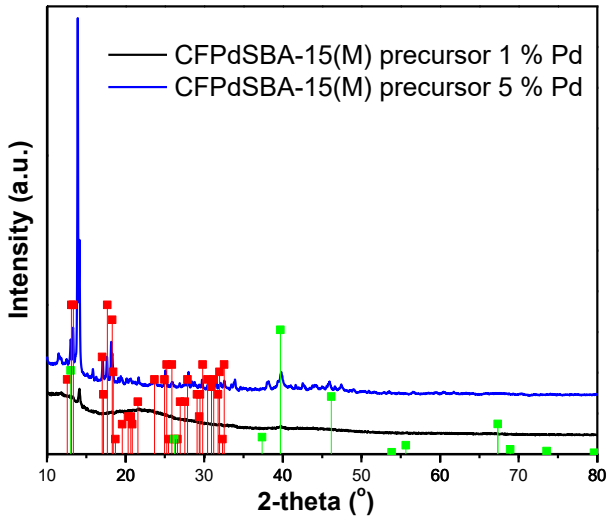

Figure 2.5 PXRD patterns of CFPdSBA-15(M) precursor with different Pd loading, (■) standard cerium oxalate hydrate (JCPDS 20-0268), (■) standard palladium (JCPDS 72-0710).

In the wide-angle PXRD pattern (Figure 2.5), the CFPdSBA-15(M) precursor showed peaks at low angle: 2θ = 11.7°, 14.0°. These peaks correspond to the interlayer spacing of the layered structure of the cerium compound.[121] This is similar to the PXRD pattern of cerium formate-reduced palladium prepared in previous work.[62] Furthermore, the CFPdSBA-15(M)

precursor with 5% Pd loading also showed sharp peaks assigned to palladium and cerium oxalate peaks, which demonstrated the reduction of Pd^{2+} to Pd in this step, and was consistent with the presence of some larger particles on the surface. As expected, increased loading of CFPdSBA-15(M) led to decreased surface area and pore volume (Table 2.2). For CFPdSBA-15(M) 1% Pd precursor, the surface area decreased by 191 m^2/g, and the pore volume decreased by 0.2 cm^3/g. For CFPdSBA-15(M) 5% Pd precursor, the surface area decreased by 290 m^2/g and pore volume decreased by 0.4 cm^3/g. However, in both materials the pore sizes are nearly the same, which indicates that the catalyst was loaded inside channels instead of blocking the openings to the channels.

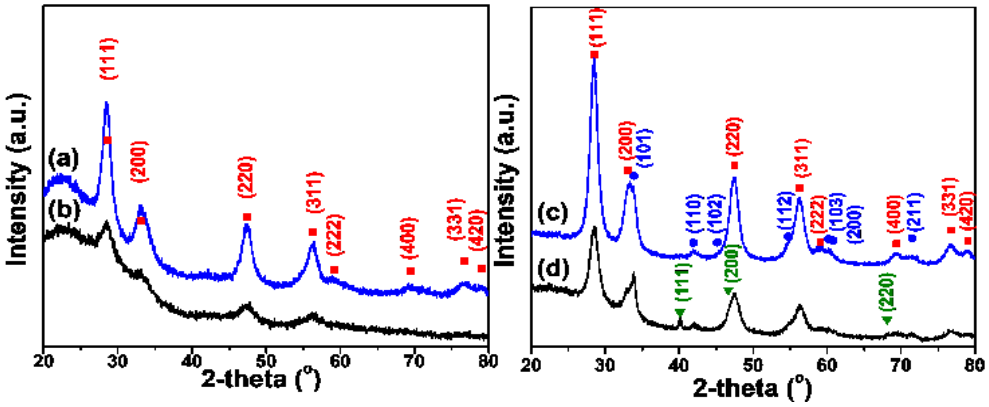

Figure 2.6 PXRD patterns of (a) PdCFPdSBA-15(M) 1% Pd, (b) CFPdSBA-15(M) 1% Pd, (c) PdCFPdSBA-15(M) 5% Pd, and (d) CFPdSBA-15(M) 5% Pd. (■) standard Cerianite – (Ce), syn-CeO_2 (JCPDS 75-9470), (●) standard Palladinite, syn – PdO (JCPDS 43-1024), and (▼) standard Palladium, syn – Pd (JCPDS 65-2867).

Cerium formate can reduce palladium(II) to palladium(0), forming cerium carbonate. Consistent with this, peaks around 1465 and 881 cm^{-1} in the FT-IR spectrum may be due to the carbonate ion vibrational modes.[122]

If CFPdSBA-15(M) precursor is calcined directly, CeO_2/PdO on SBA-15(M) is produced (denoted as CFPdSBA-15(M)). As shown in Figure 2.6, the sample loaded with 1 wt% Pd shows only broad peaks arising from ceria and no obvious palladium oxide peaks. This may be a result of the reduced amount of PdO and how well it is dispersed. For the 5 wt% Pd loaded sample, the PXRD pattern shows peaks characteristic of ceria, palladium, and palladium oxide. The presence of Pd peaks indicates the calcination time or temperature was insufficient to fully oxidize the Pd.

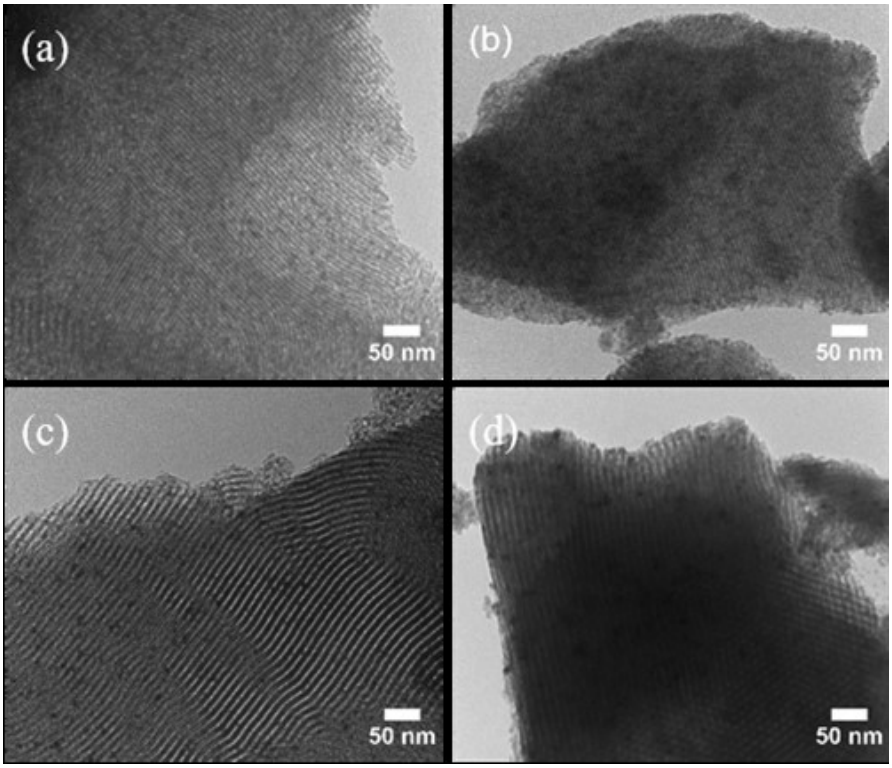

Figure 2.7 TEM images of CFPdSBA-15(M) 1%Pd (a) before calcination and (b) after calcination, and CFPdSBA-15(M) 5%Pd (c) before calcination and (d) after calcination.

In the TEM images (Figure 2.7), both CFPdSBA-15(M) precursor and CFPdSBA-15(M) (before and after calcination) show well-resolved small black spots inside the SBA-15(M) channels, consistent with the catalyst being successfully loaded into the channels of SBA-15(M).

Finally, by using SAR to reduce Pd a second time and then calcining, nanostructured $PdO/CeO_2/PdO$ on SBA-15(M) was produced (denoted as PdCFPdSBA-15(M)). The low-angle PXRD pattern (Figure 2.3) for this material still shows (100), (110), and (200) reflections, indicating that the hexagonal nanostructure of the SBA-15 was retained.

Wide-angle PXRD data (Figure 2.6) for the sample with 1 wt% Pd loading show only ceria peaks, similar to the CFPdSBA-15(M) calcined sample. For the sample with 5 wt% Pd loading, both ceria and palladium oxide peaks are observed. With increased loading, the PdO particles reached sizes that result in the observation of diffraction. In contrast with CFPdSBA-15(M) 5% Pd that has been calcined directly, PdCFPdSBA-15(M) 5% Pd does not show Pd peaks. This is because after reducing Pd a second time by SAR, the Pd is distributed more evenly. During calcination, all of the Pd(0) is oxidized to palladium oxide.

Interestingly, BET data show that the surface area and pore volume of Pd/CF/PdSBA-15(M) increased compared to that of CF/PdSBA-15(M) following calcination, consistent with decomposition and loss of organic groups from the pores. This was supported by FT-IR spectra of the calcined samples, which are very similar to those for SBA-15 and confirm the decomposition of carbonate, oxalate groups and APTS during calcination.

TEM images (Figure 2.8a-d) of the calcined samples reveal well-resolved small nanoparticles within the SBA-15(M) channels. The size of twenty individual PdO/CeO_2 nanoparticles inside the silica pores were measured to investigate the size distribution of the catalysts. The particles within PdCFPdSBA-15(M) are 3.6 ± 0.5 nm in diameter for 1 wt% Pd

loading and 7.2 ± 0.7 nm in diameter for the 5 wt% Pd-loaded sample. EDX mapping images (Figure 2.9) indicated that PdO/CeO_2 catalysts are inside the pores of silica. The ceria distribution was uniform, which covered the surface of silica and the nanospherical PdO located inside the channel of SBA-15. The lattice fringes corresponding to the different crystalline domains of the PdO/CeO_2 could be observed from high-resolution transmission electron microscopy (HRTEM) (Figure 2.10).

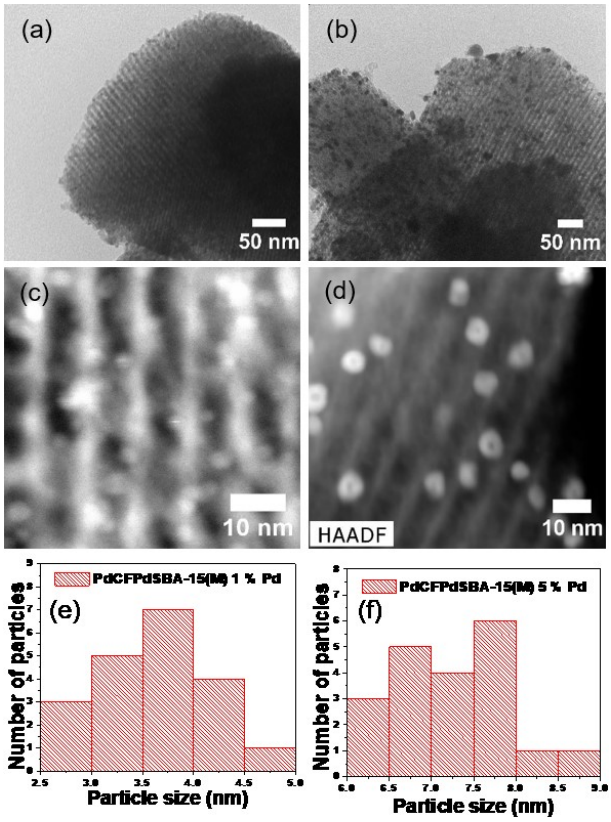

Figure 2.8 (a) TEM image, (c) HAADF image and (e) particle size distribution of PdCFPdSBA-15(M) with 1%Pd loading; (b) TEM image, (d) HAADF image and (f) particle size distribution of PdCFPdSBA-15(M) with 5%Pd loading.

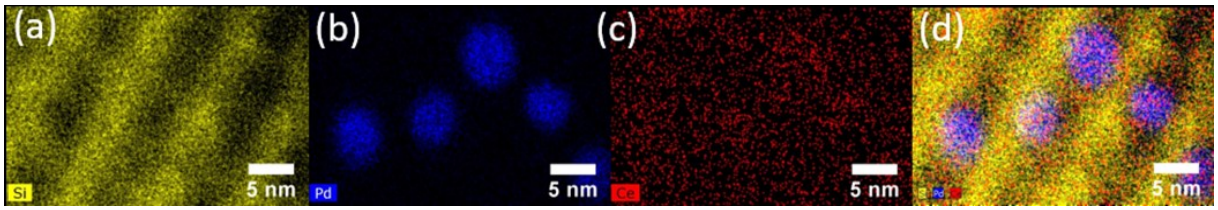

Figure 2.9 Energy dispersive X-ray spectroscopy (EDX) elemental mapping of (a) Si, (b) Pd, (c) Ce and (d) overlay of the Si Ce and Pd distributions for PdCFPd SBA-15 with 5% Pd catalyst.

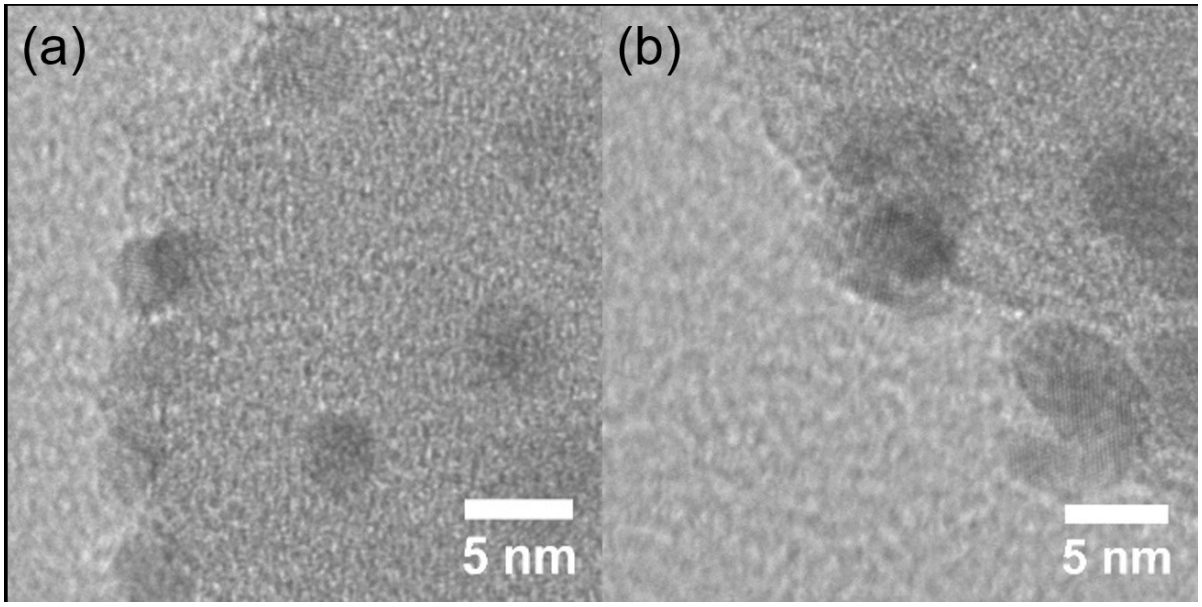

Figure 2.10 HRTEM image of PdCFPdSBA-15(M) with 1%Pd loading (a) and PdCFPdSBA-15(M) with 5%Pd loading (b).

Table 2.3 EDX data of samples with different amounts of catalyst loading on SBA-15(M)

Sample	Pd (wt%)	Ce (wt%)
CFPdSBA-15(M) 1wt%Pd	0.9	8.6
PdCFPdSBA-15(M) 1wt%Pd	1.0	5.0
CFPdSBA-15(M) 5wt%Pd	4.5	30.3
PdCFPdSBA-15(M) 5wt%Pd	5.3	18.5

EDX data were used to determine the amount of catalyst loading. After the second Pd loading step (step 2), the weight percentage of Pd increased slightly compared with the Pd loading after step 1 (Table 2.3). The final Pd weight percentage is nearly identical to the calculated loading. However, the weight percentage for Ce is only about half of the theoretical loading. This may be attributed to the loss of cerium during the hydrothermal process. Some of the ceria coating on SBA-15 may be removed during the hydrothermal treatment and subsequent centrifugation, resulting in only half of the expected cerium loading.

2.3.2 Catalytic methane oxidation

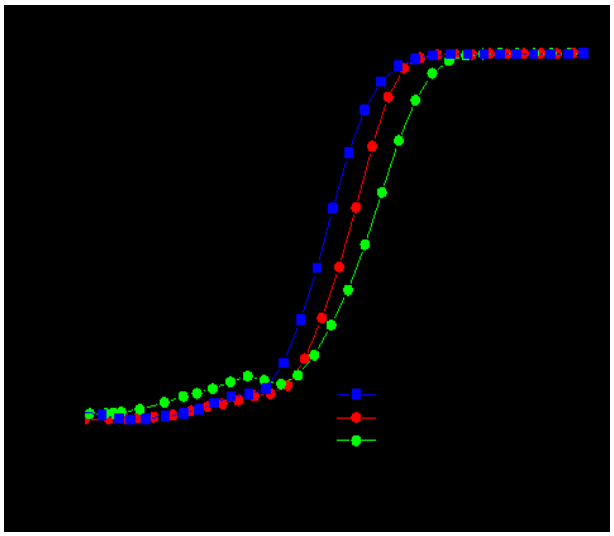

Figure 2.11 TPO reaction of different catalysts that were calcined at 400 °C for 3 h at the rate of 5 °C/min.

The LTMOX activity of the materials was investigated by temperature-programmed oxidation (TPO) measurements. Data for PdO/CeO_2/PdO on SBA-15(M) and CeO_2/PdO on SBA-15(M) with different Pd loadings are shown in Figure 2.11. PdCFPdSBA-15(M) with 5 wt% Pd loading shows excellent activity, achieving 50% methane conversion at ~290 °C and 100%

conversion at ~360 °C. CFPdSBA-15(M) 5% Pd samples prepared without using the SAR method to reduce Pd a second time showed poorer catalytic activity (50% conversion at 338 °C). The difference in catalytic performance between these two samples is attributed to a combination of structural differences and the small increase in the amount of Pd after the second deposition step. For the sample with 1 wt% Pd, the temperature at which 50% methane conversion is achieved was above 350 °C. A control sample prepared by coating PdCF on the external surface of SBA-15 exhibited similar activity as shown in Figure 2.12.

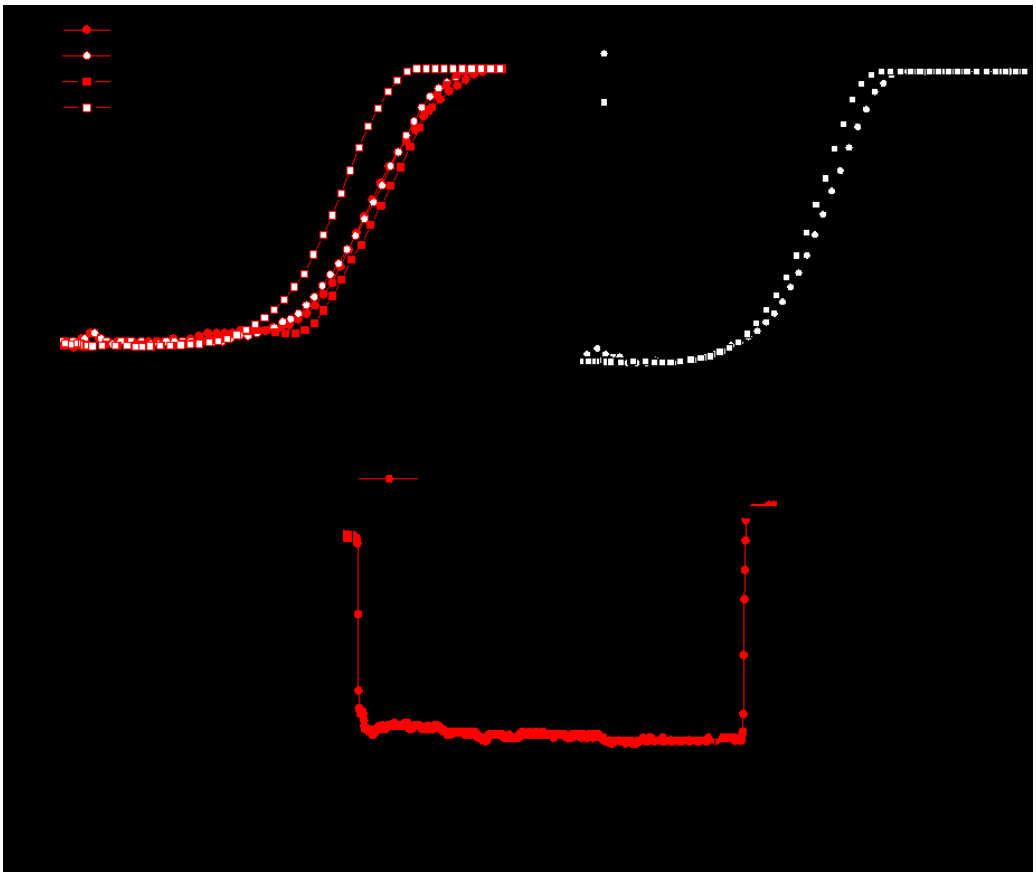

Figure 2.12 TPO curves showing the catalytic activity before and after water injection for PdCFPdSBA-15(M) and control catalysts with different Pd loading: (a) 1% Pd and (b) 5% Pd. (c) stability of the control catalysts with 1% Pd (at 370 °C) and 5% Pd (at 320 °C) loading in the presence of 5% water.

For methane oxidation catalysts to be useful in automotive applications, they must be stable in the presence of water vapor. To evaluate the stability of the new materials to water, we measured the methane oxidation catalysis of PdCFPdSBA-15 with 1% Pd when 5% water was injected at 370 °C (Figure 2.13). The activity rapidly decreased from 98 to ~50% after water injection; however, this is more stable than the activity in the presence of water for the control samples where the catalyst is not inside of a mesoporous host (Figure 2.12c). For the catalysts with 5% Pd loading, water was injected at 320 °C, and the activity decreased from 83 to 5%. After about 20 h, water was removed from the stream and the catalyst activity recovered to 100% conversion, even better than its initial activity. The water treatment appears to enhance the catalytic activity: when the TPO was measured for samples after water treatment, they showed improved performance. The 100% conversion temperature for 5% Pd catalysts decreased from 360 to 314 °C; for 1% Pd-loaded materials, it decreased from 395 to 355 °C.

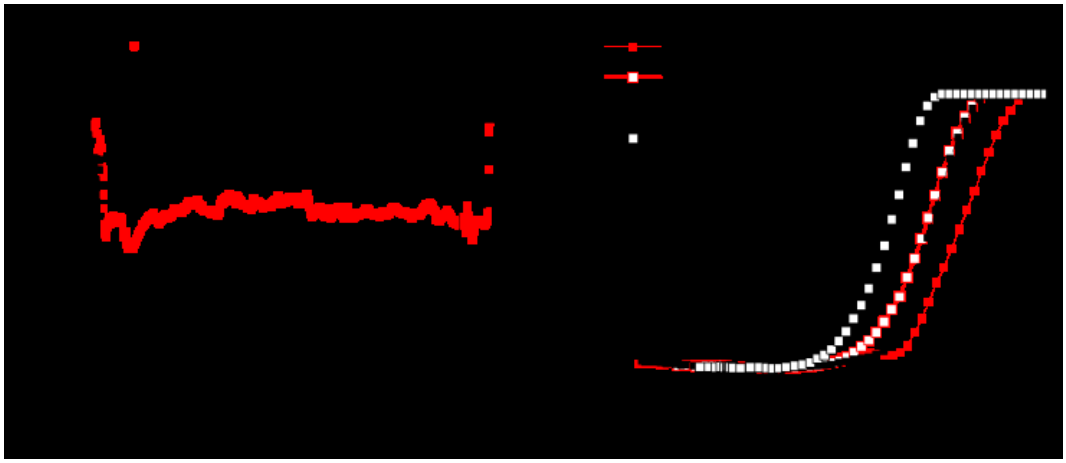

Figure 2.13 (a) Effect of 5% water for PdCFPdSBA-15(M) catalysts with 1% Pd (at 370 °C) and 5% Pd (at 320 °C) loading. (b) TPO curves showing the catalytic activity before and after water injection. Samples showed large improvement in catalytic activity after the water treatment.

During the injection of water, the rapid loss of activity may arise from the chemisorption of hydroxyl groups on the active sites of the surface, which compete with CH_4 adsorption.[74] The effect of water was more pronounced with the catalyst with greater Pd loading: the catalytic activity for 5% Pd loading catalysts decreased ~78% but only decreased by ~48% for the catalysts with 1% Pd loading. Nonetheless, immediately after removal of the water, both catalysts completely recovered their activities.

The behavior of catalysts in the presence of different amounts of water was also studied. In separate experiments, PdCFPdSBA-15 catalysts with 5% Pd were exposed to 2 and 5% water at 320 °C. The drop in catalytic activity was noticeably smaller at the lower concentration of water (Figure 2.14). Interestingly, after the initial drop in catalytic activity, the catalysts gradually recovered from ~10% conversion to around 50% in the presence of 2% water vapor.

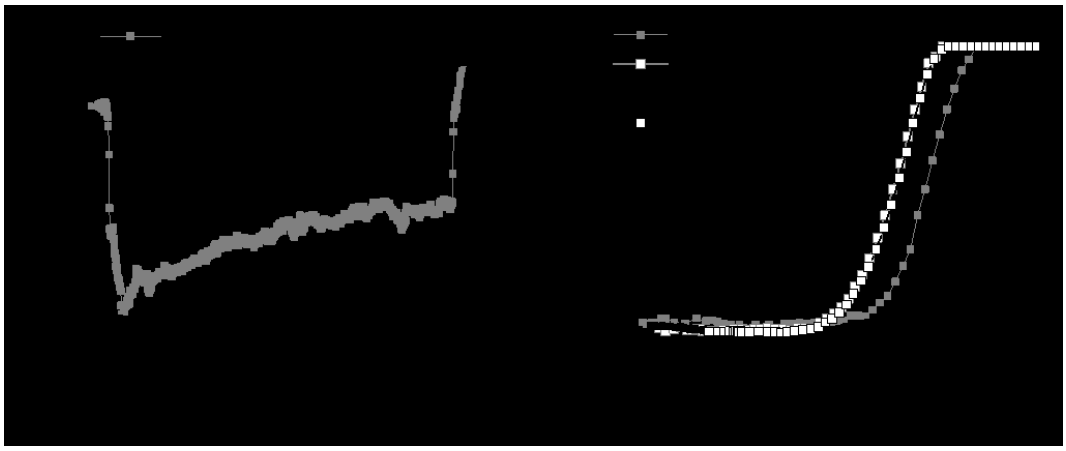

Figure 2.14 (a) Methane conversion measured for PdCFPdSBA-15(M) with 5% Pd upon introduction of 2% or 5% water. (b) Catalytic activity of samples before and after water treatment as measured by TPO experiments.

Furthermore, after water was removed, both catalysts recovered completely and showed better activity than before the water stability experiment. When the samples were again tested by TPO measurements, the temperature for 100% conversion decreased by about 50 °C. Therefore, water concentration only influences the performance of catalysts while they are exposed to water vapor. After the water is removed, the catalysts recover completely.

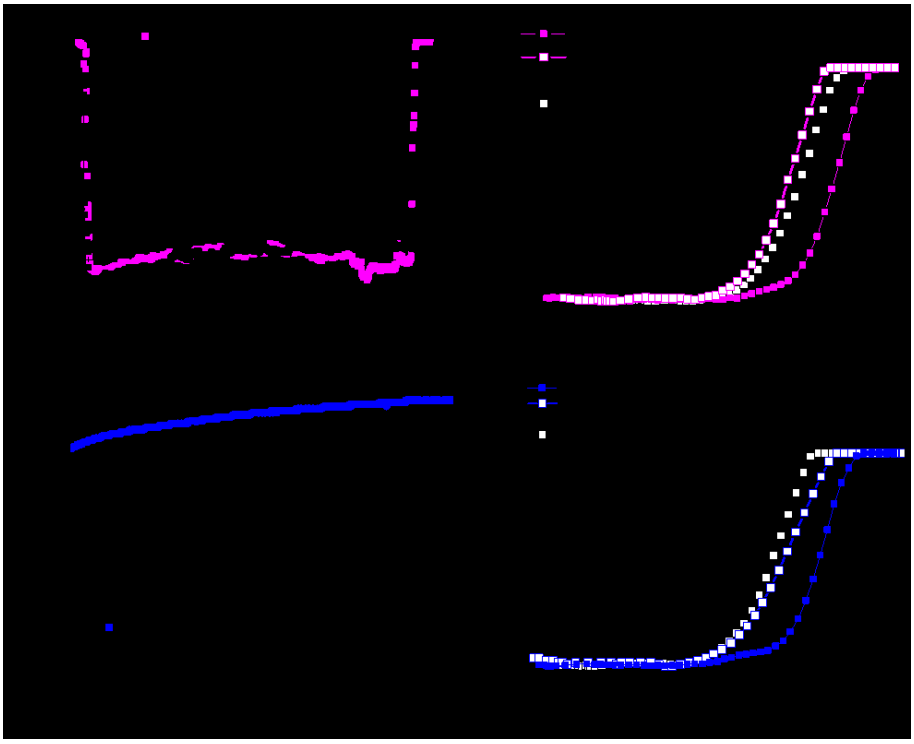

Figure 2.15 (a) Water stability test in the presence of 5% water for PdCFPdSBA-15(M) with 5% Pd calcined for either 3 h or 15 h at 400 °C before testing, (b) comparison of catalytic activity before and after water stability test, (c) thermal stability and water stability for PdCFPdSBA-15(M) with 5% Pd calcined at 400 °C for 15 h before test, and (d) comparison of the catalytic activity before and after water stability or thermal stability test.

It is interesting to see the increased activity in the presence of water vapor and better performance for the used catalysts. We thought that perhaps the samples needed a longer calcination time. To test this, PdCFPdSBA-15(M) with 5% Pd was calcined for 15 h at 400 °C before testing. Figure 2.15 shows the TPO measurements of the samples and the water stability tests. The performance of the sample calcined for 15 h was almost identical to the ones calcined for 3 h, indicating that calcination time is not the major factor.

Next, we measured the thermal stability of the samples at 320 °C without injection of water. The activity increased gradually from 80 to 100% conversion. From this experiment, it seems that the enhanced activity may not actually be due to the presence of water but due to reactivation of the catalysts by the reaction gases.

To better understand this phenomenon, the used catalysts were characterized by TEM, PXRD and X-ray photoelectron spectroscopy (XPS). TEM images of used PdCFPdSBA-15(M) with 5% Pd catalysts after water stability and thermal stability tests (Figure 2.16) showed that the channeled structure of SBA-15 was maintained. There appears to be some PdO/CeO_2 sintering to form larger particles, but most catalysts were still well confined in the pores of SBA-15. For the control samples, larger catalyst particles are sintered into big particles on the external surface of SBA-15 (Figure 2.17). The PdO/CeO_2 catalysts loading inside the channel of SBA-15 can be confined by the silica template and inhibited sintering. Therefore, PdCFPdSBA-15(M) catalysts show very good stability during the methane oxidation reaction.

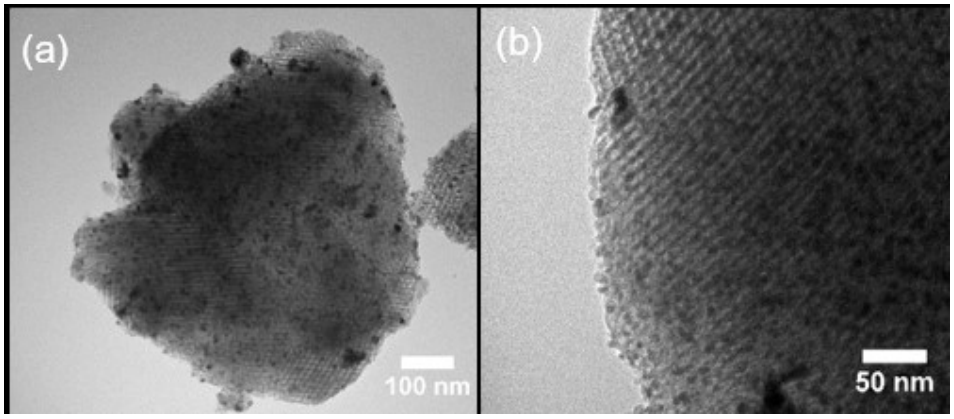

Figure 2.16 TEM images for PdCFPdSBA-15(M) with 5% Pd catalysts (a) after water stability test, and (b) after thermal stability test.

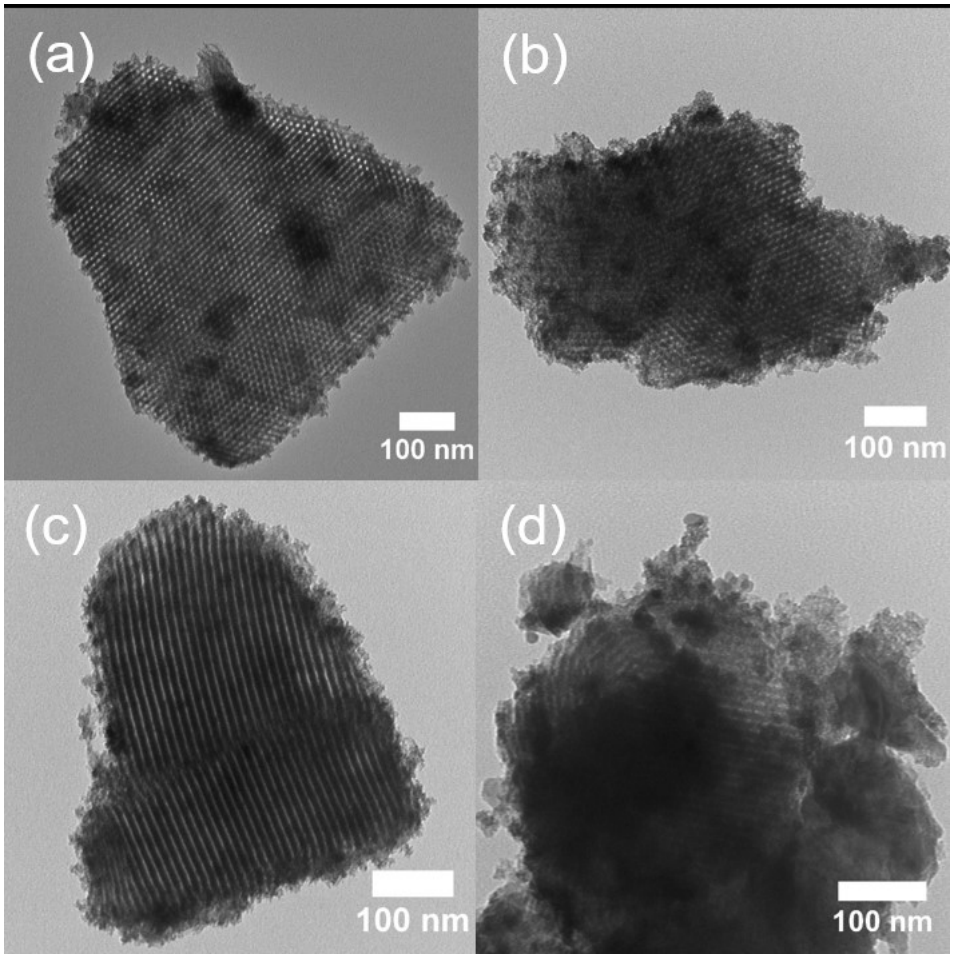

Figure 2.17 TEM images for control catalysts with different Pd loading: fresh catalysts (a) 1% Pd, (b) 5% Pd, catalysts after water stability test (c) 1% Pd and (d) 5% Pd.

The PXRD pattern of the used catalyst is similar to that of the fresh catalyst (Figure 2.18). After the thermal stability test, only broad peaks assigned to CeO_2 and PdO are observed in the PXRD. The particle size calculated by the Scherrer equation was similar for the fresh and used catalysts, which demonstrates that the catalyst size does not change significantly under the catalysis testing conditions (Table 2.4).

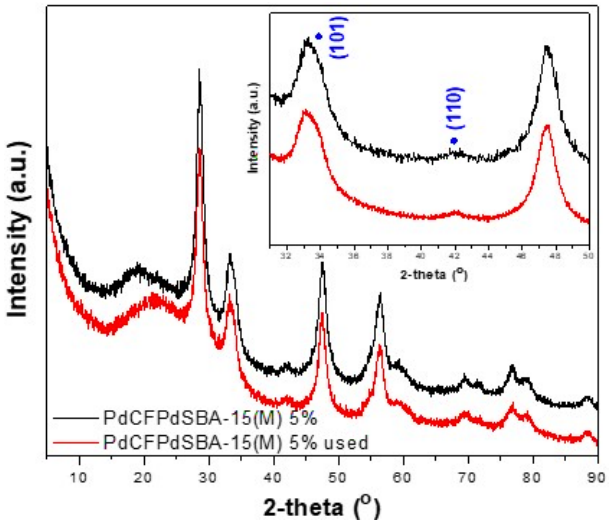

Figure 2.18 PXRD patterns for PdCFPdSBA-15(M) 5%Pd before and after thermal stability test. Inset: enlarged Pd diffraction pattern. (●)Palladinite standard, syn – PdO (JCPDS 43-1024).

Table 2.4 Particle size of PdCFPdSBA-15(M) 5%Pd catalysts before and after thermal stability test calculated by Scherrer equation.

Catalysts	PdO particle size (nm)	CeO_2 particle size (nm)
PdCFPdSBA-15(M) 5%Pd before stability test	6.9	6.4
PdCFPdSBA-15(M) 5%Pd after stability test	7.1	6.5

High-resolution XPS spectra showed a clear difference before and after catalytic testing. (Figure 2.19, Table 2.5) The Pd binding energy decreased, and the peak broadened after methane oxidation, showing both Pd and PdO peaks. In contrast, only PdO was observed by XPS of the fresh catalysts. This indicates that the reaction gas reduced the PdO to Pd.[3] Although Pd(0) was observed by XPS, crystalline Pd was not observed in the PXRD of the used catalyst. The Pd may be present in nanoparticles that are too small to show diffraction. Moreover, the Ce 3d peaks for the fresh sample show a pure CeO_2 pattern with about 6% Ce^{3+}.[123] For the used catalyst, the percentage of Ce^{3+} increased to about 10%, resulting in weakening of the Ce-O bond and increased oxygen mobility.[123]

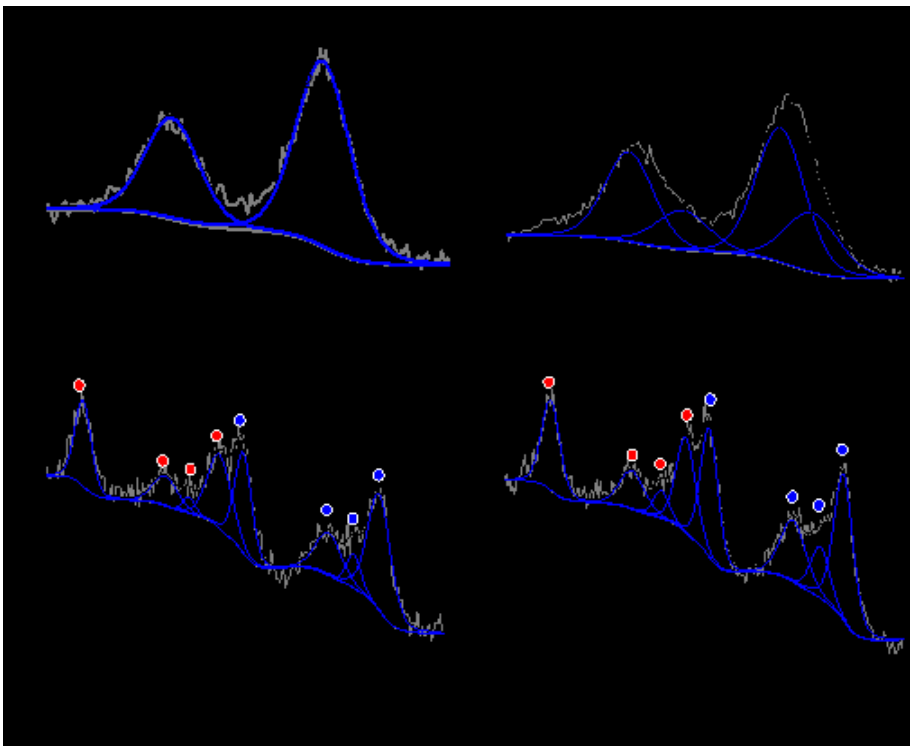

Figure 2.19 XPS spectra for PdCFPdSBA-15(M) 5% Pd before and after thermal stability test. (a) Pd 3d peaks, (b) Ce 3d peaks (● represent Ce $3d_{3/2}$, and ● represent Ce $3d_{5/2}$) for fresh catalysts. (c) Pd 3d peaks, (d) Ce 3d peaks for used catalysts.

Table 2.5 XPS data for catalysts of PdCFPdSBA-15(M) 5% Pd before and after thermal stability test.

Element	Catalysts	Binding energy (eV)	Oxidation state
Ce	Fresh	883.7, 889.5, 899.3, 902.1, 908.3, 917.8	+4
		886.6, 905.6	+3
	Used	883.3, 889.1, 899.0, 901.7, 908.0, 917.5	+4
		886.0, 904.5	+3
Pd	Fresh	337.4, 342.6	+2
	Used	337.3, 342.6	+2
		336.2, 340.7	0

The formation of Pd during the reaction increases the number of oxygen vacancies on the surface. Both the PdO and oxygen vacancies play important roles in the C-H dissociation on catalysts.[84] The increased catalytic activity may be attributed to the increased oxygen vacancies that promote the dissociation of the first C-H bond of methane.

2.4 Conclusions

Nanoparticles of $PdO/CeO_2/PdO$ supported on SBA-15 were prepared by impregnation and surface-assisted reduction. Using the SAR method within the pores of a mesoporous host (SBA-15) allowed us to constrain the size of the catalytic nanoparticles and to obtain an even distribution of catalyst inside the channels of silica. The catalyst system $PdO/CeO_2/PdO$ on SBA-15 shows high activity for low-temperature methane oxidation, and the high activity is attributed to the small size and good distribution of Pd on CeO_2 and also $PdO/CeO_2/PdO$ on SBA-15. In addition, the water stability of the catalysts was studied. After the injection of water, the activity clearly decreased. However, the activity increased gradually afterwards and was even better than for fresh catalysts after water was removed. The improved catalytic activity during the reaction is attributed to the formation of Pd(0), which increased oxygen vacancies. These results demonstrate a new way to make stable methane oxidation catalysts that may be useful for catalytic convertors in natural gas engines.

Chapter 3: Bowtie-shaped $NiCo_2O_4$ Catalysts

3.1 Introduction

Pd-based catalysts show excellent activity, but the high price and low abundance of palladium are limiting factors to practical application.[124] Moreover, the hydrothermal stability and SO_2 tolerance for PdO catalysts still need to be improved.

For this reason, the development of alternative catalysts based on non-noble metals is attractive.[125] For example, Co_3O_4 exhibits good activity for methane combustion attributed to a spinel-type structure with variable Co oxidation states and a high density of oxygen vacancies on the surface.[87] Additionally, the specific exposed facets and morphology of Co_3O_4 plays an important role in the catalysis.[89-90]

Compared with single metal oxides, bimetallic $NiCo_2O_4$ has been shown to have better catalytic activity due to structural disorder,[100] making this a particularly enticing candidate for catalysis, as well as for energy conversion and storage applications.[101] Nanostructured $NiCo_2O_4$ with a high surface area would be an excellent candidate for a methane combustion catalyst.

Here, we report the preparation of $NiCo_2O_4$ nanostructures with an unusual bowtie shape that show high catalytic activity for low-temperature methane combustion. The catalysts are synthesized by a hydrothermal method followed by calcination, and a surfactant is used in order to expose active $NiCo_2O_4$ facets to improve the catalytic performance. Having investigated the growth mechanism of the bowtie shaped particles, we find that the Co/Ni ratio, additives used, and the hydrothermal reaction time all influence the morphology of the nanostructures. These $NiCo_2O_4$ nanocrystals show excellent activity for complete methane combustion.

3.2 Experimental

3.2.1 Preparation of bowtie-shaped $NiCo_2O_4$

Cobalt(II) nitrate hexahydrate (0.291 g, 1.00 mmol) and nickel(II) nitrate hexahydrate (0.146 g, 0.500 mmol) were dissolved in 20 mL of deionized water. A solution of oleylamine (4 mL, 12 mmol) in 10 mL of ethanol was added to the solution with vigorous stirring. The mixture was stirred for 30 min to yield a green gel, which was transferred to a 45 mL Teflon-lined stainless steel autoclave. The sealed reaction vessel was heated to 180 °C for 12 h. After cooling the mixture to room temperature, the yellow mother liquor was removed and the light pink precipitate was transferred to a centrifuge tube. The precipitate was washed by centrifugation three times with 40 mL ethanol. The product was dried at 80 °C for 5 h which yields ~ 0.10 g, and then calcined in a furnace at various temperatures (350, 400, or 450 °C) for 3 h under air. The yield was ~ 0.08 g after calcination.

3.2.2 Preparation of Ni/Co hydroxides with different metal ratios

Samples were prepared where the Ni:Co ratio was varied with mole ratios of 0:1 (no nickel), 1:2, 2:1, and 1:0 (no cobalt). In each preparation, the total amount of metal nitrate added was kept at 1.5 mmol, and the appropriate mixture of nickel and cobalt nitrates was dissolved in 20 mL of water. A solution of 4 mL of oleylamine in 10 mL of ethanol was added to the aqueous solution with vigorous stirring for 30 min. The mixture was sealed in a 45 mL sealed high pressure reaction vessel and heated to 180 °C for 12 h. After cooling the mixture, the precipitate was collected and washed with ethanol for 3 times by centrifugation. The product was dried at 80 °C for 5 h and yields ~ 0.10 g. Finally, the sample was calcined at 450 °C for 3 h.

3.2.3 Preparation of $NiCo_2(OH)_6$ with various amines

In a small flask, 12 mmol of one of ammonium hydroxide, hexylamine, decylamine, dodecylamine or hexadecylamine were mixed with 10 mL of ethanol. (It was necessary to heat the dodecylamine and hexadecylamine ethanol mixtures to 60 °C in order to dissolve the amine). The amine/ethanol solution was added to a mixture of cobalt(II) nitrate hexahydrate (0.291 g, 1.00 mmol) and nickel(II) nitrate hexahydrate (0.146 g, 0.500 mmol) dissolved in 20 mL of deionized water. After each mixture was stirred for 30 min, it was transferred to a 45 mL sealed high pressure reaction vessel and heated to 180 °C for 12 h. After the reaction mixture cooled, the precipitate was collected and washed with ethanol for 3 times by centrifugation. The product was dried at 80 °C for 5 h and yields ~ 0.09 g. Finally, the sample was calcined at 450 °C for 3 h.

3.2.4 Preparation of Ni/Co hydroxide under N_2

Mixtures of Ni/Co nitrate with different metal ratios (Ni:Co = 0:1, 1:2, 1:0) were dissolved in 20 mL of deionized water under a flow of N_2 in a 100 mL three necked flask. A solution of 4 mL of oleylamine in 10 mL of ethanol was injected into the solution with a 20 mL syringe. After the mixture was stirred for 30 min, the precipitate was quickly transferred into a sealed high pressure reaction vessel and the mixture was heated at 180 °C for 12 h. The product was then collected and washed with ethanol three times by centrifugation. The product was dried at 80 °C for 5 h and yields about 0.10 g.

3.2.5 Instrumentation

PXRD analysis was carried out on a Bruker D8 Advance X-ray diffractometer with Cu Kα radiation at 40 mA and 40 kV. Samples were scanned from 5° to 90° 2θ with 0.03° step size and a

rate of 1 step per second. TEM images were collected with a Hitachi H7600 electron microscope with an accelerating voltage of 80 kV. SEM images were obtained with a Hitachi S-4700 field emission SEM operating at 5 kV accelerating voltage. EDX spectra of the samples were conducted on a Hitachi S2600 Variable Pressure SEM with an X-ray detector. HRTEM images and EDX mapping data were collected on a FEI Tecnai Osiris S/TEM at an operating voltage of 200 kV. The tomography study was performed on a FEI Tecnai Osiris S/TEM with tilt angles ranging from -60° to +60°. The data were collected with tilt steps of 1° from -60° to -50° and 50° to 60°, and steps of 2° from -50° to 50°. Images were first aligned by FEI Xpress3D and then modeled with Amira software. XPS data were measured in an ion-pumped chamber (1×10^{-9} Torr) of the Leybold Max200 spectrometer (Al Kα, hν = 1486.6 eV). Thermal stability was examined using Netzsch TG 209F1 Libra under N_2 with temperatures varied from 100 to 800 °C at a heating rate of 10 °C/min. The CO uptake of $NiCo_2O_4$ catalysts was obtained on a Micromeritics AutoChem 2920 analyzer. The sample was purged with helium at 373 K for 2 h to remove moisture, and then cooled to 323 K. The CO uptake was determined by passing pulses of CO over the sample at 323 K and measuring the CO adsorbed using a thermal conductivity detector (TCD). A CO : active site adsorption stoichiometry of 1:1 was assumed. Therefore CO uptake was used to characterize the number of active sites.

3.2.6 Methane combustion catalysis

Temperature-programmed CH_4 oxidation (TPO) was used to analyze the catalytic performance of the new materials. The flow mixture contained 1000 ppmv CH_4, 10% (V/V) O_2, balanced by Ar and He to get a total flow rate of 150 mL (STP) min^{-1} (gas hourly space velocity 90,000 mL (STP)$\cdot g^{-1} \cdot h^{-1}$). The catalyst sample (0.1000 g) was diluted with 2.5000 g SiC and then

transferred into a stainless steel fixed-bed microreactor. The reactor was heated from room temperature to 500 °C at a rate of 5 °C min^{-1}. A VG ProLab quadrupole mass spectrometer (QMS; ThermoFisher Scientific) was used to analyze the composition of emitted gas and conversion was calculated by the yield of CO_2 and total carbon balance. Water stability of the catalysts was measured over approximately a 12 h period at a constant temperature with 5% H_2O added to the dry feed gas prior to the preheater using a liquid syringe pump (Harvard Apparatus Model 44).

3.3 Results and Discussion

3.3.1 Synthesis of bowtie-shaped $NiCo_2O_4$

The substantial interest in using Ni/Co oxide nanostructures for catalysis, including low-temperature methane oxidation, motivated us to investigate high surface area materials with controlled morphology. We hypothesized that using a surfactant in the synthesis of $NiCo_2O_4$ would enhance the exposure of active facets in the resulting metal oxide through templating and, consequently, enhance the catalytic activity of the resulting materials. In our work, $NiCo_2O_4$ nanocrystals were prepared by calcining a Ni/Co hydroxide precursor, which was synthesized using a hydrothermal method. The surfactant oleylamine was used as a base to precipitate Ni^{2+} and Co^{2+} and to control the morphology of crystals. The green gel that formed after stirring the mixture of metal salts and oleylamine for 30 min was heated at 180 °C to crystallize the metal hydroxide precursor. Powder X-ray diffraction (PXRD) of the product (Figure 3.1) showed peaks between

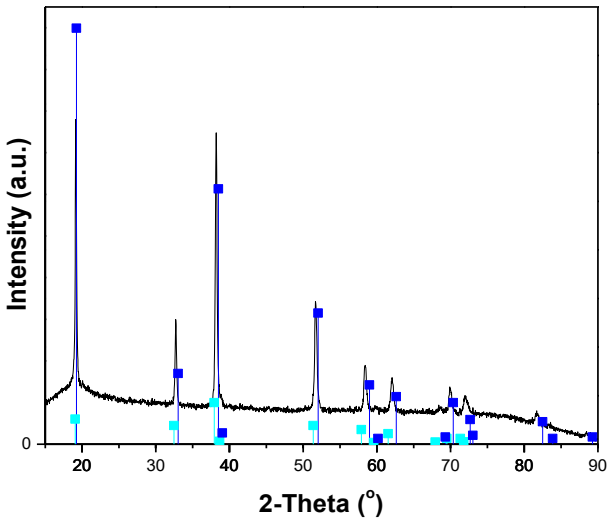

Figure 3.1 PXRD data for nickel cobalt hydroxide ($NiCo_2(OH)_6$), (■) standard cobalt hydroxide β – $Co(OH)_2$ (JCPDS 30-0443), (■) Theophrastite, syn β – $Ni(OH)_2$ (JCPDS 59-0462).

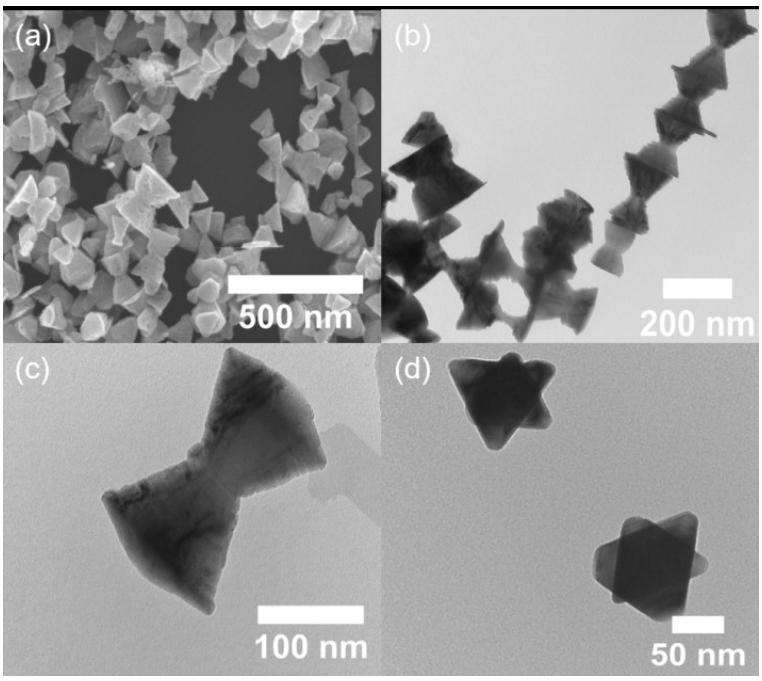

Figure 3.2 (a) Scanning electron microscopy (SEM) image of $NiCo_2(OH)_6$. (b) Transmission electron microscopy (TEM) image of $NiCo_2(OH)_6$. (c) Bowtie-shaped nanostructure viewed from the side. (d) Bowtie-shaped nanostructure viewed from the end, revealing the staggered arrangement of the pyramidal bases in the structure.

those of standard β-$Co(OH)_2$ and β-$Ni(OH)_2$, consistent with the formation of a mixed-metal hydroxide, $NiCo_2(OH)_6$. Energy dispersive X-ray (EDX) analysis of the product indicated that the Ni/Co ratio was 1:2.To our surprise, the synthesized crystals were shaped like bowties (Figure 3.2). Wide-view electron micrographs of the $NiCo_2(OH)_6$, revealing that virtually all of the nanostructures are bowtie-shaped when viewed from the side, although there are a small number of nanosheets and trapezoids (half of a bowtie) present. The morphology of the crystals was studied from different viewing angles, demonstrating that the bowtie-shaped nanocrystals consist of two trigonal pyramids with connected tips and staggered pyramidal bases (Figures 3.2c and 3.2d).

The hydroxide compounds were next calcined at elevated temperature under air to form porous $NiCo_2O_4$. The nickel cobalt hydroxide decomposed at about 250 °C (Figure 3.3a), and weight loss completed below 300 °C, so calcination temperatures of 350, 400, and 450 °C were selected. PXRD patterns (Figure 3.3b) of the materials after calcination at these temperatures all show diffraction peaks corresponding to nickel cobalt oxide (JCPDS 20-0781).

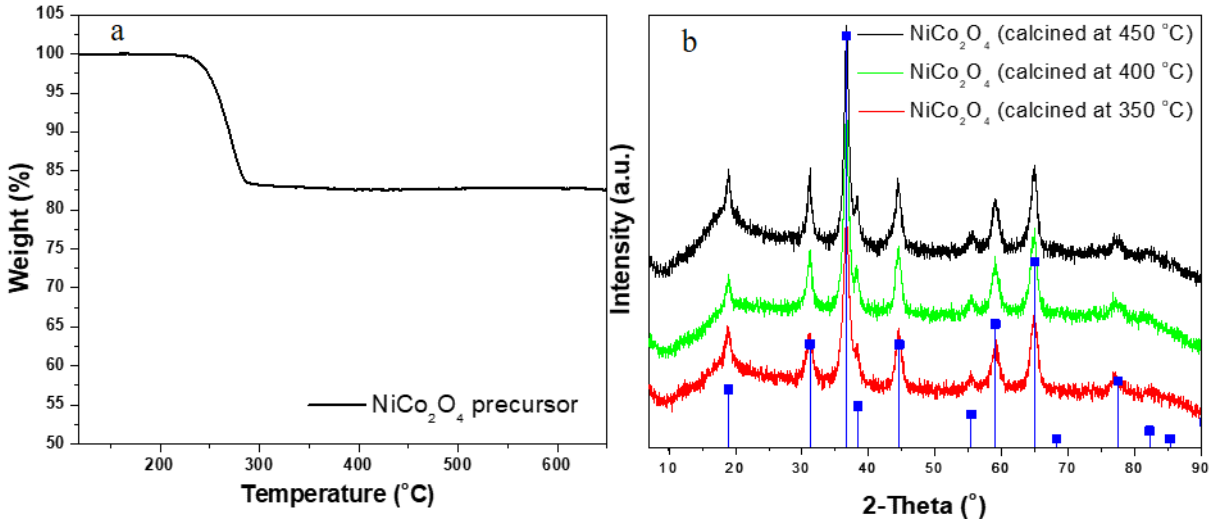

Figure 3.3 (a) TGA for $NiCo_2O_4$ precursor. (b) PXRD patterns for $NiCo_2O_4$ calcined at different temperatures. (■) Nickel cobalt oxide-$NiCo_2O_4$ (JCPDS 20-0781).

When the bowtie-shaped $NiCo_2O_4$ crystals were examined by high-resolution transmission electron microscopy (HRTEM, Figure 3.4), it is apparent that they are porous, and that the pore structure varies with calcination temperature. The {011} planes are the dominant exposed planes of the bowtie $NiCo_2O_4$ around the pores. These planes are normal to the set of $(11\bar{1})$ and $(\bar{1}1\bar{1})$ facets with a lattice spacing of 0.47 nm. EDX elemental mapping shows that cobalt and oxygen are distributed evenly throughout the structure, while nickel is concentrated more on the bottom

edge of the bowtie-shaped structures. In comparison, $NiCo_2O_4$ calcined at 450 °C has larger pores on the surface and the dominant exposed plane was {011} both inside and outside the pores (Figure 3.5). The surface area for $NiCo_2O_4$ calcined at 350 °C is 65 m^2/g (Table 3.1), which is higher than that for the same material calcined at 400 °C (33 m^2/g) and 450 °C (only 10 m^2/g). The pore size for $NiCo_2O_4$ calcined at 350 °C is ~5-10 nm. These results are consistent with the observations from the TEM images. The low surface area for the samples calcined at 400 or 450 °C suggests that in these cases the observed pores are not accessible for gas adsorption.

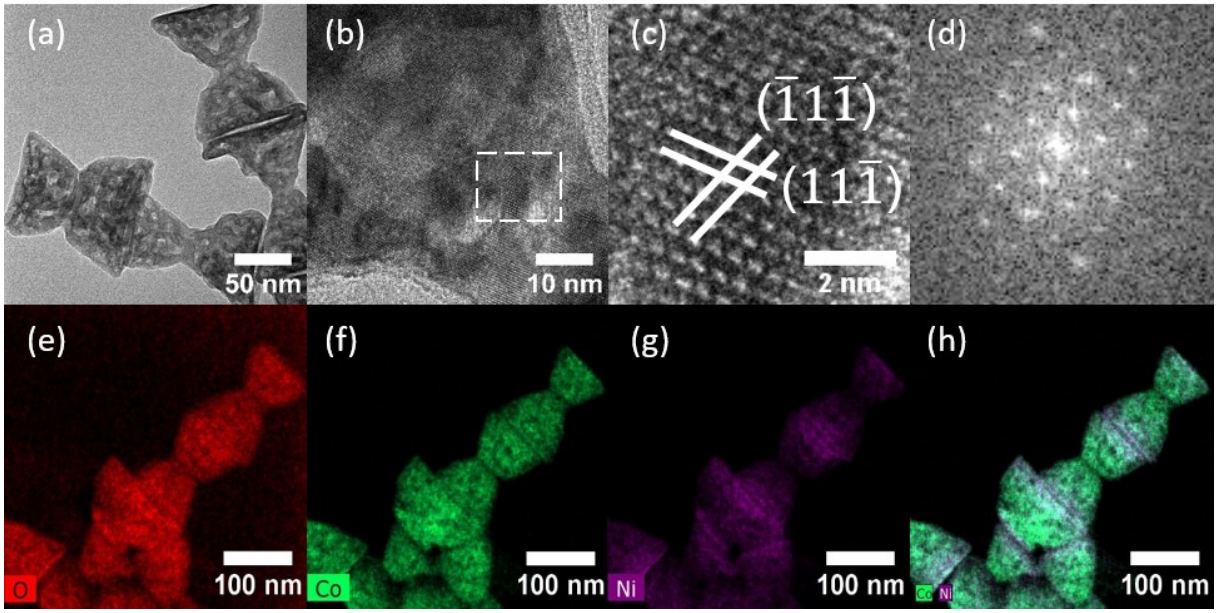

Figure 3.4 Analysis of bowtie-shaped $NiCo_2O_4$ nanocrystals calcined at 350 °C. (a) TEM image; (b) HRTEM image; (c) enlarged HRTEM image of the area marked in (b); FFT pattern of the area marked in (b); (e-h) EDX elemental mapping images showing the distribution of O, Co, Ni, and all three elements.

Table 3.1 Surface area, average particle size, and CO chemisorption results of $NiCo_2O_4$ catalysts calcined at different temperature

Catalysts	Surface Area [m^2/g]	Particle size [2] [nm]	CO uptake [$\mu mol/g_{cat}$]
$NiCo_2O_4$ calcined at 350 °C	65	7.0	48.4
$NiCo_2O_4$ calcined at 400 °C	33	8.4	30.1
$NiCo_2O_4$ calcined at 450 °C	10	9.1	18.8

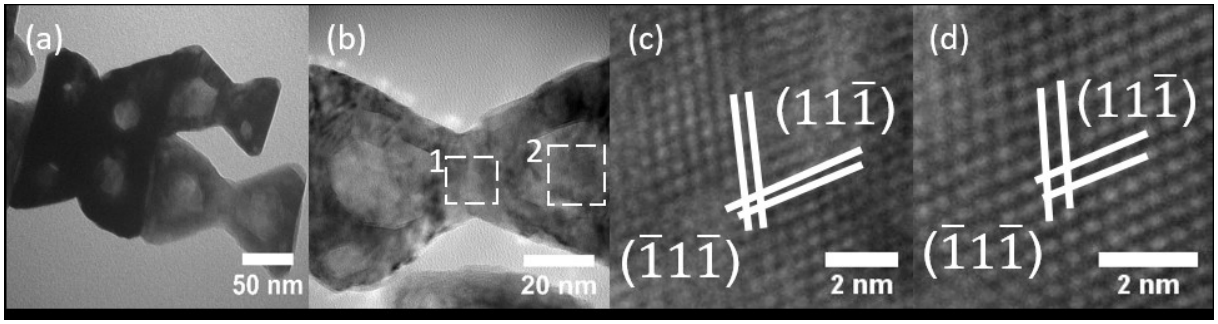

Figure 3.5 (a) TEM, (b) HRTEM, (c) enlarged HRTEM image of the area 1 marked in (b), (d) enlarged HRTEM image of the area 2 marked in (b) for bowtie-shaped $NiCo_2O_4$ nanocrystals calcined at 450 °C

3.3.2 Growth mechanism

To better understand the origin of the distinctive bowtie morphology observed in the $NiCo_2O_4$ nanocrystals, we systematically varied the synthesis conditions and parameters to see how the changes influenced the structures that emerged. First, the hydrothermal annealing time was varied between 0 and 12 h. In each case, the metal nitrate salts were combined with oleylamine and stirred for 30 min to give a green gel. Hydrothermal treatment of this gel was conducted for 0-12 h, then the precipitate was collected by centrifugation, washed with ethanol, and dried at

[2] Average particle size was calculated by applying the Scherrer equation to the (220) facet of $NiCo_2O_4$ in Figure 3.3.

80 °C in an oven. The structure of the resulting nickel cobalt hydroxide prepared with different hydrothermal reaction times was examined by TEM, HRTEM, EDX, SEM and PXRD methods.

Before hydrothermal treatment, the precipitate contains mainly irregular particles with the size of 7.1 ± 0.9 nm (Figure 3.6). The PXRD pattern of the precipitate (Figure 3.7) indicates the formation of crystalline $NiCo_2(OH)_6$. After hydrothermal treatment for 30 min, overlapping hexagonal nanoplates were formed as shown in Figure 3.8. HRTEM analysis shows that these hexagonal nanosheets are terminated with $\{10\bar{1}0\}$ planes and stacked along the <0001> axis. It is interesting to note that the distribution of Co and Ni in the particles is not uniform across the nanoplates. EDX elemental mapping shows that the cobalt is evenly distributed on the nanoplates whereas nickel is mostly found on the edge of the plates; nearly no nickel is found in the center of the hexagonal plates.

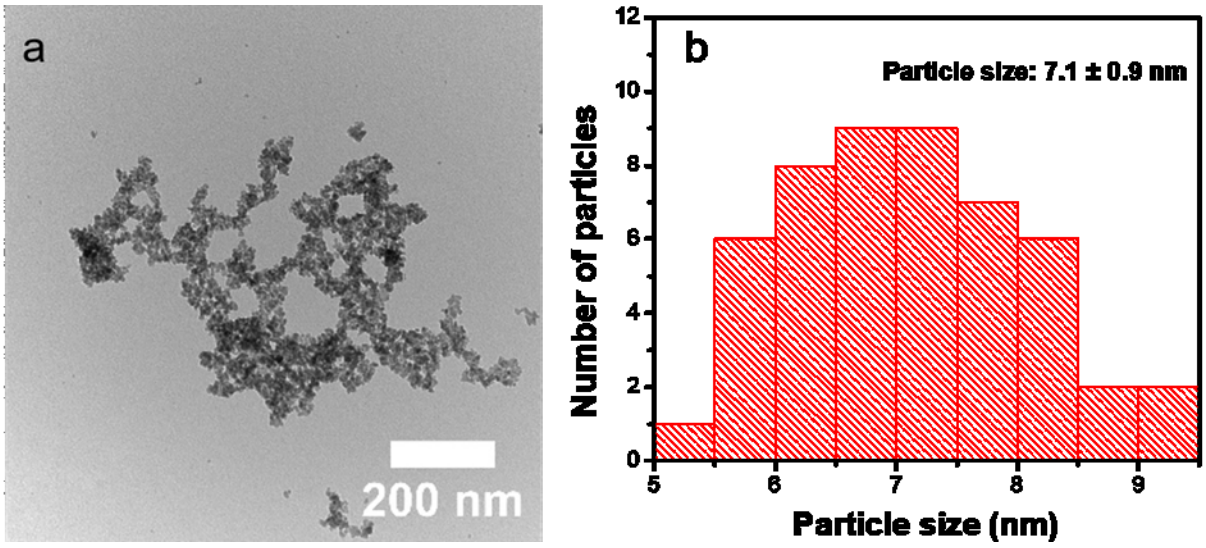

Figure 3.6 a. TEM image and b. particle size distribution for nickel cobalt hydroxide compounds before hydrothermal treatment.

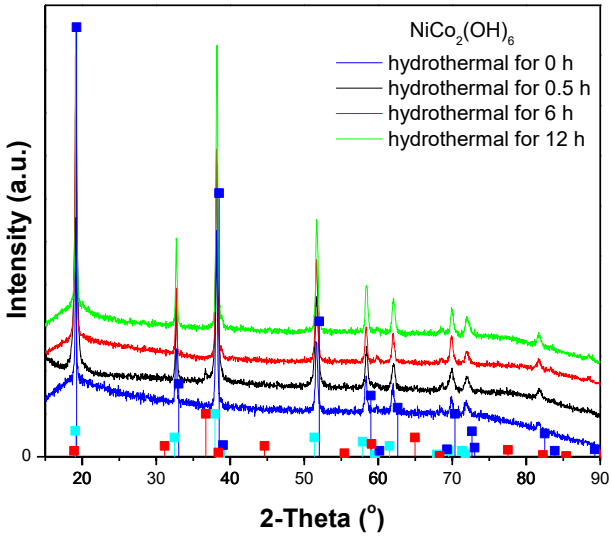

Figure 3.7 PXRD patterns for $NiCo_2(OH)_6$ with different hydrothermal reaction times. (■) standard cobalt hydroxide β – $Co(OH)_2$ (JCPDS 30-0443), (■) Theophrastite, syn β – $Ni(OH)_2$ (JCPDS 59-0462), (■) Nickel cobalt oxide-$NiCo_2O_4$ (JCPDS 20-0781).

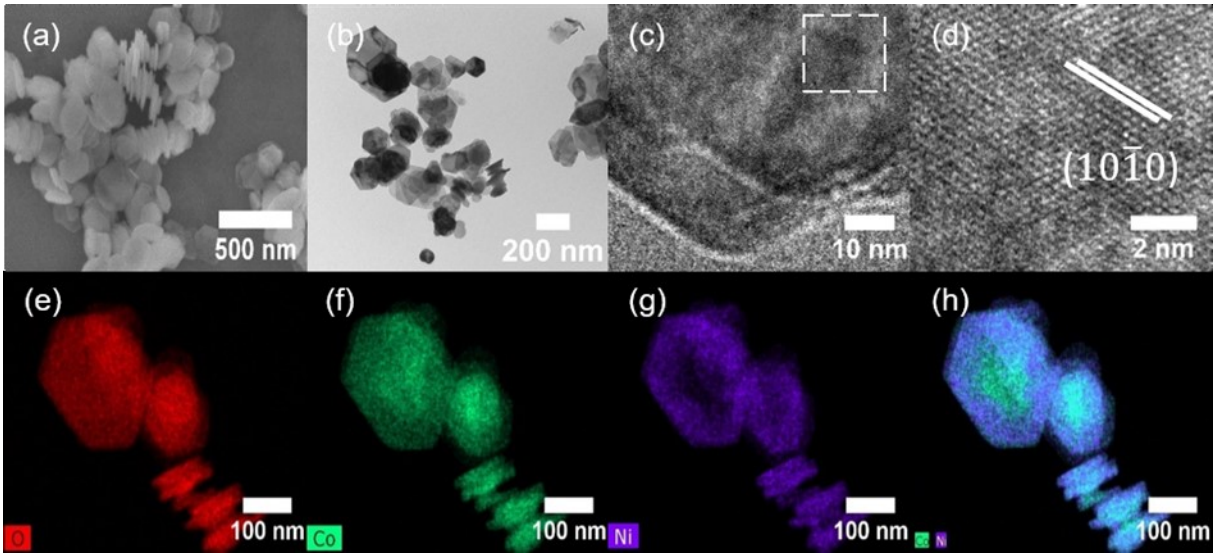

Figure 3.8 Analysis of $NiCo_2(OH)_6$ product obtained after 30 min hydrothermal treatment. (a) SEM image; (b) TEM image; (c) HRTEM image; (d) enlarged HRTEM image of the area marked in (c); (e-g) EDX mapping images of O, Co, and Ni; (h) EDX mapping image showing an overlay of the Ni and Co distributions.

When the reaction time extended beyond 90 min, the narrow plates in the middle of two stacked nanoplates developed along the <0001> direction (Figure 3.9). There are dislocations around the center of the hexagonal plate, possibly due to the uneven distribution of Co and Ni. Crystals grow on these surface dislocations with a higher growth rate. At the same time, the hexagonal plate gradually transforms to a trigonal shape. EDX elemental mapping indicates that the distribution of Ni and Co is uniform between the two hexagonal plates (Figure 3.9 (f, g)).

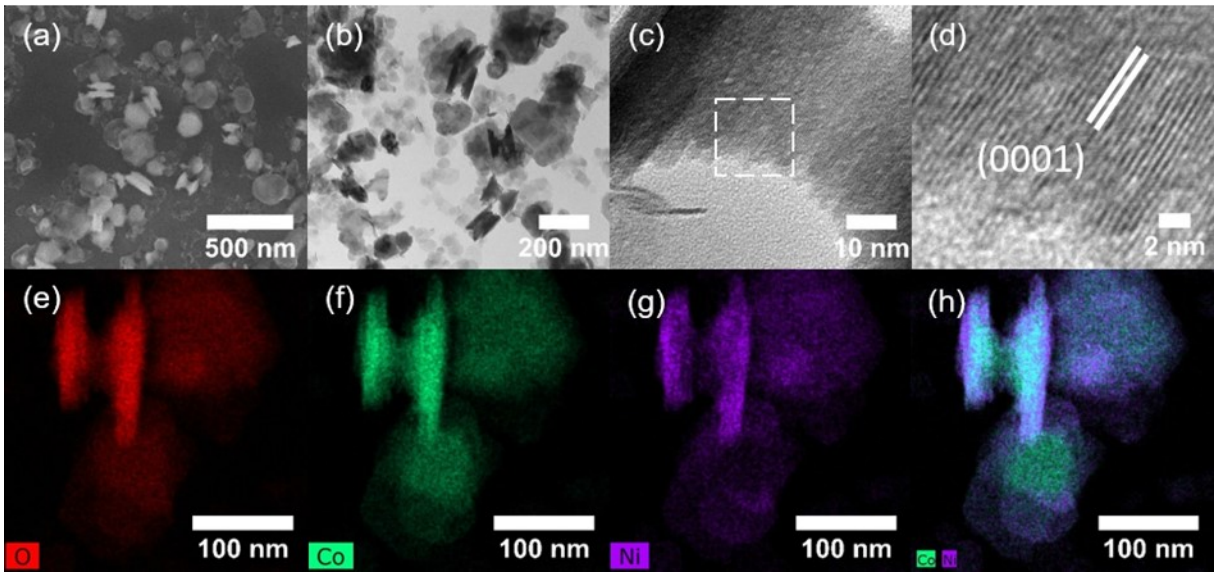

Figure 3.9 Analysis of $NiCo_2(OH)_6$ product obtained after 90 min hydrothermal treatment. (a) SEM image; (b) TEM image; (c) HRTEM image; (d) enlarged HRTEM image of the area marked in (c); (e-g) EDX mapping images of O, Co, and Ni; (h) EDX mapping image showing an overlay of the Ni and Co distributions.

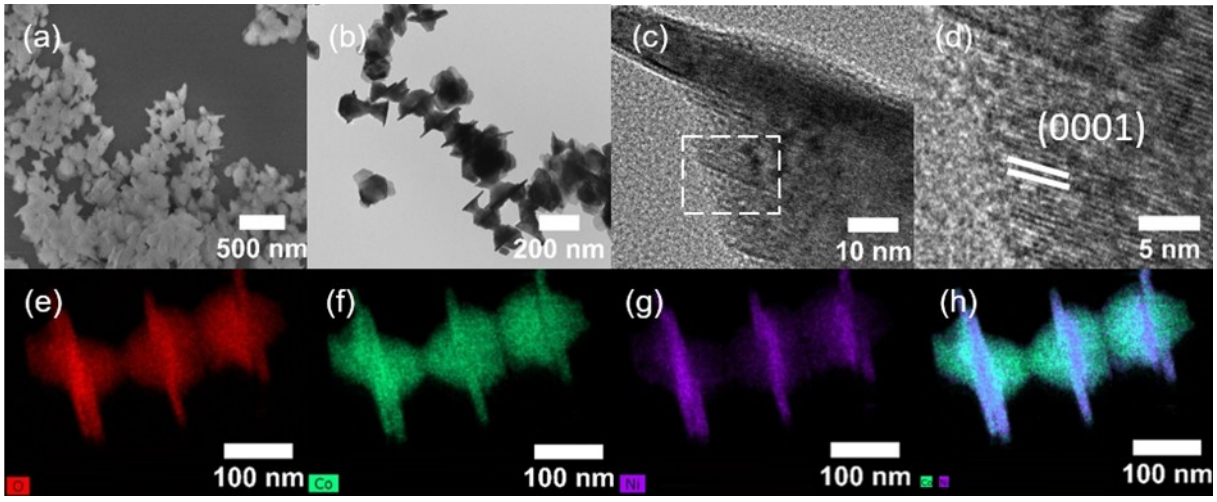

Figure 3.10 Analysis of $NiCo_2(OH)_6$ product obtained after 3 h hydrothermal treatment. (a) SEM image; (b) TEM image; (c) HRTEM image; (d) enlarged HRTEM image of the area marked in (c); (e-g) EDX mapping images of O, Co, and Ni; (h) EDX mapping image showing an overlay of the Ni and Co distributions.

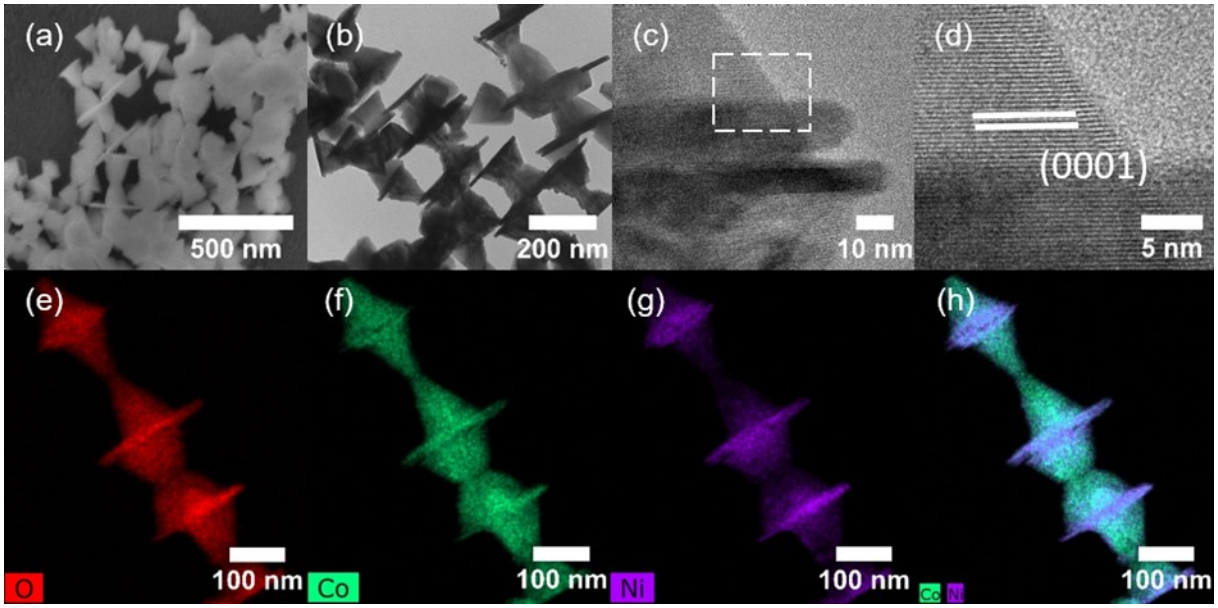

Figure 3.11 Analysis of $NiCo_2(OH)_6$ obtained after 6 h hydrothermal treatment. (a) SEM image; (b) TEM image; (c) HRTEM image; (d) enlarged HRTEM image of the area marked in (c); (e-g) EDX mapping images of O, Co, and Ni; (h) EDX mapping image showing an overlay of the Ni and Co distributions.

Furthermore, when the hydrothermal reaction time was extended to 3 h or 6 h, the middle plates continued growing along the <0001> directions and the formation of bowtie-shaped crystals is observed (Figure 3.10, Figure 3.11). The parent nanosheets are still recognizable in the bowtie structure. Finally, after 12 h hydrothermal treatment, the parent nanosheets are essentially absent and fused into the bowtie structure. EDX mapping (Figure 3.12) shows that cobalt is evenly distributed over the nanostructure, but nickel is more concentrated at the base of the bowtie, where the parent nanosheets form the structure.

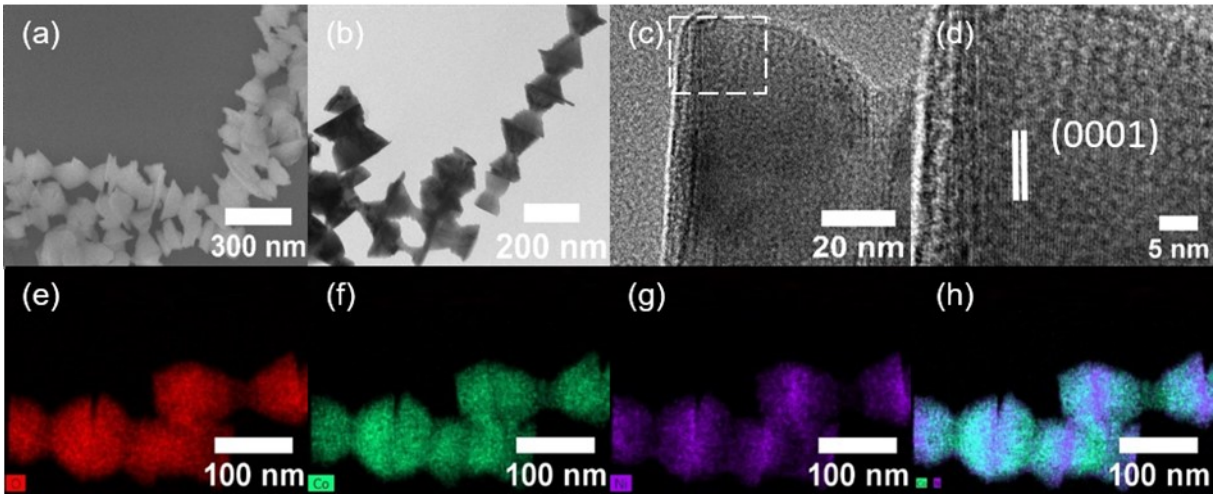

Figure 3.12 Analysis of $NiCo_2(OH)_6$ obtained after 12 h hydrothermal treatment. (a) SEM image; (b) TEM image; (c) HRTEM image; (d) enlarged HRTEM image of the area marked in (c); (e-g) EDX mapping images of O, Co, and Ni; (h) EDX mapping image showing an overlay of the Ni and Co distributions.

PXRD patterns of the samples after 0.5, 6, and 12 h hydrothermal reaction time are shown in Figure 3.7. After 0.5 h, crystalline nickel cobalt hydroxide was formed, but a small amount of crystalline nickel cobalt oxide crystals was also present. After 6 or 12 h, only nickel cobalt

hydroxide was observed, indicating that the nickel cobalt oxide precursor transformed into the hydroxide compound during the hydrothermal process.

A cartoon illustration of the growth of the bowtie shaped nanocrystals is shown in Scheme 3.1. Initially, nickel and cobalt hydroxides with an irregular structure are formed at room temperature. During hydrothermal treatment, hexagonal thin plates are formed at an early stage. A middle plate formed between two hexagonal plates and continued growing along the <0001> direction. Simultaneously, the hexagonal sheets transformed into trigonal plates. After 12 h, the bowtie-shaped nanocrystals are formed.

To better understand the role of the components in the formation of the bowtie-shaped nanocrystals, we investigated the variation of several parameters, including the metal ratio, capping agents, and presence of oxygen.

Scheme 3.1 Proposed growth model for bowtie-shaped nanocrystals.

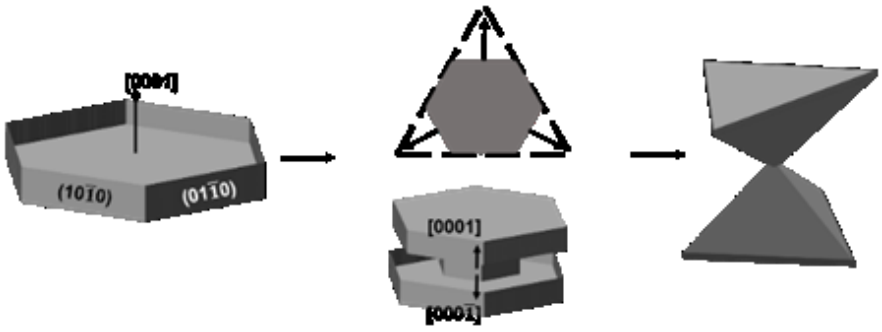

3.3.3 Effect of the nickel to cobalt ratio on morphology

We investigated the influence of the Ni/Co ratio on the morphology of the products. The hydrothermal reaction (180 °C, 12 h) was conducted with Ni:Co ratios varying from 1:0 (only nickel) to 0:1 (only cobalt). After each hydrothermal reaction, the hydroxide compounds were

collected by centrifugation, dried, and then analyzed. As anticipated, PXRD patterns of the samples prepared with either only cobalt or only nickel matched the standard patterns for β-$Co(OH)_2$ and β-$Ni(OH)_2$, respectively. For samples prepared with intermediate proportions of Ni:Co (e.g., $NiCo_2(OH)_6$ $NiCo(OH)_4$ and $Ni_2Co(OH)_6$), the diffraction peaks are located between those for standard β-$Co(OH)_2$ and β-$Ni(OH)_2$, (Figure 3.13). As the percentage of nickel is increased, the (100) and {011} peaks shift gradually to higher angle (Figure 3.13 inset). Plots of d spacing for the (100) and {011} reflections versus mole fraction of Ni in the samples obeyed Vegard's law (Figure 3.14), indicating formation of a solid solution. EDX data also confirmed that the Ni/Co ratios were 2, 1 and 0.5 for $Ni_2Co(OH)_6$, $NiCo(OH)_4$ and $NiCo_2(OH)_6$, respectively, which correspond to the theoretical values.

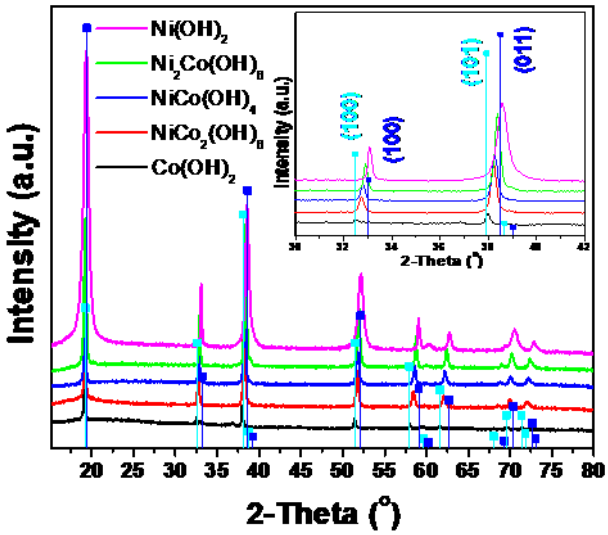

Figure 3.13 PXRD patterns for nickel and cobalt hydroxide with different Ni/Co ratios. (■) standard cobalt hydroxide – $Co(OH)_2$ (JCPDS 30-0443), (■) Theophrastite, syn – $Ni(OH)_2$ (JCPDS 59-0462).

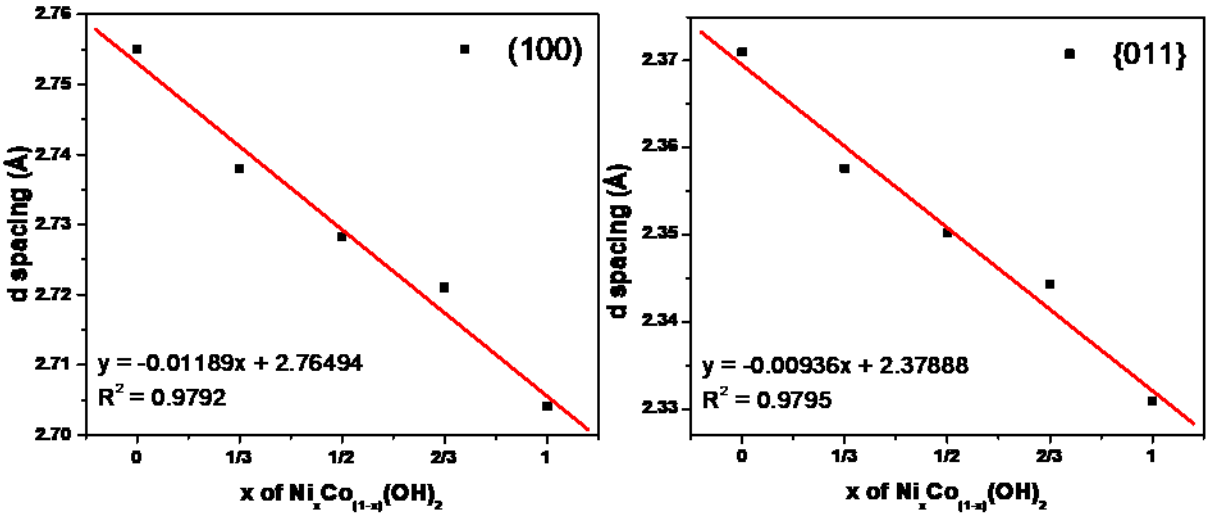

Figure 3.14 Linear fit of d-spacing for $Ni_xCo_{(1-x)}(OH)_2$ to the mole fraction of nickel in $Ni_xCo_{(1-x)}(OH)_2$. The left plot shows the fit of the (100) peak and the right plot shows the plot for the {011} peak.

Electron micrographs of the products obtained with different Ni:Co ratios are shown in Figure 3.15. Pure $Ni(OH)_2$ forms hexagonal plates, with each of the sides ranging from about 100 nm to 500 nm in length, and with thicknesses below 10 nm. We propose that during the hydrothermal process, surfactant largely covers the {0001} facets and limits growth in the <0001> direction, and instead the crystals grow along the $<10\bar{1}0>$ direction to form hexagonal sheets. As the cobalt content is increased, the growth rate in the <0001> direction increases. Thus, $Ni_2Co(OH)_6$ forms thicker hexagonal plates that are ~100 nm in length along the edges and ~20 nm thick. $NiCo(OH)_4$ forms trapezoids with ~40 nm thickness. With higher cobalt content, the hexagonal structure transforms into a trigonal structure. The distribution of Ni and Co is relatively even in the $NiCo(OH)_4$ and $Ni_2Co(OH)_6$ crystals (Figure 3.16, 3.17). In terms of morphology, the majority of the $NiCo_2(OH)_6$ nanocrystals are bowtie shaped, but for pure $Co(OH)_2$, only irregular thin plates and irregular nanocrystals are formed.

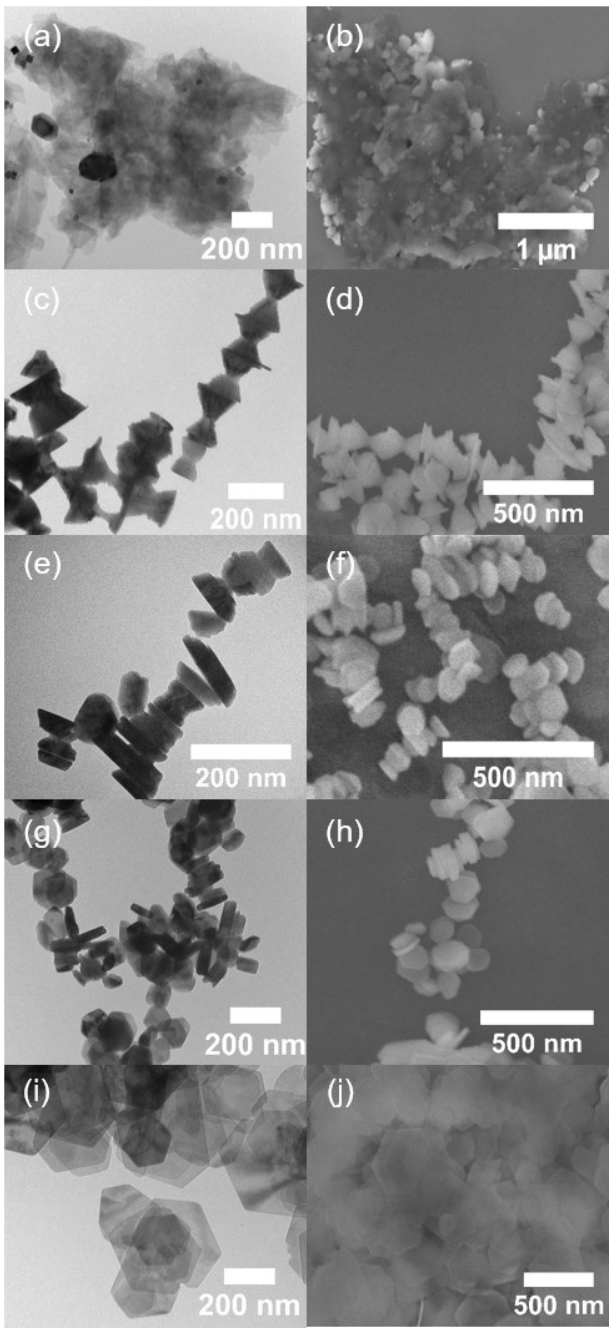

Figure 3.15 TEM (a, c, e, g, i) and SEM (b, d, f, h, j) images for Ni, Co hydroxide compounds with different Ni/Co ratios. Ni:Co ratios are 0:1 in (a), (b); 1:2 in (c), (d); 1:1 in (e), (f); 2:1 in (g), (h) and 1:0 in (i), (j).

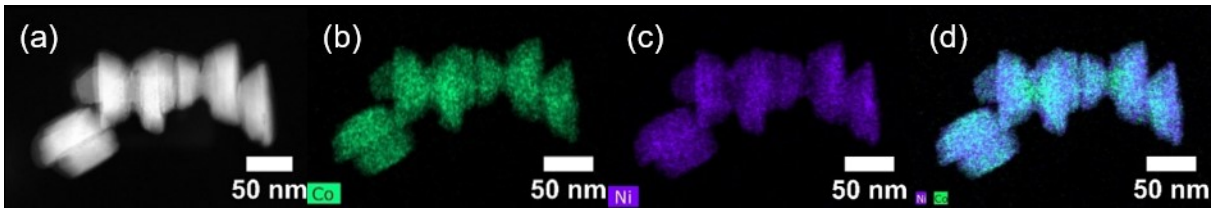

Figure 3.16 HAADF image for $NiCo(OH)_4$ (a), EDX mapping images of Co (b), and Ni (c), overlay of the Ni and Co distributions (d).

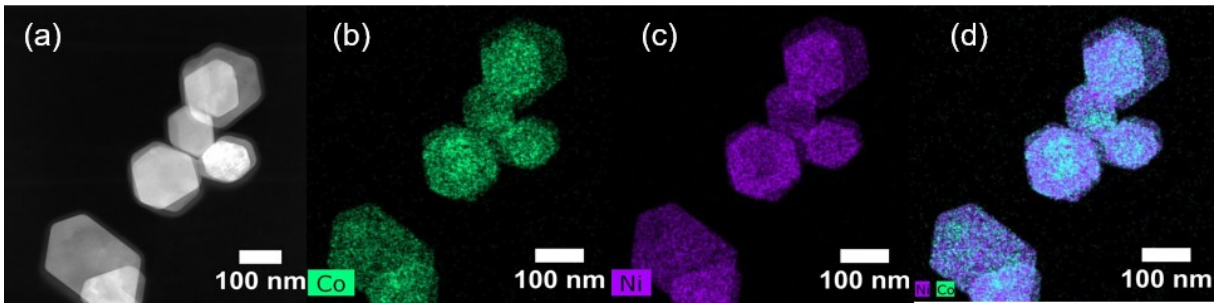

Figure 3.17 HAADF image for $Ni_2Co(OH)_6$ (a), EDX mapping images of Co (b), and Ni (c), overlay of the Ni and Co distributions (d).

3.3.4 Effect of different capping agents on morphology

We wondered whether the oleylamine was a critical component of the growth of the bowtie-shaped nanostructures. To investigate the role of oleylamine, Ni/Co hydroxide was prepared using different amines, and the morphologies are shown in Figure 3.18. We found that the shapes of the nanocrystals are strongly influenced by the amine that is used. Hexagonal nanosheets and cubic nanocrystals were formed when ammonium hydroxide or hexadecylamine were used as capping agents. Trigonal pyramidal nanosheets and bowtie-shaped nanocrystals formed with decylamine and dodecylamine as structure-directing agents. With hexylamine as a capping agent, trigonal pyramidal and sharp nanorods were formed. It is interesting that oleylamine,

with a bent molecular chain that inhibits close packing, yields the most predictable and reproducible morphology. This is in contrast to a previous report[126] that showed oleylamine disrupted the formation of well-defined bowtie-shaped structures because it fails to pack well. In our system, close-packing of the alkyl amine does not appear to play an important role in the formation of the bowtie shaped nanocrystals.

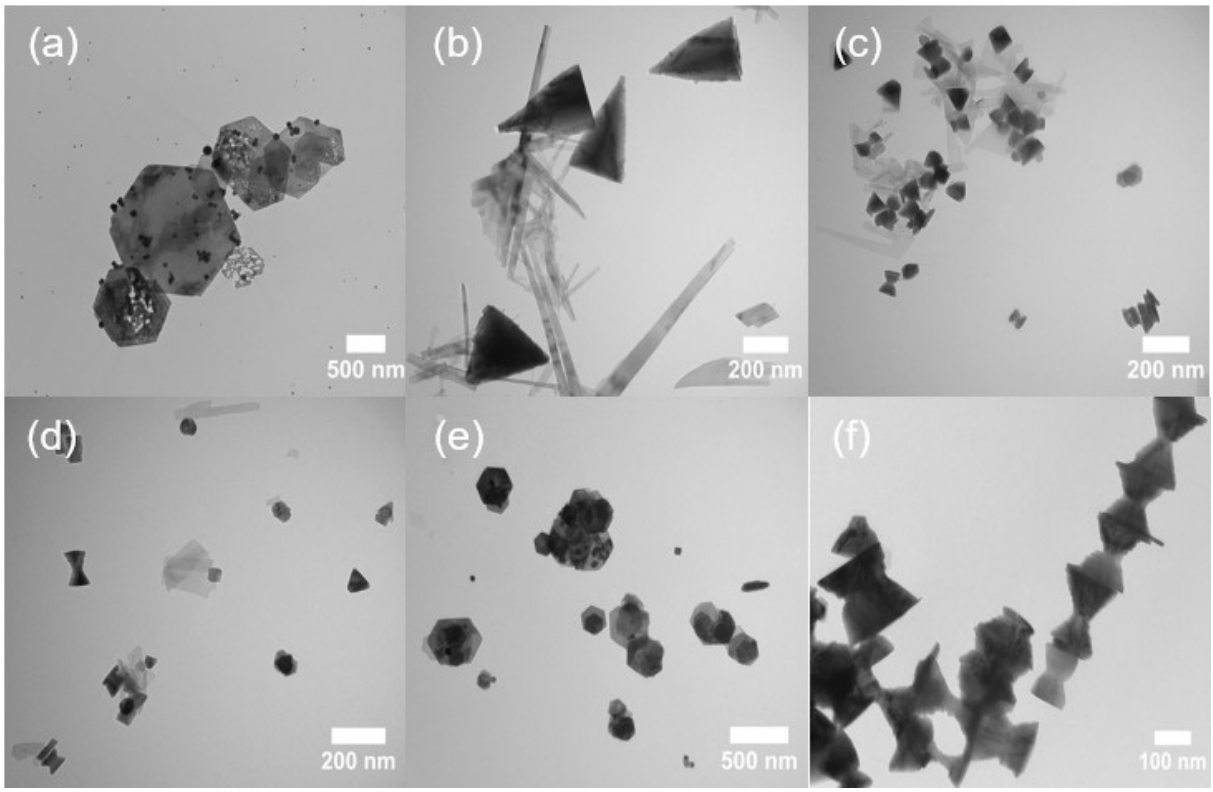

Figure 3.18 TEM images of $NiCo_2(OH)_6$ prepared with different amine. (a) ammonium hydroxide, (b) hexylamine, (c) decylamine, (d) dodecylamine, (e) hexadecylamine and (f) oleylamine.

3.3.5 Effect of air on morphology

We hypothesized that oxygen present during the synthesis might have a role in the selective crystallization of the bowtie-shaped nanocrystals. To test this hypothesis, we carried out a control

experiment under N_2; the structure of the product is shown in Figure 3.19. Interestingly, hexagonal nanoplates of $NiCo_2(OH)_6$ were formed under N_2 whereas carrying out the preparation with the same conditions but under an air atmosphere reproducibly gives exclusively bowtie-shaped nanocrystals. This suggests that redox chemistry is involved in the bowtie formation process, but it is not clear whether redox changes in the cobalt or nickel are involved. When $Ni(OH)_2$ was prepared, hexagonal plates were produced under both air and N_2. Interestingly, the preparation of $Co(OH)_2$ yielded hexagonal plates under N_2 but irregular nanosheets and nanocrystals were formed under air. We therefore postulate that the oxidation of some Co^{2+} to Co^{3+} occurs under air, and this plays a role in the structural organization of the material. PXRD data (Figure 3.13) supports this argument, showing peaks attributed to Co_3O_4 impurities in $Co(OH)_2$ synthesized under air. Furthermore, in the synthesis of bimetallic $NiCo_2(OH)_6$ under air, the redox reaction happens during the hydrothermal process. The PXRD pattern in Figure 3.7 indicates the formation of Co_3O_4 impurities after hydrothermal treatment for 0.5 hours. These impurities are no longer present after reaction for 6 hours. Therefore, synthesis under air may result in redox reactions occurring during the preparation that affect the rates of growth and etching of the nanocrystals, thus influencing the final structure of the product. This result is in agreement with a previous report,[127] which showed that a strong reducing environment preferentially generates Ni-Cu hexagonal nanoplates, whereas triangular nanoplates were produced in a weaker reducing environment. The final structures were affected by the competition of the reduction rate of Ni(II) and the etch rate of Ni(0).

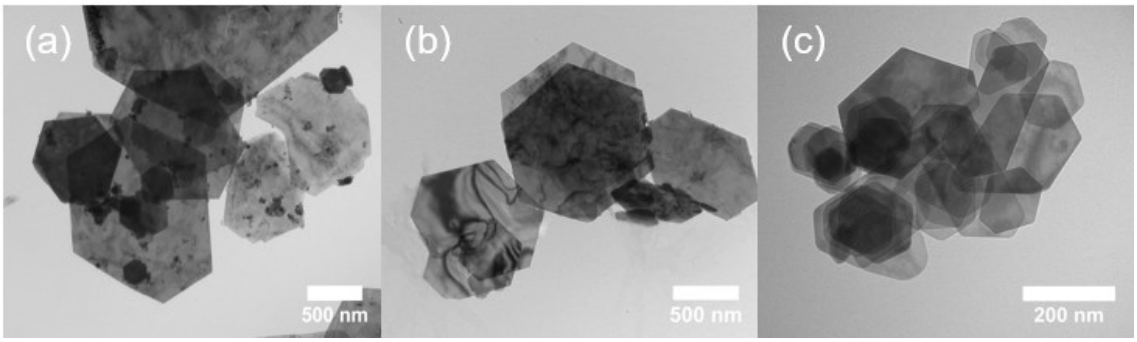

Figure 3.19 TEM images of (a) $Co(OH)_2$, (b) $NiCo_2(OH)_6$, (c) $Ni(OH)_2$ prepared under N_2.

3.3.6 Catalytic performance for methane combustion

To investigate the low-temperature methane oxidation activity of bowtie-shaped $NiCo_2O_4$ catalysts, the catalytic performance was studied by temperature-programmed oxidation (TPO) measurements under similar gas compositions to those found in the exhaust stream in NGVs (0.1% CH_4 and 10% O_2, with He/Ar used to balance the gas flow to give a total flow rate of 150 mL/min and space velocity of 90,000 mL/(g·h)). Bowtie-shaped $NiCo_2O_4$ calcined at 350 °C shows excellent activity, achieving 50% methane conversion at ~338 °C and 100% conversion at ~410 °C (Figure 3.20a). The $NiCo_2O_4$ calcined at higher temperatures (400 and 450 °C) showed a shift of the TPO curve to higher temperatures, with 100% conversion at ~430 and 450 °C, respectively.

CO chemisorption experiments were used to titrate the surface metal atoms of the catalysts in order to determine the number of active sites. These experiments reveal that as the calcination temperature is increased, the surface area of the catalyst decreased, resulting in fewer exposed active sites (Table 3.1) and, consequently, lower catalytic activity. Turnover frequency (TOF) was calculated based on the active sites (Equation 3.1, Table 3.2).

$$TOF = \frac{reactant\ flowrate\left(\frac{\mu mol}{s}\right) \times conversion}{quantity\ of\ sites\left(\frac{\mu mol}{g}\right) \times catalyst\ weight\ (g)} \qquad \text{Equation 3.1}$$

Interestingly, $NiCo_2O_4$ calcined at 450 °C has the highest TOF, which indicates that this material exhibits the best catalytic performance for methane oxidation per catalytic site. The dependence of TOF on $NiCo_2O_4$ particle size (Figure 3.21) shows that the larger particle size catalysts exhibit higher activity per catalytic site.

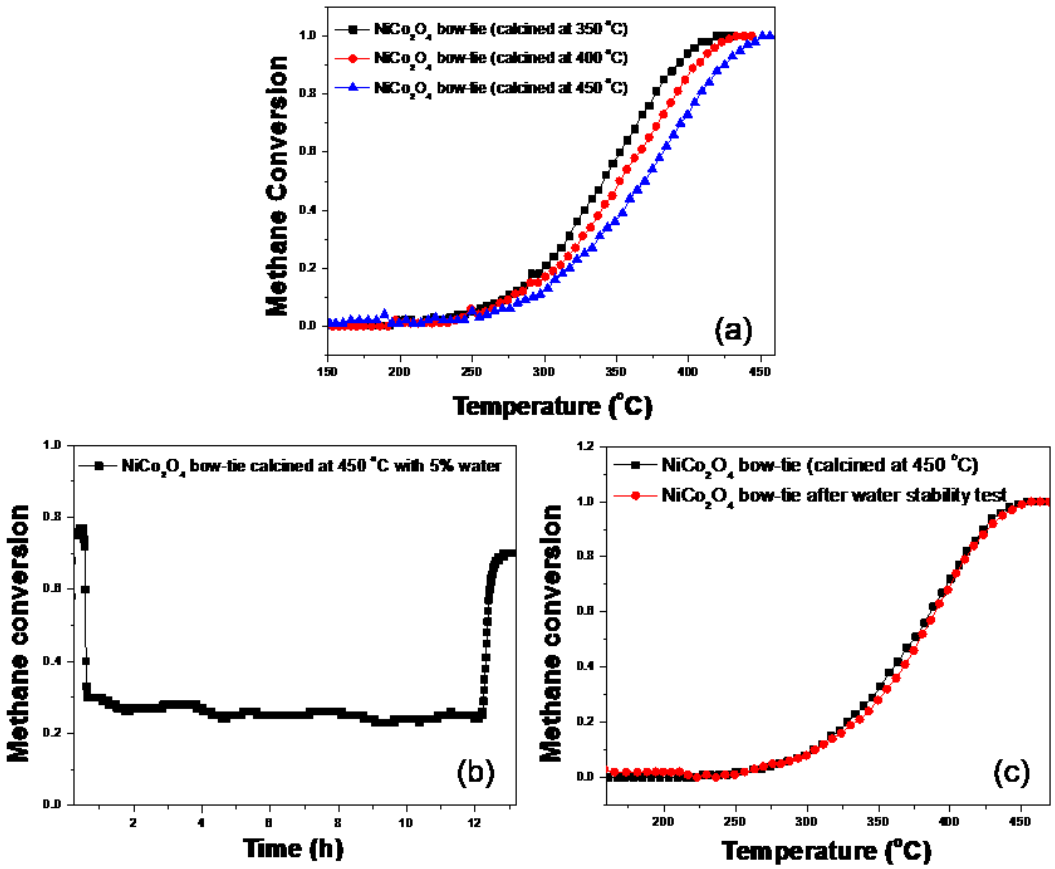

Figure 3.20 (a) TPO curves for bowtie-shaped $NiCo_2O_4$ prepared with different calcination temperature. (b) Water stability test for $NiCo_2O_4$ catalysts (calcined at 450 °C) under 5% water at 410 °C. (c) TPO curves for the fresh $NiCo_2O_4$ catalysts and after water stability test.

Table 3.2 TOF (at 270 °C) for $NiCo_2O_4$ catalysts.

Catalysts	TOF (s^{-1})
$NiCo_2O_4$ calcined at 350 °C	0.00207
$NiCo_2O_4$ calcined at 400 °C	0.00296
$NiCo_2O_4$ calcined at 450 °C	0.00355

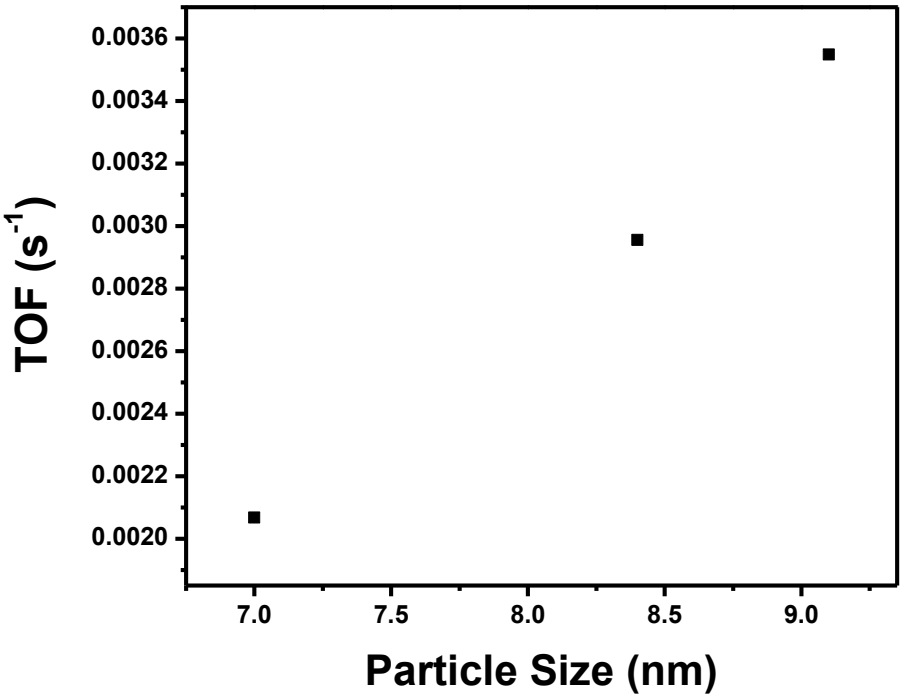

Figure 3.21 Dependence of TOF on $NiCo_2O_4$ particle size.

The XPS spectra of the catalysts (Figure 3.22, Table 3.3) indicate that the ratio of lattice oxygen to surface oxygen (O_{latt}/O_{ads}) increases with increasing calcination temperature. It has been reported that lattice oxygen plays an important role for methane oxidation,[128] which may explain why the catalyst calcined at 450 °C is more active per site. In summary, the $NiCo_2O_4$ catalyst calcined at 350 °C with higher surface area and more surface active sites shows the best catalytic performance, while the $NiCo_2O_4$ catalyst calcined at 450 °C has larger particle size and more surface lattice oxygen atoms, but is more active per site for methane oxidation.

Table 3.3 XPS data for $NiCo_2O_4$ catalysts calcined at different temperature.

Catalysts	O_{latt}/O_{ads}	Ni^{2+}/Ni^{3+}	Co^{2+}/Co^{3+}
$NiCo_2O_4$ calcined at 350 °C	0.59	2.1	0.49
$NiCo_2O_4$ calcined at 400 °C	0.71	2.0	0.48
$NiCo_2O_4$ calcined at 450 °C	1.37	2.2	0.45

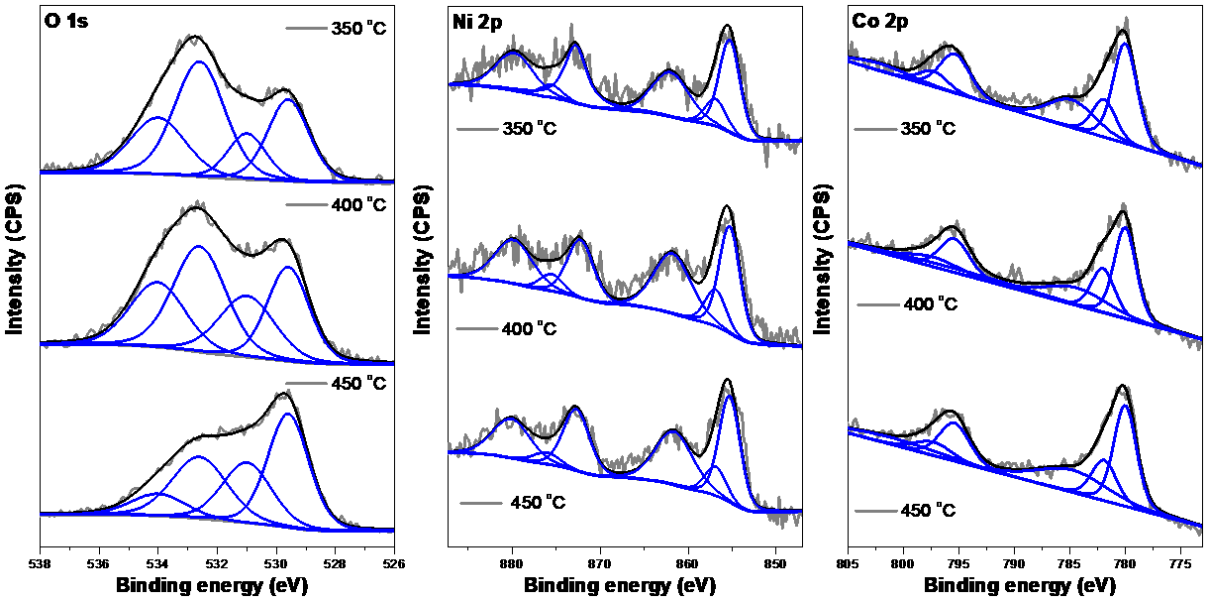

Figure 3.22 XPS spectra of O_{1s}, Ni_{2p}, Co_{2p} for the $NiCo_2O_4$ catalysts calcined at different temperature (350, 400, 450 °C).

After the conclusion of the catalysis test, the morphology of $NiCo_2O_4$ calcined at 350 °C was re-examined by TEM. The pores in $NiCo_2O_4$ were expanded relative to those observed before calcination (Figure 3.23), and are similar in size to those observed in $NiCo_2O_4$ calcined at 450 °C.

The performance of catalysts with different Ni/Co ratio and different amine treatment were also studied. The Ni/Co ratio influences the catalytic activity, with the order of activity being $NiCo_2O_4 > NiCoO_x > Ni_2CoO_x \approx NiO_2 > Co_3O_4$ (Figure 3.24). For $NiCo_2O_4$ prepared with different amines (Figure 3.25), the bowtie-shaped and trigonal pyramidal catalysts showed similar catalytic performance, superior to the catalysts with hexagonal sheet morphology. This result is consistent with a previous report that showed the exposure of (110) plane (bowtie and trigonal pyramidal

catalysts) is more active, because the low barrier on (110) crystal is responsible for high reactivity of $NiCo_2O_4$ catalysts.[87]

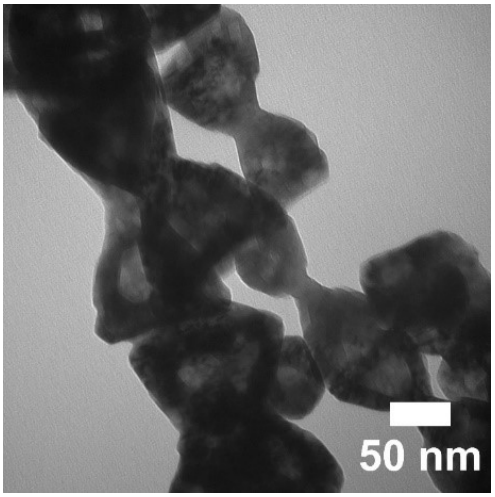

Figure 3.23 TEM image of the $NiCo_2O_4$ nanocatalysts after catalysis testing.

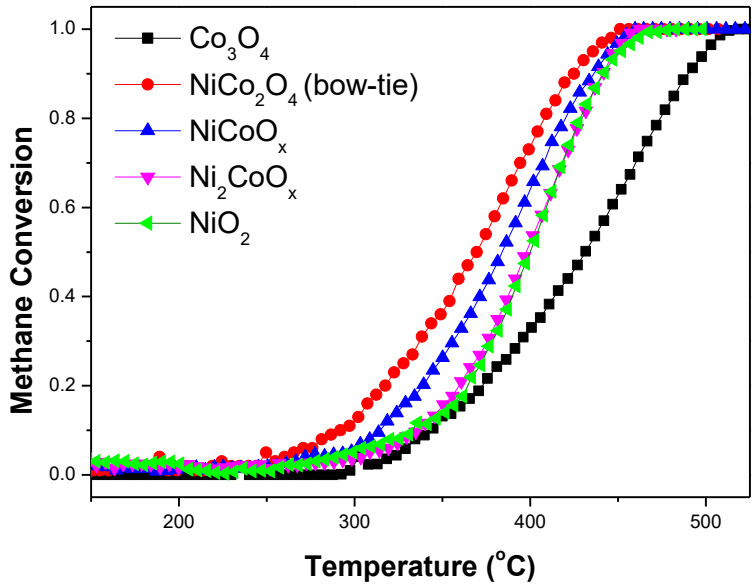

Figure 3.24 TPO curves for the Ni/Co oxides prepared with varying Ni/Co ratios.

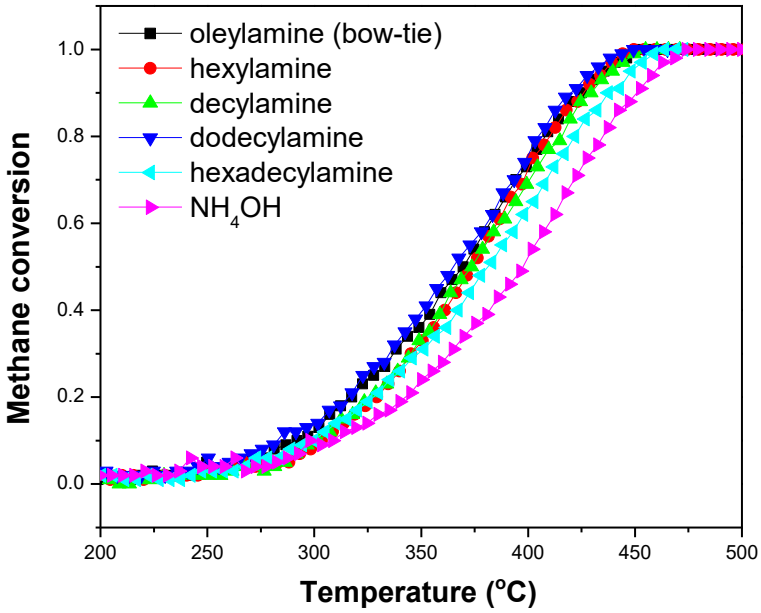

Figure 3.25 TPO curves for $NiCo_2O_4$ prepared with different amines.

The catalytic behavior of bow-tie shaped $NiCo_2O_4$ (calcined at 450 °C) in the presence of 5% water in the gas stream at 410 °C was investigated. As shown in Figure 3.20b, the catalytic activity was stable at ~ 76% conversion before injection of water. After water addition, the activity rapidly decreased to 30% and then decreased slowly to 25% over 12 h. When the water was removed from the gas mixture, the activity recovered to 70%. The catalytic performance for the used catalysts after water stability testing was also studied and the TPO curve is shown in Figure 3.20c. The light-off curve was nearly the same as for fresh catalyst, suggesting that the decreased activity observed during water injection is mostly due to the competition of H_2O and CH_4 for the active sites on $NiCo_2O_4$ rather than degradation of the structure. After water was removed, the structure, surface area and catalytic activity returned to almost the original state. Thus, the addition of water suppresses the methane conversion, but the effect is reversible.

3.4 Conclusions

We have developed a method to synthesize novel bowtie-shaped $NiCo_2O_4$ nanocrystals. By varying the hydrothermal treatment time, we gained a detailed understanding of the growth mechanism of these unusual structures. Furthermore, the ratio of Ni:Co in the materials was optimized to form the bowtie-shaped structures. These $NiCo_2O_4$ nanocatalysts display excellent activity for methane oxidation. The calcination temperature affects the catalytic activity with the bowtie-shaped $NiCo_2O_4$ calcined at 350 °C showing the best catalytic performance with 100% conversion at 410 °C (GHSV=90,000 mL (STP)$\cdot g^{-1} \cdot h^{-1}$), while $NiCo_2O_4$ calcined at 400 or 450 °C showed slightly poorer activity with complete conversion at ~430 or 450 °C. However, the thermal and hydrothermal stability for $NiCo_2O_4$ spinel catalysts should be further improved for practical usage. These non-noble metal catalysts have potential to be used in NGVs or in other industrial applications.

Chapter 4: Highly Stable $CoCr_2O_4$ Catalysts and Monolith Coating

4.1 Introduction

In automobiles, 3-way catalytic convertors are used to treat exhaust, removing SO_x and NO_x, and oxidizing CO and hydrocarbons. Unfortunately, methane oxidation in the exhaust of NGVs is a much more challenging prospect owing to the lower temperature of the exhaust stream in NGVs (less than 500-550 °C), as well as the low concentration (~1000 ppm) and high stability of methane.[9] In addition, catalysts must remain active in the presence of water vapor, SO_x, and NO_x. For these reasons, there is a great deal of effort being devoted to develop stable catalysts that can oxidize methane at low temperature and remain stable under NGV operating conditions.

Over the past decade, there have been significant advances in the development of nanostructured catalysts based on non-noble metals.[91, 129-130] Transition metal oxides such as Co_3O_4 nanocatalysts have shown catalytic activities comparable to Pd-based catalysts.[88] Unfortunately, Co_3O_4 showed poor thermal and hydrothermal stability. With higher calcination temperatures or in the presence of water, the catalytic activity for Co_3O_4 decreased substantially. Ordonez *et al.*[86] explored the use of numerous metal oxides for methane oxidation and reported that Cr_2O_3 shows the best stability for methane combustion in real emission conditions containing water and other gases that typically deactivate catalysts. However, the catalytic activity of Cr_2O_3 is not competitive with precious metal catalysts.

The results for Co_3O_4 and Cr_2O_3 catalysts suggest that an approach involving mixed-metal oxides may result in enhanced stability while maintaining high catalytic activity. Recently, $CoCr_2O_4$ spinel-type oxide catalysts, synthesized by a sol-gel or co-precipitation method, have

been applied to methane oxidation. Hu *et al.*[96] prepared $CoCr_2O_4$ by a sol-gel method and the catalyst showed 90% conversion of methane to CO_2 at 750 °C (GHSV = 48,000 h^{-1}). Chen *et al.*[103] prepared a series of cobalt chromium oxides with different Co/Cr ratios via co-precipitation and evaluated these for methane combustion. $CoCr_2O_4$ showed the best catalytic activity with 90% conversion at 464 °C (GHSV = 36,000 h^{-1}) and excellent resistance to water vapor. Although these results are promising and demonstrate the potential of Co/Cr mixed oxides in methane oxidation catalysis, the catalytic activity for $CoCr_2O_4$ is still insufficient to meet the demanding conditions encountered in NGVs.

We hypothesized that $CoCr_2O_4$ nanoparticles may offer the best potential for improved catalysis. Here, we report a facile solvothermal method for the synthesis of $CoCr_2O_4$ nanospheres using benzyl alcohol as both a reducing and structure-directing agent. The structure and catalytic performance of the new materials for methane combustion are investigated in detail. The $CoCr_2O_4$ nanospheres show superior catalytic activity and excellent stability in the presence of water and SO_2.

4.2 Experimental

4.2.1 Preparation of $CoCr_2O_4$ nanocrystals

Cobalt(II) nitrate hexahydrate ($Co(NO_3)_2 \cdot 6H_2O$, 0.5867 g, 2.000 mmol) and chromium(III) nitrate nonahydrate ($Cr(NO_3)_3 \cdot 9H_2O$, 1.614 g, 4.000 mmol) were dissolved in 20 mL methanol. Benzyl alcohol (3 mL, 29.00 mmol) was added and the solution was stirred for 1 h. The mixture was then transferred to a 45 mL Teflon-lined stainless steel autoclave. The sealed reaction vessel was maintained at 180 °C for different lengths of time (1, 3, 6, 8, 12, 24 h). After the reaction cooled to ambient conditions, the autoclave contents were collected by suction filtration. The dark green product was washed with ethanol three times, then dried at 100 °C for 2 h and calcined at 500 °C for 3 h (yields are summarized in Table 4.1). The theoretical yield was 0.47 g, and the yield achieved for all samples was higher than 89 %. The catalysts are identified by the solvothermal reaction time used (e.g. 1h, 3h, 6h, 8h, 12h and 24h).

Table 4.1 Yields of $CoCr_2O_4$ prepared with different solvothermal reaction times

Solvothermal reaction time for $CoCr_2O_4$	Yield after solvothermal reaction (g)	Yield after calcination (g)
1 h	0.65	0.42
3 h	0.69	0.42
6 h	0.75	0.43
8 h	0.75	0.45
12 h	0.75	0.45
24 h	0.68	0.44

4.2.2 Preparation of $CoCr_2O_4$ nanocrystals without adding benzyl alcohol

As a control experiment, $CoCr_2O_4$ was prepared without benzyl alcohol addition as follows: Cobalt(II) nitrate hexahydrate ($Co(NO_3)_2 \cdot 6H_2O$, 0.5867 g, 2.000 mmol) and chromium(III) nitrate

nonahydrate ($Cr(NO_3)_3 \cdot 9H_2O$, 1.614 g, 4.000 mmol) were added to 20 mL methanol and stirred. The mixture was then transferred to a 45 mL Teflon-lined stainless steel autoclave and the sealed reaction vessel was maintained at 180 °C for different lengths of time (1, 8, 24 h). After the reaction was cooled to ambient temperature, the autoclave contents were collected by suction filtration and the dark green product was washed with ethanol three times. Finally, the sample was dried at 100 °C for 2 h and calcined under air at 500 °C for 3 h. The samples were labeled as **Control-1h**, **Control-8h** and **Control-24h** and the yields are summarized in Table 4.2.

Table 4.2 Yields of $CoCr_2O_4$ without adding benzyl alcohol

Solvothermal reaction time for $CoCr_2O_4$	Yield after solvothermal reaction (g)	Yield after calcination (g)
Control-1h	0.62	0.42
Control-8h	0.64	0.42
Control-24h	0.60	0.41

4.2.3 Preparation of Co_3O_4 and Cr_2O_3 nanocrystals

Cobalt(II) nitrate hexahydrate ($Co(NO_3)_2 \cdot 6H_2O$, 1.749 g, 6.000 mmol) or chromium(III) nitrate nonahydrate ($Cr(NO_3)_3 \cdot 9H_2O$, 2.401 g, 6.000 mmol) were dissolved in 20 mL methanol. Benzyl alcohol (3 mL, 29 mmol) was added and the solution was stirred for 1 h. The mixture was then transferred to a 45 mL Teflon-lined stainless steel autoclave. The sealed reaction vessel was heated at 180 °C for 8 h. After the reaction cooled to ambient conditions, the autoclave contents were collected by suction filtration. The dark green product was washed with ethanol three times, then dried at 100 °C for 2 h and calcined at 500 °C for 3 h.

4.2.4 Preparation of $CoCr_2O_4$ by the co-precipitation method with NaOH

Cobalt(II) acetate tetrahydrate ($Co(CH_3CO_2)_2 \cdot 4H_2O$, 0.8303 g, 3.333 mmol) and chromium(III) acetate hydrate ($Cr(CH_3CO_2)_3 \cdot H_2O$, 4.022 g, 6.667 mmol) were dissolved in 40 mL deionized water at 70 °C while stirring. A sodium hydroxide solution (prepared by dissolving 1.067 g NaOH in 10 mL H_2O) was added to the metal salt solution dropwise and the mixture was stirred for 1 h at 70 °C. Afterward, the precipitate was collected by filtration, washed with H_2O and dried in an oven at 100 °C for 8 h. Finally, the product was calcined at 500 °C for 3 h.

4.2.5 Preparation of $CoCr_2O_4$ by the co-precipitation method with NH_4OH

Cobalt(II) nitrate hexahydrate ($Co(NO_3)_2 \cdot 6H_2O$, 0.7276 g, 2.500 mmol) and chromium(III) nitrate nonahydrate ($Cr(NO_3)_3 \cdot 9H_2O$, 2.001 g, 5.000 mmol) were dissolved in 30 mL deionized water. 10 wt% NH_4OH solution (10 mL NH_4OH diluted with 20 mL H_2O) was added to the above metal salt solution dropwise until the pH equaled to 9, then the mixture was stirred for 1 h. The precipitate was obtained by filtration, washed with H_2O and dried in oven at 100 °C for 8 h. Finally, the product was calcined at 500 °C for 3 h.

4.2.6 Monolith coating by modified wash coating method

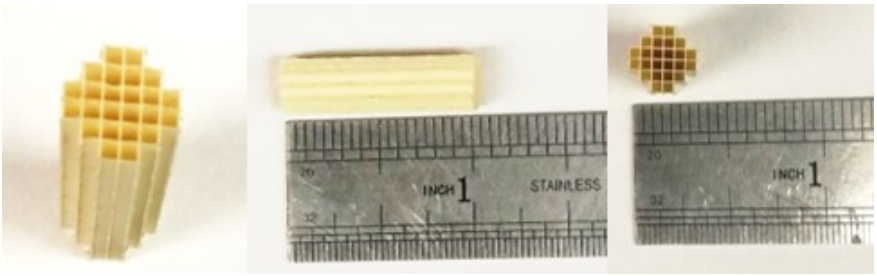

Figure 4.1 Photographs of the monolith used for coating and catalysis test: 1 inch in length, 24 cells.

Commercial cordierite monolithic substrates (Corning, 400 cpsi) were used as supports. A catalyst suspension was prepared by mixing the calcined $CoCr_2O_{4\ 8h}$ catalysts and colloidal alumina solution. Typically, 3.3 mL colloidal alumina solution and 2.0 g $CoCr_2O_{4\ 8h}$ catalysts were added to 6.7 mL water under stirring to obtain the suspension. The monolith (Figure 4.1, ~0.35 g) was dipped into the above suspension for 5 min. Then the monolith was taken out with tweezers. Excess solvent was removed by shaking the monolith and blowing on it with compressed air. Afterwards, the monolith was placed in front of a heat gun (~300 °C) for ~10 min to get a quick calcination. Then the monolith was blown with compressed air again to remove the loose coating. The dipping and quick calcination steps were repeated to obtain 0.10 g coating before the monolith was calcined in a furnace at 500 °C for 7 h in air. Finally, the above steps were repeated to apply another 0.10 g coating and calcine at the same conditions to obtain 0.20 g catalyst loading in total. The coated monolith was labeled as CBAl monolith.

4.2.7 Monolith coating by normal coating method as control

A coated monolith was also synthesized by two other modified wash-coating methods as control samples. The catalyst suspension was prepared by mixing 2.0 g $CoCr_2O_{4\ 8h}$ precursor and 3.3 mL colloidal alumina solution with 6.7 mL water. The monolith (~0.35 g) was immersed into this suspension for 5 min. Then the monolith was taken out and blown with compressed air to remove the excess solution that blocked channels. After that, the monolith was placed in a furnace and calcined at 500 °C for 7 h. Finally, the above steps were repeated to apply another coat of catalyst to the monolith; the coated monolith labeled as NCNBAl monolith.

For the second coating process, the catalyst suspension was prepared the same as for the first control method. After dipping and removing excess coating, the monolith was placed in front

of a heat gun (~300 °C) for about 10 min to get a quick calcination. The dipping and quick calcination steps were repeated to obtain 0.10 g coating. The monolith was calcined at 500 °C for 7 h. Finally, the above steps were repeated to obtain 0.20 g catalyst coating in total; this sample is labeled the NCBAl monolith.

4.2.8 Big monolith coating for engine test

Figure 4.2 Photograph of the coated big monolith (400 cpsi, 11 cm in height, 7.6 cm in diameter). Scale bar 1 cm.

The size of the big monolith is shown in Figure 4.2. $CoCr_2O_4$ 8h catalysts were prepared by the same method to get about 100 g. Then, 166.5 mL colloidal alumina solution and 100.0 g $CoCr_2O_4$ 8h catalysts were added to 333.5 mL H_2O, and stirred for 30 min to get a uniform slurry. The big monolith was then immersed into the slurry for 5 min. The monolith was taken out and excess slurry trapped in the channels was removed by blowing on the monolith with compressed air. After that, the monolith was placed in a 500 mL beaker covered with heating tape and the heating temperature was set to 320 °C. A heat gun (~300 °C) was used to accelerate the calcination. After ~20 min, the monolith was cooled down and excess loose material was removed by blowing the monolith with compressed air. The dipping and quick calcination steps were repeated to obtain

~60 g coating. Then the monolith was calcined in a furnace at 500 °C for 7 h. Finally, the above steps were repeated to get another 60 g coating and the final monolith was calcined under the same conditions again to obtain ~120 g catalyst loading in total.

4.2.9 Characterization

Powder X-ray diffraction (PXRD) data were collected with a Bruker D8 Advance X-ray diffractometer using Cu Kα radiation at 40 mA, 40 kV. For the monolith sample, a slice of monolith was cut off and stuck onto the sample holder for X-ray diffraction measurement. Fourier transform infrared (FT-IR) spectroscopy was conducted on a PerkinElmer Frontier FT-IR spectrometer. Brunauer–Emmett–Teller (BET) surface areas were measured by N_2 adsorption at 77 k using a Micromeritics Accelerated Surface Area & Porosity (ASAP) 2020 system. High-resolution transmission electron microscopy (HRTEM) images were collected on a FEI Tecnai G2 electron microscope with an accelerating voltage of 200 kV. Scanning electron microscopy (SEM) images were recorded on a Hitachi S-4700 FESEM operating at 5 kV accelerating voltage. Energy-dispersive X-ray (EDX) data were obtained with a Hitachi S2600 Variable Pressure SEM with an X-ray detector. EDX mapping data were collected on a FEI Tecnai Osiris S/TEM at an operating voltage of 200 kV. X-ray photoelectron spectroscopy (XPS) data were obtained using a Leybold Max200 spectrometer with an ion-pumped chamber (1×10^{-9} Torr). Thermal stability was examined using Netzsch TG 209F1 Libra under N_2. The change of weight as temperatures increased from 100 to 800 °C at a heating rate of 10 °C/min was recorded. The CO uptake, H_2 reduction (H_2-TPR) and O_2 desorption (O_2-TPD) were obtained on a Micromeritics AutoChem 2920 analyzer. The sample was purged with helium at 100 °C for 2 h to remove moisture, and then cooled to 50 °C before adsorption. CO uptake was used to characterize the active sites on the

surface of the catalysts. The sample was reduced by 9.5 mol% H_2/Ar at 500 °C with a flow rate of 50 mL/min, then cooled down to 50 °C under a flow of He (50 mL/min), and pulses of 0.5 mL CO were added into the flow of He. CO adsorption was measured using a thermal conductivity detector (TCD). The addition of CO was repeated until no adsorption was detected. The reducibility of materials were measured by H_2-TPR and O_2-TPD. For H_2-TPR, catalysts were treated under 9.5 mol% H_2/Ar at 500 °C with 10 °C/min heating rate and held at 500 °C for 30 min. For the O_2 desorption experiment, the material was exposed to O_2 at 100 °C for 1 h. Then the flow gas was changed to He and the system was cooled to 50 °C for 90 min in order to remove the physically adsorbed O_2. After that, the sample was heated up to 500 °C under He for desorption measurement.

4.2.10 Methane combustion catalysis

Catalytic performance was evaluated by temperature-programmed CH_4 oxidation (TPO) in a gas mixture containing 1000 ppmv CH_4, 10% (V/V) O_2, and Ar, He balance at a flow rate of 300 mL/min. The powder catalyst (0.1000 g) was mixed with 2.5000 g SiC and then transferred into a stainless steel fixed-bed microreactor. For the coated small monolith, it was covered with a thin layer of quartz wool outside and loaded into the stainless steel reactor. Then the reactor was heated from room temperature to 600 °C at a rate of 5 °C min^{-1} while the composition of emitted gas was analyzed by a VG ProLab quadrupole mass spectrometer (QMS; ThermoFisher Scientific). Conversion was calculated by determination of the yield of CO_2 and total carbon balance. Stability studies of the catalysts were conducted at 500 °C with 10% H_2O and 5 ppm SO_2 added to the dry feed gas prior to the preheater.

4.3 Results and Discussion

4.3.1 Characterization of the $CoCr_2O_4$ precursor

Nanospheres of $CoCr_2O_4$ were prepared by a solvothermal method using benzyl alcohol as structure-directing agent. A mixture of cobalt(II) nitrate, chromium(III) nitrate, benzyl alcohol, and methanol were treated at 180 °C in a sealed autoclave (see Experimental section for details). After the reaction cooled, the powder ($CoCr_2O_4$ precursor) was isolated by filtration. The filtrate and isolated products were characterized by FT-IR spectroscopy, elemental analysis (EA), powder X-ray diffraction (PXRD), thermogravimetric analysis (TGA) and energy dispersive X-ray (EDX) analysis.

FT-IR spectroscopy was used to study the reaction mixture prior to the solvothermal reaction, and the filtrate following the reaction (Figure 4.3). Before the solvothermal reaction, peaks due to methanol (broad band at 3318 cm^{-1}, ν(C-H)) and benzyl alcohol (1019 cm^{-1}, ν(C-O); ~1495 cm^{-1}, phenyl ring vibrations; ~3000 cm^{-1} ν(C-H))[131] were observed. After solvothermal reaction for 24 h, and removal of the remaining methanol by rotary evaporation, a peak at 1700 cm^{-1} (ν(C=O))[132] was present, indicative of the formation of benzaldehyde, in addition to peaks attributed to benzyl alcohol. This suggests a fraction of the benzyl alcohol was oxidized to form benzaldehyde during the solvothermal reaction. Solvothermal reaction of the mixture of methanol and benzyl alcohol under the same conditions without cobalt or chromium salts present did not yield any benzaldehyde, indicating that the metal salts are involved in the oxidation of benzyl alcohol to benzaldehyde.

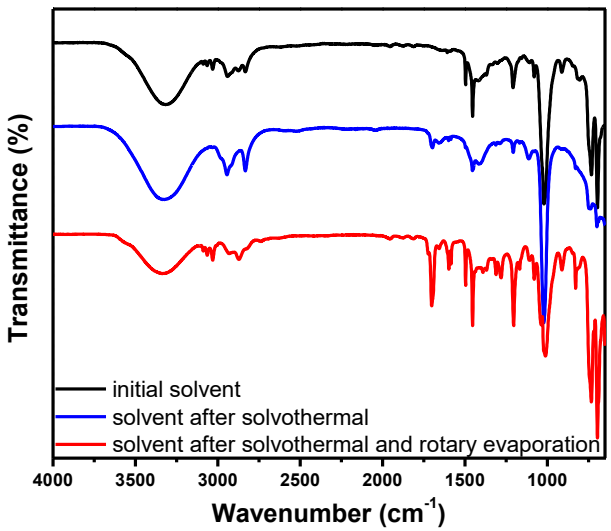

Figure 4.3 FT-IR spectra for the solvent before and after solvothermal process.

The precipitate collected from the solvothermal reaction was washed, dried and characterized. PXRD analysis of the isolated powder showed only a broad featureless pattern, indicating that the as-formed product is essentially amorphous (Figure 4.4). HRTEM images in appendix B (Figure B.1) showed that these $CoCr_2O_4$ precursors have non-distinct boundaries, which indicated incomplete crystallization. Weak cobalt oxide ($Co_{2.74}O_4$) peaks appear in the PXRD pattern of the sample after one hour of solvothermal reaction. As the solvothermal reaction time is increased, the intensity of these peaks decreased, suggesting that the ratio of $Co_{2.74}O_4$ in the precursor decreased. FTIR spectra of the product indicate the presence of both benzoate groups and alkoxy groups (Figure 4.5). Strong bands at 1594 and 1394 cm^{-1} are assigned to asymmetric and symmetric C=O stretching of carboxylate groups, respectively. Peaks at 1068, 1025, and 1177 cm^{-1} are due to C-H phenyl in-plane bending, and a peak at 1495 cm^{-1} is assigned to phenyl stretching modes. Medium strength bands at 2931, 2825 cm^{-1} are assigned to the antisymmetric and symmetric stretching modes of CH_3. The strong band at 1022 cm^{-1} is attributed to C-O

stretching.[133] Solvothermal reaction of the mixture of metal salts in methanol without adding benzyl alcohol was carried out under the same conditions; FTIR spectra of the product obtained in this case indicated the presence of formate and alkoxy groups (Figure 4.6).

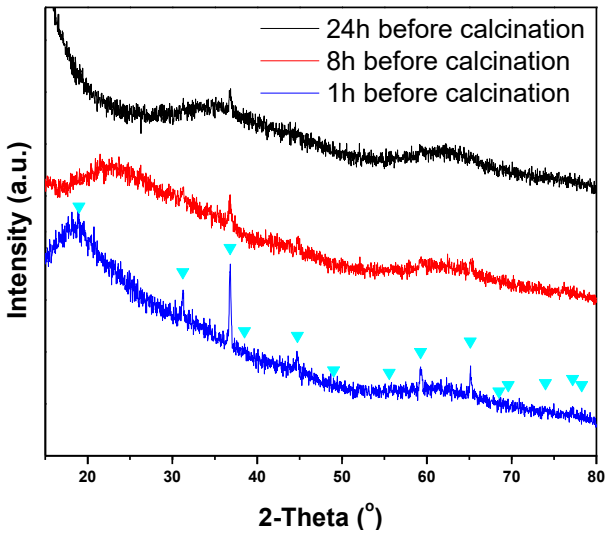

Figure 4.4 PXRD pattern of $CoCr_2O_4$ precursor (before calcination) with different times of solvothermal treatment (1 h, 8 h, 24 h). (▼) Spinel, syn – $Co_{2.74}O_4$ (JCPDS 78-5614).

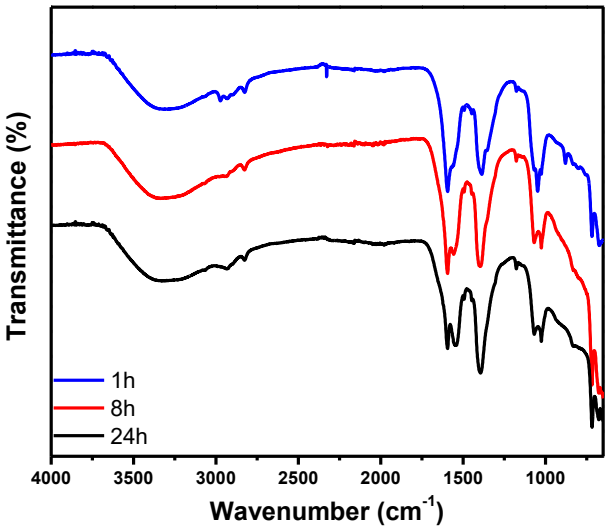

Figure 4.5 FTIR spectra for $CoCr_2O_4$ precursors prepared with different solvothermal reaction times.

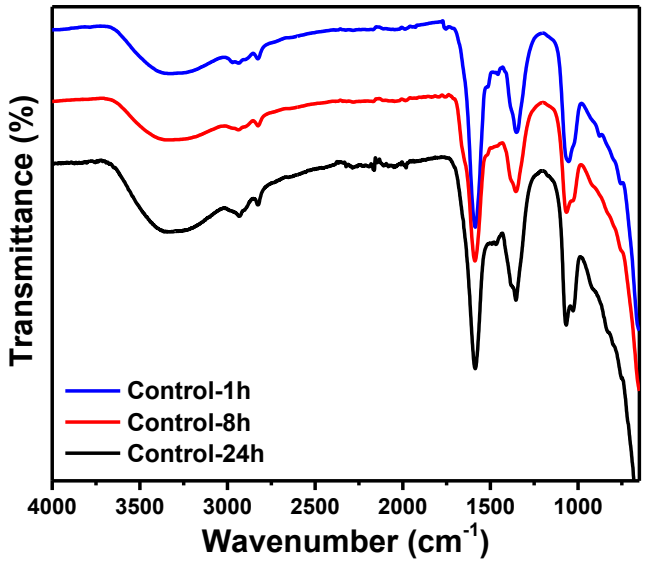

Figure 4.6 FTIR spectra for $CoCr_2O_4$ precursors prepared with different solvothermal reaction times without adding benzyl alcohol. Strong peaks at 1586 and 1355 cm^{-1} are due to the asymmetric and symmetric C=O stretching of salts of carboxylic acids. Medium bands at 2935 and 2823 cm^{-1} are assigned to the antisymmetric and symmetric stretching of CH_3, respectively. A strong band at 1031 cm^{-1} is due to the C-O stretching.

Elemental ratios in the samples were determined by EDX and EA; these data are summarized in Table 4.3. Based on the carbon analysis, addition of benzyl alcohol resulted in the precursor trapping more organic groups (e.g., methoxy or benzoate groups). These results are also in agreement with the TGA results (Figure 4.7). The $CoCr_2O_4$ precursor prepared with 24 hours of hydrothermal reaction time lost more mass than a sample prepared for the same reaction time with no benzyl alcohol present during the heating process.

In summary, under high temperature and pressure, cobalt and chromium alkoxy benzoate composites co-precipitated, yielding a green powder. At the same time, Co^{2+} and Cr^{3+} catalyzed the oxidation of benzyl alcohol to benzaldehyde and benzoate. The benzoate groups may bind with cobalt and chromium ions and coat the surface of precipitates. Furthermore, part of Co^{2+} salts are

oxidized to Co_3O_4 at an early stage. Co_3O_4 nanoparticles are reduced back to Co^{2+} and combined with Cr^{3+} to gradually form $CoCr_2O_4$ precursor.

Table 4.3 Weight percentage of different elements for $CoCr_2O_4$ precursor.

$CoCr_2O_4$ precursor	Co (wt%)	Cr (wt%)	C (wt%)	O (wt%)	H (wt%)
1h	9.1	15.9	33.0 (11.2)[a]	42.0	(3.1)
8h	14.1	25.7	28.9 (11.9)	31.3	(3.7)
24h	14.2	22.6	30.3 (12.8)	32.9	(3.4)
Control-1h	21.5	40.0	16.4	22.2	
Control-8h	22.3	39.7	16.1	22.0	
Control-24h	22.5	41.5	16.0 (5.0)	21.0	(3.7)

The data in parentheses are EA results

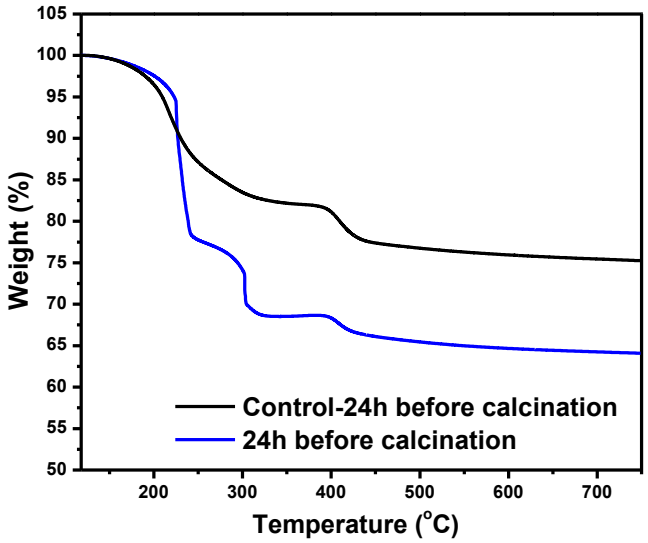

Figure 4.7 Thermogravimetric analysis (TGA) traces under N_2 for the $CoCr_2O_4$ precursors (before calcination) prepared with or without adding benzyl alcohol during the solvothermal reaction.

4.3.2 Characterization of calcined $CoCr_2O_4$ nanospheres

The $CoCr_2O_4$ precursor was subsequently calcined at 500 °C in air for 3 h, during which time it decomposed to oxide. PXRD data (Figure 4.8) show that the major product matches the standard cochromite $CoCr_2O_4$ (JCPDS 22-1084). There is also a small amount of Co_3O_4 and Cr_2O_3 present at the early stages of the reaction (short solvothermal reaction time). With longer solvothermal treatment, the peaks for Co_3O_4 and Cr_2O_3 decreased in intensity relative to $CoCr_2O_4$, and were completely absent after about 8 hours solvothermal reaction time. (The enlarged PXRD pattern is shown in Figure 4.9).

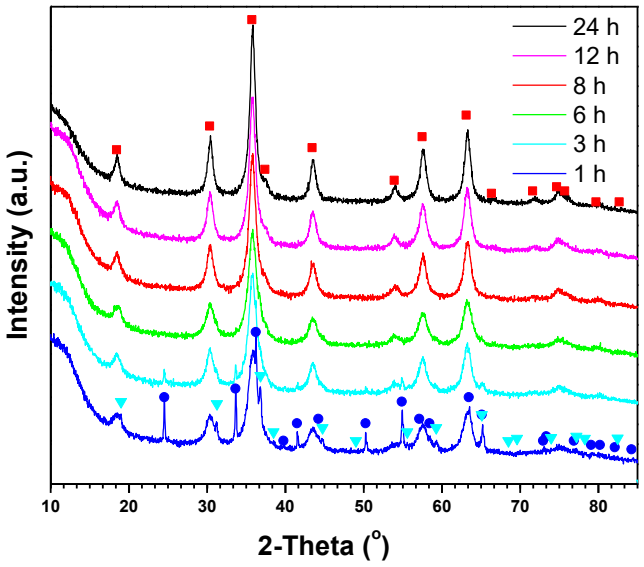

Figure 4.8 PXRD patterns for $CoCr_2O_4$ prepared with different solvothermal reaction times. (■) Cochromite, syn – $CoCr_2O_4$ (JCPDS 22-1084). (▼) Spinel, syn – $Co_{2.74}O_4$ (JCPDS 78-5614). (●) Eskolaite, syn – Cr_2O_3 (JCPDS 38-1479).

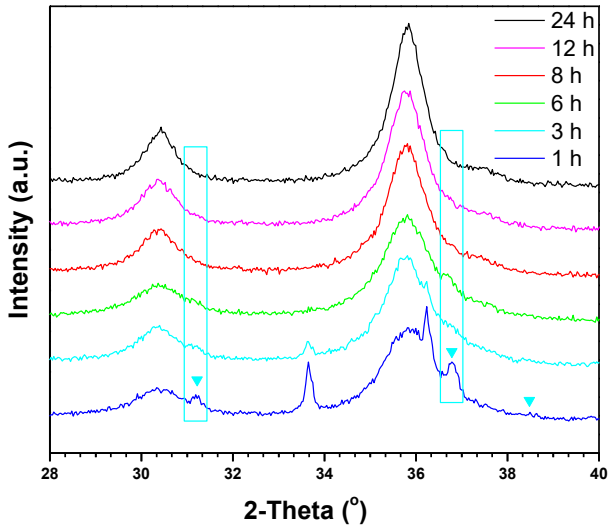

Figure 4.9 Expanded view of the PXRD patterns for $CoCr_2O_4$ prepared with different solvothermal reaction times. (▼) Spinel, syn – $Co_{2.74}O_4$ (JCPDS 78-5614).

The morphology and structure of the nanocrystalline $CoCr_2O_4$ were investigated by SEM, PXRD, EDX mapping, high-resolution transmission electron microscopy (HRTEM) and X-ray photoelectron spectroscopy (XPS). Samples were prepared with different solvothermal reaction times (1 - 24 h) in order to explore the growth process of the $CoCr_2O_4$ nanoparticles. As shown in Figure 4.10, large nanospheres (500-800 nm) decorated with smaller nanoparticles (< 100 nm) initially form. As the solvothermal reaction time increased, the number of parasitic nanoparticles decreased and the large nanospheres appeared to have a smoother surface. After 24 h, all of the small nanoparticles are gone and the surface of the isolated nanospheres is smooth.

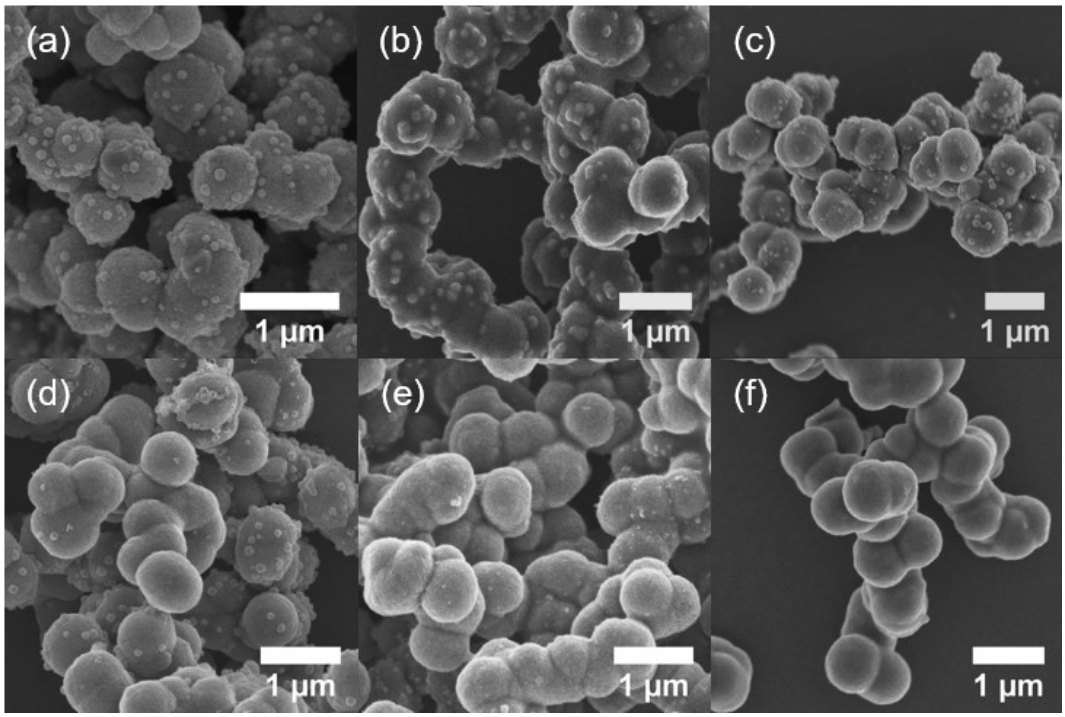

Figure 4.10 SEM images of $CoCr_2O_4$ prepared with different solvothermal reaction times. (a) 1 h, (b) 3 h, (c) 6 h, (d) 8 h, (e) 12 h, (f) 24 h.

PXRD data (Figure 4.8) of $CoCr_2O_4$ shows broadening of the diffraction peaks arising from small domain sizes. The Scherrer equation was applied to calculate particle sizes of the crystalline $CoCr_2O_4$ components (Table 4.4), and it is evident that the nanodomains (about 6-10 nm) of $CoCr_2O_4$ grow larger with increasing solvothermal reaction times. Owing to overlap between the peaks due to Co_3O_4 and Cr_2O_3 and other phases, as well as the effects of background noise, it was not possible to estimate the particle sizes of Co_3O_4 and Cr_2O_3, though broadening of the peaks suggests that they are also small.

Table 4.4 Crystallite size calculated with the Scherrer equation for two specific PXRD peaks of $CoCr_2O_4$ catalysts.

Sample	Particle size determined from (220) (nm)	Particle size determined from (311) (nm)
6 h	7.0	6.1
8 h	8.6	7.2
12 h	9.0	7.5
24 h	10.4	8.4

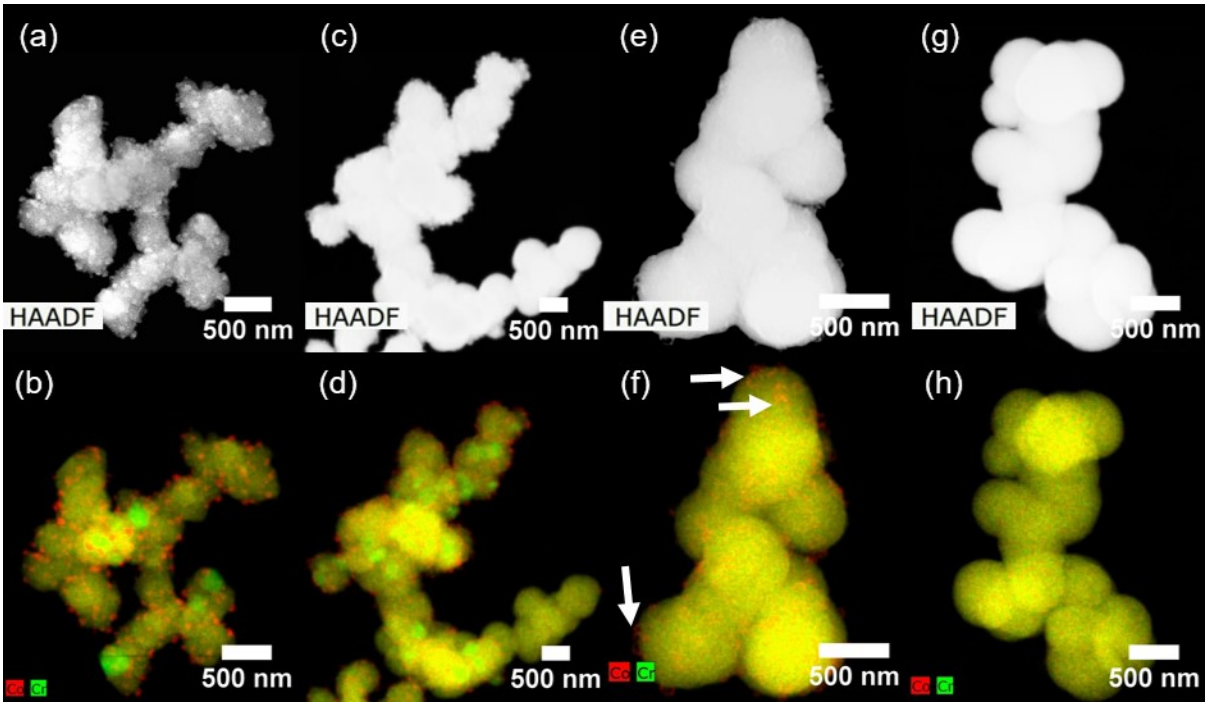

Figure 4.11 High-angle annular dark field (HAADF) images and EDX mapping for $CoCr_2O_4$ catalysts with different solvothermal reaction times. (a, b) 1h, (c, d) 3 h, (e, f) 8 h, (g, h) 24 h.

The samples prepared with solvothermal reaction times of 1, 3, 8 and 24 hours were selected for characterization by EDX mapping. Using this technique, the parasitic nanoparticles are assigned to Co_3O_4 (Figure 4.11). It is interesting to observe that after 1 h solvothermal reaction, the Co_3O_4 nanoparticles are solid, while after 8 hours, they appear to be hollow spheres (Figure 4.11(f) white arrow). In enlarged SEM images (Figure 4.12), several nanospheres are split open,

revealing their hollow structures. Due to the finite crystal size of hollow nanostructured Co_3O_4 and its diminishing quantity with increasing reaction time, the peak for Co_3O_4 in the PXRD is not present after 8 h. The large $CoCr_2O_4$ nanospheres contain a small amount of crystalline Cr_2O_3 (particle size is ~200 nm, measured according to EDX mapping in Figure 4.11b) after one hour of solvothermal treatment. After three hours, the crystal size of Cr_2O_3 decreased (to ~100 nm) and these nanocrystals are distributed more evenly on the surface of the $CoCr_2O_4$. Co and Cr are homogeneously mixed in the large nanospheres prepared with longer solvothermal reaction times (8 h, 24 h). These results are in agreement with the PXRD data.

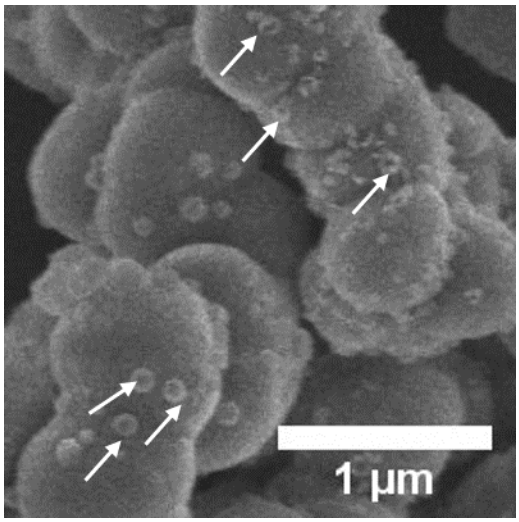

Figure 4.12 SEM image for $CoCr_2O_4$ with 8 h solvothermal treatment. The white arrow points to the hollow structure or breakage of Co_3O_4.

In the preparation conducted without adding benzyl alcohol, after one hour of solvothermal treatment (**Control-1h**), separate Co_3O_4 and Cr_2O_3 phases are apparent (Figure 4.13). After 8 h reaction time, the solid Co_3O_4 is transformed to the hollow structure (**Control-8h**). After 24 hours

reaction time, hollow Co_3O_4 can still be observed (**Control-24h**) and the particle size of $CoCr_2O_4$ is not uniform. The addition of benzyl alcohol may facilitate redox reactions of the transition metal ions, enabling the formation of homogeneous mixed oxide structures. Furthermore, the use of benzyl alcohol appears to control the particle size of $CoCr_2O_4$ nanospheres, possibly through surface capping with benzoate groups formed through oxidation of benzyl alcohol.

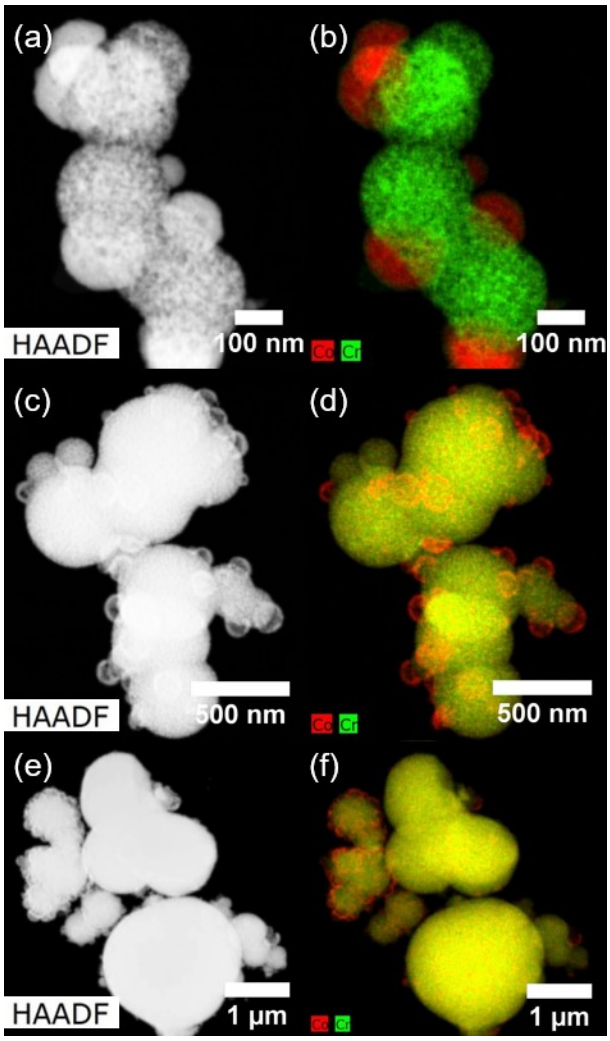

Figure 4.13 High-angle annular dark field (HAADF) images and EDX mapping for $CoCr_2O_4$ catalysts formed without benzoic acid for different solvothermal times. (a, b) Control-1h, (c, d) Control-8h, (e, f) Control-24h.

To further analyze the products, we undertook a detailed HRTEM study of the materials. The large nanospheres formed from the aggregation of nanocrystals with sizes around 10 nm in diameter (Figure 4.14), which agrees with the domain size calculated from the PXRD data by the Scherrer equation. Lattice fringes with 0.48 nm spacing are observed on the large nanospheres and

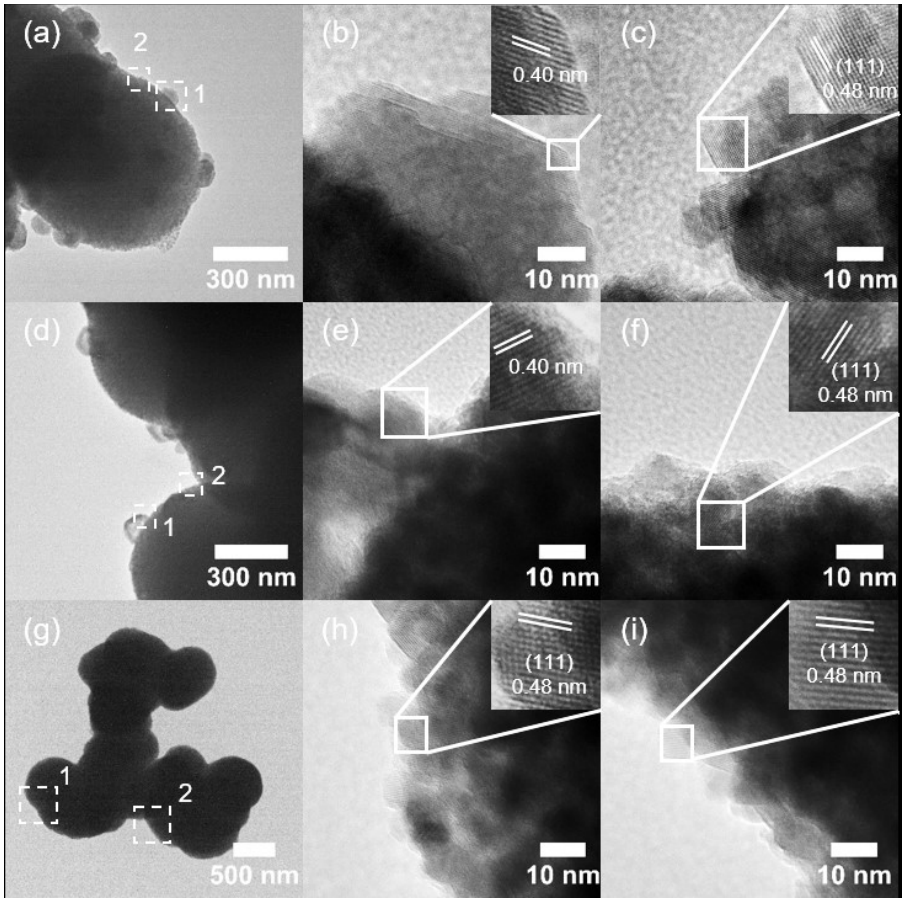

Figure 4.14 HRTEM images of $CoCr_2O_4$ prepared with different solvothermal reaction times. (a-c) 1 h, (d-f) 8 h, and (g-i) 24 h. The center column shows enlargements of "Region 1" identified in the image in the TEM image in the left-hand column. The right-hand column shows enlargements of "Region 2" identified in the TEM image in the left-hand column. Each row shows a TEM image (left) followed by enlargements of region 1 (center) and region 2 (right).

correspond to the (111) planes of $CoCr_2O_4$. The lattice spacing for the nanoparticles located on the surface of the nanospheres is 0.40 nm, assigned to the (200) planes of Co_3O_4.

Based on these data, chromium and cobalt precursor nanoparticles aggregate to form larger nanospheres early in the solvothermal reaction process. Solid Co_3O_4 nanoparticles anchor to the surface of these nanospheres, then with increased heating time, the nanospheres grow even larger and the Co_3O_4 nanoparticles change from solid to hollow and finally break apart. After 24 h of hydrothermal treatment, the Co_3O_4 nanoparticles are no longer present and the $CoCr_2O_4$ nanospheres have a smooth surface (Scheme 4.1).

Scheme 4.1 Process for the formation of $CoCr_2O_4$ Spherical Nanoparticles.

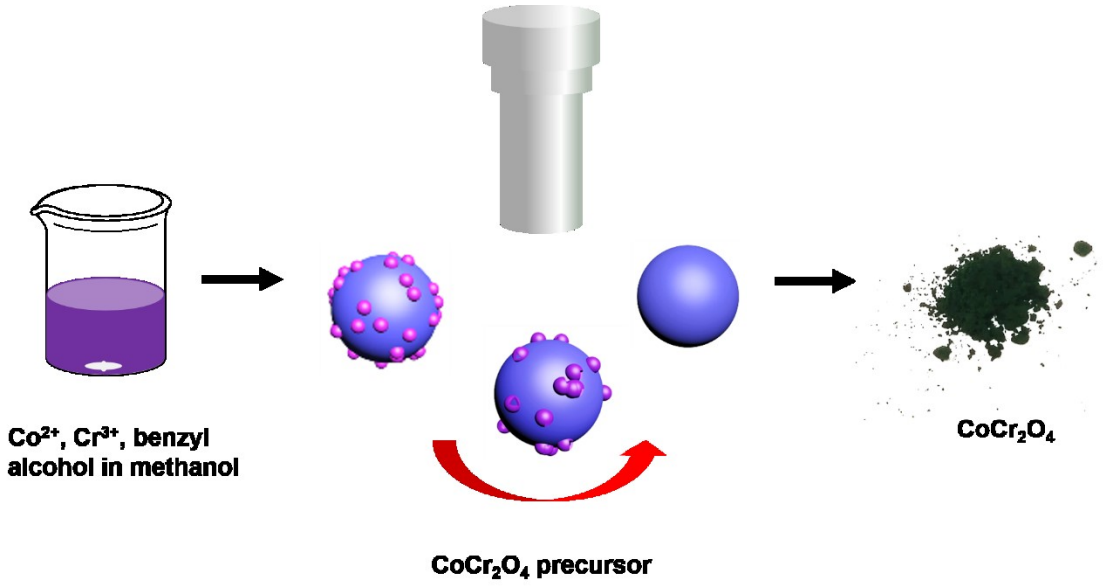

Nitrogen adsorption-desorption analysis was used to determine the surface area and pore size distribution of the products at each stage of the reaction (Table 4.5). The Brunauer-Emmett-Teller (BET) analysis gives a surface area of around 100 $m^2\ g^{-1}$ with a pore size of about 6 nm.

There are no significant differences between the samples prepared with different solvothermal reaction times.

Table 4.5 N_2 adsorption data for $CoCr_2O_4$ prepared with different solvothermal reaction times.

Sample	Surface area (m^2 g^{-1})	Pore size (nm)	Pore volume (cm^3 g^{-1})
1 h	102	6.8	0.17
3 h	106	6.4	0.15
6 h	108	6.2	0.16
8 h	101	6.0	0.15
12 h	108	6.4	0.17
24 h	114	6.2	0.18
Control-24h	103	6.0	0.16

XPS spectra of $CoCr_2O_4$ were used to assess the surface composition of the catalysts prepared with different solvothermal reaction times. In the O 1s spectra (Figure 4.15), a peak at 530.7 eV is assigned to surface lattice oxygen (O_{latt}), while a peak at 532.1 eV is characteristic of adsorbed oxygen (O_{ads}), and a peak at 533.2 eV is due to carbonate or adsorbed water species.[134] The sample prepared with the addition of benzyl alcohol has significant carbonate coverage on the surface which may increase the resistance of the catalyst to poisoning by impurities in the gas stream. The peaks at 578.7 and 576.9 eV are assigned to Cr^{6+} and Cr^{3+}, respectively.[135] It was proposed in previous studies that a large amount of adsorbed oxygen species benefits the adsorption and activation of reactants, and a higher surface ratio of Cr^{6+}/Cr^{3+} improves the low-temperature reducibility.[136] These data for our samples are summarized in Table 4.6. The ratio of Cr^{6+}/Cr^{3+} for the sample prepared with benzyl alcohol is higher than for the control sample (**Control-24h**). The control sample contained more lattice O and less adsorbed O on the surface. Based on the surface elemental ratio (Co/Cr in Table 4.6), there is more cobalt detected on the surface for the control sample. Cobalt oxide is more active but less stable than chromium oxide,

so the control sample may be less stable than the catalysts prepared with benzyl alcohol. From the XPS data, it appears that the addition of benzyl alcohol changes the surface elemental ratio and surface coverage of the catalysts and this may affect their activity and stability.

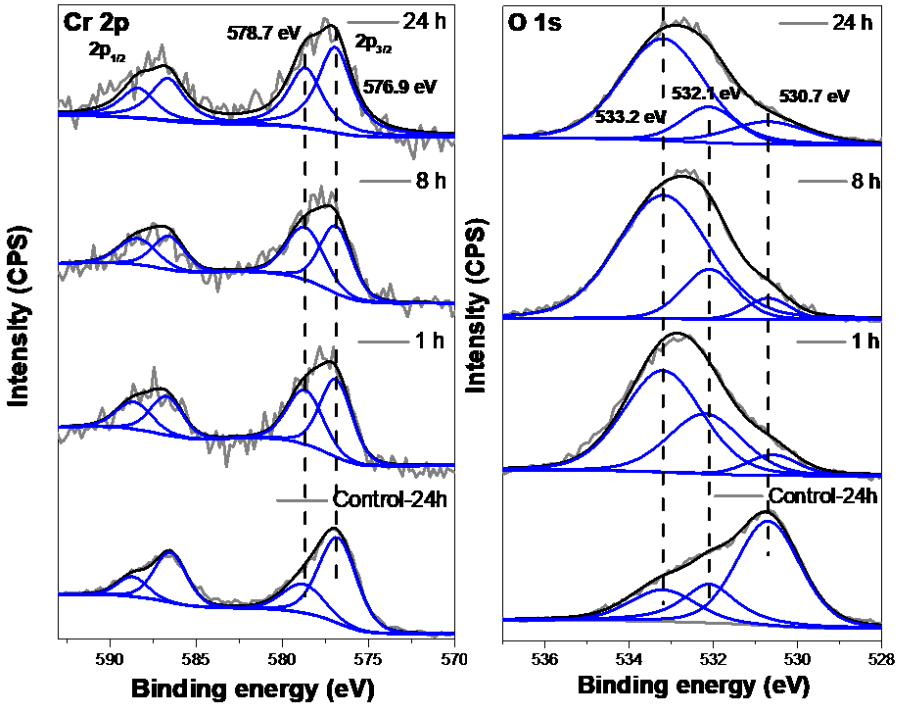

Figure 4.15 XPS spectra of Cr 2p and O 1s for $CoCr_2O_4$ with different solvothermal reaction times.

Table 4.6 XPS data for the $CoCr_2O_4$ with different solvothermal reaction times.

$CoCr_2O_4$	Cr^{6+}/Cr_{total}	O_{latt}/O_{ads}	Co/Cr
1h	0.32	0.24	0.14
8h	0.37	0.33	0.12
24h	0.36	0.93	0.14
Control-24h	0.22	2.5	0.34

4.3.3 Catalytic performance for methane combustion

We investigated the $CoCr_2O_4$ nanomaterials prepared with different solvothermal reaction times for catalytic methane oxidation. In a typical experiment, a sample of metal oxide was diluted with SiC, a mixture of methane (1000 ppm) and O_2 (10%) balanced by Ar was passed over the catalyst, and the conversion of methane to CO_2 was measured as a function of temperature. This temperature-programmed oxidation (TPO) experiment results in a light-off curve, giving the conversion as a function of temperature. The light-off curves measured for the $CoCr_2O_4$ catalysts are shown in Figure 4.16 (all catalysts were tested after calcination at 500 °C). The overall activities are as follows: 1 h ≈ 3 h ≈ 6 h ≈ 8 h > 12 h > 24 h. $CoCr_2O_4$ catalysts, prepared with solvothermal reaction times less than 24 h all achieved 100% conversion below 500 °C.

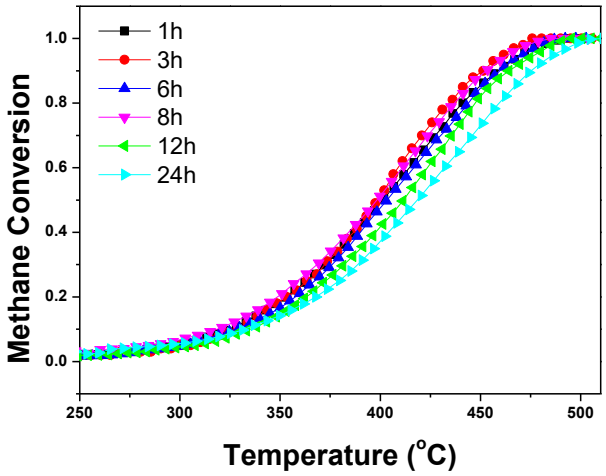

Figure 4.16 Temperature-programmed oxidation (TPO) test for $CoCr_2O_4$ with different solvothermal reaction times, calcined at 500 °C for 3 h.

The catalysts prepared with solvothermal reaction times of 1 h, 8 h, and 24 h were selected for further stability studies and the results are shown in Figure 4.17. It was observed that with addition of 10% water and 5 ppm SO_2 to the gas feed at 500 °C, the activity for $CoCr_2O_4$ prepared with 24 h solvothermal reaction time dropped immediately from 98% to 80% activity. After ~12 h treatment with this gas mixture (at 500 °C), the activity remained stable at ~78%. The water and SO_2 flows were then cut off for several hours and the system cooled down to room temperature. A second cycle was then conducted continuously for another 10 h. It is evident that in the second run, after injection of water and SO_2, the activity decreased to 78% and remained stable until the water and SO_2 flows were stopped, at which point the activity recovered to 95%. The activity for $CoCr_2O_4$ prepared for 8 h dropped to 92% in the presence of SO_2 and water, then the activity gradually decreased to 88% and remained relatively stable at this value. For the second run, the activity remained stable at 88% with SO_2 and water present, and fully recovered to 100% after removing the SO_2 and water. The catalysts prepared with only 1 h solvothermal treatment showed

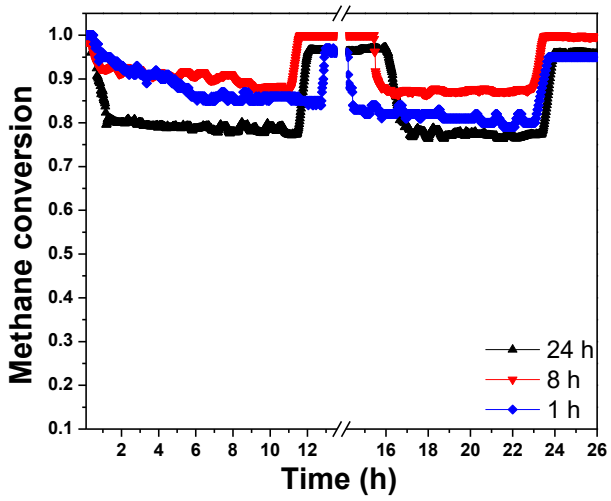

Figure 4.17 Stability study with injection of 10% water and 5 ppm SO_2 at 500 °C for $CoCr_2O_4$ catalysts with 1, 8 and 24 h solvothermal reaction time and then calcined at 500 °C for 3 h.

slightly poorer stability. After injection of SO_2 and water, their activity continuously decreased from 100% to about 82%, and the activity returned to 94% after removing SO_2 and water. Among the samples studied, $CoCr_2O_4$ prepared with 8 h solvothermal treatment exhibited the best stability.

The catalytic activity and stability measurements for the catalysts prepared without addition of benzyl alcohol during the solvothermal reaction are shown in Figure 4.18. We observe that the control catalysts prepared with a longer solvothermal treatment time showed lower methane conversion temperatures, which is opposite to the trend for $CoCr_2O_4$ prepared with benzyl alcohol. Furthermore, the light off curve for **Control-24h** is similar to that for $CoCr_2O_4$ prepared in 8 h. **Control-1h** and **Control-8h** show nearly the same catalytic performance, but they are less active than all the catalysts prepared with benzyl alcohol. As for the stability, the conversion for control catalysts decreased more in the presence of water and SO_2 (Table 4.7). Thus, the control catalysts show poorer stability compared with those prepared using benzyl alcohol, which is in agreement with the conclusions drawn from the XPS data.

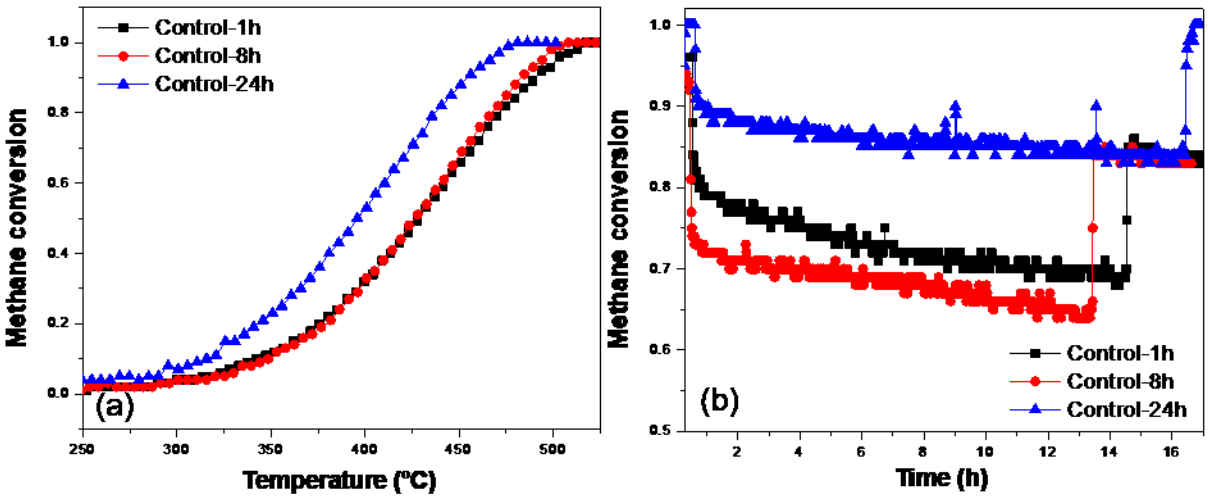

Figure 4.18 Catalytic performance in dry (a) and wet (b) conditions for control $CoCr_2O_4$ samples prepared without benzyl alcohol.

Table 4.7 Comparison of stability for the $CoCr_2O_4$ catalysts prepared with and without adding benzyl alcohol.

$CoCr_2O_4$	Conversion drops at the beginning of H_2O and SO_2 injection	Conversion in the presence of SO_2 and H_2O within 13 h	Decreased conversion in total
24 h	98-80% (Δ = 18%)	80-78% (Δ = 2%)	20%
Control-24h	100-90% (Δ = 10%)	90-84% (Δ = 6%)	16%
8 h	100-92% (Δ = 8%)	92-88% (Δ = 4%)	12%
Control-8h	95-75% (Δ = 20%)	75-66% (Δ = 8%)	28%
1 h	-	99-85% (Δ = 14%)	14%
Control-1h	96-82% (Δ = 14%)	82-69% (Δ = 13%)	28%

The $CoCr_2O_4$ catalyst prepared with 8 h solvothermal reaction time was selected to conduct a durability study. The catalyst was heated to 500 °C in 20 min under the flowing MOX gas mixture (1000 ppm CH_4, 10% O_2), then 10% water and 5 ppm SO_2 were injected into the gas feed. After 12-25 h, water and SO_2 flow were stopped and the reaction continued for another 2 h to probe reversibility. For the first run, the conversion decreased about 5% in the presence of water and SO_2 over 12 h (Figure 4.19 and Table 4.8). The observed loss of activity under water and SO_2 decreased after several cycles. After seven runs, the conversion was stable at 78% in wet conditions with SO_2 present, and 93% in dry conditions. There were no significant differences for the final three runs. The $CoCr_2O_4$ catalyst therefore shows excellent stability and durability for low temperature methane combustion in the presence of water and SO_2. The stability of $CoCr_2O_4$ was compared with other types of catalysts. As shown in Table 4.9, for Pd-based catalysts, the formation rate of palladium sulfate can be slowed by doping with Pt or adding a porous shell, and they show good initial stability. However, because the sulfating deactivation is irreversible, they are not able to maintain high activity over longer reaction times. Compared with non-noble metal catalysts, $CoCr_2O_4$ prepared in this work shows the best catalytic performance. It maintained the high stability characteristic of Cr_2O_3, but was more active than pure Cr_2O_3. As well, it is even more

stable in the presence of both H_2O and SO_2 than other catalysts under the effect of a single component.

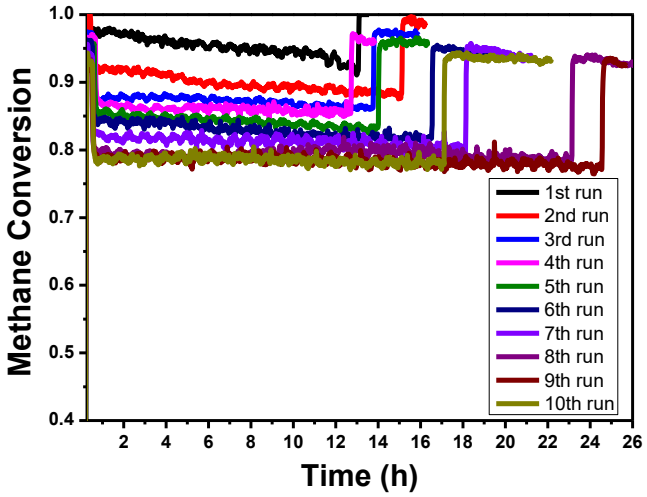

Figure 4.19 Durability study with injection of 10% water and 5 ppm SO_2 at 500 °C for $CoCr_2O_4$ 8h catalyst.

Table 4.8 Summary of stability results for the $CoCr_2O_4$ 8h catalyst (10 cycles).

$CoCr_2O_4$ 8h	Time (h)	Conversion in the presence of H_2O and SO_2 (%)	Reversibility (%)
1st run	13	96-91	100-100
2nd run	15	92-88	100-99
3rd run	13.5	87-86	97-97
4th run	12.5	87-85	96-96
5th run	14	85-83	95-95
6th run	16.5	84-81	96-95
7th run	18	82-80	94-94
8th run	23	80-78	93-93
9th run	24.5	79-77	92-92
10th run	17	78-78	93-93

Table 4.9 Comparison of stability for methane combustion with literature.

Catalysts	Condition		Time (h)	Stability in feed gas	Reversibility $\Delta T_{50\%}$ (°C)	reference
$CoCr_2O_4$ 8h	10% H_2O, 5 ppm SO_2 at 500 °C		170	100%-78%	30	This work
0.33Pt-0.67Pd /$MnLaAl_{11}O_{19}$	3% H_2O, 1000 ppm SO_2	670 °C	10	100%-99%	60	81
		495 °C	5	93%-93%	-	
Pd-CeNW@SiO_2	5% H_2O, 20 ppm SO_2 at 450 °C		10	100%-100%	-	83
	5% H_2O, at 375 °C		24	100%-75%	-	
$PdPt/Al_2O_3$	5% H_2O, 10 ppm SO_2 at 500 °C		4	87%-10%	-	137
Cr_2O_3	Emission from a coke oven, with NH_3, N_2, H_2, H_2O, CO, CO_2, SO_2 and H_2S at 450 °C		40	100%-90%	-	86
$La_{0.9}Ce_{0.1}CoO_3$			35	95%-75%	-	
$10Ce/Co_3O_4$	5% H_2O, at 450 °C		150	75%-40%	10	138
$LaCoO_3$	100 ppm SO_2 at 600 °C		3	-	60	139

To investigate the reasons underlying the catalyst deactivation, the spent catalysts were analyzed by TEM, EDX mapping and PXRD. After the durability test, the aggregation of large chromium oxide particles was observed through EDX mapping (Figure 4.20). Moreover, regular cobalt oxide nanoparticles (~100 nm) were distributed on the surface of the nanospheres (Figure 4.21). These results are in agreement with the PXRD data (Figure 4.22). As well, new diffraction peaks appeared in the $CoCr_2O_4$ 8 h sample after the durability test, assigned to Cr_2O_3. Particle sizes (Table 4.10) for the used catalysts are all larger than the fresh ones, and the sintering of the nanoparticles may be responsible for the deactivation of catalysts. No sulfur was detected by XPS or EDX in the catalysts after SO_2 treatment, demonstrating that no stable sulfate or sulfide compounds form that bind to the surface and poison the catalyst, indicating that the catalysts display good tolerance to sulfur compounds.

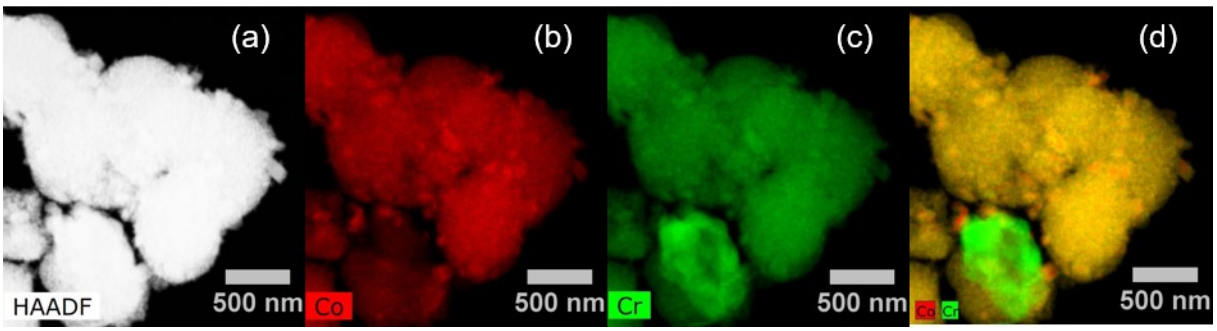

Figure 4.20 EDX mapping for $CoCr_2O_4$ 8 h catalysts after durability test.

Table 4.10 Particle size calculated with the Scherrer equation for the fresh and used catalysts.

Sample	Particle size from (220) (nm)	Particle size from (311) (nm)
8h fresh	8.6	7.2
8h used	9.4	8.6
8h long used	14.7	11.8
24h fresh	10.4	8.4
24h used	10.6	8.7
Control-24h fresh	7.2	6.3
Control-24h used	7.5	6.7

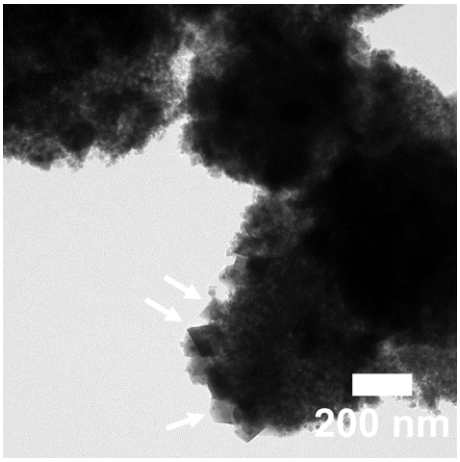

Figure 4.21 TEM image for $CoCr_2O_4$ 8 h after durability test. The white arrow points to the sintered Co_3O_4 particles.

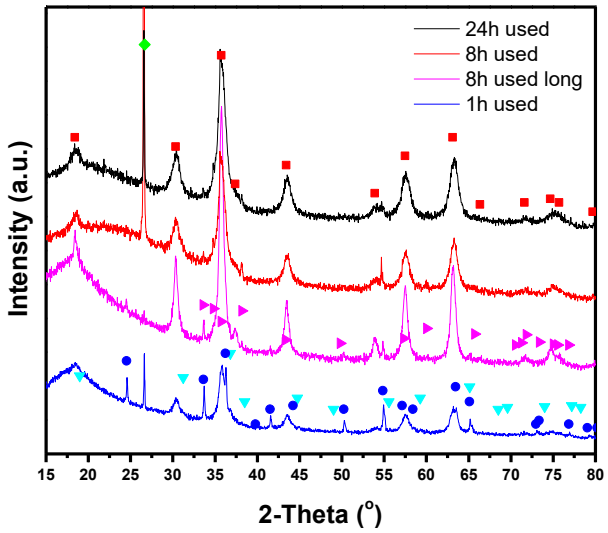

Figure 4.22 PXRD patterns for used $CoCr_2O_4$ catalysts. (■) Cochromite, syn – $CoCr_2O_4$ (JCPDS 22-1084). (▼) Spinel, syn – $Co_{2.74}O_4$ (JCPDS 78-5614). (●) Eskolaite, syn – Cr_2O_3 (JCPDS 38-1479). (♦) Quartz, syn – SiO_2 (JCPDS 79-1910). (►) Moissanite 4H – SiC (JCPDS 72-4532).

4.3.4 Kinetic studies of different catalysts

For comparison, we synthesized Co_3O_4 and Cr_2O_3 using the same hydrothermal method and $CoCr_2O_4$ by the co-precipitation method using different precipitation agents (NH_4OH and NaOH). The catalytic performances of the materials are compared (Figure 4.23), and the activities for the catalysts are as follows: $CoCr_2O_{4\ 8h} \approx CoCr_2O_{4\ Control\text{-}24h} > Co_3O_4 > CoCr_2O_{4\ NH4OH} > Cr_2O_3 > CoCr_2O_{4\ NaOH}$. We calculated apparent activation energies (E_a) based on Arrhenius plots for methane oxidation (Appendix B.1). As shown in Figure 4.23(b), Co_3O_4 has the lowest activation energy (E_a = 46.5 kJ/mol), and Cr_2O_3 has the highest among the tested catalysts. Addition of cobalt into chromium oxide to give $CoCr_2O_4$ catalysts lowers the methane activation barrier compared with pure Cr_2O_3. However, $CoCr_2O_{4\ 8h}$ and $CoCr_2O_{4\ Control\text{-}24h}$ with the same excellent activities have different activation energies. $CoCr_2O_{4\ NaOH}$ has a lower activation energy but is less active than Cr_2O_3. Therefore, activation energy is not the only effect on catalytic activity.

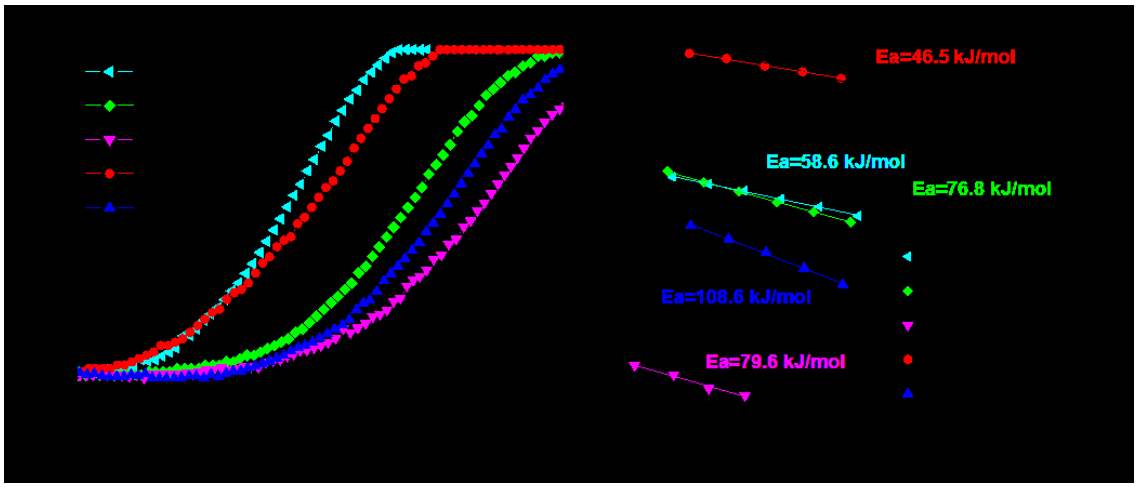

Figure 4.23 (a) TPO measurements for different catalysts. (b) Arrhenius plots of different catalysts.

CO chemisorption experiments were used to calculate the number of active sites for the catalysts, and turn-over frequency (TOF) was calculated based on the number of active sites. The catalysts with lower E_a have higher TOF (Table 4.11). This indicates that the catalysts with lower activation energy are more effective for methane combustion on a per site basis. Catalysts with more effective active sites but without enough exposed sites may not exhibit the best catalytic performance. Although Co_3O_4 is more active per site, it has fewer active sites exposed and, as a consequence, it is not as active as $CoCr_2O_{4\ 8h}$ or $CoCr_2O_{4\ Control\text{-}24h}$. Above all, both the efficiency and the number of active sites determine the final catalytic performance.

Table 4.11 Active sites, E_a, TOF and $T_{50\%}$ of catalysts.

Catalysts	Active sites (μmol/g)	E_a (kJ/mol)	TOF at 330 °C (s^{-1})	$T_{50\%}$ (°C)
$CoCr_2O_4$ 8h	27.3	71.5	0.0090	396
$CoCr_2O_4$ Control-24h	23.1	58.6	0.0101	396
$CoCr_2O_4$ NH4OH	8.8	76.8	0.0077	484
$CoCr_2O_4$ NaOH	7.8	79.6	0.0041	537
Co_3O_4	8.9	46.9	0.0348	415
Cr_2O_3	22.0	108.6	0.0010	510

4.3.5 Catalytic mechanism for methane oxidation

To better understand the catalytic mechanism, the reducibility and chemical states of the catalysts were investigated. The reducibility was measured by H_2-TPR (temperature-programmed reduction). The H_2-TPR profile of Co_3O_4 shows two reduction peaks (Figure 4.24), which indicated reduction of Co^{3+} to Co^{2+} and Co^{2+} to Co^0. Cr_2O_3 exhibits a peak at ~ 212 °C that is ascribed to the reduction of Cr^{6+} to Cr^{3+}. However, the initial reduction temperatures for $CoCr_2O_4$ samples, even those prepared by different methods, are lower than for Co_3O_4 or Cr_2O_3. According to a previous study,[128] due to the equilibrium $Cr^{6+} + 3Co^{2+} \leftrightarrow Cr^{3+} + 3Co^{3+}$, the reducibility of Cr^{6+} and Co^{3+} may be further improved. The lower reduction temperature may indicate higher oxygen mobility. Therefore, the lower reduction temperature is attributed to the synergistic effect of Cr^{6+} and Co^{3+}, and surface oxygen species. Catalysts consuming more H_2 at lower temperature indicates higher reducibility. As summarized in Table 4.12, the relative reducibility of the different catalysts is $CoCr_2O_4$ Control-24h > $CoCr_2O_4$ 8h > $CoCr_2O_4$ NH4OH > $CoCr_2O_4$ NaOH. The H_2-TPR for $CoCr_2O_4$ precipitated by NH_4OH or NaOH shows peaks from 250 to 400 °C. For $CoCr_2O_4$ prepared by the solvothermal method, the peaks from 250 to 400 °C are very weak. This indicates that the combination of Co and Cr in $CoCr_2O_4$ prepared by the solvothermal method is better than the co-precipitation method. Above all, the spinel $CoCr_2O_4$ catalysts prepared by the solvothermal

method improved the interaction between Co and Cr elements, which further enhanced the reducibility at low temperature.

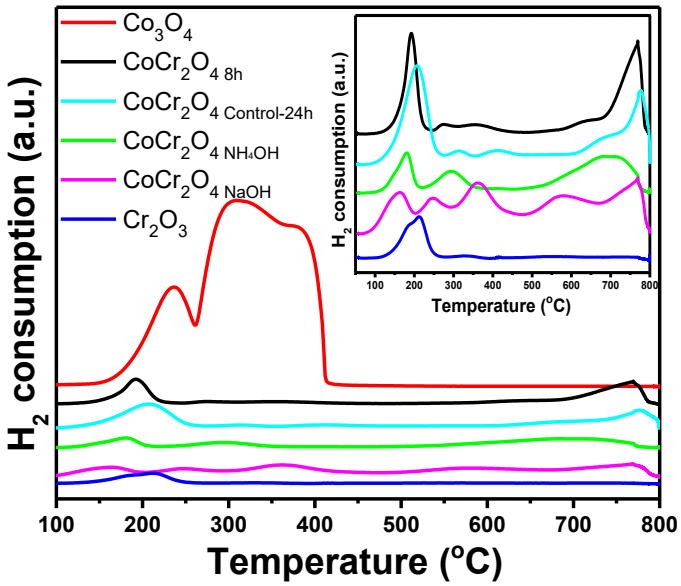

Figure 4.24 H_2-TPR profiles of different catalysts, the inset shows enlarged H_2-TPR profiles for different $CoCr_2O_4$ and Cr_2O_3 catalysts.

Previous reports indicated that oxidative reactions over Co_3O_4 follow a redox cycle of $Co^{3+} \leftrightarrow Co^{2+}$,[140] and the rate-determining step of C-H dissociation accompanies metal oxide reduction.[141] Therefore, easily-reduced oxide catalysts contribute to the initial high activity for low temperature methane oxidation. As shown in Figure 4.24, for pure Co_3O_4, the reduction of Co^{3+} consumed a lot of H_2 at low temperature, which indicates that the Co^{3+} can be easily reduced. Thus, Co^{3+} ions are considered to play an important role during methane oxidation. However, the easy reduction may lead to a higher mobility of cobalt ions, which results in agglomeration and poor stability. This explains the phenomenon that after long-term stability tests, Co_3O_4 crystals appear on the surface and Cr_2O_3 is sintered within the $CoCr_2O_4$ catalysts. The synergistic effect of

chromium and cobalt in the spinel structure improves the reducibility and stability of the catalysts. The presence of Cr^{6+} may cause the $CoCr_2O_4$ to have more defects exposed on the surface of catalysts. This is expected to improve the oxygen chemisorption and contribute to catalytic methane combustion. Most importantly, the catalysts with better reducibility exhibit higher TOF for low temperature methane combustion (Table 4.12), which is in agreement with the proposed mechanism.

Table 4.12 H_2 consumption determined by H_2-TPR.

$CoCr_2O_4$	H_2 consumption T<250 °C (mmol/g (reduction temperature (°C)))	TOF (s^{-1})
$CoCr_2O_4$ 8h	0.39 (192)	0.0090
$CoCr_2O_4$ Control-24h	0.42 (207)	0.0101
$CoCr_2O_4$ NH4OH	0.16 (180)	0.0077
$CoCr_2O_4$ NaOH	0.12 (171)	0.0041
Co_3O_4	0.62 (233)	0.0348
Cr_2O_3	0.18 (212)	0.0010

After dissociation of the C-H bonds, oxygen mobility contributes to further oxidizing intermediates to eventually yield CO_2 and H_2O. Oxygen mobility was assessed using O_2-TPD. $CoCr_2O_4$ catalysts exhibit lower O_2 desorption temperature compared with pure metal oxide (Figure 4.25). This indicates improved oxygen mobility after incorporation of Cr into the spinel cobalt oxide structure which is in agreement with the H_2-TPR results. The poor oxygen mobility for Co_3O_4 explains why there is lower methane oxidation activity compared to $CoCr_2O_4$, after initiation of the reaction.

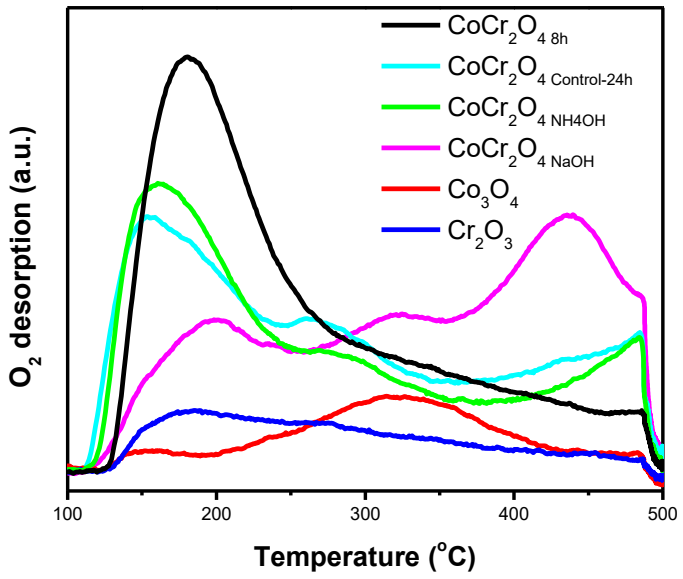

Figure 4.25 O_2-TPD profiles of different catalysts.

XPS spectra were collected to investigate the surface chemical state and composition. Given the large differences in catalytic activity for pure Co_3O_4 and Cr_2O_3 catalysts, the surface Co/Cr ratio may play an important role in catalysis. Also, the presence of easily reduced Co^{3+}, Cr^{6+} and adsorbed oxygen improves the catalytic methane oxidation and Co_3O_4 exhibits the lowest activation energy, while Cr_2O_3 shows the highest activation energy. For $CoCr_2O_4$ catalysts, **Control-24h** has more exposed Co^{3+} compared with 8h and NH_4OH samples, so it has lower E_a (Table 4.13). $CoCr_2O_{4\ NaOH}$ has a higher Co ratio on the surface but much higher lattice O ratio, therefore, it still has higher E_a than **Control-24h**. Combined with the number of active sites, we observe that the catalysts synthesized with the same method, where the surface has more Co exposed, has a lower number of active sites. Importantly, for the $CoCr_2O_4$ 8h catalyst, the synergistic effect of Cr^{6+} and Co^{3+} improved the reducibility and gave the appropriate surface Co/Cr ratio to expose more active sites that contribute to the final catalytic conversion.

Table 4.13 XPS data summary of different catalysts

$CoCr_2O_4$	Co^{3+}/Co_{total}	Cr^{6+}/Cr_{total}	O_{latt}/O_{ads}	Co/Cr
$CoCr_2O_4$ 8h	0.32	0.37	0.33	0.12
$CoCr_2O_4$ Control-24h	0.68	0.22	2.5	0.34
$CoCr_2O_4$ NH4OH	0.41	0.34	0.51	0.10
$CoCr_2O_4$ NaOH	0.66	0.26	18	0.48
Co_3O_4	0.89	-	0.64	-
Cr_2O_3	-	0.29	2.5	-

In summary, spinel $CoCr_2O_4$ nanospheres were synthesized by a solvothermal method and evaluated for oxidation of methane. The structure, catalytic activity, stability and catalytic mechanism were investigated. With different solvothermal reaction times, the catalysts show different structure and catalytic performance. The new materials display very good sulfur tolerance, and the $CoCr_2O_4$ prepared with 8 h solvothermal reaction time shows the best stability in the presence of water and SO_2. Because there is no sulfate formation under SO_2 addition, $CoCr_2O_4$ is more stable than all Pd-based catalysts and many other metal oxide catalysts. Among the catalysts with excellent durability, it exhibits the best catalytic activity.

4.3.6 Characterization for $CoCr_2O_4$ catalysts coated monolith

In order to apply the new materials described above to the practical problem of LTMOX in NGV exhaust, we took the further step to develop prototype exhaust stream catalysts with the $CoCr_2O_4$ nanoparticle catalysts. This was done by coating a cordierite monolith with an array of flow-through channels for the gas stream. Catalysts were loaded onto the monolith as discussed in the experimental section. Three monoliths with different coating conditions were prepared for comparison. The dipping mixture with calcined $CoCr_2O_4$ was labeled as C, and that using $CoCr_2O_4$ precursor was labeled as NC. Then the monolith treated with the heat gun was denoted by B, and

that without the heat gun treatment was denoted by NB. The dipping agent containing colloidal Al_2O_3 was labeled with Al. According to these, three types of monoliths were labeled as CBAl, NCBAl and NCNBAl monolith. The pure cordierite monolith with 1 inch in length and 24 cells is about 0.35 g. After coating, it was found that CBAl and NCBAl monolith could obtain 0.20 g catalysts loading, while NCNBAl monolith could only achieve 0.08 g coating. It was noted that the catalyst coating on the NCNBAl monolith was not well-bonded and it fell off easily by shaking the monolith. These monoliths were cut to observe the catalyst coating in detail. As shown in Figure 4.26, the coating on the NCNBAl monolith was loose and distributed mostly on the outside wall of the monolith with very little coated inside the channels. On the other hand, the revised method used to give monoliths NCBA1 and CBA1 gave uniform coatings on both the outside wall and inside the channels of the monolith as shown in Figure 4.27 and 4.28.

Figure 4.26 Photographs of NCNBAl monolith with 0.08 g catalysts coating: a. outside, b. inside, c. top view. Scale bar 1 cm.

Figure 4.27 Photographs of NCBAl monolith with 0.20 g catalysts coating: a. outside, b. inside, c. top view. Scale bar 1 cm.

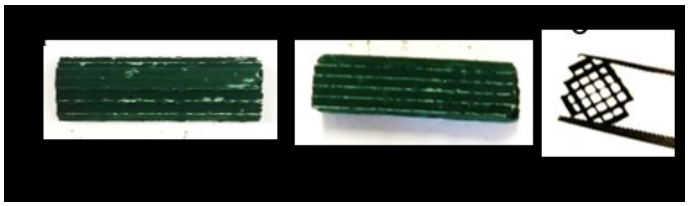

Figure 4.28 Photographs of CBAl monolith with 0.20 g catalysts coating: a. outside, b. inside, c. top view. Scale bar 1 cm.

SEM was used to further investigate the quality of the catalyst coating. As shown in Figure 4.29, the coating layer on the NCNBAl monolith has many cracks, which explains why the coating easily falls off. With the addition of a quick calcination step with a heat gun, the number of cracks decreased significantly for NCBAl monolith as shown in Figure 4.30. According to TGA results (Figure 4.31), the weight for $CoCr_2O_4$ precursor declined about 35% during calcination and the Al_2O_3 lost about 5 wt.%. The weight loss was due to the decomposition of organic ligands to CO_2 and H_2O and evaporation of solvent. We propose that the cracks result from weight loss during the calcination process. Therefore, we applied the calcined $CoCr_2O_4$ catalysts instead of $CoCr_2O_4$ precursor to prepare a dipping suspension. Combined with a pre-calcination step, a smooth, uniform and firm coating was finally obtained for CBAl monolith. As shown in Figure 4.32, there are no cracks in the coating. The enlarged image in Figure 4.32 d shows that the coating is made from the aggregation of $CoCr_2O_4$ nanospheres. EDX mapping showing good homogeneity across the coated monolith, which indicates that elements are evenly distributed along the monolith.

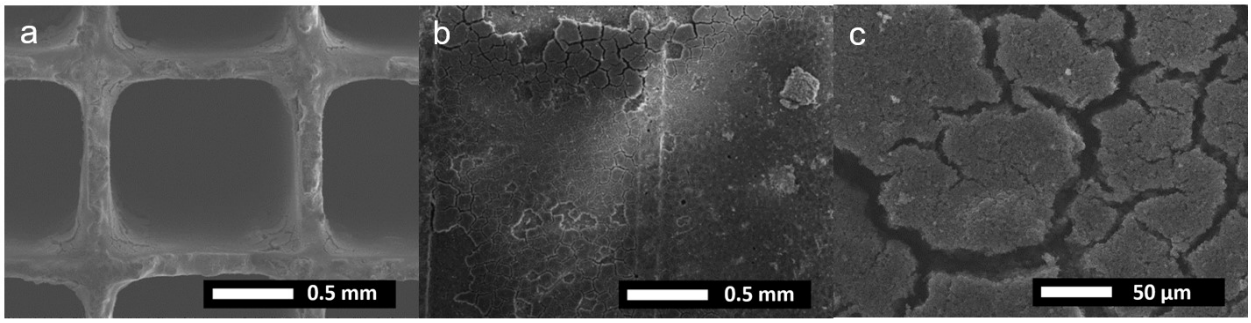

Figure 4.29 SEM images for NCNBAl monolith. a top view of monolith; b, c outside view of coated wall.

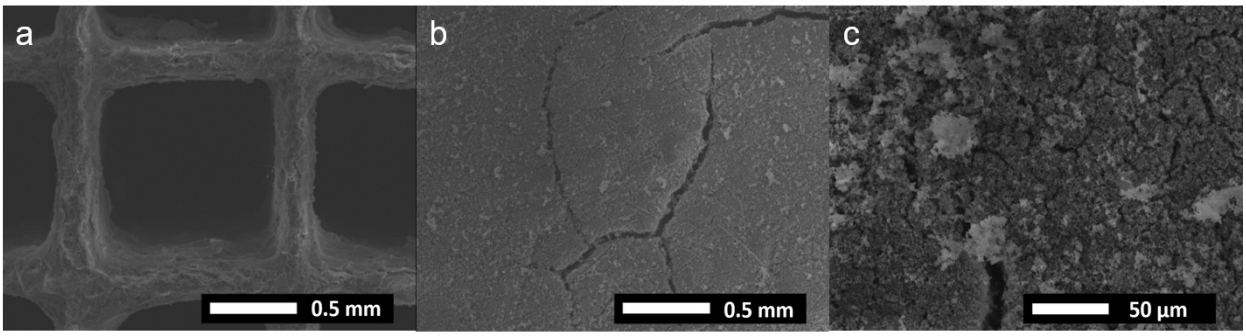

Figure 4.30 SEM images for NCBAl monolith. a top view of monolith; b, c outside view of coated wall.

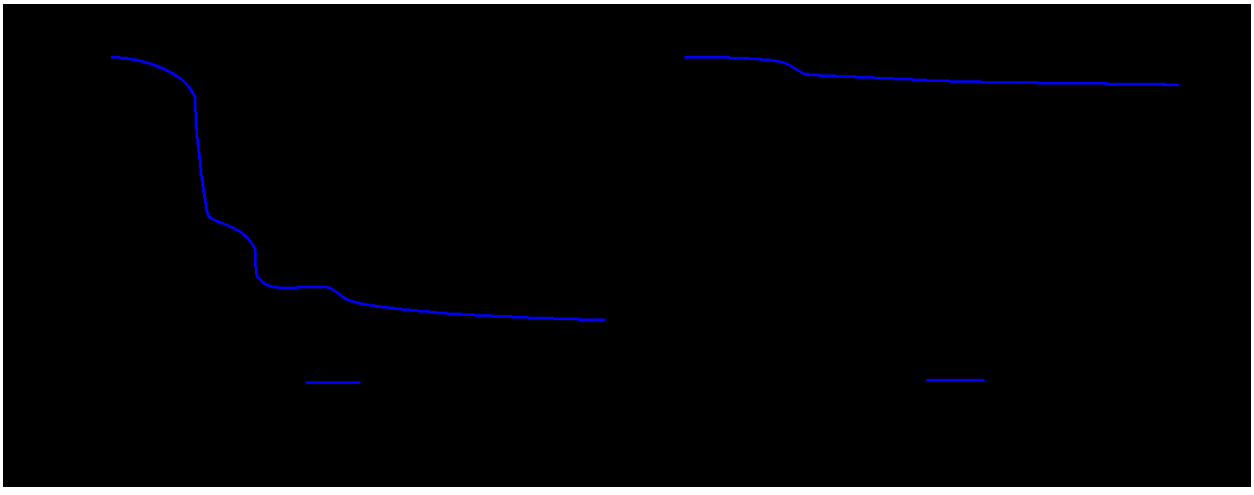

Figure 4.31 TGA for a. $CoCr_2O_4$ precursor and b. colloidal Al_2O_3 under N_2 with temperatures varied from 100 to 800 °C at a heating rate of 10 °C/min.

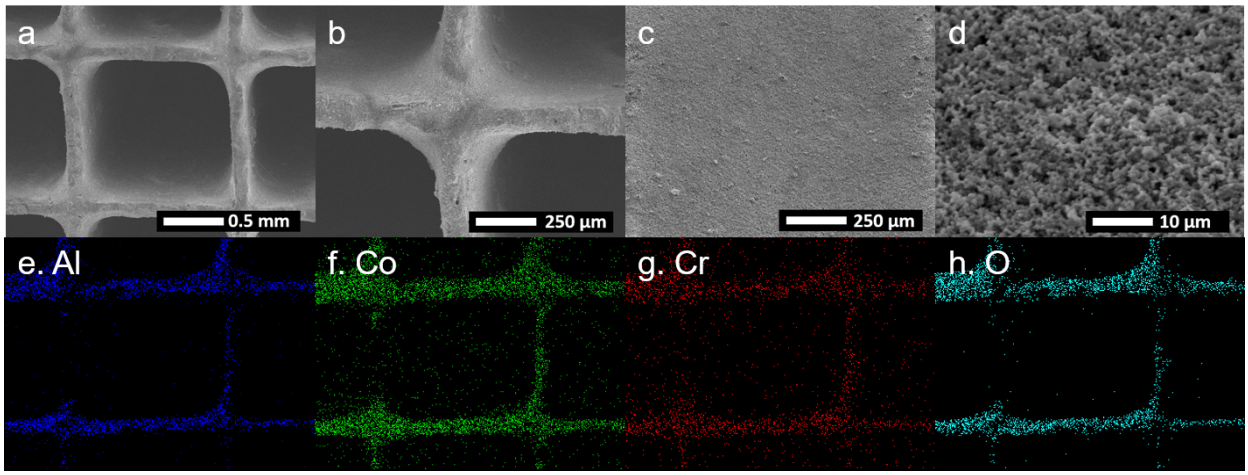

Figure 4.32 SEM and elemental mapping for coated monolith. a, b top view of monolith; c, d outside view of coated wall; EDX mapping of different elements: e. Al, f. Co, g. Cr, h. O.

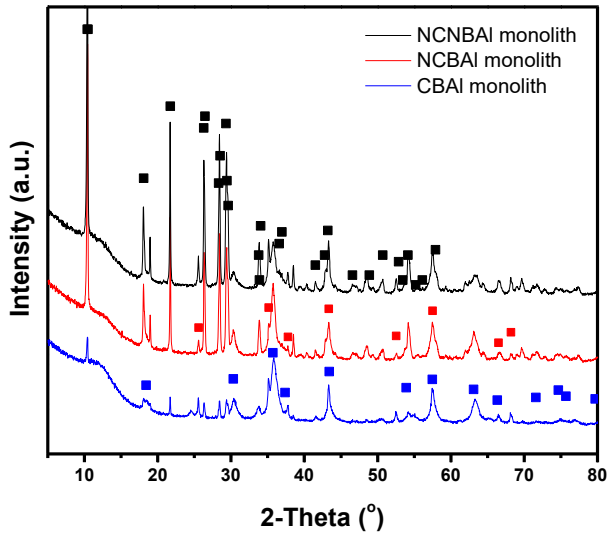

Figure 4.33 PXRD patterns of coated monolith. (■) Cordierite, syn – $Mg_2Al_4Si_5O_{18}$ (JCPDS 75-8484), (■) Corundum, syn – Al_2O_3 (JCPDS 70-5679), (■) Cochromite, syn – $CoCr_2O_4$ (JCPDS 22-1084).

PXRD patterns were measured to investigate the crystallinity of the catalyst coating on different monoliths. It was found that NCNBAl monolith with low catalyst loading and large cracks exhibited higher intensity of cordierite phase due to the exposure of bare monolith (Figure

4.33). For the NCBAl monolith with higher catalyst loading, the intensity of spinel $CoCr_2O_4$ and Al_2O_3 increased significantly. The PXRD pattern of the CBAl monolith showed even more spinel $CoCr_2O_4$ and less cordierite phase due to the uniform coating.

4.3.7 Catalytic methane combustion performance for coated monolith

Methane combustion activity was investigated for the coated monoliths via temperature-programmed oxidation. As compared in Figure 4.34 a, the CBAl monolith exhibited the best catalytic activity, with 100% conversion at ~480 °C. On the other hand, the other two types of coated monolith did not show 100% conversion below 500 °C. Therefore, we selected the CBAl monolith for further stability tests. It can be observed that, in the presence of H_2O and SO_2, the coated monolith maintains high methane conversion, which stabilizes at 88% after 4 cycles (~ 50 h). Compared with powder $CoCr_2O_4$ catalysts, the CBAl monolith shows decreased catalytic activity, which may be because the macroporous structure of the monolith decreases the interaction between catalysts and reagents. Nevertheless, it shows excellent catalytic stability under H_2O and SO_2 treatment.

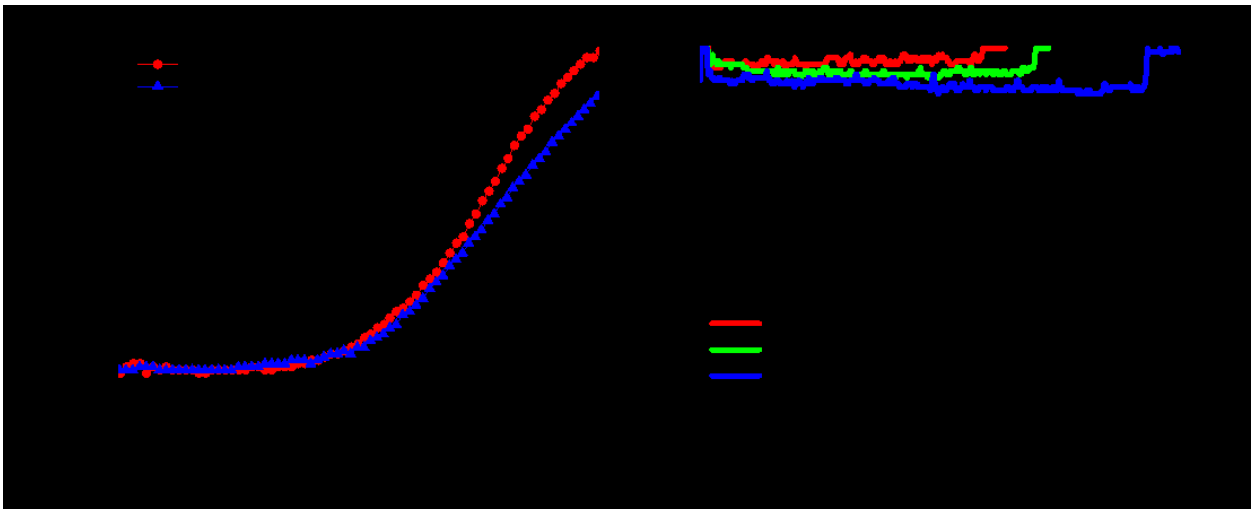

Figure 4.34 TPO and stability results of coated monolith: a. the gas mixture contains 1000 ppm CH_4, 10% O_2, and the flow rate was 300 mL/min; b. 10% H_2O and 5 ppm SO_2 were injected into the dry gas feed at the beginning and removed after 10 to 18 hours for CBAl monolith.

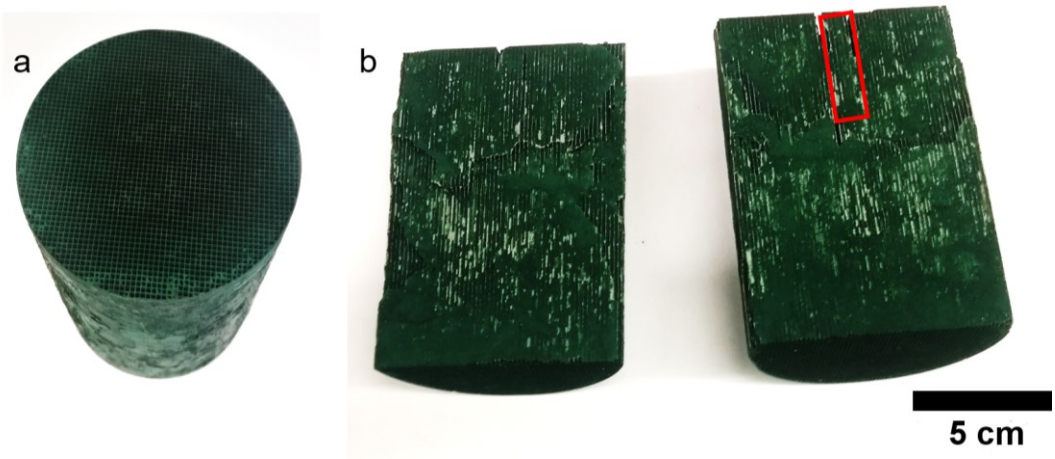

Figure 4.35 Photographs for coated big monolith (400 cpsi, 11 cm in height, 7.6 cm in diameter) a. outside and b. cross-section of big monolith. The small monolith cut for testing was at the position highlighted by red rectangle in b.

Furthermore, this monolith coating method can be scaled up. As shown in Figure 4.35, the big monolith (~ 500 mL) was coated with 120 g of catalyst by the same method used to make

CBA1. We cut the big monolith to investigate the quality of coating. Nearly no channels were blocked from the top view, and the coating looks uniform both inside and outside monolith. We cut off a small monolith (24 cells, 1 inch in length) from top part (Figure 4.35 red rectangle) for characterization. SEM images in Figure 4.36 indicates the coating was smooth and uniform without any obvious cracks. Catalytic activity and stability were also studied.

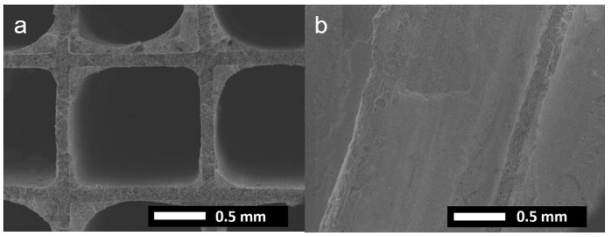

Figure 4.36 SEM images for big, coated monolith.

The monolith maintained good catalytic behavior for methane oxidation. (Figure 4.37) In the presence of 10% H_2O and 5 ppm SO_2, the coated monolith showed 90% conversion after 2 cycles (~28 hours). The developed non-noble metal $CoCr_2O_4$ catalysts and new monolith coating method have potential to solve the problem of CH_4 emission for NGVs.

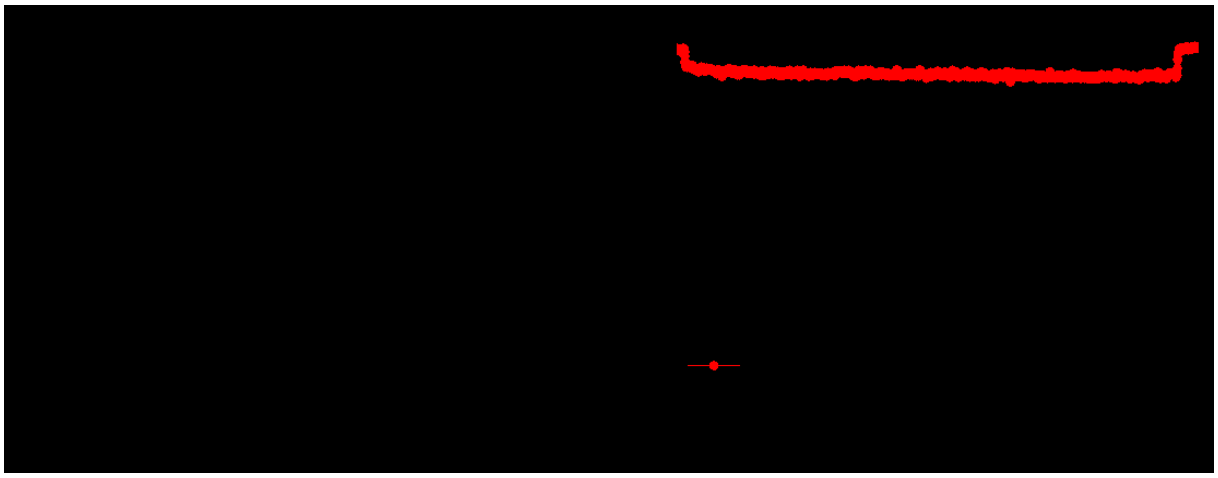

Figure 4.37 TPO and stability results of cut big monolith: a. the gas mixture contains 1000 ppm CH_4, 10% O_2, and the flow rate was 300 min/L; b. 10% H_2O and 5 ppm SO_2 were injected into the dry gas feed at the beginning and removed after 12 or 15 hours.

4.4 Conclusions

New $CoCr_2O_4$ nanospheres were synthesized by a hydrothermal method using benzyl alcohol. The catalytic performance of these noble metal-free nanospheres was optimized for oxidation of methane to CO_2 as evaluated at a high space velocity of 180,000 mL/(g·h), reaching 100% conversion below 500 °C. Importantly, samples prepared with 8 h solvothermal treatment exhibit excellent stability, maintaining 80% conversion in the presence of 10% H_2O and 5 ppm SO_2 after 10 cycles (~170 h). Furthermore, these powder samples were loaded onto a monolith by a modified wash-coating method, and they maintained excellent catalytic activity and stability. The highly stability gives these nanomaterials valuable potential for application in natural gas vehicles.

Chapter 5: MnO_2 Aerogel Supported Catalysts

5.1 Introduction

Manganese oxide exhibits good catalytic performance for oxidation reactions due to its various stable oxidation states and outstanding oxygen storage capacity.[92, 94] Recently, nanowire MnO_2 aerogels have been prepared and used in catalysis as supports for catalysts with excellent activity.[142] Aerogels are ultralight materials with a high amount of macropores.[143] The 3D network structure not only facilitates mass transfer, but also distributes the catalysts more evenly which facilitates the exposure of more active sites for reaction.[144] This unique structure makes manganese oxide an excellent support for catalyst loading for low temperature methane oxidation.

In this work, two types of nanowire MnO_2 aerogel-supported catalysts were prepared. First, MnO_2 was used as a skeletal support and mixed with other catalysts. Pd/CeO_2 prepared by the SAR method was incorporated into MnO_2 with low Pd loading. Non-noble metal mesoporous Co_3O_4 with CeO_2 or CuO was mixed with nanowire MnO_2 to increase the catalytic activity while using only inexpensive metals. Second, the negative charge on the surface of MnO_2 was used to trap Pd^{2+} and yield PdO-coated MnO_2. Furthermore, the MnO_2 nanowires were modified to obtain a concave surface and trap Pd^{2+} into these depressed regions on the surface of MnO_2.

5.2 Experimental

5.2.1 Preparation of nanowire MnO_2

Nanowire MnO_2 was prepared based on a previous report.[145] K_2SO_4 (3.485 g, 20.00 mmol) was dissolved in 36 mL water at 40 °C. $MnSO_4 \cdot H_2O$ (1.352 g, 8.000 mmol) and $(NH_4)_2S_2O_8$ (1.825 g, 8.000 mmol) was added to the solution and was stirred for 20 min. The mixture was then transferred to a Teflon container and sealed, then heated at 180 °C for 12 h. After cooling, the Teflon container was opened and the dark brown residue was transferred to a beaker and washed with deionized water until the pH of the washings was 7. The resulting MnO_2 nanowires were stored in deionized water for further use.

5.2.2 Preparation of meso Co_3O_4

Cobalt acetate (2.490 g, 10.00 mmol) was dissolved in 40 mL water with stirring at 70 °C. NaOH (0.8000 g, 20.00 mmol) was dissolved in 10 mL of water and added dropwise to the solution. The mixture was stirred for 1 h and the resulting product was then washed with water three times by centrifugation.

5.2.3 Preparation of ceria and copper oxide doped meso Co_3O_4

The synthesis of ceria and copper oxide doped meso Co_3O_4 was done by a similar procedure to that described in Section 5.2.2, except that cerium acetate or copper acetate was added together with cobalt acetate and the amount of NaOH was increased. Typically, for the preparation of CuO (5 wt%) CeO_2 (20 wt%) on Co_3O_4, 2.490 g (10.00 mmol) cobalt acetate, 1.183 g (3.729 mmol) cerium acetate, and 0.323 g (1.778 mmol) copper acetate were dissolved in 40 mL water

and heated to 70 °C. 1.400 g (35.00 mmol) NaOH dissolved in 10 mL water was added dropwise to the above mixture and stirred for 1 h. The product was washed with water by centrifugation.

5.2.4 Preparation of nanowire MnO_2 aerogel supported Co_3O_4 based catalysts

0.6081 g nanowires MnO_2 obtained from Section 5.2.1 was stirred with 1.403 g doped meso Co_3O_4 catalysts acquired from Section 5.2.3 in 100 mL deionized water and centrifuged, washed with water three times (3 x 100 mL). The mixture was then frozen in liquid nitrogen and freeze dried in a Pilot-size VirTis Vitual 50 L Freeze Dryer for 1 day. After drying, the sample was calcined at 200, 350, or 550 °C for 3 h.

5.2.5 Preparation of nanowire MnO_2 aerogel supported Pd/CF catalysts

Pd/CF on nanowire MnO_2 was prepared for comparison purposes. Pd/CF was synthesis according to the previous reports.[62] First, 0.8700 g (2.000 mmol) $Ce(NO_3)_3 \cdot 6\ H_2O$ was dissolved in 15 mL ethylene glycol, and then the mixture was transferred to a 23 mL Teflon-lined stainless steel autoclave and kept at 145 °C for 15 h. After that, the sample was centrifuged with ethanol three times and dried in an oven at 65 °C for 12 h. $Pd(NO_3)_2$ (0.0043 g, 0.0187 mmol) was dissolved in 20 mL water with stirring, followed by addition of 0.3130 g (1.140 mmol) cerium formate, and then stirred for 24 h. The product was collected by centrifugation with water. Finally, the Pd/CF was mixed with 0.1986 g nanowire MnO_2 and centrifuged and washed with water for three times. The product was dried using a freeze drier and calcined at 400 °C for 3 h.

5.2.6 Preparation of nanowire MnO_2 aerogel supported PdO catalysts

$Pd(NO_3)_2$ (0.0301 g, 0.1306 mmol) was dissolved in 35 mL H_2O. 0.1 M NaOH aqueous solution was added dropwise into the Pd^{2+} solution to adjust the pH to 10 by adding aqueous 0.1 M NaOH solution dropwise. MnO_2 nanowires (0.4474 g, 5.146 mmol) were added to the mixture, and the pH was readjusted to 10 with addition of more 0.1 M NaOH. After stirring the mixture at 65 °C for 5 h, the precursor was collected by centrifugation, freeze dried, and calcined at 400 °C for 3 h.

5.2.7 Preparation of modified nanowire MnO_2 support PdO catalysts

MnO_2 nanowires (0.4000 g, 4.601 mmol) were dissolved in a solution of 60 mL ethanol, 12 mL conc. ammonium hydroxide and 20 mL or water. TEOS (0.6 mL, 2.687 mmol) was then added into the mixture with vigorous stirring. After continuous stirring for 1 h, the precipitate was collected by centrifugation and freeze dried to obtain silica-coated MnO_2. The sample was subsequently calcined in a tube furnace under air at 500 °C for 3 h. After cooling, the sample was calcined under 10% H_2 (balanced with Ar) for 5 h. The protective shell of SiO_2 was then removed by dispersing MnO_2 @ SiO_2 (0.1543 g) in aqueous base (prepared by dissolving 1.14 g of NaOH in 20 mL H_2O) with stirring for 30 min. The product was collected by centrifugation and washed with water until the washings were neutral. Finally, the sample was placed in a furnace and calcined at 500 °C under air for another 3 h. PdO was loaded using the same method described in Section 5.2.6.

5.2.8 Characterization

PXRD pattern was obtained by Bruker D8-Advance with Cu Kα radiation at 40 kV and 40 mA. SEM images were acquired on Hitachi S-4700 Field Emission SEM at 20 kV, and TEM images were collected on Hitachi H7600 TEM at 80 kV. HRTEM measurement was carried out on a FEI Tecnai G2 Twin TEM at 200 kV. EDX data were achieved via Hitachi S-2600 Variable Pressure SEM with an X-ray detector. For zeta potential measurements, the sample was dissolved in deionized water to get 0.01 M aqueous solution and measured by NanoBrook Omni (DLS/Zeta). N_2 adsorption was carried out using a Micromeritics Accelerated Surface Area & Porosity (ASAP) 2020 system to obtain surface area, pore size and pore volume.

5.3 Results and Discussion

5.3.1 Synthesis of aerogel MnO_2 nanowires support

Nanowire MnO_2 was prepared by a hydrothermal method. During freeze-drying, the aerogel MnO_2 was shaped by the container. As shown in Figure 5.1, after removing water, a cylindrical MnO_2 aerogel monolith was obtained. The diffraction peaks acquired by PXRD analysis (Figure 5.2) matched the standard α-MnO_2. The morphology was characterized by SEM and TEM, and the data are shown in Figure 5.3. The MnO_2 nanowires have diameters of about 20 to 30 nm, and their length is about 2 to 5 μm. The free-standing, 3D monolithic structure was formed due to the intertwined MnO_2 nanowires. As shown in Figure 5.3a, macropores are clearly evident in the material. This porous structure leads to the formation of a lightweight aerogel, which has excellent potential to serve as a catalyst support. The surface of the MnO_2 is negatively charged as determined by zeta potential analysis; this is beneficial for loading positively charged precursors onto the nanowire surface.

Figure 5.1 Photograph of MnO_2 aerogel after freeze-drying.

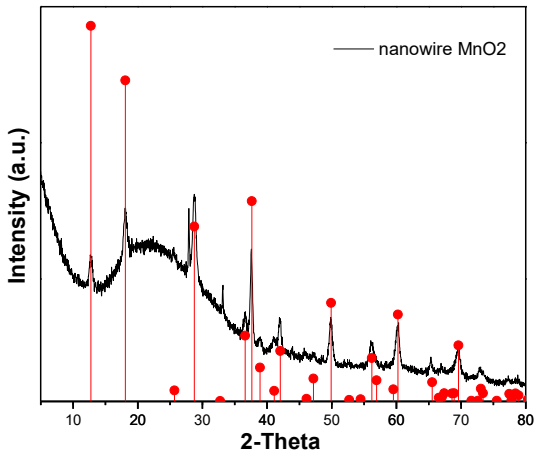

Figure 5.2 PXRD pattern for nanowire MnO_2. Standard peak: manganese oxide α-MnO_2 (JCPDS 72-1982).

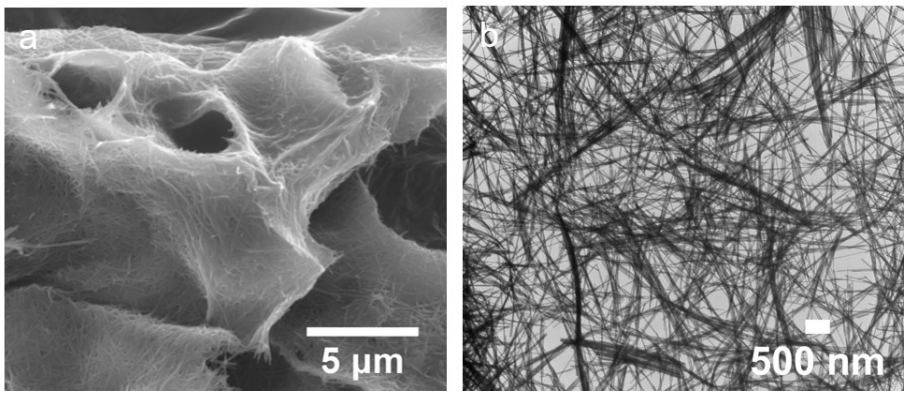

Figure 5.3 a. SEM and b. TEM images for nanowire MnO_2.

5.3.2 Synthesis of MnO_2 supported catalysts without interaction with active sites

After mixing and calcining with mesoporous Co_3O_4 based catalysts, nanowire MnO_2 supported catalyst aerogels were formed. For ceria or copper oxide-doped mesoporous Co_3O_4, the temperature plays an important role in the mesoporous structure. Different calcination temperature results in different pore size and surface area. The pores may expose different facets of Co_3O_4 and a different number of defects, which are crucial for low-temperature methane oxidation. Moreover, different types of metal oxide exhibit different reducibility and oxygen storage capability, which contributes to the catalytic activity. Therefore, we investigated different calcination temperatures

and different ceria and copper oxide loadings on mesoporous Co_3O_4/MnO_2 to develop active catalysts. MnO_2 aerogel supported Pd/CF was prepared as a control for comparison of the catalytic activity for methane combustion.

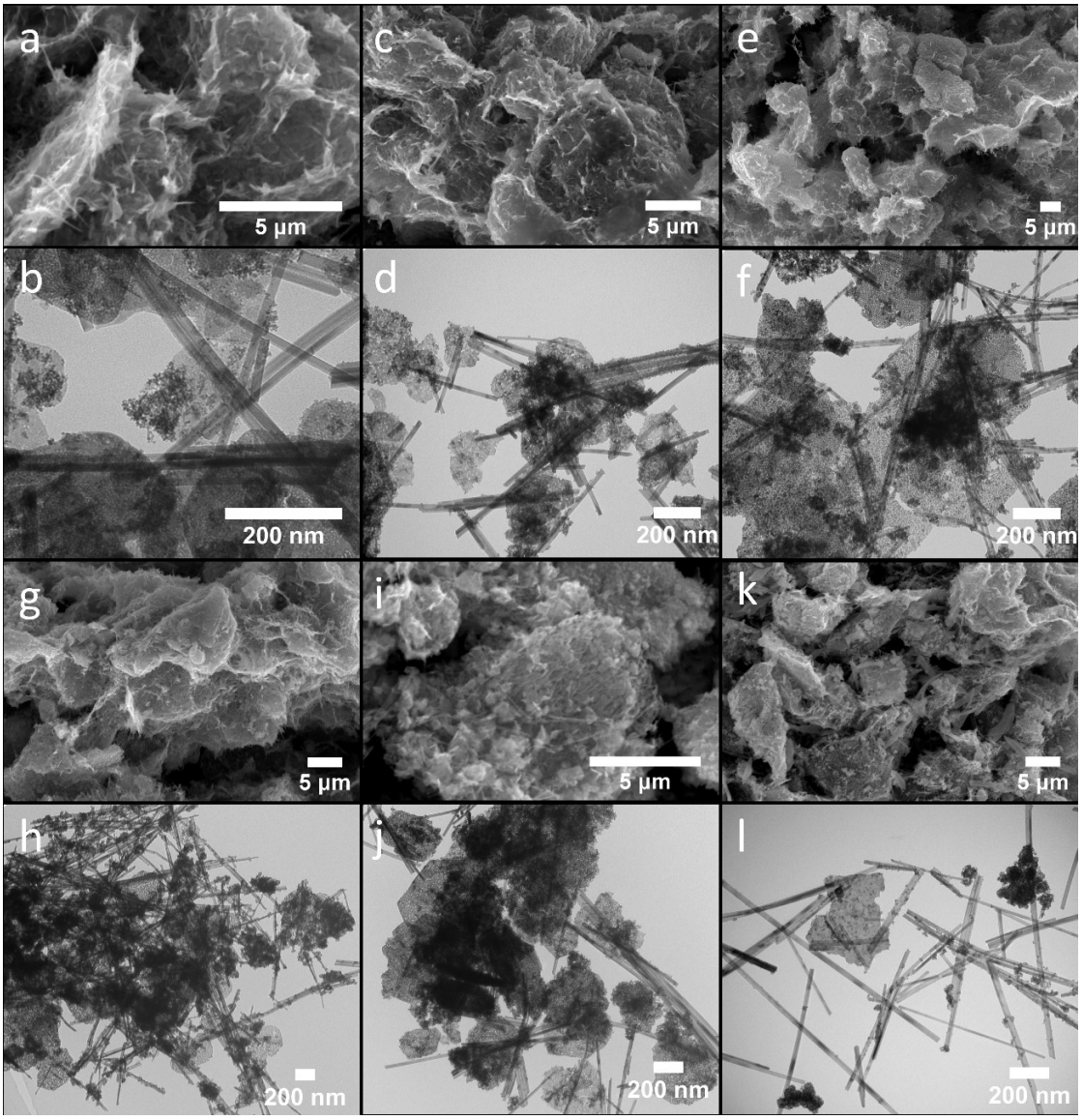

Figure 5.4 TEM and SEM images for MnO_2 supported catalysts: a, b are CeO_2 10 wt% Co_3O_4 on MnO_2 (calcined 200 °C); c, d are CeO_2 10 wt% Co_3O_4 on MnO_2 (calcined 350 °C); e, f are CeO_2 20 wt% Co_3O_4 on MnO_2 (calcined 200 °C); g, h are CeO_2 20 wt% Co_3O_4 on MnO_2 (calcined 350 °C); i, j are CuO 5 wt% CeO_2 20 wt% Co_3O_4 on MnO_2 (calcined 350 °C); k, l are Pd/CF on MnO_2 (calcined 400 °C).

SEM and TEM images of ceria-doped mesoporous Co_3O_4 / MnO_2 nanowires showed that Co_3O_4 nanosheets are distributed evenly in the nanowire MnO_2 framework (Figure 5.4). From TEM images, it can be observed that for Co_3O_4 / MnO_2 nanowires calcined at 200 °C, the pore size in the Co_3O_4 nanosheets was below 1.5 nm. On the other hand, the pores of the material calcined at 350 °C were enlarged to 4-5 nm in diameter. Thus, the pore size of Co_3O_4 nanosheets was significantly influenced by calcination temperature, with higher calcination temperatures leading to larger pores. According to TEM images, small CeO_2 particles (about 2-5 nm) were deposited on either Co_3O_4 nanosheets or MnO_2 nanowires; the size of the CeO_2 particles is nearly independent of calcination temperature. The surface areas of samples are tabulated in Table 5.1. It is apparent that the surface area increases with greater ceria loading. The smaller size of ceria nanoparticles likely contributes to higher surface area. Moreover, the surface area also increased with elevated calcination temperature, possibly due to the increased pore size and pore volume. These N_2 adsorption results are in agreement with TEM analysis.

Table 5.1 Surface area for ceria doped Co_3O_4 on MnO_2

Sample	Surface area (m^2/g)
CeO_2 10wt% Co_3O_4 on MnO_2 (200)	88
CeO_2 10wt% Co_3O_4 on MnO_2 (350)	90
CeO_2 20wt% Co_3O_4 on MnO_2 (200)	93
CeO_2 20wt% Co_3O_4 on MnO_2 (350)	113

The PXRD pattern of the cobalt hydroxide precursor calcined at 200 °C shown in Figure 5.5 matches the pattern for CoO(OH). When calcined at 350 °C, Co_3O_4 was formed and matches the diffraction pattern of $Co_{2.77}O_4$. This indicated that for this material, the ratio of Co^{3+}/Co^{2+} was increased compared with that in Co_3O_4. The increased ratio of higher oxidation state Co^{3+} ions

may have an effect on the catalytic activity. On the other hand, no peak was observed for the crystalline phase of CeO_2 due to either smaller particle size (< 7 nm) or an amorphous structure.

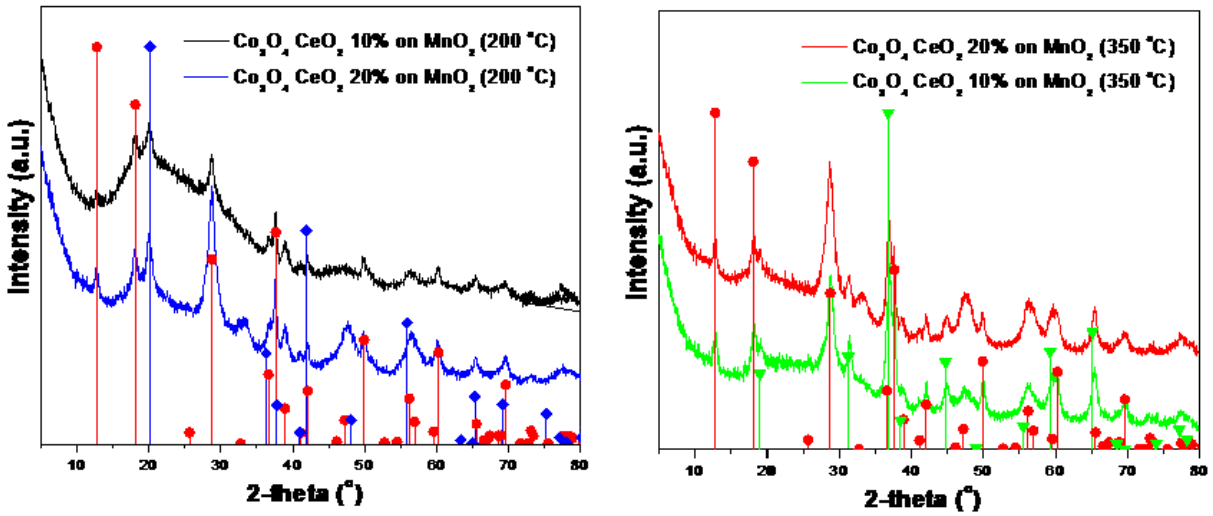

Figure 5.5 PXRD patterns for ceria doped mesoporous cobalt oxide on nanowire MnO_2. Standard peaks: red peaks are manganese oxide, α-MnO_2 (JCPDS 72-1982), blue peaks are cobalt oxide hydroxide, CoO(OH) (JCPDS 71-5039), green peaks are: cobalt oxide spinel, syn $Co_{2.77}O_4$ (JCPDS 78-5617).

Table 5.2 EDX data for MnO_2 aerogel supported catalysts.

Sample	Co wt%	Ce wt%	Mn wt%	O wt%	Cu wt%	Pd wt%
Co_3O_4 CeO_2 10% on MnO_2 (200 °C)	43.1	12.8	22.6	21.5	-	-
Co_3O_4 CeO_2 10% on MnO_2 (350 °C)	44.1	11.6	25.8	18.4	-	-
Co_3O_4 CeO_2 20% on MnO_2 (200 °C)	34.5	21.3	20.9	23.3	-	-
Co_3O_4 CeO_2 20% on MnO_2 (350 °C)	34.6	22.0	21.0	22.4	-	-
Co_3O_4 CeO_2 20% CuO 5% on MnO_2 (350 °C)	36.1	25.2	16.1	14.3	7.2	-
Pd/CF on MnO_2 (400 °C)	-	51.5	33.1	12.7	-	0.4

The ratio of different elements in the catalysts was determined by EDX (Table 5.2). The composition is similar to the theoretical loading based on the starting materials. The deviation was

below 3 wt% except for the sample of Co_3O_4 CeO_2 20% CuO 5% on MnO_2 calcined at 350 °C, where the deviation of Ce wt% was 5.2 wt%.

Methane oxidation catalytic activity was measured by temperature-programmed oxidation and the data are shown in Figure 5.6. 1000 ppm CH_4, 10 % O_2 balanced by Ar and He was flowed through the reactor to give a total flow rate of 300 mL/min. The gas hourly space velocity was 180,000 mL(STP)·g^{-1}·h^{-1}. MnO_2 supported catalysts were loaded into the reactor directly for catalytic measurement. It can be observed that 50% methane conversion was achieved for Pd/CF on MnO_2 at 350 °C, and for CuO 5 wt% CeO_2 20 wt% Co_3O_4 on MnO_2 and CeO_2 20 wt% Co_3O_4 on MnO_2 at 369 and 380 °C, respectively. The difference in $T_{50\%}$ between Pd/CF on MnO_2 and CuO 5 wt% CeO_2 20 wt% Co_3O_4 on MnO_2 was insignificant. Based on these data, we believe that by optimizing the ratio of CuO, CeO_2, Co_3O_4 and MnO_2, the same activity as Pd catalysts could potentially be achieved.

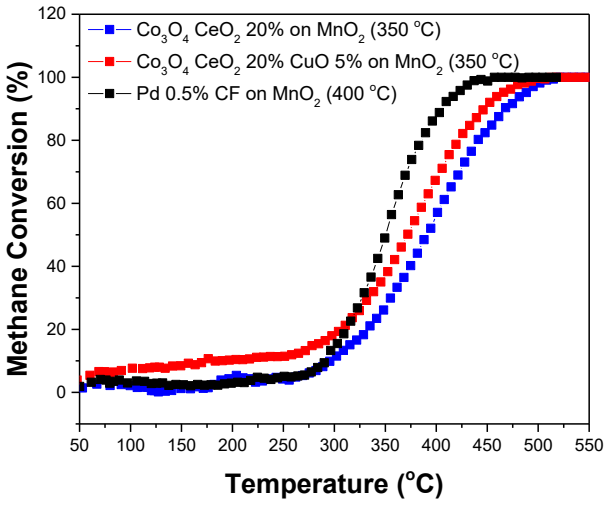

Figure 5.6 TPO curves showing the catalytic methane oxidation activity for MnO_2 aerogel supported catalysts.

5.3.3 Synthesis of MnO_2 supported catalysts (interact with active sites)

5.3.3.1 Characterization of 1 wt% PdO on MnO_2 aerogel

1 wt% PdO was loaded on the MnO_2 nanowire aerogel by the deposition-precipitation method. First, a colloidal solution of $Pd(OH)_2$ was prepared. After addition of nanowire MnO_2, the pH of the mixture decreased, possibly due to the reaction between MnO_2 and OH^-. The pH of the mixture was readjusted to 10 by dropwise addition of 0.1 M NaOH aqueous solution to ensure the precipitation of Pd^{2+} and interaction of the PdO with the MnO_2 support. After loading, washing and calcination, nanoparticles of PdO were incorporated onto the surface of MnO_2 nanowires as shown by TEM (Figure 5.7, red arrow). The PdO particle size was about 10-20 nm and EDX confirmed that the Pd loading was 1 wt%.

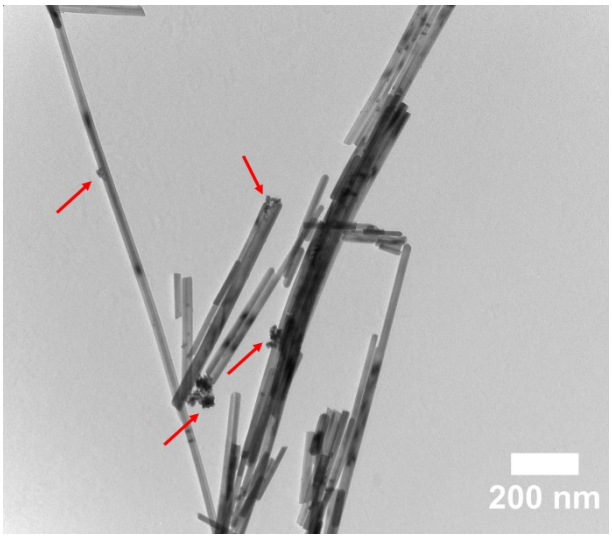

Figure 5.7 TEM image of 1 wt% PdO on MnO_2 nanowire aerogel. Red arrows point to the PdO nanoparticles.

5.3.3.2 Characterization of 1 wt% PdO on modified MnO_2 aerogel

Concave MnO_2 nanowires were prepared. The concave structure facilitates the formation of steps, kinks, and vacancies on the surface of sample and these exposed defects are beneficial for catalysis. First, the MnO_2 was covered with a silica shell to create a nano-reactor, which was used to maintain the nanowire structure. As shown in Figure 5.8, after hydrolysis of TEOS, the surface of MnO_2 was uniformly coated with a thin layer of silica with a thickness of ~ 5 nm.

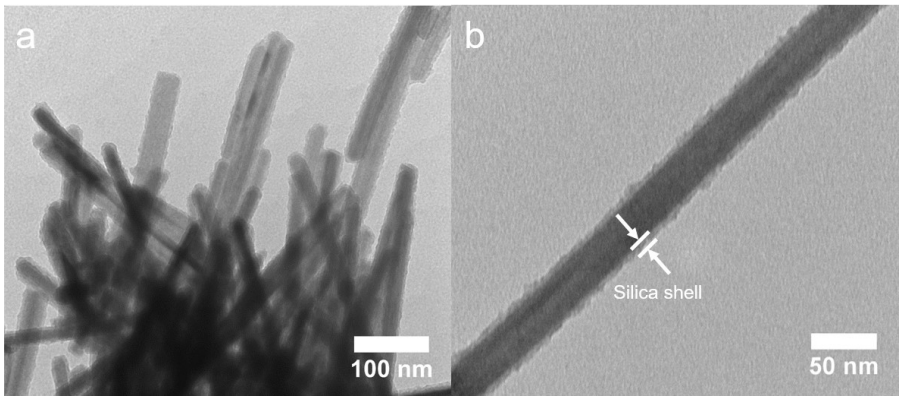

Figure 5.8 TEM images of silica-coated MnO_2 nanowires.

Calcination in air resulted in a firmly attached SiO_2 shell and removal of residual organics. MnO_2 forms a concave structure during calcination in a H_2 atmosphere. Under these reductive conditions, hydrogen reacts with oxygen to form water vapor and MnO_2 is reduced to MnO, which was confirmed by PXRD (Figure 5.11). SEM and TEM imaging of the reduced MnO_2 nanowires showed that the nanowires shrank during reduction and holes with random shapes were formed on the surface, Figure 5.9. As shown in Figure 5.9a, the surface of the MnO_2 nanowires is covered with holes that appear as dark dots in the SEM image. In the TEM images shown in Figure 5.9 b,c, the light colored parts on the nanowires are attributed to the holes. In addition, the length for part

of the nanowires decreased after H_2 treatment due to fracturing, which could be observed from both SEM and TEM images. These results show that the concave structure was successfully incorporated on the surface of MnO_2 nanowires.

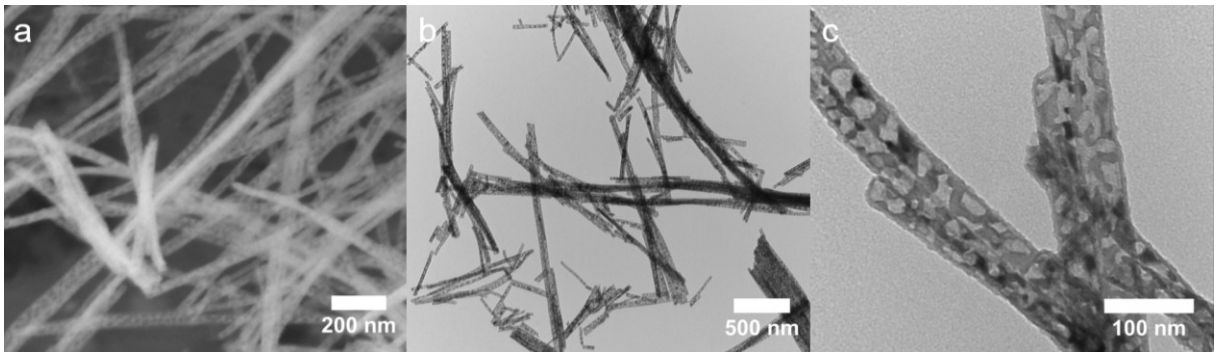

Figure 5.9 a SEM and b, c TEM images for MnO_2 @ SiO_2 reduction under H_2.

In the next step, the silica shell was removed by reaction of the reduced MnO_2 @ SiO_2 with aqueous NaOH solution, exposing the concave surface. As shown in Figure 5.10, it is clear from TEM images of the reduced MnO_2 nanowires that the silica layer was removed and the holes on the nanowire surface were exposed (red arrow). PXRD indicated that a crystalline phase transformation occurred during surface modification. As shown in Figure 5.11, the α-MnO_2 structure of the nanowires was maintained after coating them with the silica shell. No diffraction from the silica coating is evident, since the silica gel is amorphous. Under H_2 treatment, the MnO_2 is reduced to MnO. After the silica shell was removed, the MnO was not oxidized back to MnO_2 by calcination under air, but instead crystalline Mn_3O_4 is detected by PXRD. Stronger oxidizing agents like H_2O_2, which could also oxidize MnO to Mn_2O_3 were tried, but these destroyed the nanowire structure. Therefore, we used Mn_3O_4 nanowires with a concave surface as the support for PdO. As shown in Figure 5.10b, the PdO nanoparticles were loaded onto the Mn_3O_4 modified

nanowires. The distribution of PdO nanoparticles was random – they were not specifically loaded into the holes of Mn_3O_4.

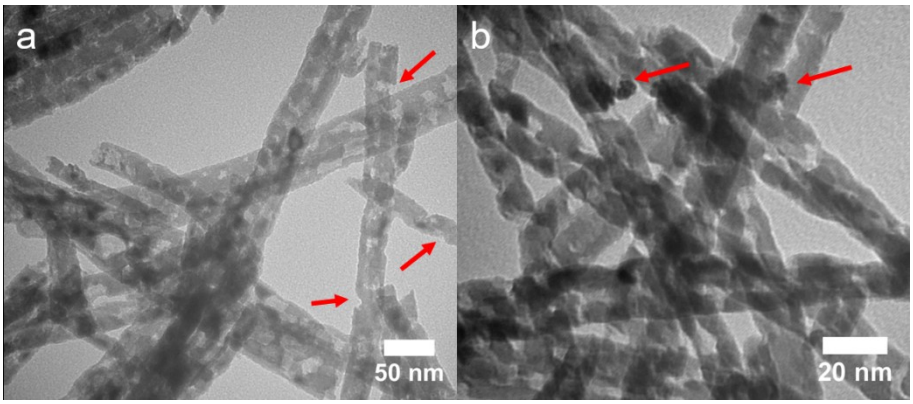

Figure 5.10 TEM images for a. MnO_2 removed SiO_2 shell, b. 1 wt% PdO loaded on surface modified MnO_2. Red arrows point to the holes on the nanowires MnO_2.

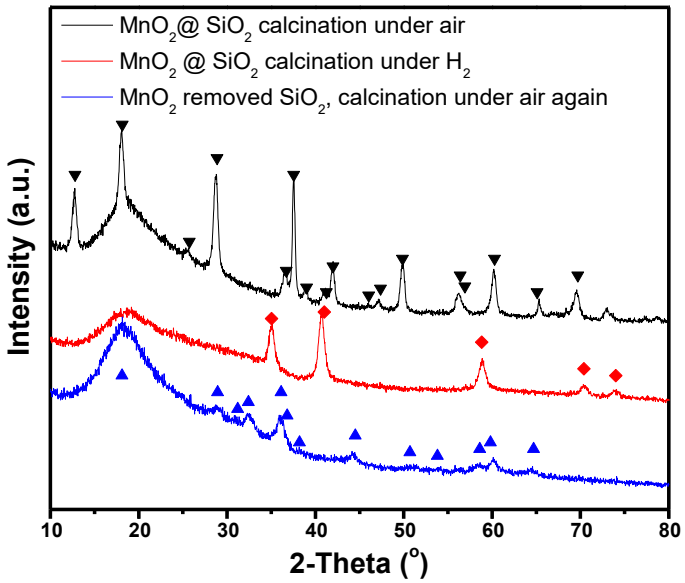

Figure 5.11 PXRD pattern for MnO_2 aerogel at different stages of the surface modification procedures. ▼ Manganese oxide, α-MnO_2 (JCPDS 72-1982), ♦ Manganosite, syn – MnO (JCPDS 75-6876), ▲ Hausmannite, syn – Mn_3O_4 (JCPDS 24-0734).

5.3.3.3 Catalytic performance of MnO_2 aerogel supported PdO.

The catalytic methane combustion performance was measured by temperature-programmed oxidation. The MnO_2 aerogel-supported PdO (0.100 g) was directly loaded into the reactor. As shown in Figure 5.12, 1 wt% PdO on MnO_2 exhibits excellent catalytic activity, giving 50% conversion at 286 °C and 100% conversion at 330 °C. However, for the 1 wt% PdO on modified MnO_2, the activity decreased significantly, giving $T_{50\%}$ at ~482 °C. After surface modification, MnO_2 was converted into Mn_3O_4, decreasing the capacity for oxygen storage and deteriorating the final activity.

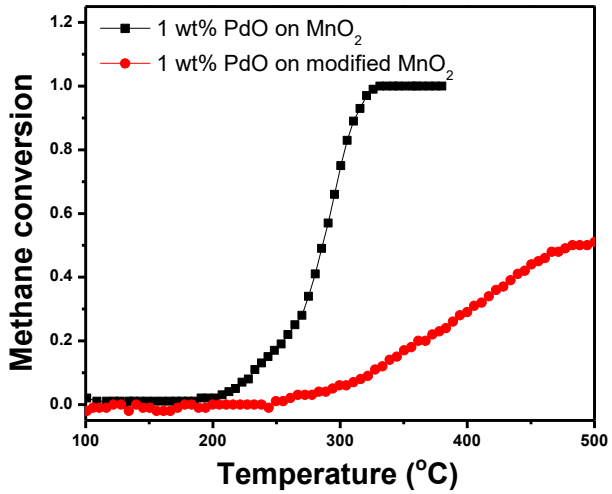

Figure 5.12 Catalytic activity for MnO_2-supported PdO catalysts.

The 1 wt% PdO on MnO_2 catalyst was selected for further hydrothermal stability and sulfur tolerance tests. For hydrothermal stability experiments, the catalyst was heated up to a given temperature (330, 350, 400 or 450 °C) under dry conditions within half an hour. After reactor reached the desired temperature and methane conversion was stable, 5% water was mixed with the feed gas and injected into the reactor. After 20 h or more, the water was cut off, and the catalysts treated under dry conditions again for another several hours to check whether or not the methane

conversion returned to previous levels. Then another TPO test was run to investigate the effect of water treatment on the catalysts. The stability results are shown in Figures 5.13 and 5.14. Because the calcination temperature of the catalysts (400 °C) is lower than the test temperature (450 °C), the structure of the catalysts may be changed during the hydrothermal stability treatment. Therefore the stability experiment was run from low to high temperature (Figure 5.13) and from high to low temperature (Figure 5.14), respectively.

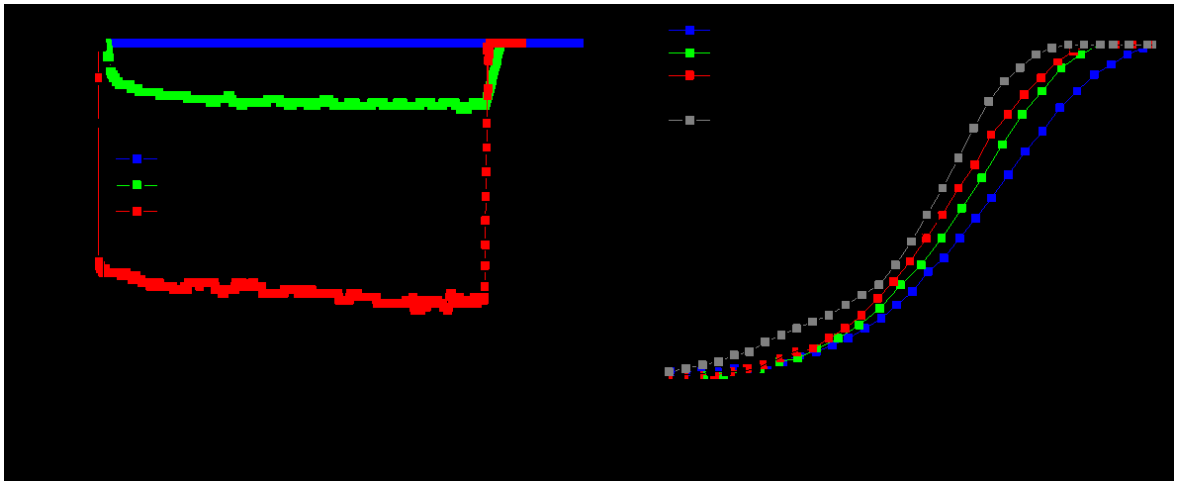

Figure 5.13 Water stability measurements at different temperature (a) and catalytic curves before/after stability test (b) for 1 wt% Pd on MnO_2. The black arrow indicated the order of measurements. The stability was tested from low to high temperature.

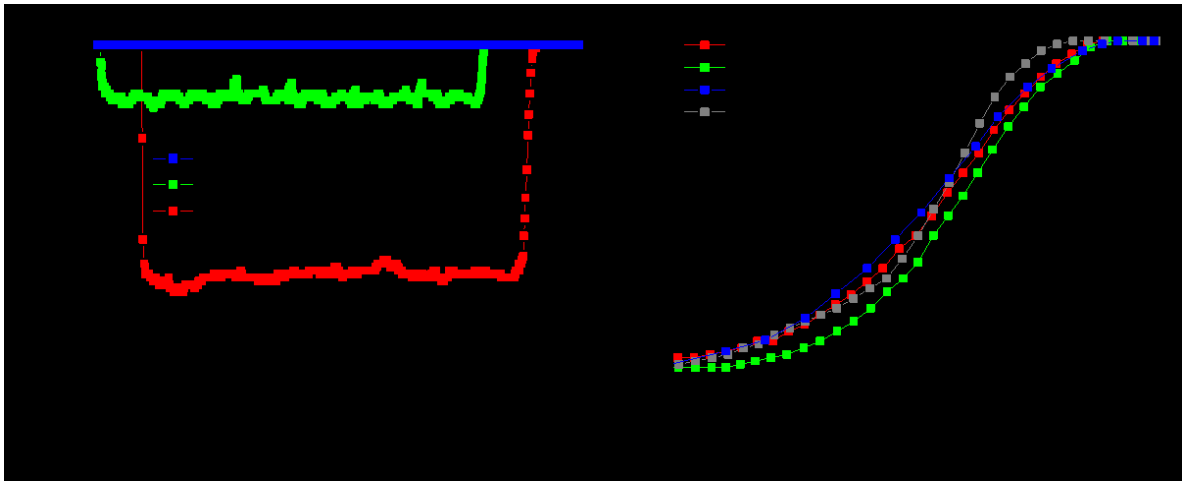

Figure 5.14 Water stability measurements at different temperature (a) and catalytic curves before/after stability test (b) for 1 wt% Pd on MnO_2. The black arrow indicated the order of measurements. The stability was tested from high to low temperature.

As summarized in Table 5.3, in the presence of water, for the sample tested from low to high temperature, it is obvious that the catalyst is deactivated during water exposure. After hydrothermal treatment at four different temperatures, the light off curve shifts 18 °C to higher temperature compared with that of the fresh catalyst. The conversion temperature for repeated measurements was within ± 5 °C. Therefore, the difference in $T_{50\%}$ indicates that water deactivated the catalysts to some extent when hydrothermal treatment was performed from low to high temperature. Furthermore, at low temperature (330 °C), the activity decreases to 0% in the presence of water, which indicates that all the active sites are blocked by H_2O molecules or OH^- etc. in this condition.

When the stability test was run with a higher initial temperature (450 °C), the methane conversion is reasonably stable. After all measurements, the difference in $T_{50\%}$ between the used sample and fresh one was below 10 °C. The similarity of these $T_{50\%}$ values indicates that the deactivation effect of water was weak for the catalysts when tested from high to low temperature.

At 330 °C, the methane conversion dropped significantly from 100% to 25% at the start of the test. Interestingly, it recovered back to 34% conversion gradually and remained at this level, which was much better than the initial catalyst test at 330 °C. To better understand this phenomenon, the catalysts were collected after the tests were completed and characterized by PXRD and HRTEM.

Table 5.3 Summary of stability result for 1 wt% PdO on MnO_2.

T for water injection (°C)	Stability in the presence of water	
	330-450	450-330
330	10%-0%	25%-34%
350	34%-26%	34%-34%
400	87%-81%	84%-84%
450	100%-100%	100%-100%
$\Delta T_{50\%}$	18 °C	<10 °C

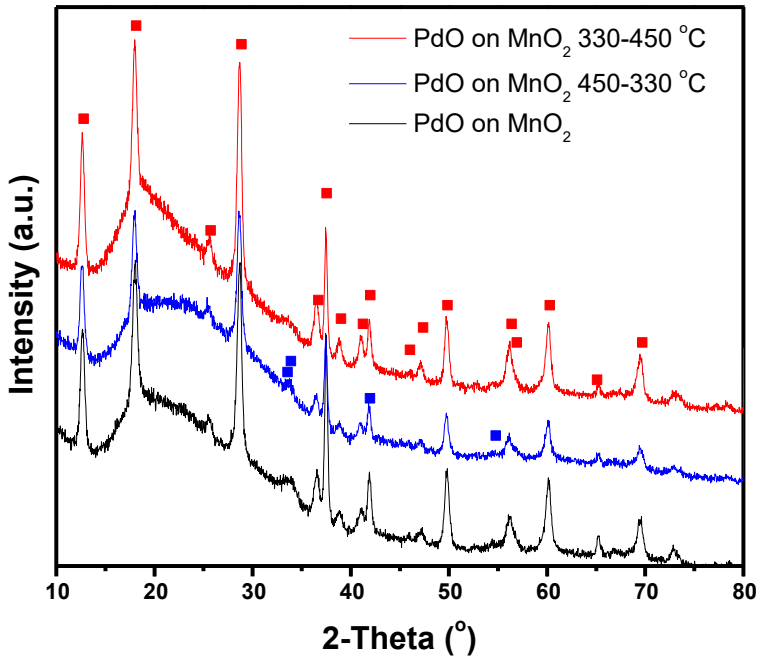

Figure 5.15 PXRD pattern for PdO on MnO_2 catalysts: fresh one compared with that after stability test. ■ Manganese oxide, α-MnO_2 (JCPDS 72-1982), ■ palladinite, syn – PdO (JCPDS 85-0624).

The PXRD pattern for the fresh and used catalysts are compared in Figure 5.15. It is observed that the intensity for the MnO_2 diffraction peaks are different. For the sample that was subjected to the stability test from 330 to 450 °C, the intensities of the MnO_2 peaks are enhanced, indicating enlarged particle size. This is attributed to the sintering of catalyst particles during the hydrothermal treatment. For PdO on MnO_2 tested from 450 to 330 °C, the intensity for the MnO_2 peaks decreased, which suggested that the particle size is reduced after a series of hydrothermal treatments, which may due to the structure not being stable under the specified operating conditions, resulting in the breakage or corrosion of the nanowire structures.

HRTEM analysis gives more information on the crystalline structure. As shown in Figure 5.16, most of the exposed lattice space for PdO nanoparticles is assigned to the (101) facet. The grain domain was enlarged for the used sample tested from low to high temperature. For the sample tested from high to low temperature, evidence for sintering in the images was not obvious.

It is proposed that high temperature reduces the attachment of H_2O molecules and speeds up the decomposition of $Pd(OH)_2$ to PdO. In addition, the transformation of PdO ↔ Pd plays an important role in the catalytic methane oxidation process. The Pd metal is more readily fused into larger particle sizes.[63] Therefore, during hydrothermal treatment, when the reaction begins at lower temperature, the accumulation of $Pd(OH)_2$ on the surface leads to more PdO sites involved in catalytic reaction. The transformation of PdO ↔ Pd during the reaction accelerates the growth of PdO particles and deactivates the catalysts. If the reaction starts at higher temperature, the effect of H_2O is reduced, decreasing the formation of $Pd(OH)_2$, and delaying the growth of PdO particles.

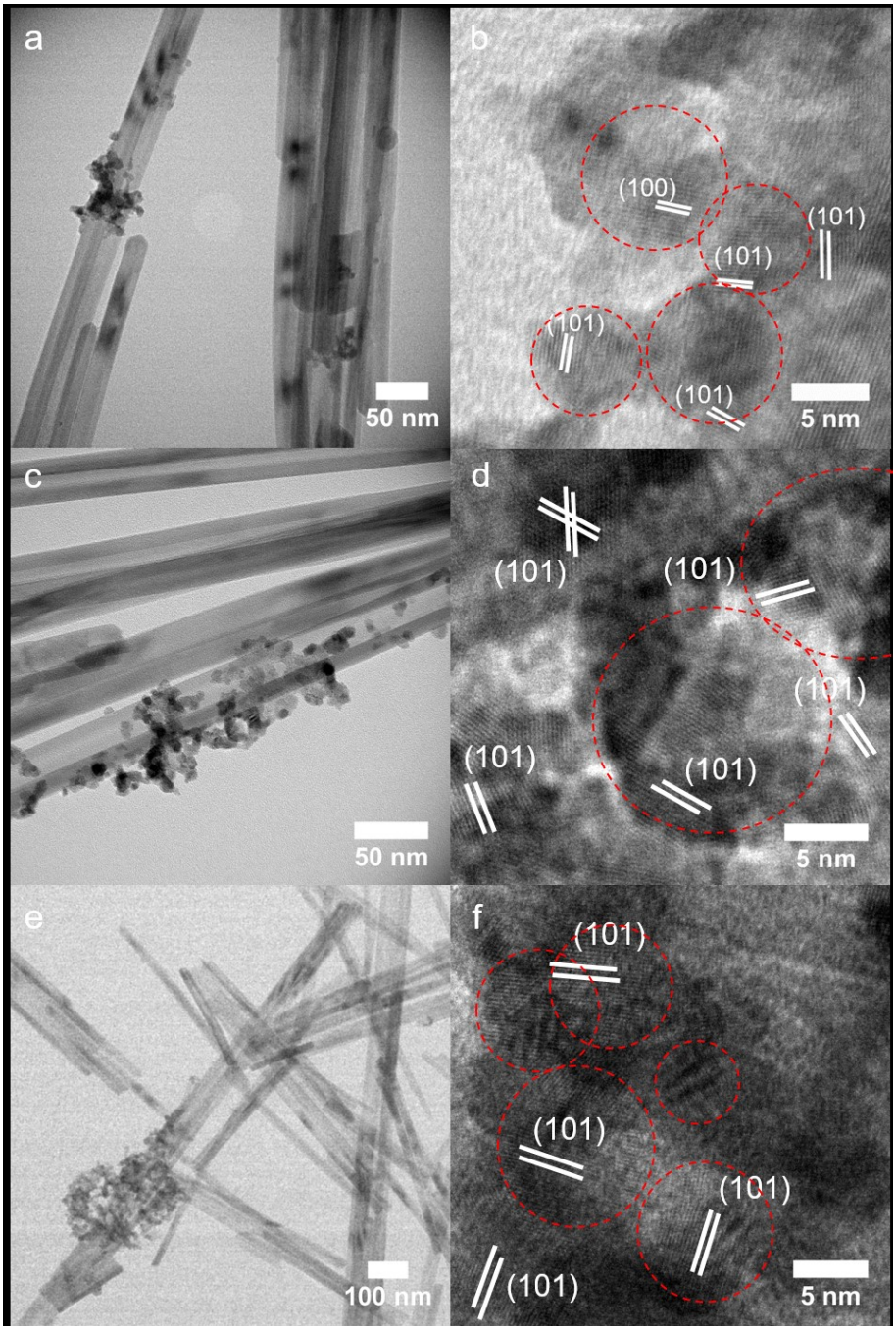

Figure 5.16 HRTEM images for PdO on MnO_2 aerogel catalysts: a,b fresh catalysts, c,d catalysts after stability tests from low to high temperature, e,f catalysts after stability tests from high to low temperature.

Finally, although there is only a small amount of SO_x in the exhaust gas from NGVs, SO_x has a significant detrimental effect on Pd-based catalysts. Therefore, good S tolerance is crucial for catalysts used in practice. An experiment was conducted at 450 °C with 1000 ppm CH_4 and 10% O_2 under dry conditions. Then 5 ppm SO_2 was mixed with the feed gas and injected into the reactor for ~24 h. After that, SO_2 was cut off and another TPO experiment was carried out to study the effect of SO_2 on the catalysts. The result for methane conversion is shown in Figure 5.17. It can be observed that during the first run, the catalysts maintained 100% conversion at 450 °C. But, the following TPO result indicates that the catalyst is substantially deactivated, with $T_{50\%}$ shifted ~15 °C to higher temperature. For the second and third runs, the conversion gradually decreased in the presence of SO_2, and the catalytic activity continuously decreased. After three cycles (~ 70 h), the $T_{50\%}$ shifted ~55 °C in total. Due to the presence of excess active sites, the catalysts appeared stable at the beginning, but the detrimental effect of SO_2 on the catalysts was significant. These effects would have to be addressed before the catalyst could be used in practice.

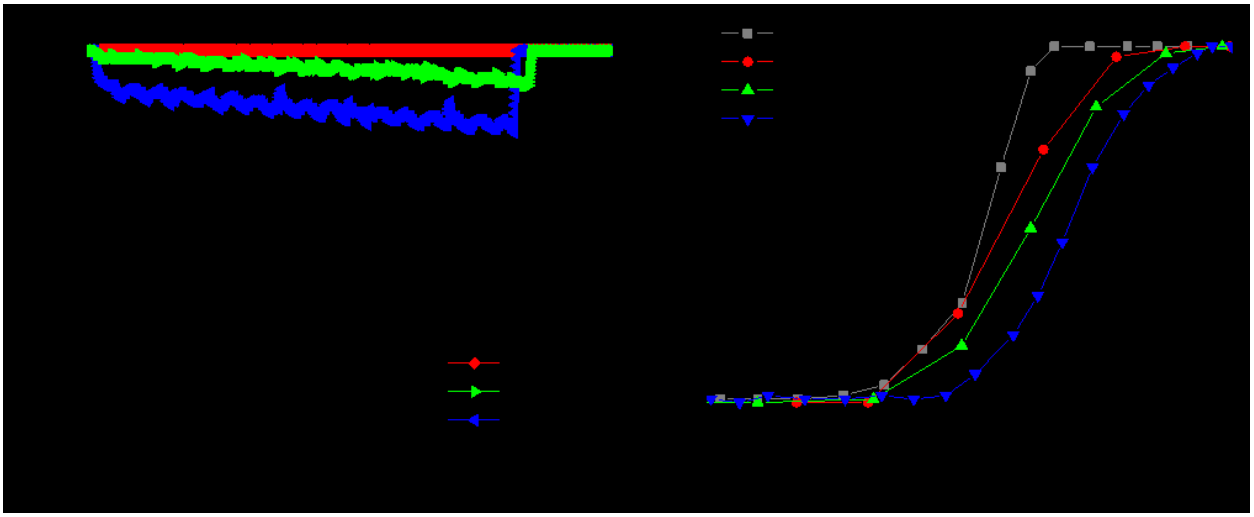

Figure 5.17 a. Methane conversion in the presence of SO_2, b. catalytic activity for 1 wt% PdO on MnO_2 before and after SO_2 treatment.

5.4 Conclusions

In a summary, a series of MnO_2 aerogel-supported catalysts have been prepared. For the catalysts using MnO_2 as a skeleton, the catalytic activity was improved by good distribution and exposure of more active sites. The non-noble metal catalysts supported on MnO_2 were comparable to the Pd-based catalysts. Then PdO was directly bound on the MnO_2 nanowires and these nanocomposites exhibited excellent catalytic activity. The hydrothermal stability was tested at different temperatures, both in heating and cooling directions, which helps to understand the deactivation mechanism in the presence of water. The S tolerance for the catalysts was poor, and will need to be further improved in the future. Although we succeeded in surface modification of the MnO_2 nanowires, the transformation from MnO_2 to Mn_3O_4 was detrimental to the catalytic activity.

Chapter 6: Conclusions

6.1 Conclusions

The aim of this thesis was to develop heterogeneous catalysts for low-temperature methane oxidation, in order to reduce the methane emission in natural gas vehicle (NGV) exhaust. In Chapter 2, I took advantage of the surface-assisted reduction (SAR) method developed in our lab previously, and incorporated highly active PdO/CeO_2 catalysts into mesoporous silica SBA-15. The ordered channels of SBA-15 were used to limit the sintering of active sites during the catalytic reaction. According to catalytic performance measurements, this material maintained excellent activity over time, and showed improved hydrothermal stability compared to unprotected PdO/CeO_2 catalysts. Even more significantly, after water vapor treatment, the material displayed enhanced activity, with $T_{50\%}$ shifted about 50 °C to lower temperature. The enhanced activity and stability were attributed to the inhibition of aggregation of PdO particles inside the ordered channels of SBA-15.

In Chapter 3, the development of non-precious metal $NiCo_2O_4$ nanostructured catalysts with novel bowtie-shaped structures was described. The formation mechanism of this unusual morphology was studied in detail. The surfactant and redox reaction during hydrothermal treatment plays an important role in the formation of the bowtie-shaped catalyst. This material was also examined as a catalyst for methane combustion. Importantly, it displayed excellent catalytic activity, with 100% conversion below 400 °C. However, the calcination temperature had a significant influence on the activity of the $NiCo_2O_4$ catalyst. The higher calcination treatment

deactivated the catalyst. Also, the catalyst displayed poor hydrothermal stability that would limit its use in practical NGV catalytic converters.

Chapter 4 focused on hydrothermal stability and sulfur tolerance of a $CoCr_2O_4$ composite material. $CoCr_2O_4$ nanospheres were synthesized by a straightforward hydrothermal method. These catalysts not only exhibited excellent catalytic activity that reached 100% conversion below 500 °C, but they also displayed remarkable stability. ~80% methane conversion was maintained with the injection of 10% water and 5 ppm SO_2 for 170 h catalytic reaction. These catalysts were coated onto a monolith by an optimized wash-coating method and tested for methane oxidation. The coated monolith showed good activity and outstanding stability. These catalysts have the potential to be adapted for use in NGVs.

To further improve the catalytic activity, Chapter 5 examines new composites of nanowire MnO_2 aerogels for low-temperature methane oxidation. A series of precious metal and non-precious metal catalysts was prepared. MnO_2 supported non-precious catalysts exhibited enhanced catalytic activity, comparable to Pd-based catalysts. Also, MnO_2 supported PdO showed excellent catalytic performance. Its hydrothermal stability and sulfur tolerance were investigated and it was found that the showed moderate hydrothermal stability but substantial deactivation upon exposure to O_2.

To conclude, several different types of nanostructured catalysts with either improved catalytic activity or enhanced hydrothermal stability have been developed in this thesis. The formation mechanism of novel structures and the properties which contribute to significant catalytic behavior have been studied in detail. Among them, PdO on aerogel MnO_2 shows the best catalytic activity. However its sulfur tolerance needs to be further improved for practical usage. $CoCr_2O_4$ shows moderate activity for methane oxidation, with complete conversion below 500 °C.

This catalyst displayed outstanding hydrothermal stability in the presence of SO_2. The $CoCr_2O_4$ coated monolith maintained catalytic activity and stability as a powder sample. The $CoCr_2O_4$ catalysts are the best catalysts I developed, which are anticipated to be useful in NGVs in the future or for other catalytic reactions.

My research has uncovered new materials and new ways to construct them. By exploring the variation of structure of nanomaterials through modifications of their synthesis, and connecting structure and composition with ultimate function, I have developed new materials that are promising for methane oxidation. It is clear that there are an enormous number of new materials and morphologies that are waiting to be discovered and explored. These new materials are likely to give highly active methane oxidation catalysts that can be applied in NGVs.

For future work, the monolith coated with $CoCr_2O_4$ nanocatalysts could be submitted for real engine test. Except for CH_4, O_2, H_2O, and SO_2 tested in lab, the exhausts from NGVs also contain other components like CO, CO_2, and NO_x, which may influence the catalytic performance. The effect of these components on catalysts for LTMOX could be explored separately and simultaneously.

Another worthwhile direction would be to investigate the transformation of catalysts and the catalytic reaction at the atomic level, in order to uncover the key for the catalysts' excellent activity and stability. Once optimized, these catalysts could be scaled up for NGVs and other industrial catalysis.

Bibliography

1. Maggio, G.; Cacciola, G., When will oil, natural gas, and coal peak? *Fuel* **2012**, *98*, 111-123.
2. Choudhary, T. V.; Banerjee, S.; Choudhary, V. R., Catalysts for combustion of methane and lower alkanes. *Appl. Catal., A* **2002**, *234*, 1-23.
3. Ciuparu, D.; Lyubovsky, M. R.; Altman, E.; Pfefferle, L. D.; Datye, A., Catalytic Combustion of Methane Over Palladium-based Catalysts. *Catal. Rev. Sci. Eng.* **2002**, *44*, 593-649.
4. Li, W.-J.; Shi, E.-W.; Zhong, W.-Z.; Yin, Z.-W., Growth mechanism and growth habit of oxide crystals. *J. Cryst. Growth* **1999**, *203,* 186-196.
5. G. Myhre, D. S., F.-M. Bréon, W. Collins, J. Fuglestvedt, J. Huang, D. Koch, J.-F. Lamarque, D. Lee, B. Mendoza, T. Nakajima, A. Robock, G. Stephens, T. Takemura, and H. Zhang, H., Anthropogenic and Natural Radiative Forcing; Climate Change 2013: The Physical Science Basis. Contribution of Working Group I to the Fifth Assessment Report of the Intergovernmental Panel on Climate Change: Cambridge University Press, Cambridge, United Kingdom and New York, NY, USA, **2013**.
6. Gélin, P.; Primet, M., Complete oxidation of methane at low temperature over noble metal based catalysts: a review. *Appl. Catal., B* **2002**, *39*, 1-37.
7. https://www.dieselnet.com/standards/.
8. Horn, R.; Schlögl, R., Methane Activation by Heterogeneous Catalysis. *Catal. Lett.* **2015**, *145*, 23-39.
9. Honkanen, M.; Kärkkäinen, M.; Viitanen, V.; Jiang, H.; Kallinen, K.; Huuhtanen, M.; Vippola, M.; Lahtinen, J.; Keiski, R.; Lepistö, T., Structural Characteristics of Natural-Gas-Vehicle-Aged Oxidation Catalyst. *Top. Catal.* **2013**, *56*, 576-585.
10. Burch, R.; Urbano, F. J., Investigation of the active state of supported palladium catalysts in the combustion of methane. *Appl. Catal., A* **1995**, *124*, 121-138.
11. Seimanides, S.; Stoukides, M., Catalytic oxidation of methane on polycrystalline palladium supported on stabilized zirconia. *J. Catal.* **1986**, *98*, 540-549.
12. Berg, M.; Järås, S., Catalytic combustion of methane over magnesium oxide. *Appl. Catal., A* **1994**, *114*, 227-241.
13. Bahlawane, N., Kinetics of methane combustion over CVD-made cobalt oxide catalysts. *Appl. Catal., B* **2006**, *67*, 168-176.
14. Zhu, G.; Han, J.; Zemlyanov, D. Y.; Ribeiro, F. H., Temperature Dependence of the Kinetics for the Complete Oxidation of Methane on Palladium and Palladium Oxide. *J. Phys. Chem. B* **2005**, *109*, 2331-2337.
15. Jodłowski, P. J.; Jędrzejczyk, R. J.; Chlebda, D.; Gierada, M.; Łojewska, J., In situ spectroscopic studies of methane catalytic combustion over Co, Ce, and Pd mixed oxides deposited on a steel surface. *J. Catal.* **2017**, *350*, 1-12.
16. Fujimoto, K.-i.; Ribeiro, F. H.; Avalos-Borja, M.; Iglesia, E., Structure and Reactivity of PdO_x/ZrO_2 Catalysts for Methane Oxidation at Low Temperatures. *J. Catal.* **1998**, *179*, 431-442.

17. Stotz, H.; Maier, L.; Boubnov, A.; Gremminger, A. T.; Grunwaldt, J. D.; Deutschmann, O., Surface reaction kinetics of methane oxidation over PdO. *J. Catal.* **2019**, *370*, 152-175.
18. Cargnello, M.; Jaén, J. J. D.; Garrido, J. C. H.; Bakhmutsky, K.; Montini, T.; Gámez, J. J. C.; Gorte, R. J.; Fornasiero, P., Exceptional Activity for Methane Combustion over Modular Pd@CeO_2 Subunits on Functionalized Al_2O_3. *Science* **2012**, *337*, 713-717.
19. Jin, J.; Li, C.; Tsang, C.-W.; Xu, B.; Liang, C., Catalytic Combustion of Methane over Pt–Ce Oxides under Scarce Oxygen Condition. *Ind. Eng. Chem. Res.* **2016**, *55*, 2293-2301.
20. Schwartz, W. R.; Pfefferle, L. D., Combustion of Methane over Palladium-Based Catalysts: Support Interactions. *J. Phys. Chem. C* **2012**, *116*, 8571-8578.
21. Onn, T. M.; Zhang, S.; Arroyo-Ramirez, L.; Chung, Y.-C.; Graham, G. W.; Pan, X.; Gorte, R. J., Improved Thermal Stability and Methane-Oxidation Activity of Pd/Al_2O_3 Catalysts by Atomic Layer Deposition of ZrO_2. *ACS Catal.* **2015**, *5*, 5696-5701.
22. Gholami, R.; Alyani, M.; Smith, K. J., Deactivation of Pd Catalysts by Water during Low Temperature Methane Oxidation Relevant to Natural Gas Vehicle Converters. *Catalysts* **2015**, *5*, 561-594.
23. Chen, C.; Yeh, Y.-H.; Cargnello, M.; Murray, C. B.; Fornasiero, P.; Gorte, R. J., Methane Oxidation on Pd@ZrO_2/Si–Al_2O_3 Is Enhanced by Surface Reduction of ZrO_2. *ACS Catal.* **2014**, *4*, 3902-3909.
24. Arroyo-Ramírez, L.; Chen, C.; Cargnello, M.; Murray, C. B.; Gorte, R. J., A comparison of hierarchical Pt@CeO_2/Si–Al_2O_3 and Pd@CeO_2/Si–Al_2O_3. *Catal. Today* **2015**, *253*, 137-141.
25. Arandiyan, H.; Dai, H.; Ji, K.; Sun, H.; Li, J., Pt Nanoparticles Embedded in Colloidal Crystal Template Derived 3D Ordered Macroporous $Ce_{0.6}Zr_{0.3}Y_{0.1}O_2$: Highly Efficient Catalysts for Methane Combustion. *ACS Catal.* **2015**, *5*, 1781-1793.
26. Setiawan, A.; Kennedy, E. M.; Dlugogorski, B. Z.; Adesina, A. A.; Stockenhuber, M., The stability of Co_3O_4, Fe_2O_3, Au/Co_3O_4 and Au/Fe_2O_3 catalysts in the catalytic combustion of lean methane mixtures in the presence of water. *Catal. Today* **2015**, *258*, 276-283.
27. Bera, P.; Hegde, M. S., Characterization and catalytic properties of combustion synthesized Au/CeO_2 catalyst. *Catal. Lett.* **2002**, *79*, 75-81.
28. Feng, Y. Z.; Rao, P. M.; Kim, D. R.; Zheng, X. L., Methane oxidation over catalytic copper oxides nanowires. *P. Combust. Inst.* **2011**, *33*, 3169-3175.
29. Hu, W.; Lan, J.; Guo, Y.; Cao, X.-M.; Hu, P., Origin to Efficient Catalytic Combustion of Methane over Co_3O_4(110): Active Low-Coordination Lattice Oxygen and Cooperation of Multi Active Sites. *ACS Catal.* **2016**, *6*, 5508−5519.
30. Pontelli, G. C.; Reolon, R. P.; Alves, A. K.; Berutti, F. A.; Bergmann, C. P., Application of cerium oxide electrospun fibers in the catalytic combustion of methane. *Appl. Catal., A* **2011**, *405*, 79-83.
31. Wang, X.; Xie, Y. C., Total oxidation of methane over La, Ce and Y modified manganese oxide catalysts. *React. Kinet. Catal. L.* **2000**, *71*, 3-11.
32. Barbato, P. S.; Di Benedetto, A.; Di Sarli, V.; Landi, G.; Pirone, R., High-Pressure Methane Combustion over a Perovskyte Catalyst. *Ind. Eng. Chem. Res.* **2012**, *51*, 7547-7558.

33. Popescu, I.; Boudjemaa, A.; Helaili, N.; Bessekhouad, Y.; Tudorache, M.; Bachari, K.; Marcu, I. C., Study of the electrical and catalytic properties of spinels with $CuFe_{2-x}Mn_xO_4$ composition (x=0, 0.4, 0.8, 1.6 and 2). *Appl. Catal., A* **2015**, *504*, 29-36.
34. Zheng, J. D.; Ren, X. G.; Song, Y. J.; Ge, X. T., Catalytic combustion of methane over iron- and manganese-substituted lanthanum hexaaluminates. *React. Kinet. Catal. L.* **2009**, *97*, 109-114.
35. Firth, J. G.; Holland, H. B., Heterogeneous Oxidation of Methane over Palladium Catalysts. *Nature* **1968**, *217*, 1252-1253.
36. Firth, J. G.; Holland, H. B., Catalytic oxidation of methane over noble metals. *T. Faraday Soc.* **1969**, *65*, 1121-1127.
37. Cullis, C. F.; Willatt, B. M., Oxidation of methane over supported precious metal catalysts. *J. Catal.* **1983**, *83*, 267-285.
38. Hicks, R.; Qi, H. H.; Young, M. L.; Lee, R. G., Effect of catalyst structure on methane oxidation over palladium on alumina. *J. Catal.* **1990**, *122*, 295-306.
39. Hoflund, G. B.; Li, Z.; Epling, W. S.; Göbel, T.; Schneider, P.; Hahn, H., Catalytic Methane Oxidation Over Pd Supported on Nanocrystalline and Polycrystalline TiO_2 Mn_3O_4, CeO_2 and ZrO_2. *React. Kinet. Catal. L.* **2000**, *70*, 97-103.
40. Murata, K.; Mahara, Y.; Ohyama, J.; Yamamoto, Y.; Arai, S.; Satsuma, A., The Metal–Support Interaction Concerning the Particle Size Effect of Pd/Al_2O_3 on Methane Combustion. *Angew. Chem. Int. Ed.* **2017**, *56*, 15993-15997.
41. Willis, J. J.; Gallo, A.; Sokaras, D.; Aljama, H.; Nowak, S. H.; Goodman, E. D.; Wu, L.; Tassone, C. J.; Jaramillo, T. F.; Abild-Pedersen, F.; Cargnello, M., Systematic Structure–Property Relationship Studies in Palladium-Catalyzed Methane Complete Combustion. *ACS Catal.* **2017**, *7*, 7810-7821.
42. Roth, D.; Gélin, P.; Primet, M.; Tena, E., Catalytic behaviour of Cl-free and Cl-containing Pd/Al_2O_3 catalysts in the total oxidation of methane at low temperature. *Appl. Catal., A* **2000**, *203*, 37-45.
43. Simplício, L. M. T.; Brandão, S. T.; Sales, E. A.; Lietti, L.; Bozon-Verduraz, F., Methane combustion over PdO-alumina catalysts: The effect of palladium precursors. *Appl. Catal., B* **2006**, *63*, 9-14.
44. Baylet, A.; Royer, S.; Marécot, P.; Tatibouët, J. M.; Duprez, D., Effect of Pd precursor salt on the activity and stability of Pd-doped hexaaluminate catalysts for the CH_4 catalytic combustion. *Appl. Catal., B* **2008**, *81*, 88-96.
45. Simone, O. D.; Kennelly, T.; Brungard, L. N.; Farrauto, J. R., Reversible poisoning of palladium catalysts for methane oxidation. *Appl. Catal.* **1991**, *70*, 87-100.
46. Yin, F.; Ji, S.; Wu, P.; Zhao, F.; Li, C., Deactivation behavior of Pd-based SBA-15 mesoporous silica catalysts for the catalytic combustion of methane. *J. Catal.* **2008**, *257*, 108-116.
47. Dai, Q.; Bai, S.; Lou, Y.; Wang, X.; Guo, Y.; Lu, G., Sandwich-like PdO/CeO_2 nanosheet@HZSM-5 membrane hybrid composite for methane combustion: self-redispersion, sintering-resistance and oxygen, water-tolerance. *Nanoscale* **2016**, *8*, 9621-9628.

48. Yoshida, H.; Nakajima, T.; Yazawa, Y.; Hattori, T., Support effect on methane combustion over palladium catalysts. *Appl. Catal., B* **2007**, *71*, 70-79.
49. Zhao, Z.; Wang, B.; Ma, J.; Zhan, W.; Wang, L.; Guo, Y.; Guo, Y.; Lu, G., Catalytic combustion of methane over Pd/SnO_2 catalysts. *Chinese J. Catal.* **2017**, *38*, 1322-1329.
50. Ercolino, G.; Stelmachowski, P.; Grzybek, G.; Kotarba, A.; Specchia, S., Optimization of Pd catalysts supported on Co_3O_4 for low-temperature lean combustion of residual methane. *Appl. Catal., B* **2017**, *206*, 712-725.
51. Hoffmann, M.; Kreft, S.; Georgi, G.; Fulda, G.; Pohl, M.-M.; Seeburg, D.; Berger-Karin, C.; Kondratenko, E. V.; Wohlrab, S., Improved catalytic methane combustion of Pd/CeO_2 catalysts via porous glass integration. *Appl. Catal., B* **2015**, *179*, 313-320.
52. Muto, K.-i.; Katada, N.; Niwa, M., Complete oxidation of methane on supported palladium catalyst: Support effect. *Appl. Catal., A* **1996**, *134*, 203-215.
53. Zou, X.; Rui, Z.; Song, S.; Ji, H., Enhanced methane combustion performance over $NiAl_2O_4$-interface-promoted Pd/γ-Al_2O_3. *J. Catal.* **2016**, *338*, 192-201.
54. Xu, P.; Zhao, X.; Zhang, X.; Bai, L.; Chang, H.; Liu, Y.; Deng, J.; Guo, G.; Dai, H., Three-dimensionally ordered macroporous $LaMnAl_{11}O_{19}$-supported Pd nanocatalysts highly active for methane combustion. *Mol. Catal.* **2017**, *439*, 200-210.
55. Li, W.; Liu, D.; Feng, X.; Zhang, Z.; Jin, X.; Zhang, Y., High-Performance Ultrathin Co_3O_4 Nanosheet Supported PdO/CeO_2 Catalysts for Methane Combustion. *Adv. Energy Mater.* **2019**, *9*, 1803583.
56. Amairia, C.; Fessi, S.; Ghorbel, A.; Rives, A., Study of the effect of the preparation route and the palladium precursor on the methane oxidation behavior over Al_2O_3-ZrO_2 supported palladium. *React. Kinet. Mech. Cat.* **2011**, *103*, 379-389.
57. Xiao, L.-h.; Sun, K.-p.; Xu, X.-l.; Li, X.-n., Low-temperature catalytic combustion of methane over Pd/CeO_2 prepared by deposition–precipitation method. *Catal. Commun.* **2005**, *6*, 796-801.
58. Ercolino, G.; Grzybek, G.; Stelmachowski, P.; Specchia, S.; Kotarba, A.; Specchia, V., Pd/Co_3O_4-based catalysts prepared by solution combustion synthesis for residual methane oxidation in lean conditions. *Catal. Today* **2015**, *257*, 66-71.
59. Colussi, S.; Gayen, A.; Farnesi Camellone, M.; Boaro, M.; Llorca, J.; Fabris, S.; Trovarelli, A., Nanofaceted Pd-O Sites in Pd-Ce Surface Superstructures: Enhanced Activity in Catalytic Combustion of Methane. *Angew. Chem. Int. Ed.* **2009**, *121*, 8633-8636.
60. Civera, A.; Negro, G.; Specchia, S.; Saracco, G.; Specchia, V., Optimal compositional and structural design of a $LaMnO_3$/ZrO_2/Pd-based catalyst for methane combustion. *Catal. Today* **2005**, *100*, 275-281.
61. Danielis, M.; Colussi, S.; de Leitenburg, C.; Soler, L.; Llorca, J.; Trovarelli, A., Outstanding Methane Oxidation Performance of Palladium-Embedded Ceria Catalysts Prepared by a One-Step Dry Ball-Milling Method. *Angew. Chem. Int. Ed.* **2018**, *57*, 10212-10216.
62. Gomathi, A.; Vickers, S. M.; Gholami, R.; Alyani, M.; Man, R. W. Y.; MacLachlan, M. J.; Smith, K. J.; Wolf, M. O., Nanostructured Materials Prepared by Surface-Assisted

Reduction: New Catalysts for Methane Oxidation. *ACS Appl. Mater. Inter.* **2015**, *7*, 19268-19273.
63. Park, J.-H.; Cho, J. H.; Kim, Y. J.; Kim, E. S.; Han, H. S.; Shin, C.-H., Hydrothermal stability of Pd/ZrO_2 catalysts for high temperature methane combustion. *Appl. Catal., B* **2014**, *160-161*, 135-143.
64. Baylet, A.; Royer, S.; Marécot, P.; Tatibouët, J. M.; Duprez, D., High catalytic activity and stability of Pd doped hexaaluminate catalysts for the CH_4 catalytic combustion. *Appl. Catal., B* **2008**, *77*, 237-247.
65. Simplício, L. M. T.; Brandão, S. T.; Domingos, D.; Bozon-Verduraz, F.; Sales, E. A., Catalytic combustion of methane at high temperatures: Cerium effect on PdO/Al_2O_3 catalysts. *Appl. Catal., A* **2009**, *360*, 2-7.
66. Wang, X.; Guo, Y.; Lu, G.; Hu, Y.; Jiang, L., An excellent support of Pd catalyst for methane combustion: Thermal-stable Si-doped alumina. *Catal. Today* **2007**, *126*, 369-374.
67. Strobel, R.; Pratsinis, S. E.; Baiker, A., Flame-made $Pd/La_2O_3/Al_2O_3$ nanoparticles: thermal stability and catalytic behavior in methane combustion. *J. Mater. Chem.* **2005**, *15*, 605-610.
68. Thevenin, P. O.; Alcalde, A.; Pettersson, L. J.; Järås, S. G.; Fierro, J. L. G., Catalytic combustion of methane over cerium-doped palladium catalysts. *J. Catal.* **2003**, *215*, 78-86.
69. Onn, T. M.; Monai, M.; Dai, S.; Fonda, E.; Montini, T.; Pan, X.; Graham, G. W.; Fornasiero, P.; Gorte, R. J., Smart Pd Catalyst with Improved Thermal Stability Supported on High-Surface-Area $LaFeO_3$ Prepared by Atomic Layer Deposition. *J. Am. Chem. Soc.* **2018**, *140*, 4841-4848.
70. Toso, A.; Colussi, S.; Padigapaty, S.; de Leitenburg, C.; Trovarelli, A., High stability and activity of solution combustion synthesized Pd-based catalysts for methane combustion in presence of water. *Appl. Catal., B* **2018**, *230*, 237-245.
71. Gao, D.; Wang, S.; Zhang, C.; Yuan, Z.; Wang, S., Methane Combustion over Pd/Al_2O_3 Catalyst: Effects of Chlorine Ions and Water on Catalytic Activity. *Chinese J. Catal.* **2008**, *29*, 1221-1225.
72. Liu, Y.; Wang, S.; Gao, D.; Sun, T.; Zhang, C.; Wang, S., Influence of metal oxides on the performance of Pd/Al_2O_3 catalysts for methane combustion under lean-fuel conditions. *Fuel Process. Technol.* **2013**, *111*, 55-61.
73. Monai, M.; Montini, T.; Chen, C.; Fonda, E.; Gorte, R. J., Methane Catalytic Combustion over Hierarchical $Pd@CeO_2/Si\text{-}Al_2O_3$: Effect of the Presence of Water. *Chemcatchem* **2015**, *7*, 2038-2046.
74. Ciuparu, D.; Perkins, E.; Pfefferle, L., In situ DR-FTIR investigation of surface hydroxyls on $\gamma\text{-}Al_2O_3$ supported PdO catalysts during methane combustion. *Appl. Catal., A* **2004**, *263*, 145-153.
75. Nassiri, H.; Hayes, R. E.; Semagina, N., Stability of Pd-Pt catalysts in low-temperature wet methane combustion: Metal ratio and particle reconstruction. *Chem. Eng. Sci.* **2018**, *186*, 44-51.
76. Goodman, E. D.; Dai, S.; Yang, A.-C.; Wrasman, C. J.; Gallo, A.; Bare, S. R.; Hoffman, A. S.; Jaramillo, T. F.; Graham, G. W.; Pan, X.; Cargnello, M., Uniform Pt/Pd Bimetallic

Nanocrystals Demonstrate Platinum Effect on Palladium Methane Combustion Activity and Stability. *ACS Catal.* **2017**, *7*, 4372-4380.
77. Lapisardi, G.; Urfels, L.; Gélin, P.; Primet, M.; Kaddouri, A.; Garbowski, E.; Toppi, S.; Tena, E., Superior catalytic behaviour of Pt-doped Pd catalysts in the complete oxidation of methane at low temperature. *Catal. Today* **2006**, *117*, 564-568.
78. Wu, Z.; Deng, J.; Liu, Y.; Xie, S.; Jiang, Y.; Zhao, X.; Yang, J.; Arandiyan, H.; Guo, G.; Dai, H., Three-dimensionally ordered mesoporous Co_3O_4-supported Au–Pd alloy nanoparticles: High-performance catalysts for methane combustion. *J. Catal.* **2015**, *332*, 13-24.
79. Wang, Y.; Arandiyan, H.; Scott, J.; Akia, M.; Dai, H., High Performance Au–Pd Supported on 3D Hybrid Strontium-Substituted Lanthanum Manganite Perovskite Catalyst for Methane Combustion. *ACS Catal.* **2016**, *6*, 6935-6947.
80. Mowery, D. L.; McCormick, R. L., Deactivation of alumina supported and unsupported PdO methane oxidation catalyst: the effect of water on sulfate poisoning. *Appl. Catal., B* **2001**, *34*, 287-297.
81. Yashnik, S. A.; Chesalov, Y. A.; Ishchenko, A. V.; Kaichev, V. V.; Ismagilov, Z. R., Effect of Pt addition on sulfur dioxide and water vapor tolerance of Pd-Mn-hexaaluminate catalysts for high-temperature oxidation of methane. *Appl. Catal., B* **2017**, *204*, 89-106.
82. Xu, P.; Zhang, X.; Zhao, X.; Yang, J.; Hou, Z.; Bai, L.; Chang, H.; Liu, Y.; Deng, J.; Guo, G.; Dai, H.; Au, C.-T., Preparation, characterization, and catalytic performance of PdPt/3DOM $LaMnAl_{11}O_{19}$ for the combustion of methane. *Appl. Catal., A* **2018**, *562*, 284-293.
83. Peng, H.; Rao, C.; Zhang, N.; Wang, X.; Liu, W.; Mao, W.; Han, L.; Zhang, P.; Dai, S., Confined Ultrathin Pd-Ce Nanowires with Outstanding Moisture and SO_2 Tolerance in Methane Combustion. *Angew. Chem. Int. Ed.* **2018**, *57*, 8953-8957.
84. Zou, X. L.; Rui, Z. B.; Ji, H. B., Core-Shell NiO@PdO Nanoparticles Supported on Alumina as an Advanced Catalyst for Methane Oxidation. *ACS Catal.* **2017**, *7*, 1615-1625.
85. Zwinkels, M. F. M.; Järås, S. G.; Menon, P. G.; Griffin, T. A., Catalytic Materials for High-Temperature Combustion. *Catal. Rev. Sci. Eng.* **1993**, *35*, 319-358.
86. Ordóñez, S.; Paredes, J. R.; Díez, F. V., Sulphur poisoning of transition metal oxides used as catalysts for methane combustion. *Appl. Catal., A* **2008**, *341*, 174-180.
87. Tao, F. F.; Shan, J.-j.; Nguyen, L.; Wang, Z.; Zhang, S.; Zhang, L.; Wu, Z.; Huang, W.; Zeng, S.; Hu, P., Understanding complete oxidation of methane on spinel oxides at a molecular level. *Nat. Commun.* **2015**, *6*, 7798.
88. Hu, W. D.; Lan, J. G.; Guo, Y.; Cao, X. M.; Hu, P., Origin of Efficient Catalytic Combustion of Methane over Co_3O_4(110): Active Low-Coordination Lattice Oxygen and Cooperation of Multiple Active Sites. *ACS Catal.* **2016**, *6*, 5508-5519.
89. Hu, L.; Peng, Q.; Li, Y., Selective Synthesis of Co_3O_4 Nanocrystal with Different Shape and Crystal Plane Effect on Catalytic Property for Methane Combustion. *J. Am. Chem. Soc.* **2008**, *130*, 16136-16137.

90. Sun, Y.; Liu, J.; Song, J.; Huang, S.; Yang, N.; Zhang, J.; Sun, Y.; Zhu, Y., Exploring the Effect of Co_3O_4 Nanocatalysts with Different Dimensional Architectures on Methane Combustion. *Chemcatchem* **2016**, *8*, 540-545.
91. Wang, H.; Chen, C.; Zhang, Y.; Peng, L.; Ma, S.; Yang, T.; Guo, H.; Zhang, Z.; Su, D. S.; Zhang, J., In situ oxidation of carbon-encapsulated cobalt nanocapsules creates highly active cobalt oxide catalysts for hydrocarbon combustion. *Nat. Commun.* **2015**, *6*, 7181.
92. Zhang, K.; Peng, X.; Cao, Y.; Yang, H.; Wang, X.; Zhang, Y.; Zheng, Y.; Xiao, Y.; Jiang, L., Effect of MnO_2 morphology on its catalytic performance in lean methane combustion. *Mater. Res. Bull.* **2019**, *111*, 338-341.
93. Wang, X.; Liu, Y.; Zhang, Y.; Zhang, T.; Chang, H.; Zhang, Y.; Jiang, L., Structural requirements of manganese oxides for methane oxidation: XAS spectroscopy and transition-state studies. *Appl. Catal., B* **2018**, *229*, 52-62.
94. Yu, Q.; Wang, C.; Li, X.; Li, Z.; Wang, L.; Zhang, Q.; Wu, G.; Li, Z., Engineering an effective MnO_2 catalyst from $LaMnO_3$ for catalytic methane combustion. *Fuel* **2019**, *239*, 1240-1245.
95. Kantserova, M. R.; Grabovaya, N. V.; Kolotilov, S. V.; Orlik, S. N., Effect of size and morphology of chromium(III) oxide nanoparticles on their catalytic properties in deep oxidation of methane. *Theor. Exp. Chem.* **2009**, *45*, 368-372.
96. Hu, J. N.; Zhao, W. Y.; Hu, R. S.; Chang, G. Y.; Li, C.; Wang, L. J., Catalytic activity of spinel oxides $MgCr_2O_4$ and $CoCr_2O_4$ for methane combustion. *Mater. Res. Bull.* **2014**, *57*, 268-273.
97. Huang, W.; Zha, W.; Zhao, D.; Feng, S., The effect of active oxygen species in nano-$ZnCr_2O_4$ spinel oxides for methane catalytic combustion. *Solid State Sci.* **2019**, *87*, 49-52.
98. Rosso, I.; Saracco, G.; Specchia, V.; Garrone, E., Sulphur poisoning of $LaCr_{0.5-x}Mn_xMg_{0.5}O_3 \cdot yMgO$ catalysts for methane combustion. *Appl. Catal., B* **2003**, *40*, 195-205.
99. Kaddouri, A.; Ifrah, S.; Bergeret, G., On the La–Cr–O Phase Change During Methane Catalytic Combustion Investigated with in situ HT-XRD. *Catal. Lett.* **2009**, *129*, 336-343.
100. Lim, T. H.; Cho, S. J.; Yang, H. S.; Engelhard, M. H.; Kim, D. H., Effect of Co/Ni ratios in cobalt nickel mixed oxide catalysts on methane combustion. *Appl. Catal., A* **2015**, *505*, 62-69.
101. Shao, C.; Li, W.; Lin, Q.; Huang, Q.; Pi, D., Low Temperature Complete Combustion of Lean Methane over Cobalt–Nickel Mixed-Oxide Catalysts. *Energy Technol.* **2017**, *5*, 604-610.
102. Trivedi, S.; Prasad, R.; Gautam, S. K., Design of active $NiCo_2O_{4-\delta}$ spinel catalyst for abatement of CO-CH_4 emissions from CNG fueled vehicles. *AICHE J.* **2018**, *64*, 2632-2646.
103. Chen, J.; Zhang, X.; Arandiyan, H.; Peng, Y.; Chang, H.; Li, J., Low temperature complete combustion of methane over cobalt chromium oxides catalysts. *Catal. Today* **2013**, *201*, 12-18.
104. Yang, Q.; Liu, G.; Liu, Y., Perovskite-Type Oxides as the Catalyst Precursors for Preparing Supported Metallic Nanocatalysts: A Review. *Ind. Eng. Chem. Res.* **2018**, *57*, 1-17.

105. Yang, X.; Gao, Q.; Zhao, Z.; Guo, Y.; Guo, Y.; Wang, L.; Wang, Y.; Zhan, W., Surface tuning of noble metal doped perovskite oxide by synergistic effect of thermal treatment and acid etching: A new path to high-performance catalysts for methane combustion. *Appl. Catal., B* **2018**, *239*, 373-382.
106. Xiang, X.-P.; Zhao, L.-H.; Teng, B.-T.; Lang, J.-J.; Hu, X.; Li, T.; Fang, Y.-A.; Luo, M.-F.; Lin, J.-J., Catalytic combustion of methane on $La_{1-x}Ce_xFeO_3$ oxides. *Appl. Surf. Sci.* **2013**, *276*, 328-332.
107. Arandiyan, H.; Scott, J.; Wang, Y.; Dai, H.; Sun, H.; Amal, R., Meso-Molding Three-Dimensional Macroporous Perovskites: A New Approach to Generate High-Performance Nanohybrid Catalysts. *ACS Appl. Mater. Inter.* **2016**, *8*, 2457-2463.
108. Arandiyan, H.; Dai, H.; Deng, J.; Liu, Y.; Bai, B.; Wang, Y.; Li, X.; Xie, S.; Li, J., Three-dimensionally ordered macroporous $La_{0.6}Sr_{0.4}MnO_3$ with high surface areas: Active catalysts for the combustion of methane. *J. Catal.* **2013**, *307*, 327-339.
109. Kim, S.; Lee, D.-W.; Lee, J. Y.; Eom, H.-J.; Lee, H. J.; Cho, I.-h.; Lee, K.-Y., Catalytic combustion of methane in simulated PSA offgas over Mn-substituted La–Sr-hexaaluminate ($La_xSr_{1-x}MnAl_{11}O_{19}$). *J. Mol. Catal. A: Chem.* **2011**, *335*, 60-64.
110. Pérez-Cadenas, A. F.; Kapteijn, F.; Moulijn, J. A., Tuning the morphology of monolith coatings. *Appl. Catal., A* **2007**, *319*, 267-271.
111. Liao, H.; Zuo, P.; Liu, M., Study on the correlation between the surface active species of Pd/cordierite monolithic catalyst and its catalytic activity. *Mater. Sci. Eng., B* **2016**, *211*, 45-52.
112. Ren, Z.; Botu, V.; Wang, S.; Meng, Y.; Song, W.; Guo, Y.; Ramprasad, R.; Suib, S. L.; Gao, P.-X., Monolithically Integrated Spinel $M_xCo_{3-x}O_4$ (M=Co, Ni, Zn) Nanoarray Catalysts: Scalable Synthesis and Cation Manipulation for Tunable Low-Temperature CH_4 and CO Oxidation. *Angew. Chem. Int. Ed.* **2014**, *53*, 7223-7227.
113. Qian, X.; Kuwahara, Y.; Mori, K.; Yamashita, H., Silver Nanoparticles Supported on CeO_2-SBA-15 by Microwave Irradiation Possess Metal–Support Interactions and Enhanced Catalytic Activity. *Chem. Eur. J.* **2014**, *20*, 15746-15752.
114. Chiang, C.-W.; Wang, A.; Mou, C.-Y., CO oxidation catalyzed by gold nanoparticles confined in mesoporous aluminosilicate Al-SBA-15: Pretreatment methods. *Catal. Today* **2006**, *117*, 220-227.
115. Yeh, Y.-Q.; Lin, H.-P.; Tang, C.-Y.; Mou, C.-Y., Mesoporous silica SBA-15 sheet with perpendicular nanochannels. *J. Colloid. Interf. Sci.* **2011**, *362*, 354-366.
116. Fan, J.; Jiang, X.; Min, H.; Li, D.; Ran, X.; Zou, L.; Sun, Y.; Li, W.; Yang, J.; Teng, W.; Li, G.; Zhao, D., Facile preparation of Cu–Mn/CeO_2/SBA-15 catalysts using ceria as an auxiliary for advanced oxidation processes. *J. Mater. Chem. A* **2014**, *2*, 10654-10661.
117. Chiang, C.-W.; Wang, A.; Wan, B.-Z.; Mou, C.-Y., High Catalytic Activity for CO Oxidation of Gold Nanoparticles Confined in Acidic Support Al-SBA-15 at Low Temperatures. *J. Phys. Chem. B* **2005**, *109*, 18042-18047.
118. Tao, Q.; Xu, Z.; Wang, J.; Liu, F.; Wan, H.; Zheng, S., Adsorption of humic acid to aminopropyl functionalized SBA-15. *Micropor. Mesopor. Mat.* **2010**, *131*, 177-185.

119. Frost, R. L.; Yang, J.; Ding, Z., Raman and FTIR spectroscopy of natural oxalates: Implications for the evidence of life on Mars. *Chinese Sci. Bull.* **2003**, *48*, 1844-1852.
120. MacLachlan, M. J.; Aroca, P.; Coombs, N.; Manners, I.; Ozin, G. A., Ring-Opening Polymerization of a [1]Silaferrocenophane Within the Channels of Mesoporous Silica: Poly(ferrocenylsilane)-MCM-41 Precursors to Magnetic Iron Nanostructures. *Adv. Mater.* **1998**, *10*, 144-149.
121. Larcher, D.; Gérand, B.; Tarascon, J.-M., Synthesis and electrochemical performances of $Li_{1+y}Mn_{2-y}O_4$ powders of well-defined morphology. *J. Solid State Electr.* **1998**, *2*, 137-145.
122. Zhai, Y.; Zhang, S.; Pang, H., Preparation, characterization and photocatalytic activity of CeO_2 nanocrystalline using ammonium bicarbonate as precipitant. *Mater. Lett.* **2007**, *61*, 1863-1866.
123. Venezia, A. M.; Pantaleo, G.; Longo, A.; Di Carlo, G.; Casaletto, M. P.; Liotta, F. L.; Deganello, G., Relationship between Structure and CO Oxidation Activity of Ceria-Supported Gold Catalysts. *J. Phys. Chem. B* **2005**, *109*, 2821-2827.
124. Zhang, Y.; Qin, Z.; Wang, G.; Zhu, H.; Dong, M.; Li, S.; Wu, Z.; Li, Z.; Wu, Z.; Zhang, J.; Hu, T.; Fan, W.; Wang, J., Catalytic performance of MnO_x–NiO composite oxide in lean methane combustion at low temperature. *Appl. Catal., B* **2013**, *129*, 172-181.
125. Jodłowski, P. J.; Jędrzejczyk, R. J.; Chlebda, D. K.; Dziedzicka, A.; Kuterasiński, Ł.; Gancarczyk, A.; Sitarz, M., Non-Noble Metal Oxide Catalysts for Methane Catalytic Combustion: Sonochemical Synthesis and Characterisation. *Nanomaterials (Basel)* **2017**, *7*, 174.
126. Watt, J.; Yu, C.; Chang, S. L. Y.; Cheong, S.; Tilley, R. D., Shape Control from Thermodynamic Growth Conditions: The Case of hcp Ruthenium Hourglass Nanocrystals. *J. Am. Chem. Soc.* **2013**, *135*, 606-609.
127. Guo, H.; Chen, Y.; Ping, H.; Wang, L.; Peng, D.-L., One-pot synthesis of hexagonal and triangular nickel–copper alloy nanoplates and their magnetic and catalytic properties. *J. Mater. Chem.* **2012**, *22*, 8336-8344.
128. Liu, C.; Xian, H.; Jiang, Z.; Wang, L.; Zhang, J.; Zheng, L.; Tan, Y.; Li, X., Insight into the improvement effect of the Ce doping into the SnO_2 catalyst for the catalytic combustion of methane. *Appl. Catal., B* **2015**, *176-177*, 542-552.
129. Li, D.; Li, K.; Xu, R.; Wang, H.; Tian, D.; Wei, Y.; Zhu, X.; Zeng, C.; Zeng, L., $Ce_{1-x}Fe_xO_{2-\delta}$ catalysts for catalytic methane combustion: Role of oxygen vacancy and structural dependence. *Catal. Today* **2018**, *318*, 73-85.
130. Zhao, H. Y.; Li, D.; Bui, P.; Oyama, S. T., Hydrodeoxygenation of guaiacol as model compound for pyrolysis oil on transition metal phosphide hydroprocessing catalysts. *Appl. Catal., A* **2011**, *391*, 305-310.
131. Higashimoto, S.; Kitao, N.; Yoshida, N.; Sakura, T.; Azuma, M.; Ohue, H.; Sakata, Y., Selective photocatalytic oxidation of benzyl alcohol and its derivatives into corresponding aldehydes by molecular oxygen on titanium dioxide under visible light irradiation. *J. Catal.* **2009**, *266*, 279-285.

132. Keresszegi, C.; Ferri, D.; Mallat, T.; Baiker, A., Unraveling the Surface Reactions during Liquid-Phase Oxidation of Benzyl Alcohol on Pd/Al_2O_3: an in Situ ATR−IR Study. *J. Phys. Chem. B* **2005**, *109*, 958-967.
133. Chen, L.; Hu, J.; Richards, R.; Prikhodko, S.; Kodambaka, S., Synthesis and surface activity of single-crystalline Co_3O_4 (111) holey nanosheets. *Nanoscale* **2010**, *2*, 1657-1660.
134. Al-Mamun, M.; Su, X. T.; Zhang, H. M.; Yin, H. J.; Liu, P. R.; Yang, H. G.; Wang, D.; Tang, Z. Y.; Wang, Y.; Zhao, H. J., Strongly Coupled $CoCr_2O_4$/Carbon Nanosheets as High Performance Electrocatalysts for Oxygen Evolution Reaction. *Small* **2016**, *12*, 2866-2871.
135. Wang, Y.; Jia, A. P.; Luo, M. F.; Lu, J. Q., Highly active spinel type $CoCr_2O_4$ catalysts for dichloromethane oxidation. *Appl. Catal., B* **2015**, *165*, 477-486.
136. Zhang, T. T.; Song, J. D.; Chen, J. X.; Jia, A. P.; Luo, M. F.; Lu, J. Q., Catalytic combustion of dichloromethane over supported $CoCr_2O_4$/TUD-1 catalysts: The effect of $CoCr_2O_4$ particle size on the modification of surface properties and the catalytic performance. *Appl. Surf. Sci.* **2017**, *425*, 1074-1081.
137. Sadokhina, N.; Smedler, G.; Nylén, U.; Olofsson, M.; Olsson, L., Deceleration of SO_2 poisoning on $PtPd/Al_2O_3$ catalyst during complete methane oxidation. *Appl. Catal., B* **2018**, *236*, 384-395.
138. Choya, A.; de Rivas, B.; González-Velasco, J. R.; Gutiérrez-Ortiz, J. I.; López-Fonseca, R., Oxidation of residual methane from VNG vehicles over Co_3O_4-based catalysts: Comparison among bulk, Al_2O_3-supported and Ce-doped catalysts. *Appl. Catal., B* **2018**, *237*, 844-854.
139. Guo, G., High specific surface area $LaMO_3$ (M = Co, Mn) hollow spheres: synthesis, characterization and catalytic properties in methane combustion. *Rsc. Adv.* **2014**, *4*, 58699-58707.
140. Jansson, J.; Palmqvist, A. E. C.; Fridell, E.; Skoglundh, M.; Österlund, L.; Thormählen, P.; Langer, V., On the Catalytic Activity of Co_3O_4 in Low-Temperature CO Oxidation. *J. Catal.* **2002**, *211*, 387-397.
141. Mahara, Y.; Murata, K.; Ueda, K.; Ohyama, J.; Kato, K.; Satsuma, A., Time Resolved in situ DXAFS Revealing Highly Active Species of PdO Nanoparticle Catalyst for CH_4 Oxidation. *Chemcatchem* **2018**, *10*, 3384-3387.
142. Long, Y.; Hui, J.-f.; Wang, P.-p.; Hu, S.; Xu, B.; Xiang, G.-l.; Zhuang, J.; Lü, X.-q.; Wang, X., α-MnO_2 nanowires as building blocks for the construction of 3D macro-assemblies. *Chem. Commun.* **2012**, *48*, 5925-5927.
143. Zhang, H.; Lin, C.; Han, T.; Du, F.; Zhao, Y.; Li, X.; Sun, Y., Visualization of the Formation and 3D Porous Structure of Ag Doped MnO_2 Aerogel Monoliths with High Photocatalytic Activity. *ACS Sustain. Chem. Eng.* **2016**, *4*, 6277-6287.
144. Rong, S.; Zhang, P.; Yang, Y.; Zhu, L.; Wang, J.; Liu, F., MnO_2 Framework for Instantaneous Mineralization of Carcinogenic Airborne Formaldehyde at Room Temperature. *ACS Catal.* **2017**, *7*, 1057-1067.
145. Jung, S. M.; Jung, H. Y.; Fang, W.; Dresselhaus, M. S.; Kong, J., A Facile Methodology for the Production of In Situ Inorganic Nanowire Hydrogels/Aerogels. *Nano. Lett.* **2014**, *14*, 1810-1817.

146. Liu, Y.-H.; Lin, H.-P.; Mou, C.-Y., Direct Method for Surface Silyl Functionalization of Mesoporous Silica. *Langmuir* **2004**, *20*, 3231-3239.

Appendices

Appendix A Supporting information for Chapter 2

A.1 Loading calculations of silica surface

After surface modification of mesoporous silica, the amount of APTS loaded on the sample was determined by elemental analysis. The loading of grafted groups (τ) was calculated by Equation A.1.1.[146] $\Delta W_N\%$ is the weight percent of nitrogen (*N*), and $\Delta W_{SiO_2}\%$ is the weight percent of SiO_2. M_N represents the atomic mass of *N*, and n is the number of *N* in one molecule of APTS.

$$\tau = \frac{\Delta W_N\% \times 1000}{\Delta W_{SiO_2}\% \times n M_N} \text{ mmol/g } SiO_2 \qquad \text{Equation A. 1.1}$$

The surface density (α) of loaded APTS was calculated from Equation A.1.2 where N_A is Avogadro's number and S_{BET} is the surface area of SBA-15.

$$\alpha = \frac{\tau N_A}{1000 S_{BET}} \times 10^{-20}\ groups/nm^2$$

Equation A. 1.2

Appendix B Supporting information for Chapter 4

B.1 Determination of activation energy

Previous research indicated that in oxidizing conditions, methane combustion follows a 1st order reaction mechanism with respect to methane. In this work, oxygen is in excess, so the reaction has a 1st order reaction mechanism with respect to CH_4. So

$$r_{CH_4} = N_{CH_4} X \quad \text{Equation B.1.1}$$

$$r_{CH_4} = \mathrm{k}[CH_4] = \left(\mathrm{A}\exp\left(-\frac{E_a}{RT}\right)\right)[CH_4] \quad \text{Equation B.1.2}$$

$$\ln r_{CH_4} = -\frac{1000E_a}{RT} + \ln A + \ln[CH_4] \quad \text{Equation B.1.3}$$

where r_{CH_4} is reaction rate (μmol/s), N_{CH_4} is methane flow rate (μmol/s), X is the conversion of methane, k is rate constant (s^{-1}), E_a is activation energy (kJ/mol), $[CH_4]$ is methane concentration (μmol) and A is a pre-exponential factor.

The amount of methane is low, so $\ln[CH_4]$ can be assumed to be approximately constant. E_a was obtained by the slope of the linear plot of $\ln r_{CH_4}$ versus 1000/T.

A conversion $X < 20\%$ was used to eliminate thermal and gas diffusion problem. At lower conversion, the active sites are insufficient to react with methane molecules, so the number of active sites has a lesser effect on activation energies. Instead, the efficiency of the active sites plays a more important role on activation energies.

B.2 Figures

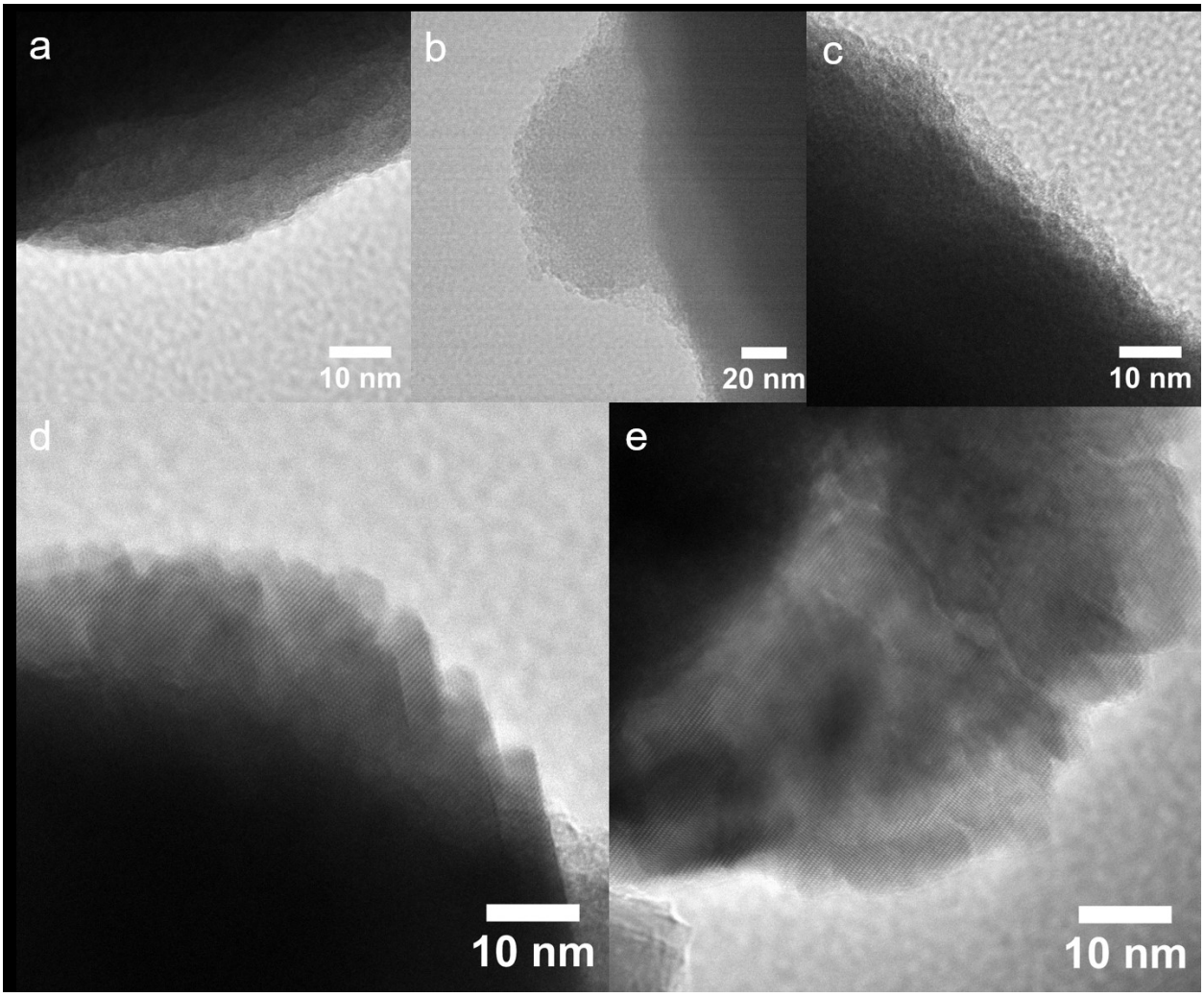

Figure B.1 HRTEM images for $CoCr_2O_4$ before calcination with different solvothermal reaction times a, d: 1 h; b, e: 8 h; c: 24 h.

Appendix C Calculation of methane conversion

The methane conversion was calculated according to the equation as follow,

$$X_{CH_4} = \frac{n_{CO_2}}{n_{CH_4} + n_{CO_2}}$$

To obtain n_{CH_4} and n_{CO_2}, a constant He flow at the rate of 20 mL(STP)/min was added to feed gas. The relative intensities of both CH_4 and CO_2 to the intensity of He was recorded. The change of flow rate ratio of $Y_{CH_4 or\ CO_2}/Y_{He}$ as a function of intensity ratio of $I_{CH_4 or\ CO_2}/I_{He}$ were listed in Table C.1, C.2 and plotted in Figure C.1, C.2 respectively for calibration.

Table C.1 Mass spectrometer (MS) calculation for CH_4/He in the constant flow of 30 mL(STP)/min O_2 and 210 mL(STP)/min Ar.

I_{He} (torr)	I_{CH4} (torr)	I_{CH4}/I_{He}	Y_{CH4}/Y_{He}
2.60E-08	1.94E-09	0.0748	0.0151
2.43E-08	1.54E-09	0.0633	0.0121
2.44E-08	1.16E-09	0.0476	0.0091
2.48E-08	7.83E-10	0.0316	0.0061
2.54E-08	3.97E-10	0.0157	0.0030
2.57E-08	1.94E-10	0.0075	0.0015

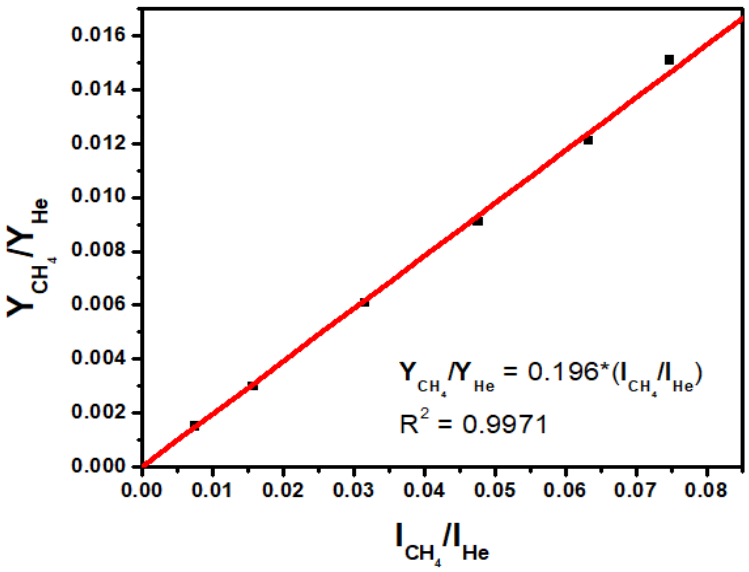

Figure C.1 MS calculation equation plot of CH_4/He

Table C.2 MS calculation for CO_2/He in the constant flow of 10 mL(STP)/min O_2 and 28 mL(STP)/min Ar.

I_{He} (torr)	I_{CO2} (torr)	I_{CO2}/I_{He}	Y_{CO2}/Y_{He}
5.70E-08	2.01E-09	3.52E-02	0.006
7.02E-08	1.87E-09	0.027	0.005
8.85E-08	1.50E-09	0.017	0.003
1.32E-07	6.41E-10	0.005	0.001

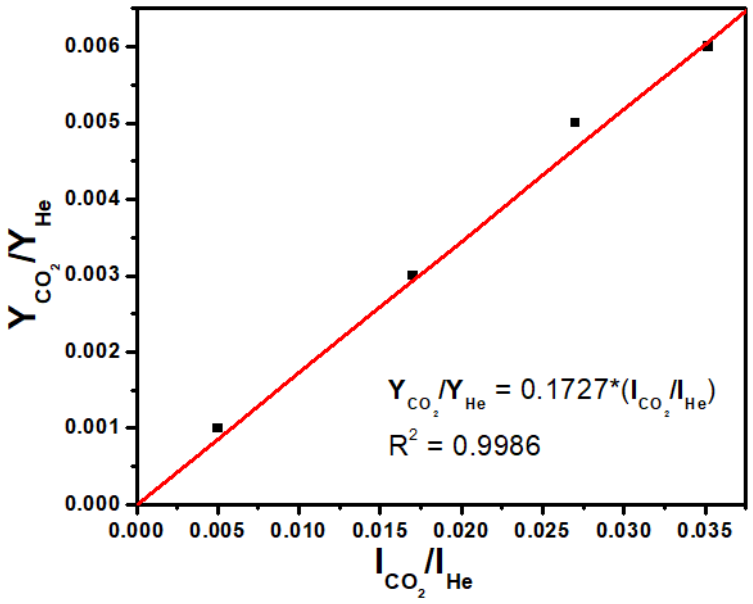

Figure C.2 MS calculation equation plot of CO_2/He.

For catalytic methane oxidation measurement, 0.3 mL/min CH_4, 20 mL/min He, 30 mL/min O_2 balanced by Ar to obtain in total of 300 mL/min flow through the catalysts. 0.1 g catalyst was diluted by 2.5 g SiC and loaded into the reactor. The reactor was heated up at the rate of 5 °C/min. The change of signal intensities for different components were recorded by MS every 40 s. At the beginning, there was a small amount of CO_2 could be detected by MS which may come from environment. So the initial ambient CO_2 is subtracted.

$$X_{CH_4} = \frac{n_{CO_2}}{n_{CH_4} + n_{CO_2}} = \frac{Y_{CO_2(corrected)}}{Y_{CH_4} + Y_{CO_2(corrected)}}$$

$$\mathrm{Y}_{CO_2(corrected)} = \mathrm{Y}_{CO_2} - Y^0_{CO_2}$$

$Y^0_{CO_2}$ indicated the initial CO_2 flow rate at room temperature.

Detailed methane conversion calculation for $CoCr_2O_4$ 8h was shown in Table C3.

Table C.3 Methane conversion calculation for $CoCr_2O_4$ 8h.

T (°C)	I_{He} (Torr)	I_{CH4} (Torr)	I_{CO2} (Torr)	I_{CH4}/I_{He}	I_{CO2}/I_{He}	Y_{CH4}/Y_{He}	Y_{CO2}/Y_{He}	Y_{CH4} (mL/min)	Y_{CO2} (mL/min)	$Y_{CO2\ corrected}$ (mL/min)	X_{CH4}
102.39	7.69E-09	5.46E-10	6.04E-11	7.10E-02	7.85E-03	1.52E-02	1.64E-03	0.3	0.03	0.01	2%
104.76	7.70E-09	5.46E-10	6.03E-11	7.09E-02	7.83E-03	1.51E-02	1.63E-03	0.3	0.03	0.01	2%
106.91	7.69E-09	5.43E-10	6.02E-11	7.06E-02	7.84E-03	1.51E-02	1.63E-03	0.3	0.03	0.01	2%
108.75	7.69E-09	5.45E-10	6.13E-11	7.08E-02	7.97E-03	1.51E-02	1.66E-03	0.3	0.03	0.01	2%
110.45	7.70E-09	5.47E-10	6.16E-11	7.11E-02	7.99E-03	1.52E-02	1.66E-03	0.3	0.03	0.01	2%
112.3	7.69E-09	5.47E-10	6.06E-11	7.12E-02	7.89E-03	1.52E-02	1.64E-03	0.3	0.03	0.01	2%
114.41	7.70E-09	5.44E-10	6.09E-11	7.06E-02	7.90E-03	1.51E-02	1.65E-03	0.3	0.03	0.01	2%
117.09	7.68E-09	5.44E-10	6.04E-11	7.08E-02	7.87E-03	1.51E-02	1.64E-03	0.3	0.03	0.01	2%
120.39	7.69E-09	5.45E-10	6.04E-11	7.08E-02	7.85E-03	1.51E-02	1.64E-03	0.3	0.03	0.01	2%
124.06	7.69E-09	5.44E-10	6.11E-11	7.08E-02	7.94E-03	1.51E-02	1.65E-03	0.3	0.03	0.01	2%
128.04	7.69E-09	5.44E-10	6.00E-11	7.07E-02	7.80E-03	1.51E-02	1.62E-03	0.3	0.03	0.01	2%
132.09	7.71E-09	5.47E-10	6.01E-11	7.09E-02	7.79E-03	1.51E-02	1.62E-03	0.3	0.03	0.01	2%
136.09	7.69E-09	5.46E-10	6.06E-11	7.10E-02	7.89E-03	1.52E-02	1.64E-03	0.3	0.03	0.01	2%
139.95	7.70E-09	5.44E-10	6.11E-11	7.07E-02	7.94E-03	1.51E-02	1.65E-03	0.3	0.03	0.01	2%
143.59	7.70E-09	5.46E-10	5.98E-11	7.09E-02	7.76E-03	1.51E-02	1.62E-03	0.3	0.03	0.01	2%
147.02	7.70E-09	5.45E-10	6.11E-11	7.08E-02	7.94E-03	1.51E-02	1.65E-03	0.3	0.03	0.01	2%
150.32	7.69E-09	5.44E-10	5.95E-11	7.07E-02	7.73E-03	1.51E-02	1.61E-03	0.3	0.03	0.01	2%
153.41	7.68E-09	5.43E-10	5.96E-11	7.07E-02	7.76E-03	1.51E-02	1.62E-03	0.3	0.03	0.01	2%
156.34	7.67E-09	5.43E-10	5.93E-11	7.08E-02	7.73E-03	1.51E-02	1.61E-03	0.3	0.03	0.01	2%
159.27	7.69E-09	5.45E-10	6.00E-11	7.08E-02	7.81E-03	1.51E-02	1.63E-03	0.3	0.03	0.01	2%
162.25	7.68E-09	5.43E-10	5.98E-11	7.07E-02	7.79E-03	1.51E-02	1.62E-03	0.3	0.03	0.01	2%
165.17	7.66E-09	5.42E-10	5.94E-11	7.07E-02	7.76E-03	1.51E-02	1.62E-03	0.3	0.03	0.01	2%
168.11	7.69E-09	5.43E-10	5.88E-11	7.07E-02	7.65E-03	1.51E-02	1.59E-03	0.3	0.03	0.01	2%
171.15	7.70E-09	5.44E-10	5.84E-11	7.07E-02	7.59E-03	1.51E-02	1.58E-03	0.3	0.03	0.01	2%
174.17	7.70E-09	5.42E-10	5.84E-11	7.04E-02	7.59E-03	1.50E-02	1.58E-03	0.3	0.03	0.01	2%
177.19	7.69E-09	5.43E-10	5.98E-11	7.06E-02	7.77E-03	1.51E-02	1.62E-03	0.3	0.03	0.01	4%

180.17	7.68E-09	5.43E-10	5.97E-11	7.07E-02	7.78E-03	1.51E-02	1.62E-03	0.3	0.03	0.01	2%
183.28	7.71E-09	5.44E-10	5.96E-11	7.06E-02	7.73E-03	1.51E-02	1.61E-03	0.3	0.03	0.01	5%
186.23	7.69E-09	5.44E-10	5.92E-11	7.08E-02	7.70E-03	1.51E-02	1.60E-03	0.3	0.03	0.01	5%
189.34	7.69E-09	5.45E-10	5.89E-11	7.09E-02	7.66E-03	1.51E-02	1.60E-03	0.3	0.03	0.01	5%
192.38	7.70E-09	5.47E-10	6.00E-11	7.10E-02	7.79E-03	1.52E-02	1.62E-03	0.3	0.03	0.01	2%
195.4	7.69E-09	5.43E-10	5.92E-11	7.07E-02	7.70E-03	1.51E-02	1.60E-03	0.3	0.03	0.01	2%
198.45	7.69E-09	5.42E-10	6.01E-11	7.05E-02	7.82E-03	1.51E-02	1.63E-03	0.3	0.03	0.01	2%
201.47	7.67E-09	5.41E-10	6.00E-11	7.05E-02	7.82E-03	1.51E-02	1.63E-03	0.3	0.03	0.01	2%
204.47	7.69E-09	5.42E-10	4.80E-11	7.05E-02	6.24E-03	1.51E-02	1.30E-03	0.3	0.03	0	0%
207.53	7.67E-09	5.41E-10	6.11E-11	7.06E-02	7.96E-03	1.51E-02	1.66E-03	0.3	0.03	0.01	2%
210.66	7.68E-09	5.40E-10	6.07E-11	7.04E-02	7.90E-03	1.50E-02	1.65E-03	0.3	0.03	0.01	2%
213.66	7.68E-09	5.42E-10	6.15E-11	7.05E-02	8.01E-03	1.51E-02	1.67E-03	0.3	0.03	0.01	2%
216.66	7.68E-09	5.42E-10	6.22E-11	7.06E-02	8.10E-03	1.51E-02	1.69E-03	0.3	0.03	0.01	3%
219.62	7.71E-09	5.43E-10	6.24E-11	7.05E-02	8.10E-03	1.51E-02	1.69E-03	0.3	0.03	0.01	3%
222.7	7.71E-09	5.42E-10	6.25E-11	7.02E-02	8.11E-03	1.50E-02	1.69E-03	0.3	0.03	0.01	3%
225.74	7.68E-09	5.41E-10	6.27E-11	7.03E-02	8.16E-03	1.50E-02	1.70E-03	0.3	0.03	0.01	3%
228.7	7.70E-09	5.43E-10	6.27E-11	7.05E-02	8.15E-03	1.51E-02	1.70E-03	0.3	0.03	0.01	3%
231.69	7.69E-09	5.41E-10	6.35E-11	7.04E-02	8.26E-03	1.50E-02	1.72E-03	0.3	0.03	0.01	3%
234.77	7.70E-09	5.40E-10	6.49E-11	7.02E-02	8.44E-03	1.50E-02	1.76E-03	0.3	0.04	0.01	3%
237.74	7.69E-09	5.40E-10	6.50E-11	7.02E-02	8.45E-03	1.50E-02	1.76E-03	0.3	0.04	0.01	3%
240.79	7.70E-09	5.42E-10	6.41E-11	7.04E-02	8.33E-03	1.50E-02	1.74E-03	0.3	0.03	0.01	3%
243.82	7.70E-09	5.39E-10	6.54E-11	7.01E-02	8.50E-03	1.50E-02	1.77E-03	0.3	0.04	0.01	3%
246.93	7.70E-09	5.40E-10	6.56E-11	7.00E-02	8.51E-03	1.50E-02	1.77E-03	0.3	0.04	0.01	3%
249.91	7.70E-09	5.42E-10	6.69E-11	7.03E-02	8.69E-03	1.50E-02	1.81E-03	0.3	0.04	0.01	3%
253	7.71E-09	5.40E-10	6.72E-11	7.00E-02	8.72E-03	1.50E-02	1.82E-03	0.3	0.04	0.01	3%
256.04	7.71E-09	5.41E-10	6.83E-11	7.02E-02	8.86E-03	1.50E-02	1.85E-03	0.3	0.04	0.01	4%
259.06	7.71E-09	5.40E-10	5.72E-11	7.01E-02	7.42E-03	1.50E-02	1.55E-03	0.3	0.03	0	2%
262.15	7.70E-09	5.36E-10	6.88E-11	6.96E-02	8.93E-03	1.49E-02	1.86E-03	0.3	0.04	0.01	4%
265.15	7.68E-09	5.35E-10	6.88E-11	6.97E-02	8.97E-03	1.49E-02	1.87E-03	0.3	0.04	0.01	4%

268.24	7.69E-09	5.35E-10	7.03E-11	6.95E-02	9.14E-03	1.48E-02	1.90E-03	0.3	0.04	0.01	4%
271.25	7.66E-09	5.32E-10	6.94E-11	6.94E-02	9.06E-03	1.48E-02	1.89E-03	0.3	0.04	0.01	4%
274.27	7.67E-09	5.32E-10	7.00E-11	6.93E-02	9.13E-03	1.48E-02	1.90E-03	0.3	0.04	0.01	4%
277.31	7.67E-09	5.30E-10	7.13E-11	6.91E-02	9.30E-03	1.48E-02	1.94E-03	0.3	0.04	0.01	4%
280.34	7.68E-09	5.30E-10	7.32E-11	6.91E-02	9.53E-03	1.48E-02	1.98E-03	0.3	0.04	0.01	4%
283.33	7.67E-09	5.28E-10	7.45E-11	6.88E-02	9.72E-03	1.47E-02	2.02E-03	0.29	0.04	0.01	5%
286.37	7.66E-09	5.28E-10	7.50E-11	6.89E-02	9.79E-03	1.47E-02	2.04E-03	0.29	0.04	0.01	5%
289.32	7.66E-09	5.26E-10	7.72E-11	6.86E-02	1.01E-02	1.47E-02	2.10E-03	0.29	0.04	0.02	5%
292.38	7.66E-09	5.24E-10	7.78E-11	6.84E-02	1.02E-02	1.46E-02	2.11E-03	0.29	0.04	0.02	5%
295.48	7.69E-09	5.21E-10	8.05E-11	6.78E-02	1.05E-02	1.45E-02	2.18E-03	0.29	0.04	0.02	6%
298.5	7.70E-09	5.21E-10	8.16E-11	6.77E-02	1.06E-02	1.45E-02	2.21E-03	0.29	0.04	0.02	6%
301.49	7.68E-09	5.19E-10	8.43E-11	6.75E-02	1.10E-02	1.44E-02	2.28E-03	0.29	0.05	0.02	6%
304.51	7.68E-09	5.16E-10	8.86E-11	6.71E-02	1.15E-02	1.43E-02	2.40E-03	0.29	0.05	0.02	7%
307.6	7.70E-09	5.16E-10	9.05E-11	6.70E-02	1.18E-02	1.43E-02	2.45E-03	0.29	0.05	0.02	7%
310.65	7.70E-09	5.14E-10	9.39E-11	6.67E-02	1.22E-02	1.43E-02	2.54E-03	0.29	0.05	0.02	8%
313.68	7.70E-09	5.10E-10	9.56E-11	6.63E-02	1.24E-02	1.42E-02	2.58E-03	0.28	0.05	0.03	8%
316.72	7.70E-09	5.04E-10	9.88E-11	6.55E-02	1.28E-02	1.40E-02	2.67E-03	0.28	0.05	0.03	9%
319.69	7.71E-09	5.04E-10	1.03E-10	6.53E-02	1.33E-02	1.39E-02	2.78E-03	0.28	0.06	0.03	10%
322.72	7.69E-09	4.99E-10	1.06E-10	6.49E-02	1.38E-02	1.39E-02	2.88E-03	0.28	0.06	0.03	10%
325.77	7.67E-09	4.92E-10	1.09E-10	6.42E-02	1.43E-02	1.37E-02	2.97E-03	0.27	0.06	0.03	11%
328.76	7.66E-09	4.88E-10	1.15E-10	6.36E-02	1.50E-02	1.36E-02	3.12E-03	0.27	0.06	0.04	12%
331.84	7.69E-09	4.84E-10	1.20E-10	6.29E-02	1.56E-02	1.34E-02	3.24E-03	0.27	0.06	0.04	13%
334.85	7.67E-09	4.77E-10	1.25E-10	6.23E-02	1.63E-02	1.33E-02	3.40E-03	0.27	0.07	0.04	14%
337.84	7.68E-09	4.73E-10	1.31E-10	6.17E-02	1.70E-02	1.32E-02	3.54E-03	0.26	0.07	0.04	15%
340.94	7.65E-09	4.67E-10	1.36E-10	6.10E-02	1.77E-02	1.30E-02	3.69E-03	0.26	0.07	0.05	15%
343.96	7.68E-09	4.61E-10	1.42E-10	5.99E-02	1.85E-02	1.28E-02	3.84E-03	0.26	0.08	0.05	17%
347.07	7.69E-09	4.53E-10	1.49E-10	5.89E-02	1.93E-02	1.26E-02	4.03E-03	0.25	0.08	0.05	18%
350.12	7.68E-09	4.46E-10	1.54E-10	5.81E-02	2.01E-02	1.24E-02	4.19E-03	0.25	0.08	0.06	19%
353.15	7.66E-09	4.38E-10	1.62E-10	5.71E-02	2.12E-02	1.22E-02	4.41E-03	0.24	0.09	0.06	20%

356.21	7.67E-09	4.28E-10	1.70E-10	5.59E-02	2.22E-02	1.19E-02	4.62E-03	0.24	0.09	0.07	22%
359.22	7.65E-09	4.19E-10	1.78E-10	5.47E-02	2.33E-02	1.17E-02	4.85E-03	0.23	0.1	0.07	23%
362.27	7.66E-09	4.10E-10	1.87E-10	5.35E-02	2.44E-02	1.14E-02	5.09E-03	0.23	0.1	0.08	25%
365.31	7.67E-09	4.04E-10	1.96E-10	5.27E-02	2.56E-02	1.13E-02	5.34E-03	0.23	0.11	0.08	26%
368.33	7.67E-09	3.94E-10	2.04E-10	5.15E-02	2.67E-02	1.10E-02	5.55E-03	0.22	0.11	0.09	28%
371.34	7.65E-09	3.83E-10	2.13E-10	5.00E-02	2.79E-02	1.07E-02	5.81E-03	0.21	0.12	0.09	30%
374.31	7.69E-09	3.73E-10	2.23E-10	4.85E-02	2.90E-02	1.04E-02	6.04E-03	0.21	0.12	0.09	31%
377.42	7.66E-09	3.61E-10	2.33E-10	4.71E-02	3.04E-02	1.01E-02	6.33E-03	0.2	0.13	0.1	33%
380.42	7.67E-09	3.51E-10	2.43E-10	4.58E-02	3.16E-02	9.77E-03	6.59E-03	0.2	0.13	0.11	35%
383.43	7.67E-09	3.38E-10	2.55E-10	4.41E-02	3.32E-02	9.41E-03	6.91E-03	0.19	0.14	0.11	37%
386.53	7.67E-09	3.28E-10	2.64E-10	4.27E-02	3.45E-02	9.13E-03	7.18E-03	0.18	0.14	0.12	39%
389.58	7.67E-09	3.15E-10	2.76E-10	4.11E-02	3.60E-02	8.78E-03	7.50E-03	0.18	0.15	0.12	41%
392.57	7.67E-09	3.03E-10	2.87E-10	3.95E-02	3.75E-02	8.44E-03	7.80E-03	0.17	0.16	0.13	44%
395.62	7.66E-09	2.91E-10	2.98E-10	3.80E-02	3.88E-02	8.11E-03	8.09E-03	0.16	0.16	0.14	46%
398.67	7.66E-09	2.78E-10	3.08E-10	3.63E-02	4.02E-02	7.76E-03	8.38E-03	0.16	0.17	0.14	48%
401.59	7.65E-09	2.64E-10	3.20E-10	3.45E-02	4.19E-02	7.38E-03	8.72E-03	0.15	0.17	0.15	50%
404.52	7.66E-09	2.52E-10	3.31E-10	3.29E-02	4.32E-02	7.03E-03	9.01E-03	0.14	0.18	0.15	52%
407.68	7.64E-09	2.37E-10	3.42E-10	3.11E-02	4.47E-02	6.64E-03	9.31E-03	0.13	0.19	0.16	55%
410.67	7.67E-09	2.26E-10	3.54E-10	2.94E-02	4.61E-02	6.29E-03	9.61E-03	0.13	0.19	0.17	57%
413.7	7.65E-09	2.13E-10	3.67E-10	2.79E-02	4.79E-02	5.95E-03	9.98E-03	0.12	0.2	0.17	59%
416.59	7.65E-09	1.99E-10	3.78E-10	2.61E-02	4.94E-02	5.56E-03	1.03E-02	0.11	0.21	0.18	62%
419.7	7.65E-09	1.87E-10	3.90E-10	2.44E-02	5.10E-02	5.21E-03	1.06E-02	0.1	0.21	0.19	64%
422.71	7.65E-09	1.74E-10	4.00E-10	2.28E-02	5.23E-02	4.86E-03	1.09E-02	0.1	0.22	0.19	66%
425.75	7.64E-09	1.62E-10	4.12E-10	2.12E-02	5.39E-02	4.52E-03	1.12E-02	0.09	0.22	0.2	69%
428.73	7.67E-09	1.49E-10	4.23E-10	1.94E-02	5.52E-02	4.15E-03	1.15E-02	0.08	0.23	0.2	71%
431.82	7.66E-09	1.38E-10	4.32E-10	1.80E-02	5.64E-02	3.84E-03	1.17E-02	0.08	0.23	0.21	73%
434.86	7.65E-09	1.25E-10	4.42E-10	1.64E-02	5.78E-02	3.50E-03	1.20E-02	0.07	0.24	0.21	75%
437.88	7.66E-09	1.15E-10	4.52E-10	1.50E-02	5.90E-02	3.21E-03	1.23E-02	0.06	0.25	0.22	77%
440.95	7.64E-09	9.86E-11	4.62E-10	1.29E-02	6.04E-02	2.75E-03	1.26E-02	0.06	0.25	0.23	80%

443.96	7.66E-09	8.93E-11	4.72E-10	1.17E-02	6.15E-02	2.49E-03	1.28E-02	0.05	0.26	0.23	82%
447.01	7.65E-09	8.22E-11	4.81E-10	1.07E-02	6.29E-02	2.29E-03	1.31E-02	0.05	0.26	0.24	84%
450.13	7.65E-09	6.67E-11	4.90E-10	8.72E-03	6.40E-02	1.86E-03	1.33E-02	0.04	0.27	0.24	87%
453.1	7.65E-09	5.95E-11	4.99E-10	7.78E-03	6.52E-02	1.66E-03	1.36E-02	0.03	0.27	0.25	88%
456.17	7.65E-09	5.20E-11	5.04E-10	6.80E-03	6.60E-02	1.45E-03	1.37E-02	0.03	0.27	0.25	90%
459.19	7.65E-09	4.39E-11	5.13E-10	5.74E-03	6.71E-02	1.23E-03	1.40E-02	0.02	0.28	0.25	91%
462.19	7.65E-09	3.68E-11	5.18E-10	4.81E-03	6.77E-02	1.03E-03	1.41E-02	0.02	0.28	0.26	93%
465.2	7.66E-09	2.99E-11	5.23E-10	3.91E-03	6.83E-02	8.35E-04	1.42E-02	0.02	0.28	0.26	94%
468.21	7.66E-09	2.19E-11	5.30E-10	2.86E-03	6.92E-02	6.10E-04	1.44E-02	0.01	0.29	0.26	96%
471.2	7.65E-09	1.84E-11	5.37E-10	2.40E-03	7.02E-02	5.13E-04	1.46E-02	0.01	0.29	0.27	96%
474.2	7.66E-09	1.23E-11	5.40E-10	1.61E-03	7.04E-02	3.44E-04	1.47E-02	0.01	0.29	0.27	97%
477.21	7.66E-09	9.00E-12	5.45E-10	1.17E-03	7.11E-02	2.51E-04	1.48E-02	0.01	0.3	0.27	98%
480.26	7.66E-09	5.16E-12	5.50E-10	6.74E-04	7.19E-02	1.44E-04	1.50E-02	0	0.3	0.27	99%
483.38	7.63E-09	3.43E-12	5.54E-10	4.49E-04	7.26E-02	9.60E-05	1.51E-02	0	0.3	0.28	99%
486.39	7.63E-09	-1.02E-12	5.59E-10	-1.34E-04	7.33E-02	-2.86E-05	1.53E-02	0	0.31	0.28	100%
489.38	7.66E-09	-4.57E-12	5.61E-10	-5.97E-04	7.33E-02	-1.27E-04	1.53E-02	0	0.31	0.28	100%
492.42	7.65E-09	-3.44E-12	5.65E-10	-4.50E-04	7.39E-02	-9.60E-05	1.54E-02	0	0.31	0.28	100%
495.49	7.66E-09	-5.03E-12	5.69E-10	-6.57E-04	7.43E-02	-1.40E-04	1.55E-02	0	0.31	0.28	100%
498.39	7.64E-09	-7.43E-12	5.71E-10	-9.73E-04	7.47E-02	-2.08E-04	1.56E-02	0	0.31	0.29	100%
501.46	7.64E-09	-1.11E-11	5.72E-10	-1.45E-03	7.49E-02	-3.11E-04	1.56E-02	-0.01	0.31	0.29	100%
504.45	7.64E-09	-1.22E-11	5.74E-10	-1.60E-03	7.52E-02	-3.41E-04	1.57E-02	-0.01	0.31	0.29	100%
507.43	7.63E-09	-1.04E-11	5.78E-10	-1.36E-03	7.57E-02	-2.91E-04	1.58E-02	-0.01	0.32	0.29	100%

Appendix D Repeatability for TPO measurements

Table D.1 Repeatability analysis for TPO curves at $T_{50\%}$ and $T_{90\%}$.

Catalysts		Conversion temperature (°C)			average	S.D.
		Repeat 1	Repeat 2	Repeat 3		
PdCFPdSBA-15(M) 5%Pd	50%	301	295	296	297.3	3.2
	90%	335	327	323	328.3	6.1
$NiCo_2O_4$ (calcined at 450 °C)	50%	375	377	380	377.3	2.5
	90%	423	425	429	425.6	3.1
$CoCr_2O_4$ (8h)	50%	398	402	394	398.0	4.0
	90%	453	451	454	452.6	1.5

Appendix E Mass transfer effect

E.1 Internal and external mass transfer calculation

The mass transfer effect was checked by the Weisz-Prater criterion (C_{WP}) and Mears' criterion (C_M) for internal and external diffusion respectively. (methane conversion = 100%)

$$C_{WP} = \frac{-r_{CH_4}\rho_{bSiC}d_p^2}{D_{eff}C_{sur}} < 1 \; ; \; C_M = \frac{-r_{CH_4}\rho_{bSiC}d_p n}{k_c C_{CH_4}} < 0.15$$

$-r_{CH_4}$: Methane reaction rate (mol/(kg_{cat}·s)), $-r_{CH_4}$=2.22E-3 mol/(kg_{cat}·s);

ρ_{bSiC}: Catalyst density of both catalyst and SiC (g/cm^3), ρ_{bSiC}=1.595E3 kg/m^3;

d_p: particle diameter (m), the catalysts was sieved to obtain the size in the range of 90-354 μm before loaded into reactor, so the mean particle size, d_p=2.2E-4 m;

n: Reaction order for CH_4, n=1;

k_c: External mass transfer coefficient (m/s), k_c=0.417 m/s;

C_{CH_4}: Bulk concentration of CH_4 (mol/m^3), C_{CH_4}=0.0202 mol/m^3;

D_{eff}: Effective diffusivity (m^2·s), D_{eff}=1.5E-3 (m^2·s);

C_{sur}: CH_4 concentration at the external surface of the catalyst (mol/m^3), $C_{sur} \approx C_{CH_4}$=0.0202 mol/m^3.

C_{WP}=5.656E-3 < 1

C_M=0.092 < 0.15

Therefore, internal and external diffusion effects could be neglected for methane oxidation reaction.

Appendix F Chemicals

F.1 Chapter 2

Cerium(III) nitrate hexahydrate (Sigma-Aldrich, 99%), palladium nitrate dihydrate (Strem Chemicals Inc.), ethylene glycol (Fisher Scientific), (3-aminopropyl)trimethoxysilane (APTS) (Sigma-Aldrich, 97%), and potassium oxalate monohydrate (J.T. Baker Chemical Co.) were used without further purification.

F.2 Chapter 3

Cobalt(II) nitrate hexahydrate (Sigma-Aldrich, ≥ 98%), nickel(II) nitrate hexahydrate (Sigma-Aldrich, ≥ 98.5%), oleylamine (Sigma-Aldrich, technical grade, 70%), hexylamine (Aldrich Chemical Company, Inc. ≥99%) decylamine (Aldrich Chemical Company, Inc. ≥95%) dodecylamine (Aldrich Chemical Company, Inc. ≥99%) hexadecylamine (Aldrich Chemical Company, Inc. 99%) ammonium hydroxide (Fisher Scientific 28.0-30.0%) were used without further purification.

F.3 Chapter 4

Cobalt(II) nitrate hexahydrate (Sigma-Aldrich, ≥ 98%), chromium(III) nitrate nonahydrate (Fisher Scientific, > 96%), cobalt(II) acetate tetrahydrate (Alfa Aesar, 98%), chromium(III) acetate hydrate (Matheson Coleman & Bell Manufacturing Chemists, Inc.), sodium hydroxide (Sigma-Aldrich, ≥ 97.0%), ammonium hydroxide (Fisher Scientific, 28.0 to 30.0 w/w %), methanol (Sigma-Aldrich, ≥ 99.8%), benzyl alcohol (Sigma-Aldrich, ≥ 99%), cordierite monolith (Corning,

400 cpsi), colloidal alumina solution (ULTRA TEC Manufacturing, Inc., GammaSol Colloidal Alumina -0.05 micron), and other solvents were used without further purification.

F.4 Chapter 5

Manganese sulfate monohydrate (Sigma-Aldrich, ≥ 98 %), potassium sulfate (Sigma-Aldrich, ≥ 99 %), ammonium persulfate (Sigma-Aldrich, ≥ 98 %), cobalt(II) acetate tetrahydrate, (Alfa Aesar, 98%), cerium(III) acetate sesquihydrate, (Alfa Aesar, 99.9%) copper acetate (B & A Chemical, Inc.), sodium hydroxide (Sigma-Aldrich, ≥ 98%), cerium(III) nitrate hexahydrate (Sigma-Aldrich, 99%), palladium nitrate dihydrate (Strem Chemicals Inc.), ethylene glycol (Fisher Scientific), tetraethyl orthosilicate (TEOS, Sigma-Aldrich, 98%), ammonium hydroxide (Fisher Chemical, 28.0 to 30.0 w/w %), and other solvents were used without further purification.